CHARACTERIZATION OF CONTINUOUS SPATIAL PARTICLE ATOMIC LAYER DEPOSITION

by

JULIA MARILYN HARTIG

B.S., Purdue University, 2016

M.S., University of Colorado, 2019

A thesis submitted to the
Faculty of the Graduate School of the
University of Colorado in partial fulfillment
of the requirement for the degree of
Doctor of Philosophy
Department of Chemical and Biological Engineering
2022

Committee Members:
Alan Weimer
Will Medlin
Robert Davis
Richard Regueiro
Debanjan Mukherjee

Hartig, Julia Marilyn (Ph.D., Chemical Engineering)
Characterization of continuous spatial particle atomic layer deposition
Thesis directed by Professor Alan W. Weimer

By continuously conveying powder through alternating regions of precursor gas via linear vibration, continuous spatial particle ALD reactors were developed to satisfy the low cost and high throughput requirements of large-scale powder processing applications. While mesoscale and atomic-scale simulations have revealed details about the kinetics and molecular transport behavior of ALD processes, models which resolve the coupled gas-solid flow dynamics within particle ALD reactors are still lacking in the literature. This thesis introduces a series of models and experimental measures, in order of increasing complexity, to investigate the multiphase fluid dynamics, heat and mass transfer, and chemical reactions in continuous spatial particle ALD reactors.

A combined experimental and continuum-scale modeling campaign was developed to investigate the gas-solids flow behavior during particle ALD. Discrete element method (DEM) simulations with a fluctuating gravity model for vibration revealed solids plug flow behavior and hopping convection of the powder bed during linear vibration. By kinematically driving a layer of particles approximating the porous baseplate, the gas phase was incorporated in a computational fluid dynamics-discrete element method (CFD-DEM) model to explore the effects of aeration velocity and particle cohesion on the solids flow behavior. To improve powder bed agitation and mixing during convection, different porous mesh baffle designs were explored and incorporated into the baseplate. High speed videography and particle imaging velocimetry (PIV) captured the particle trajectories during vibration to determine the best design for powder mixing. Incorporating insights from the DEM simulations, the high computational expense associated with reactor-scale CFD simulations of particle ALD was reduced significantly by treating the powder bed as a moving porous media (MPM). The new MPM model approach revealed material properties and operating conditions that impact the final product uniformity and the species fractions in the effluent stream. Experimental characterization of the powder substrates and porous reactor baseplates using optical microscopy, surface profilometry, x-ray computed tomography (XRCT), powder rheometry, porometry, porosimetry, and particle size analysis provided application-specific inputs to the CFD-DEM and MPM models.

Dedicated to my wonderful friends & family

ACKNOWLEDGEMENTS

I am incredibly thankful to all who have provided me with support and guidance during my graduate work. My advisor, Alan Weimer, has shown me what innovative chemical processing solutions and out-of-the-box thinking can bring to a research problem and I thank him for that. His emphasis on experimental validation pushed me to understand the limits of my models and strive for high levels of modeling-experimental agreement that I would not have thought were possible. At the University of Colorado, Dragan Meijic, Paul Wingrove, and Charles Bown at the machine shop are responsible for almost all of the custom parts on the continuous reactor. Your combined design and machining expertise has taught me countless lessons such as how not to design an o-ring groove and why stainless steel welding is both a work of art and a science. Dragan in particular has given endless feedback that shaped the direction of my thesis and taught me how much patience and attention to detail is required to become a first-rate machinist. Lucas Jones and Dana Schultz at the electrical shop have always given gracious and detailed responses to my many electronics questions. I've learned so much from your experience and have tremendous appreciation for the value of an expert opinion. My labmates in Team Weimer, our postdoc Kent Warren, and many others in the engineering department too numerous to count have provided meaningful discussions that challenged me to level up my data visualization skills and pushed me to think carefully about my design of experiments.

I would also like to acknowledge the support of my collaborators. At Anton Paar, I would like to thank Abhishek Shetty and Vidumin Dahanayake for providing expertise in powder rheometry and porous media characterization as well as organizing and running analysis of our samples. You went above and beyond to explain not only what measurements you could take, but why we run certain experiments and how the data is interpreted and collected. I am forever grateful for the opportunity to learn from you. My mentors at Sandia National Laboratories, Judith Brown and Dan Bolintineanu, have also supported me in many ways. Judy's solid mechanics expertise and affable nature as a mentor made it easy for me to ask questions and try out new things as an intern. Dan's extensive coding background taught me how important it is to use the right tool for the job, including blending programming languages in ways that take advantage of their strengths, when solving complex problems. Your willingness to tailor our project to my interests made me feel appreciated as a student and an individual. I am sure I will use the skills you taught me in my professional career and beyond.

The aerial arts community at Vertical Fusion deserves a special shout out for their boundless positive energy throughout my 5 years in the PhD program. I have met so many inspiring people in this unlikely gathering place for highly educated STEM professionals. I would especially like to thank my friends Alaina, Sarah, Kayla, Lauren, and Elise who have always been there for emotional support. You are always down to try new things and lift my spirits. Aerial classes are the highlight of my week and I am so grateful to have an activity outside of research that leaves me feeling energized and ready to tackle any challenges at work the next day.

Finally, I could not have completed my thesis without the support and encouragement from my family. I thank my younger sister Kara, who could relate to my struggles as a fellow PhD student and whose confidence is contagious. I would also like to acknowledge my two fantastic parents, Marilyn and Paul Hartig, both Ph.D. recipients themselves who have always celebrated my successes – no matter how small – and assured me of my strengths in times of doubt. Last but not least, I want to thank my amazing fiance Alex Weaver and his dog Ricky, who were always there to comfort me after days of disappointing results. With his keen critical thinking skills and saintlike patience, Alex has acted as a sounding board and participated in late night discussions that inevitably improved my research and kept the bigger picture in sight. You are a constant inspiration and I look forward to more journeys with you.

None of this work would have been possible without the funding provided by the National Science Foundation (NSF GOALI proposal #1852824) and the Graduate Assistance in Areas of National Need (GAANN) program titled "Professional Preparation of Chemical Engineers for Rebuilding the Nation's Infrastructure". This work utilized resources from the University of Colorado Boulder Research Computing Group, which is supported by the National Science Foundation (awards ACI-1532235 and ACI-1532236), the University of Colorado Boulder, and Colorado State University.

TABLE OF CONTENTS

CHAPTER 1. INTRODUCTION

LIST OF TABLES

LIST OF FIGURES

CHAPTER 1

INTRODUCTION

1.1 Overview of Particle Atomic Layer Deposition

Atomic layer deposition (ALD) is a vapor phase coating technique that deposits thin films on substrate surfaces[1, 2]. An ALD film is grown by exposing the substrate to alternating reactant or “precursor” doses that react with surface functional groups to produce a solid film (**Figure 1.1**, adapted from [3]). Precursors are typically liquids or solids at room temperature and delivered to an ALD reactor as a gas from a vapor draw or bubbler precursor delivery manifold. The precursor flow is usually transported to the chamber with an inert carrier gas such as nitrogen or argon. Purge doses are performed between precursor doses to remove any unreacted precursor and gaseous byproducts. The shortest repeating unit of precursor and purge steps is referred to as a single ALD cycle. One ALD cycle is repeated as many times as necessary to grow an ALD film with the required final thickness.

The self-limiting nature of heterogeneous half-reactions in ALD enables the production of nanoscale conformal and pinhole-free films[4, 5]. ALD is a flexible technique that can be used to deposit many solid inorganic films on a variety of substrate materials[4]. Topographically diverse structures with deep trenches are a common example of a classically difficult deposition scenario where ALD performs well[5, 6]. ALD chemistries with high growth rates (*i.e.* many metal oxide chemistries) provide an economically viable route to the manufacture of nanoscale coatings. ALD is used widely in the semiconductor industry to deposit films for capacitors, transistors and gap dielectrics[7]. Other applications for ALD include photovoltaics, microelectronics, lighting displays, catalysis, and batteries[1, 6, 8].

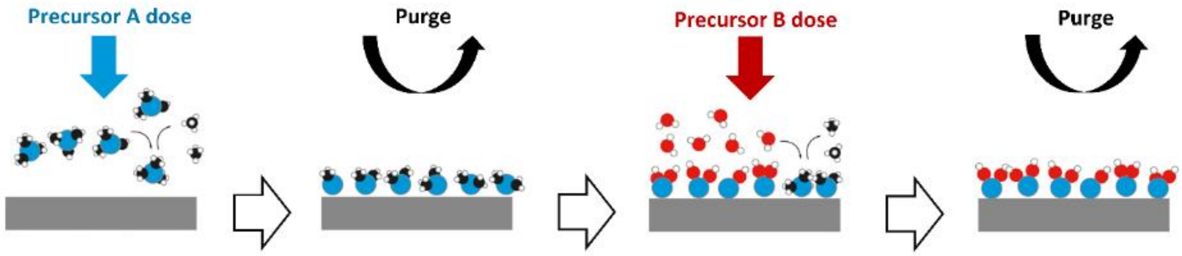

Figure 1.1. Illustration of a sample binary ALD process (two reactants: precursor A and precursor B). Reactants are introduced to a chamber containing the substrate (grey) with purge doses in between to remove any unreacted precursor and gaseous byproducts

The Al_2O_3 (alumina) ALD process referred to throughout this thesis is one of the most well-studied and efficient ALD processes known[4, 6]. Many favorable features of alumina ALD have contributed to its status as a popular ALD chemistry. Alumina ALD can be performed with a variety of precursors[4] but the most common are trimethylaluminum (TMA) and water vapor. TMA has fast heterogeneous reaction kinetics, is thermally stable well above 350°C[9], and has a high vapor pressure enabling short cycle times. Unlike some more challenging chemistries, methyl ligands are easily removed during the water dose, producing films with low carbon contamination[4]. Most ALD chemistries require reactor temperatures >150°C but alumina ALD has been demonstrated down to temperatures as low as 33°C[10]. O/Al ratios close to the expected value of 1.5 can be achieved at many deposition temperatures but temperatures exceeding 200°C are needed for low hydrogen contamination (H atom% <5)[10, 11].

Particle ALD refers to ALD on particle substrates[1]. The ability of ALD to produce conformal, nonporous films without line of sight to the surface is a desirable feature when coating a porous material[12] or a bed of particles. Other thin film deposition techniques such as liquid spray injection, precipitation, sol-gel processing[13], and chemical vapor deposition (CVD) tend to produce porous films on particle surfaces[14]. Agitation is a critical component of particle ALD systems. Without agitation, particle agglomerates may be coated instead of individual primary particles[15, 16]. Nanoparticles are particularly prone to agglomeration and form complex agglomerate structures hundreds of microns in size during fluidization[17-21]. Particle ALD has recently seen commercial success in the battery field where alumina ALD has been used on cathode powders to improve capacity retention[22, 23].

1.2 Typical Reactor Configurations for Particle ALD

The particle ALD coating process is typically performed using rotary drum reactors[24] or fluidized bed reactors[25-27]. Particle ALD has also been performed in fixed bed reactors[15, 28-30] but the lack of powder mixing in these systems can prevent uniform and fast precursor saturation from occurring at all particle surfaces[31]. Only agitated particle bed systems will be considered here. These batch ALD reactors are also referred to as “temporal” ALD systems because the precursors are dosed at different points in time.

Fluidized bed particle ALD is usually performed in a stainless steel tube within a furnace (**Figure 1.2**, adapted from [27]). Powder is loaded into the fluidization column and supported over a porous distributor plate. Precursor and purge gases are introduced to the fluidization chamber in an alternating fashion until the desired film thickness is achieved.

The total flow rate is held at a velocity $u > u_{mf}$ sufficient to fluidize the powder where u_{mf} is the minimum fluidization velocity. Fluidization occurs when the pressure drop across the bed is equal to the apparent powder bed weight divided by the bed cross-sectional area (**Figure 1.3**)[32]. The reactor in most particle ALD systems is maintained at low pressures during deposition to promote short precursor transit times to the particle surface (P < 10 Torr)[33]. Film growth is monitored indirectly through in-situ mass spectrometry of the product gases, precursor "breakthrough" and any molecular fragments of these gases[27].

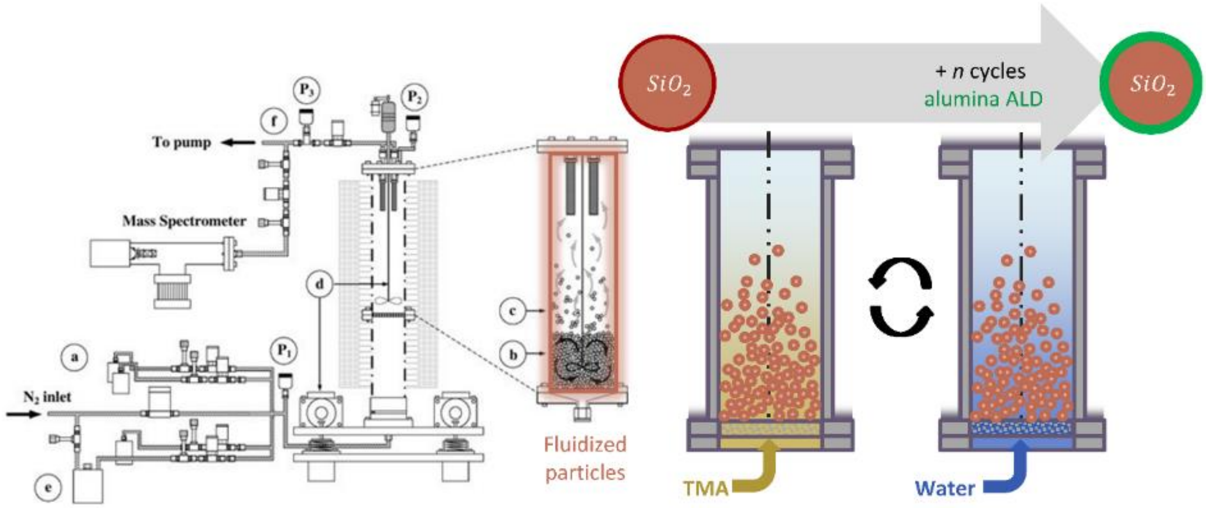

Figure 1.2. Representation of a fluidized bed particle ALD setup with alumina ALD on silica particles. Labels correspond to (a) the precursor dosing zone, (b) the particle bed, (c) the splash zone, (d) the source of mechanical agitation (*i.e.* a stirring rod or vibromotors), (e) the precursor bubbler zone, and (f) an in-situ mass spectrometer for real-time gas sampling. Pressure sensors for monitoring vacuum level and powder fluidization are also labeled as P_1, P_2 and P_3

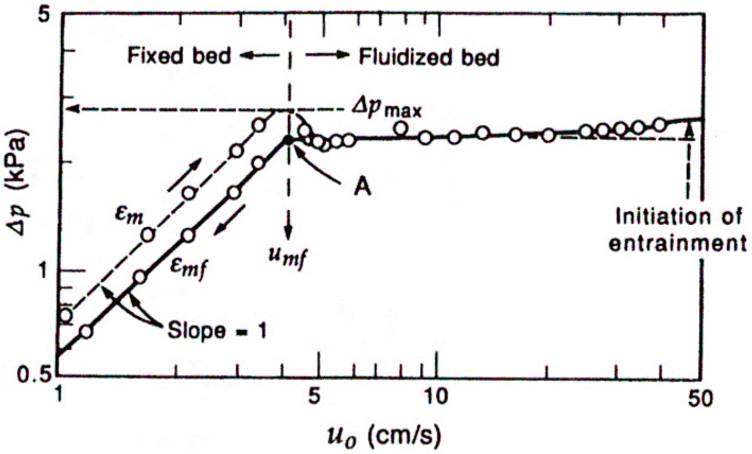

Figure 1.3. A typical fluidization curve (pressure drop versus superficial gas velocity, taken from [34])

With appropriately tuned operating conditions, gas-solid fluidization provides a favorable environment for particle ALD. High heat and mass transfer rates can be achieved in fluidized beds due to rapid particle mixing[34]. Particle surface sites are continuously exposed to precursor gas during fluidization, leading to high precursor utilization. Nanoparticles are well dispersed due to the continuous formation and breakage of complex agglomerates[18, 35]. Convective particle currents also dissipate local hot spots to maintain nearly isothermal reactor conditions[27].

It is worth noting that the fluidization dynamics depend on particle size and density. Particles with diameters >100 μm may belong to the Geldart A, B, or D classifications[36]. Geldart A "aeratable" powders exhibit a smooth fluidization region before bubbling as superficial gas velocity increases (**Figure 1.4c** and **1.4d**). Geldart B "bubbling" powders exhibit bubbles immediately at the minimum fluidization velocity. Geldart D particles spout during fluidization and are rarely encountered in particle ALD because of their large size. Most particle ALD substrates of commercial interest need high surface areas and are in the fine Geldart C category (diameter <20 μm). Geldart C "cohesive" particles are prone to gas channeling and require external agitation for smooth fluidization[18, 20].

Nanoparticles with a narrow particle size distribution and low bulk density can achieve smooth fluidization termed “agglomerate particulate fluidization” (APF) unlike dense and large nanoparticles with “agglomerate bubbling fluidization” (ABF) behavior[37]. Fluidization characteristics can also change in the presence of water vapor[38, 39] or a thin film[40].

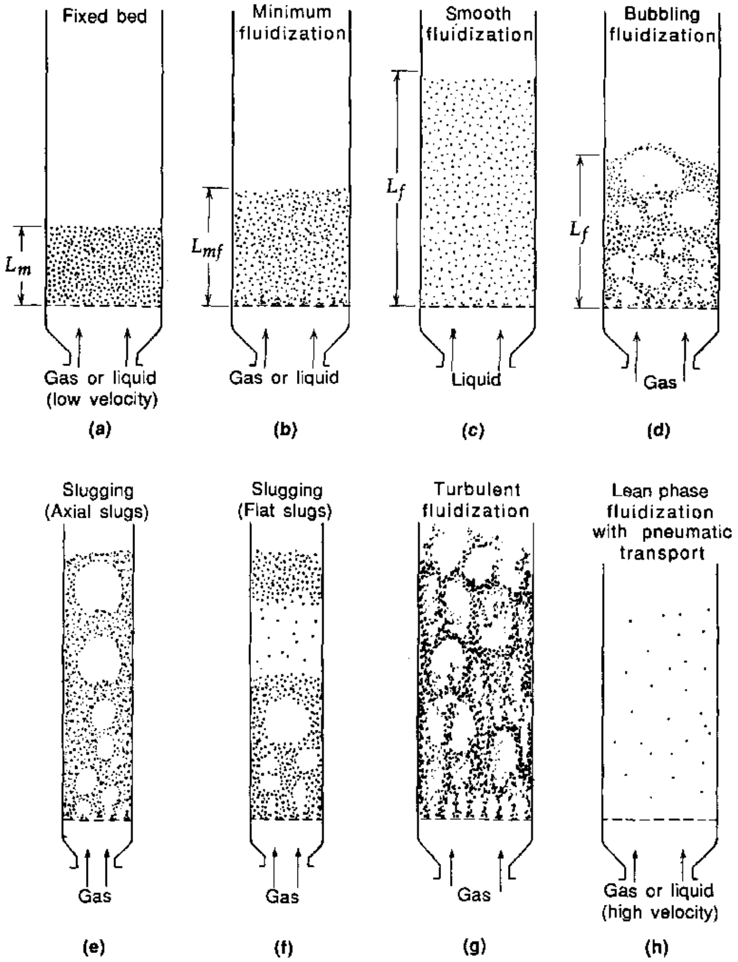

Figure 1.4. Types of fluidization behavior, roughly ordered by increasing gas velocity (taken from [34])

Continuous flow dilutes the precursor gas and can lead to poor precursor utilization efficiencies[24, 41]. ALD chemistries with low reactive sticking coefficients are particularly susceptible to low precursor efficiencies in a fluidized bed particle ALD setup[42]. Rotary drum particle ALD reactors were developed as an alternative batch ALD system with a more flexible gas residence time (**Figure 1.5**). Like fluidized bed particle ALD systems, rotary drum particle ALD reactors typically use a stainless steel housing enclosed in a furnace[24]. Particles are loaded into a porous metal cylinder inside a vacuum chamber and rotated with a manipulator at a set rotation speed to induce particle mixing[23, 43]. Precursors can be introduced into the reactor headspace as static pulses[24] or continuously[44]. Rotary drum particle ALD is typically performed under low pressure or vacuum conditions[24, 45]. Particles do not need to be fluidized so conditions such as lower reactor pressures with no carrier gas can be obtained. Other aspects of the system design from precursor delivery manifolds to product gas analysis are similar to the fluidized bed particle ALD setup. A hybrid design, the rotating fluidized bed (RFB), has also been reported[46].

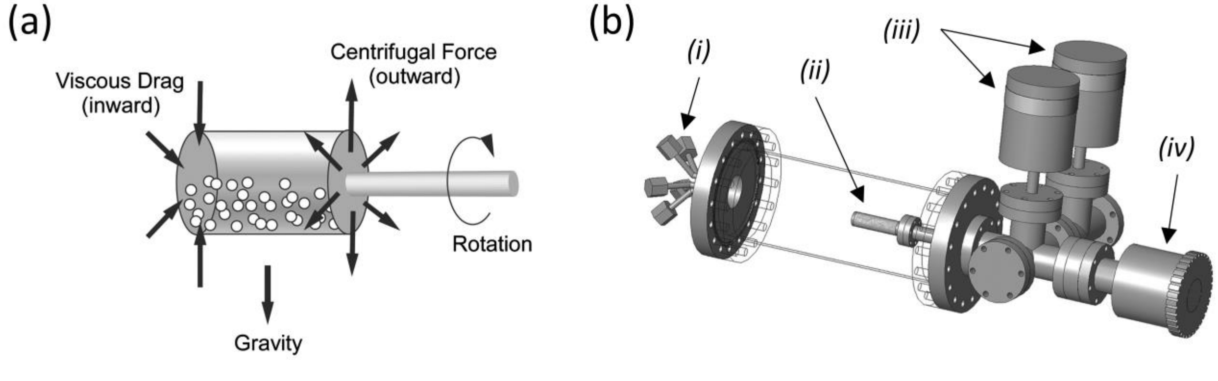

Figure 1.5. (a) Forces on particles in the rotary drum reactor. (b) Schematic diagram of the rotary drum reactor. Labels correspond to (i) dosing flange, (ii) porous cylinder, (iii) capacitance manometers for pressure monitoring, and (iv) rotary manipulator for drum rotation. Figures taken from [24]

Applications requiring high deposition rates are limited by the low throughput of batch particle ALD processes. Achieving multiple cycles of ALD in a high-throughput “semicontinuous” batch setup requires multiple reactors in series, leading to a large system footprint and substantial overhead costs. Spatial ALD, where precursor regions are spatially separated by alternating purge zones so that all ALD reactions can occur simultaneously, was developed to overcome the throughput limitations of batch ALD[7]. The substrate is moved through alternating regions of precursor to grow a multiple ALD cycle film. Typical spatial ALD processes use a wrapped rotary drum[47, 48], gas bearing track[7], roll-to-roll[49] or rotary head[50] mechanism for transporting the substrate which are not compatible with easily fluidized and elutriated particulate materials. A continuous particle ALD process has been developed based on pneumatic transport[51] but requires a long reactor to compensate for the higher convection velocity. A cost-effective continuous process capable of coating large quantities of powder (3,000-12,000 kg/day) is still needed to meet the high throughput, low cost requirements of the battery industry and others[52].

1.3 Description of Continuous Spatial Particle ALD

Continuous vibrating reactors for atomic layer deposition (CVR-ALD) were developed to enable high powder throughput while maintaining low capital costs. Also known as continuous spatial particle ALD, CVR-ALD reactors use directional vibration to transport particles through alternating regions of precursor and purge gas (**Figure 1.6**). The CVR-ALD system at the University of Colorado was designed to perform four cycles of alumina ALD with alternating doses of nitrogen purge gas, TMA vapor, nitrogen purge gas, and water vapor. Powder travels over a porous baseplate or “frit” material through which the precursor and purge gases are dosed. A pneumatic actuator (**Figure 1.7**) with a self-reversing piston oscillates beneath the reactor, shaking the system along an elliptic trajectory composed of extension (forward and up) and retraction (backward and down) cycles. Particles are thrown into a forward convection cycle using this “linear vibration” process.

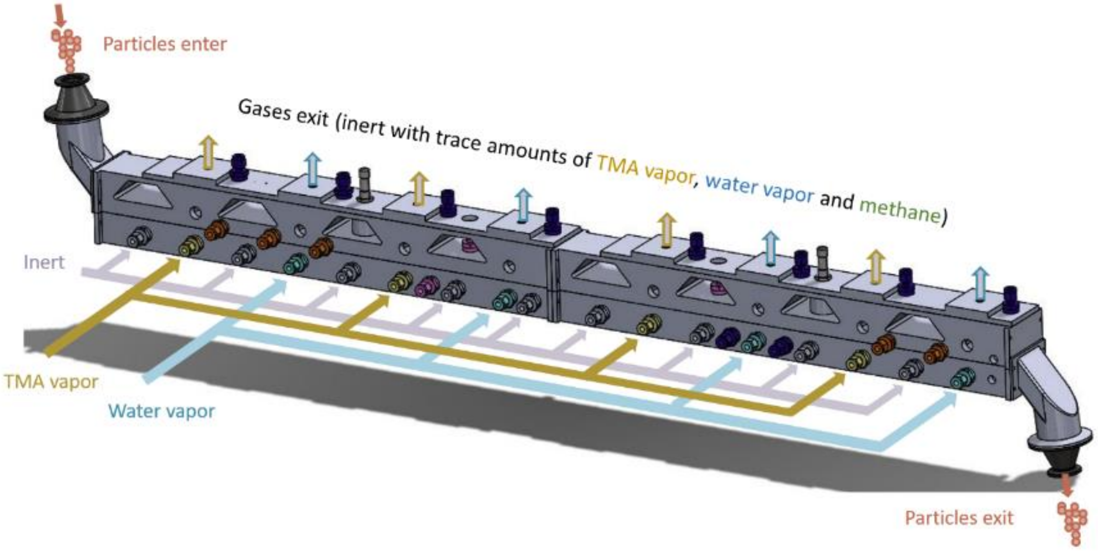

Figure 1.6. CAD model for the CVR-ALD reactor system at the University of Colorado. Particles are fed into the reactor from a hopper (not shown) and pass through alternating precursor and purge zones in an enclosed stainless steel housing. Gases flow up through a porous distributor plate and the particle bed before leaving through the top manifold

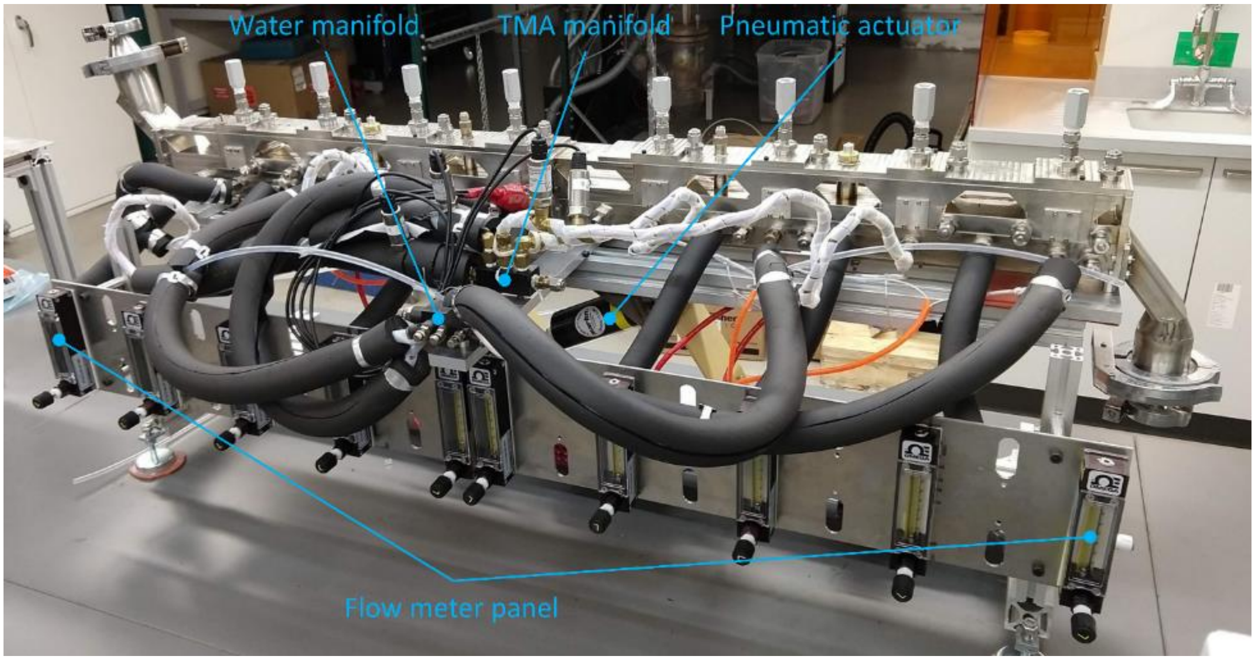

Figure 1.7. Photo of the CVR-ALD reactor outside of the fume hood with labels for the TMA manifold, water manifold, and flow meter panel for purge gas dosing. Auxiliary components (precursor dosing manifolds, electrical boxes, hopper, and catch pan) are not shown

Several features of CVR-ALD differ from the rotary and fluidized bed batch reactors. CVR-ALD reactors typically run at atmospheric pressure conditions. Fluidized bed particle ALD can be performed at atmospheric pressure[53-55] but is most often done at low pressure. Usually, gases in CVR-ALD are dosed into the chamber at velocities below the powder's minimum fluidization velocity. The powder bed must maintain intermittent contact with the vibrating reactor baseplate so particles are conveyed consistently throughout the reactor. Vibration both agitates particle-particle contacts and controls powder convection speed. In rotary and fluidized bed reactors, agitation is used to induce particle mixing only. The cross-flow spatial ALD reactor configuration is also a more compact high-throughput system. Particle transport speed is controlled primarily by vibration intensity, not gas flow rate, so reactor footprints are small compared to semicontinuous fluidized beds and continuous pneumatic conveying systems[51] with similar powder throughput.

1.4 Modeling Approaches to Dense Gas-Solid Flows

The flow dynamics inside CVR-ALD reactors are more complex than their batch particle ALD counterparts. Concurrent dosing with multiple inlets and outlets produces multidimensional flow patterns. Interactions between the dense conveying powder bed and upward-flowing gas are highly coupled. Additional challenges such as "trapped" precursors[53] and difficulty purging molecularly adsorbed water[56] are encountered at atmospheric pressure, particularly at the <200°C temperatures typical for CVR-ALD. Experiments to explore powder bed surface titration uniformity and predict spatial precursor gas distribution would require an expensive sensor setup. Continuum-scale modeling is proposed as an alternative route to continuous spatial particle ALD optimization.

Large-scale gas-solid flow models differ in whether each phase is treated as a continuum (Eulerian) or as composed of discrete entities (Lagrangian). Some of the most popular models are best understood in the context of a fluidized bed (**Figure 1.8**). Only Models 2-5 will be discussed here. Model 2 is the two-fluid model (TFM) or Eulerian-Eulerian approach where both the gas and solids are treated as interpenetrating continua. Closures for solids-phase stress are needed to account for the granular nature of the solids. Spatial resolution of the numerical result for an Eulerian-Eulerian model depends on the mesh cell size; a decrease in mesh cell size produces a finer solution. At the other end of the spectrum, Model 5, is a molecular dynamics (MD) model or Lagrangian-Lagrangian approach. In a gas-particle system, MD will often (but not always) treat the granular material particles and individual gas molecules as discrete entities which interact and collide over time. Models 3 and 4 take an intermediate Eulerian-Lagrangian approach by treating the gas phase as a continuum and the solid particles as discrete entities. In the "unresolved" discrete particle model of Model 3, also known as the discrete element model (DEM), the mesh grid cells are larger than the particles and gas-particle drag laws are needed for interphase coupling. Model 4 takes a "resolved" discrete particle model approach where mesh grid cells are smaller than the particles and interphase exchanges are handled as a boundary condition at the particle surface. Model 4 is also known as the direct numerical simulation (DNS) method[57]. Models 2 and 3 (TFM and CFD-DEM) are most commonly seen at the fluidized bed reactor scale for biomass pyrolysis[58, 59], combustors[60] and nanoparticle fluidization[61, 62]. CFD simulations have been performed and published for temporal ALD[63-66] and spatial ALD[67-70] on planar substrates but not on particles.

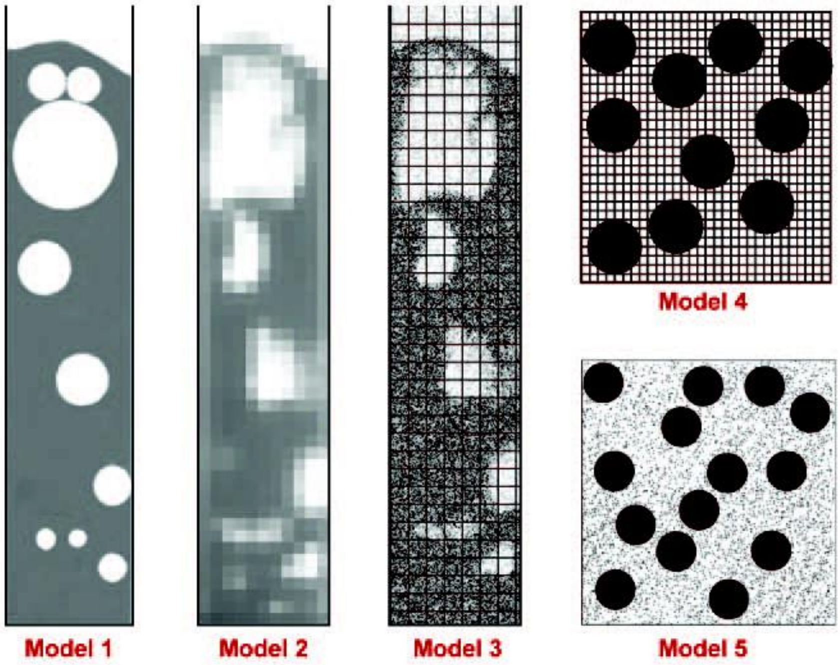

van der Hoef MA, et al. 2008.
Annu. Rev. Fluid Mech. 40:47–70

Figure 1.8. Graphical representation of various models used for simulating dense gas-solid flow: (1) the discrete bubble model, (2) the two-fluid model, (3) the unresolved discrete particle model, (4) the resolved discrete particle model, and (5) the molecular dynamics model. Only models 1-3 are used for simulating actual gas-fluidized beds. Taken from [71]

The decision to pursue an Eulerian or Lagrangian approach should take the solution accuracy required and computational resources available into consideration. MD simulations can provide detailed, molecular-level resolution of the discrete interactions in gas-solid flows but are restricted to simulation sizes <1 mm and not exceeding 10^5 particles[71, 72]. Larger scales can be simulated with an Eulerian approach but details of the sub-grid-scale flow behavior are lost[73]. Some flow structures may be more amenable to a continuum versus a discrete modeling treatment. Friction, cohesive interparticle forces, polydispersity, non-sphericity, and surface roughness are handled indirectly in a continuum model[57] as modifications to the closure relations and integrated models (i.e. population balance modeling for agglomeration[74]). Sub-grid mesoscale features[72] are also notoriously difficult to incorporate accurately into a continuum model. However, when working with stresses and pressures from gas-solid suspension rheology data, the continuum approach may be more direct than a force-balance-based method like the Lagrangian approach. A CFD-DEM approach was chosen to analyze interactions between the particles, the reactor and the gas in the CVR-ALD system at small scales. For larger reactor-scale simulations where the resolution of powder bed dynamics is not needed, an Eulerian-based moving porous media model was selected.

The breadth of relevant scales and the dynamic reactor motion in CVR-ALD present significant CFD-DEM modeling challenges. The 48” x 0.5” x 1.75” particle flow channel from the four-cycle CVR-ALD system in **Figure 1.7**, filled to a 3-mm bed height with 50-micron spheres, would contain around 75 million particles. Particle counts exceeding 10^6 are near the practical upper limit for modern supercomputer calculations[75] and beyond the computational resources available to students at the University of Colorado. The simulation domain size must be reduced to avoid computationally expensive simulations. Instead of simulating the entire reactor, we will focus on a small slice of interest in “2.5D”. A semi-periodic box model with periodic boundaries on all vertical walls, a velocity inlet through the bottom plane and a pressure outlet through the top plane was used to simulate the CVR-ALD system (**Figure 1.9**). This approach allows us to shrink our simulation size to $10^4 - 10^5$ particles for a more computationally tractable simulation.

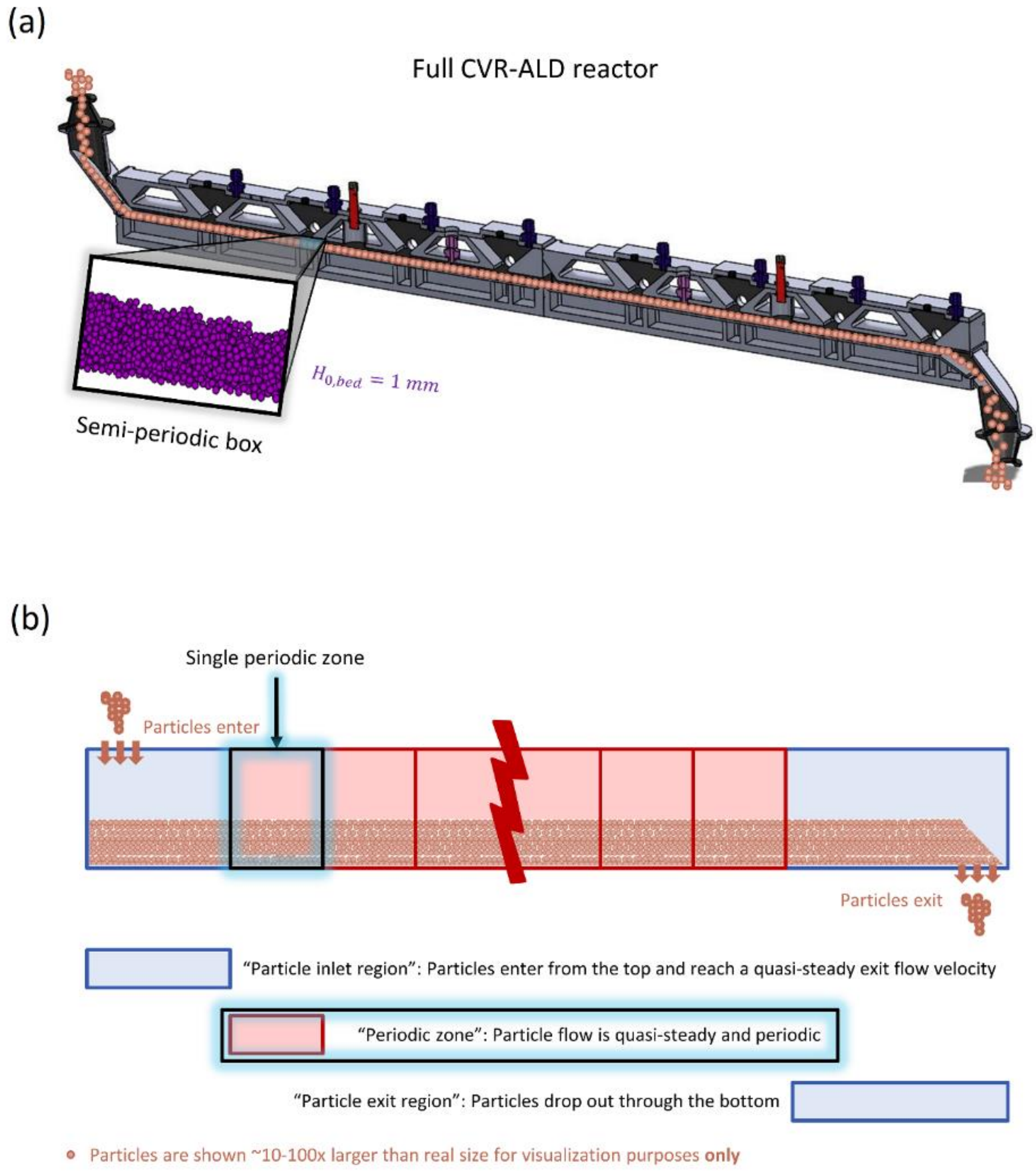

Figure 1.9. (a) Semi-periodic box model in the context of a section view of the full CVR-ALD reactor. (b) Representative regions of the CVR-ALD reactor corresponding to the periodic zones

1.5 Thesis Topics

The goal of this thesis is to better understand and predict continuous spatial particle ALD reactor behavior. Applying CVR-ALD reactors to new particle sizes, substrate materials, and ALD chemistries will require some knowledge of the reacting gas-solid flow dynamics. The topics below were identified as crucial in the pursuit of a predictive CVR-ALD modeling strategy. Experimental characterization was performed throughout this thesis to inform modeling inputs and validate the model results.

1.5.1 Discrete Element Method Modeling (Chapter 2)

Previous studies on vibratory convection have focused on the transport of objects[76] and coarse granular media[77, 78]. Little is known about the powder bed dynamics of fine powder during vibratory convection. In fact, many aspects of vibratory conveyor operation and optimization are industry know-how that is not well documented in textbooks or publications. DEM simulations were performed to investigate particle-particle and particle-wall interactions and the role of the vibration waveform during vibratory convection. Removing the gas phase by using pure DEM (solids-only) simulations allows us to isolate and explore powder bed-baseplate interactions without the confounding effects of drag.

1.5.2 Aeration and Cohesion Effects (Chapter 3)

DEM simulations only describe the powder bed flow behavior in the absence of drag. The assumption that gas-phase effects on powder bed dynamics can be ignored because dosing gas velocities are low may not be valid for vibrating atmospheric pressure reactors containing small particles. Fine powders frequently used in CVR-ALD are characterized by low minimum fluidization velocities relative to the vibrating reactor velocity magnitude and drag may not be negligible. By taking a new modeling approach to the vibrating reactor housing, aeration was incorporated into a CFD-DEM model for the powder bed. Data for several particle sizes was used to explore the connection between minimum fluidization velocity, van der Waals cohesion magnitude, and bulk powder convection speed under vibratory convection.

1.5.3 Powder Mixing and Self-Diffusion (Chapter 4)

In Chapters 2 and 3, plug flow of the solids phase was observed under vibratory convection. Bed particles maintained similar coordination networks and little relative motion was observed between particles over many vibration cycles. Precursors with poor reactive sticking coefficients or low vapor pressures may not have enough residence time in the CVR-ALD reactor to fully saturate the particle surface in the absence of powder bed mixing. To facilitate powder bed turnover for slower and more challenging ALD chemistries, baffles were added to the frit. Particle image velocimetry (PIV) experiments with several baffle designs and CFD-DEM simulations of flow over a sawtooth obstruction were used to investigate the effect of frit baffles on powder flow behavior.

1.5.4 A Moving Porous Media Model (Chapter 5)

CFD-DEM simulations are not a computationally efficient method for simulating reactor-scale particle ALD. Even a single CVR-ALD precursor zone model with periodic vertical boundaries would contain around one million 50-micron particles. Many ALD applications involve <20-micron particles[1], further decreasing the economic viability of a CFD-DEM approach. Continuum treatment of the powder bed is needed to resolve the gas-solid flow in a single precursor zone without sacrificing computational efficiency. A moving porous media model was developed to answer questions about precursor utilization and surface titration uniformity on the reactor scale.

References

[1] A.W. Weimer, Particle atomic layer deposition, Journal of Nanoparticle Research, 21 (2019) 9.
[2] M. Ritala, M. Leskelä, Atomic layer deposition, Handbook of Thin Films, Elsevier2002, pp. 103-159.
[3] A.R. Barron, осаждение атомных слоев, 2020.
[4] R.L. Puurunen, Surface chemistry of atomic layer deposition: A case study for the trimethylaluminum/water process, Journal of applied physics, 97 (2005) 9.
[5] S.M. George, Atomic layer deposition: an overview, Chemical reviews, 110 (2010) 111-131.
[6] E. Granneman, P. Fischer, D. Pierreux, H. Terhorst, P. Zagwijn, Batch ALD: Characteristics, comparison with single wafer ALD, and examples, Surface and coatings technology, 201 (2007) 8899-8907.
[7] P. Poodt, D.C. Cameron, E. Dickey, S.M. George, V. Kuznetsov, G.N. Parsons, F. Roozeboom, G. Sundaram, A. Vermeer, Spatial atomic layer deposition: A route towards further industrialization of atomic layer deposition, Journal of Vacuum Science & Technology A: Vacuum, Surfaces, and Films, 30 (2012) 010802.
[8] F. Zaera, The surface chemistry of atomic layer depositions of solid thin films, The journal of physical chemistry letters, 3 (2012) 1301-1309.
[9] A. Paranjpe, S. Gopinath, T. Omstead, R. Bubber, Atomic layer deposition of AlO x for thin film head gap applications, Journal of the Electrochemical Society, 148 (2001) G465.
[10] M. Groner, F. Fabreguette, J. Elam, S. George, Low-temperature Al2O3 atomic layer deposition, Chemistry of materials, 16 (2004) 639-645.
[11] C. Guerra-Nuñez, M. Döbeli, J. Michler, I. Utke, Reaction and growth mechanisms in Al2O3 deposited via atomic layer deposition: elucidating the hydrogen source, Chemistry of Materials, 29 (2017) 8690-8703.
[12] E.-L. Lakomaa, Atomic layer epitaxy (ALE) on porous substrates, Applied surface science, 75 (1994) 185-196.
[13] C. Brinker, A. Hurd, P. Schunk, G. Frye, C. Ashley, Review of sol-gel thin film formation, Journal of Non-Crystalline Solids, 147 (1992) 424-436.
[14] G.S. Czok, J. Werther, Liquid spray vs. gaseous precursor injection—its influence on the performance of particle coating by CVD in the fluidized bed, Powder technology, 162 (2006) 100-110.
[15] J. Ferguson, A. Weimer, S. George, Atomic layer deposition of boron nitride using sequential exposures of BCl3 and NH3, Thin Solid Films, 413 (2002) 16-25.
[16] M.Q. Snyder, S.A. Trebukhova, B. Ravdel, M.C. Wheeler, J. DiCarlo, C.P. Tripp, W.J. DeSisto, Synthesis and characterization of atomic layer deposited titanium nitride thin films on lithium titanate spinel powder as a lithium-ion battery anode, Journal of power sources, 165 (2007) 379-385.
[17] W. Yao, G. Guangsheng, W. Fei, W. Jun, Fluidization and agglomerate structure of SiO2 nanoparticles, Powder Technology, 124 (2002) 152-159.
[18] L.F. Hakim, J.L. Portman, M.D. Casper, A.W. Weimer, Aggregation behavior of nanoparticles in fluidized beds, Powder Technology, 160 (2005) 149-160.
[19] L. de Martín, W.G. Bouwman, J.R. van Ommen, Multidimensional nature of fluidized nanoparticle agglomerates, Langmuir, 30 (2014) 12696-12702.

[20] C. Zhu, Q. Yu, R.N. Dave, R. Pfeffer, Gas fluidization characteristics of nanoparticle agglomerates, AIChE Journal, 51 (2005) 426-439.

[21] J.R. van Ommen, J.M. Valverde, R. Pfeffer, Fluidization of nanopowders: a review, Journal of nanoparticle research, 14 (2012) 1-29.

[22] A.L. Hoskins, W.W. McNeary, S.L. Millican, T.A. Gossett, A. Lai, Y. Gao, X. Liang, C.B. Musgrave, A.W. Weimer, Nonuniform growth of sub-2 nanometer atomic layer deposited alumina films on lithium nickel manganese cobalt oxide cathode battery materials, ACS Applied Nano Materials, 2 (2019) 6989-6997.

[23] Y.S. Jung, A.S. Cavanagh, A.C. Dillon, M.D. Groner, S.M. George, S.-H. Lee, Enhanced stability of LiCoO2 cathodes in lithium-ion batteries using surface modification by atomic layer deposition, Journal of The Electrochemical Society, 157 (2009) A75.

[24] J. McCormick, B. Cloutier, A. Weimer, S. George, Rotary reactor for atomic layer deposition on large quantities of nanoparticles, Journal of Vacuum Science & Technology A: Vacuum, Surfaces, and Films, 25 (2007) 67-74.

[25] J.R. Wank, S.M. George, A.W. Weimer, Nanocoating individual cohesive boron nitride particles in a fluidized bed by ALD, Powder Technology, 142 (2004) 59-69.

[26] L.F. Hakim, S.M. George, A.W. Weimer, Conformal nanocoating of zirconia nanoparticles by atomic layer deposition in a fluidized bed reactor, Nanotechnology, 16 (2005) S375.

[27] D.M. King, J.A. Spencer II, X. Liang, L.F. Hakim, A.W. Weimer, Atomic layer deposition on particles using a fluidized bed reactor with in situ mass spectrometry, Surface and Coatings Technology, 201 (2007) 9163-9171.

[28] E.-L. Lakomaa, S. Haukka, T. Suntola, Atomic layer growth of TiO2 on silica, Applied surface science, 60 (1992) 742-748.

[29] P. Voigt, E. Haimi, J. Lahtinen, Y.W. Cheah, E. Mäkelä, T. Viinikainen, R.L. Puurunen, Nickel supported on mesoporous zirconium oxide by atomic layer deposition: initial fixed-bed reactor study, Topics in Catalysis, 62 (2019) 611-620.

[30] V.E. Strempel, R. Naumann d’Alnoncourt, M. Drieß, F. Rosowski, Atomic layer deposition on porous powders with in situ gravimetric monitoring in a modular fixed bed reactor setup, Review of Scientific Instruments, 88 (2017) 074102.

[31] J. Van Ommen, A. Goulas, Atomic layer deposition on particulate materials, Materials Today Chemistry, 14 (2019) 100183.

[32] D. Longrie, D. Deduytsche, C. Detavernier, Reactor concepts for atomic layer deposition on agitated particles: A review, Journal of Vacuum Science & Technology A: Vacuum, Surfaces, and Films, 32 (2014) 010802.

[33] S. George, A. Ott, J. Klaus, Surface chemistry for atomic layer growth, The Journal of Physical Chemistry, 100 (1996) 13121-13131.

[34] D. Kunii, O. Levenspiel, Fluidization engineering, Butterworth-Heinemann1991.

[35] Z. Zhao, D. Liu, J. Ma, X. Chen, Fluidization of nanoparticle agglomerates assisted by combining vibration and stirring methods, Chemical Engineering Journal, 388 (2020) 124213.

[36] D. Geldart, Types of gas fluidization, Powder technology, 7 (1973) 285-292.

[37] Z. Li, J. Li, X. Liu, R. Chen, Progress in enhanced fluidization process for particle coating via atomic layer deposition, Chemical Engineering and Processing-Process Intensification, 159 (2021) 108234.

[38] F. Raganati, R. Chirone, P. Ammendola, Gas–solid fluidization of cohesive powders, Chemical Engineering Research and Design, 133 (2018) 347-387.

[39] C.M. Boyce, Gas-solid fluidization with liquid bridging: A review from a modeling perspective, Powder Technology, 336 (2018) 12-29.

[40] J. Ma, J.R. van Ommen, D. Liu, R.F. Mudde, X. Chen, S. Pan, C. Liang, Fluidization dynamics of cohesive Geldart B particles. Part II: Pressure fluctuation analysis, Chemical Engineering Journal, 368 (2019) 627-638.

[41] S. Adhikari, S. Selvaraj, D.H. Kim, Progress in powder coating technology using atomic layer deposition, Advanced Materials Interfaces, 5 (2018) 1800581.
[42] J. Ferguson, K. Buechler, A. Weimer, S. George, SnO2 atomic layer deposition on ZrO2 and Al nanoparticles: pathway to enhanced thermite materials, Powder Technology, 156 (2005) 154-163.
[43] C. Wilson, J. McCormick, A. Cavanagh, D. Goldstein, A. Weimer, S. George, Tungsten atomic layer deposition on polymers, Thin Solid Films, 516 (2008) 6175-6185.
[44] M.W. Coile, M.J. Young, J.A. Libera, A.U. Mane, J.W. Elam, High-capacity rotary drum for atomic layer deposition onto powders and small mechanical parts in a hot-walled viscous flow reactor, Journal of Vacuum Science & Technology A: Vacuum, Surfaces, and Films, 38 (2020) 052403.
[45] D. Longrie, D. Deduytsche, J. Haemers, K. Driesen, C. Detavernier, A rotary reactor for thermal and plasma-enhanced atomic layer deposition on powders and small objects, Surface and Coatings Technology, 213 (2012) 183-191.
[46] C.-L. Duan, Z. Deng, K. Cao, H.-F. Yin, B. Shan, R. Chen, Surface passivation of Fe3O4 nanoparticles with Al2O3 via atomic layer deposition in a rotating fluidized bed reactor, Journal of Vacuum Science & Technology A: Vacuum, Surfaces, and Films, 34 (2016) 04C103.
[47] P. Maydannik, T. Kääriäinen, D. Cameron, An atomic layer deposition process for moving flexible substrates, Chemical Engineering Journal, 171 (2011) 345-349.
[48] K. Sharma, R.A. Hall, S.M. George, Spatial atomic layer deposition on flexible substrates using a modular rotating cylinder reactor, Journal of Vacuum Science & Technology A: Vacuum, Surfaces, and Films, 33 (2015) 01A132.
[49] P.S. Maydannik, T.O. Kääriäinen, K. Lahtinen, D.C. Cameron, M. Söderlund, P. Soininen, P. Johansson, J. Kuusipalo, L. Moro, X. Zeng, Roll-to-roll atomic layer deposition process for flexible electronics encapsulation applications, Journal of Vacuum Science & Technology A: Vacuum, Surfaces, and Films, 32 (2014) 051603.
[50] P. Poodt, A. Lankhorst, F. Roozeboom, K. Spee, D. Maas, A. Vermeer, High-speed spatial atomic-layer deposition of aluminum oxide layers for solar cell passivation, Advanced materials, 22 (2010) 3564-3567.
[51] J.R. van Ommen, D. Kooijman, M.d. Niet, M. Talebi, A. Goulas, Continuous production of nanostructured particles using spatial atomic layer deposition, Journal of Vacuum Science & Technology A: Vacuum, Surfaces, and Films, 33 (2015) 021513.
[52] G.N. Parsons, J.W. Elam, S.M. George, S. Haukka, H. Jeon, W. Kessels, M. Leskelä, P. Poodt, M. Ritala, S.M. Rossnagel, History of atomic layer deposition and its relationship with the American Vacuum Society, Journal of Vacuum Science & Technology A: Vacuum, Surfaces, and Films, 31 (2013) 050818.
[53] R. Beetstra, U. Lafont, J. Nijenhuis, E.M. Kelder, J.R. van Ommen, Atmospheric pressure process for coating particles using atomic layer deposition, Chemical Vapor Deposition, 15 (2009) 227-233.
[54] W.E. Kessels, M. Putkonen, Advanced process technologies: Plasma, direct-write, atmospheric pressure, and roll-to-roll ALD, Mrs Bulletin, 36 (2011) 907-913.
[55] A. Goulas, J.R. Van Ommen, Atomic layer deposition of platinum clusters on titania nanoparticles at atmospheric pressure, Journal of Materials Chemistry A, 1 (2013) 4647-4650.
[56] J.S. Jur, G.N. Parsons, Atomic layer deposition of Al2O3 and ZnO at atmospheric pressure in a flow tube reactor, ACS Applied Materials & Interfaces, 3 (2011) 299-308.
[57] J. Wang, Continuum theory for dense gas-solid flow: A state-of-the-art review, Chemical Engineering Science, 215 (2020) 115428.
[58] L. Lu, X. Gao, J.-F. Dietiker, M. Shahnam, W.A. Rogers, MFiX based multi-scale CFD simulations of biomass fast pyrolysis: A review, Chemical Engineering Science, 248 (2022) 117131.
[59] K. Papadikis, A. Bridgwater, S. Gu, CFD modelling of the fast pyrolysis of biomass in fluidised bed reactors, Part A: Eulerian computation of momentum transport in bubbling fluidised beds, Chemical Engineering Science, 63 (2008) 4218-4227.

[60] C.G. Philippsen, A.C.F. Vilela, L. Dalla Zen, Fluidized bed modeling applied to the analysis of processes: review and state of the art, Journal of Materials Research and Technology, 4 (2015) 208-216.

[61] D. Liu, B.G. van Wachem, R.F. Mudde, X. Chen, J.R. van Ommen, An adhesive CFD-DEM model for simulating nanoparticle agglomerate fluidization, AIChE Journal, 62 (2016) 2259-2270.

[62] D. Liu, B.G. van Wachem, R.F. Mudde, X. Chen, J.R. van Ommen, Characterization of fluidized nanoparticle agglomerates by using adhesive CFD-DEM simulation, Powder Technology, 304 (2016) 198-207.

[63] A. Yanguas-Gil, J.A. Libera, J.W. Elam, Reactor scale simulations of ALD and ALE: Ideal and non-ideal self-limited processes in a cylindrical and a 300 mm wafer cross-flow reactor, Journal of Vacuum Science & Technology A: Vacuum, Surfaces, and Films, 39 (2021) 062404.

[64] M.R. Shaeri, T.-C. Jen, C.Y. Yuan, Reactor scale simulation of an atomic layer deposition process, Chemical Engineering Research and Design, 94 (2015) 584-593.

[65] Z. Deng, W. He, C. Duan, B. Shan, R. Chen, Atomic layer deposition process optimization by computational fluid dynamics, Vacuum, 123 (2016) 103-110.

[66] P.O. Oviroh, R. Akbarzadeh, D. Pan, R.A.M. Coetzee, T.-C. Jen, New development of atomic layer deposition: processes, methods and applications, Science and technology of advanced materials, 20 (2019) 465-496.

[67] W. Cong, Z. Li, K. Cao, G. Feng, R. Chen, Transient analysis and process optimization of the spatial atomic layer deposition using the dynamic mesh method, Chemical Engineering Science, 217 (2020) 115513.

[68] D. Pan, Numerical study on the effectiveness of precursor isolation using N2 as gas barrier in spatial atomic layer deposition, International Journal of Heat and Mass Transfer, 144 (2019) 118642.

[69] D. Pan, T.-C. Jen, C. Yuan, Effects of gap size, temperature and pumping pressure on the fluid dynamics and chemical kinetics of in-line spatial atomic layer deposition of Al2O3, International Journal of Heat and Mass Transfer, 96 (2016) 189-198.

[70] M.B.M. Mousa, J.S. Ovental, A.H. Brozena, C.J. Oldham, G.N. Parsons, Modeling and experimental demonstration of high-throughput flow-through spatial atomic layer deposition of Al2O3 coatings on textiles at atmospheric pressure, Journal of Vacuum Science & Technology A: Vacuum, Surfaces, and Films, 36 (2018) 031517.

[71] M.A. van der Hoef, M. van Sint Annaland, N. Deen, J. Kuipers, Numerical simulation of dense gas-solid fluidized beds: a multiscale modeling strategy, Annu. Rev. Fluid Mech., 40 (2008) 47-70.

[72] W. Ge, Q. Chang, C. Li, J. Wang, Multiscale structures in particle–fluid systems: Characterization, modeling, and simulation, Chemical Engineering Science, 198 (2019) 198-223.

[73] S. Sundaresan, Modeling the hydrodynamics of multiphase flow reactors: current status and challenges, AIChE Journal, 46 (2000) 1102-1105.

[74] K.M. Kellogg, P. Liu, C.Q. LaMarche, C.M. Hrenya, Continuum theory for rapid cohesive-particle flows: general balance equations and discrete-element-method-based closure of cohesion-specific quantities, Journal of Fluid Mechanics, 832 (2017) 345-382.

[75] A. Munjiza, P.W. Cleary, Industrial particle flow modelling using discrete element method, Engineering Computations, (2009).

[76] A. Redford, G. Boothroyd, Vibratory feeding, Proceedings of the Institution of Mechanical Engineers, 182 (1967) 135-152.

[77] E. Sloot, N.P. Kruyt, Theoretical and experimental study of the transport of granular materials by inclined vibratory conveyors, Powder Technology, 87 (1996) 203-210.

[78] E. Simsek, S. Wirtz, V. Scherer, H. Kruggel-Emden, R. Grochowski, P. Walzel, An experimental and numerical study of transversal dispersion of granular material on a vibrating conveyor, Particulate Science and Technology, 26 (2008) 177-196.

CHAPTER 2

DISCRETE ELEMENT METHOD MODELING

2.1 Abstract

Fine powder convection in continuous vibrating reactors for particle atomic layer deposition (CVR-ALD) is not well understood so cohesive discrete-element-method (DEM) simulations were performed to investigate the solids flow behavior. Using a Fast Fourier Transform (FFT) algorithm, we constructed a sum-of-sines model for the reactor kinematics based on accelerometer data. Accelerometer results and DEM simulations revealed the role of high-frequency excitations and need for backsliding and sticking avoidance in horizontal conveyors at low-g accelerations. From these observations, we propose a novel sawtooth excitation to enable convection of cohesive fine powders at low flow velocities. The model results were compared to data from an in-house continuous spatial particle ALD reactor.

2.2 Introduction

In both batch and continuous particle ALD, vibration is incorporated to improve gas flow uniformity through the powder bed. Vibration leads to agitation in dense particle regions, helping to break up plugs and prevent particle interlocking[1, 2]. Mechanical, acoustic and magnetic agitation are commonly used in fine powder fluidized beds to destabilize cohesive channels and suppress slugging[3-5]. Bed agitation also promotes efficient gas-particle and particle-particle mixing[6]. In a continuous vibrating spatial particle ALD reactor, linear vibration transports particles through alternating gas zones with moderate-frequency, low-amplitude oscillations [7]. Thus, optimized vibratory convection can accomplish two goals simultaneously: transporting particles and promoting gas-solid contact. Prior experiments and simulations have demonstrated that higher vibration intensities lead to bed compaction[8, 9] and smaller mean agglomerate sizes in fluidized beds of fine cohesive powders[9, 10]. It is unknown whether these trends with vibration intensity can be extended to a continuous spatial particle ALD reactor, where vibration is two-dimensional and gas velocities are below fluidization.

The dual role of vibration, among other features, makes continuous spatial particle ALD complex as compared to its fluidized bed predecessor. Although previous works cover many reactor-scale experimental[11] and numerical[12-14] studies of spatial ALD on flat substrates, continuous vibrating spatial ALD on particle substrates was only developed and commercialized within the last decade[15]. As a result, the behavior of particles inside continuous vibrating reactors (CVRs) is still not well understood. Modeling results for an ALD system where a powder substrate is driven by vibratory convection are lacking in literature. Some studies have been published on a continuous spatial particle ALD system driven by pneumatic convection[16], but to the authors' knowledge, there are no published papers on CVR-ALD.

The relationship between vibration intensity and time-averaged powder convection velocity is still not well defined. Historically, algebraic expressions[7, 17] have been developed and single-particle or rigid body simulations[18-22] have been performed to investigate this behavior, but empirically fitted coefficients and lack of particle-particle collision treatment prevent these models from being predictive. DEM simulations have also been used to predict mean convection velocity of coarse powders in vibrating sieves[23], banana screens[24], and vibratory bowl feeders[25]. Prior investigations into linear vibratory conveyors and feeders have focused on particle shape[26], the so-called "reactive effect"[27], vibrator stall[28], and particle dispersion[29].

However, DEM simulations of fine powders in vibratory conveyors, where cohesive effects play a strong role, are still needed to investigate and improve powder flow behavior in CVR-ALD. Processing of fine (Geldart A) and ultrafine (Geldart C) powders are of great interest to more than just the ALD community[30]. Lessons learned on improving the flowability of powders in CVR-ALD reactors will have pertinence to other fine powder processes such as coating, drying and granulation[8]. DEM simulations, and ultimately CFD-DEM, could answer some key questions about particle-particle and particle-gas interactions during linear vibration. Here, we investigate the key particle-particle and particle-wall interactions in CVR-ALD using DEM modeling.

2.3 Methods

2.3.1 Discrete Element Method Equations

In the discrete element method, individual particles are tracked by solving Newton's equation of motion for translation velocity $\vec{u}^i$ and rotational velocity $\vec{\omega}^i$ of each particle i with mass m^i:

$$m^i \frac{\partial \vec{u}^i}{\partial t} = \sum \vec{F}^i = m^i \vec{g}^i + \sum_j \vec{F}_C^{i,j} + \vec{F}_D^i + \sum_k \vec{F}_{vdW}^{i,k} \tag{2-1}$$

$$I^i \frac{\partial \vec{\omega}^i}{\partial t} = \sum \vec{T}^i = \sum_j \vec{r}^{i,j} \times \vec{F}_C^{i,j} \tag{2-2}$$

where $\vec{g}^i$ is the gravitational acceleration; $\sum_j \vec{F}_C^{i,j}$ the sum of all P-P and P-W contact forces with each collision partner j; $\vec{F}_D^i$ the particle-fluid drag force; $\sum_k \vec{F}_{vdW}^{i,k}$ the sum of all van der Waals cohesive forces with each cohesive partner k; I^i the particle's moment of inertia; $\sum \vec{T}^i$ the total torque; and $\vec{r}^{i,j}$ the displacement vector from the center of particle i to its contact point with collision partner j. Pure granular flow (neglecting particle-fluid drag force term $\vec{F}_D^i$) will be considered in this study. This approach is common when modeling systems with gas velocities much lower than the minimum fluidization velocity u_{mf}[8] and has shown good agreement with experiments when modeling vibratory systems[1, 29], including vibratory conveyors[29]. CVR-ALD reactors operate below fluidization, resulting in fluid-particle drag forces that are small compared to cohesive forces (**Figure 2.1**). At sufficiently low reactor pressures P << 10 Torr typical of fluidized bed particle ALD, where the particle Knudsen number Kn_p (ratio of gas mean free path to particle diameter) exceeds 1[31] and drag forces are small at the relative velocities seen in CVR-ALD, we expect a pure DEM approach to accurately simulate the powder bed dynamics. By removing the fluid phase in this work, we can isolate solids-only interactions like vibration induced liftoff without the confounding effects of drag.

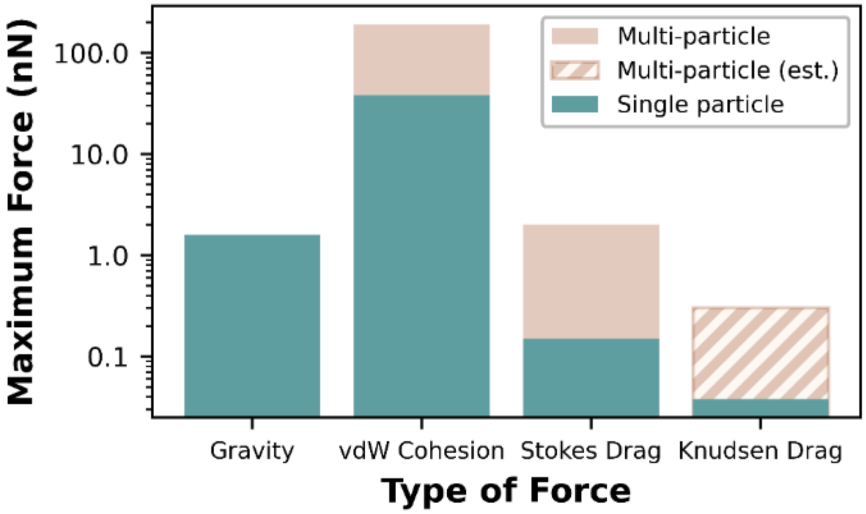

Figure 2.1. Approximate maximum forces due to gravity, van der Waals cohesion, and Stokes drag or Knudsen drag (for Kn=1). Details on these calculations can be found in **Supplemental Material A**.

DEM takes the soft-sphere approach, where overlap is directly calculated for each collision, to resolve the contact forces. Soft-sphere contact models use a network of springs and dashpots normal and tangential to the point of contact to approximate the contact mechanics. A slider in the tangential direction accounts for finite Coulomb friction. The linear spring-dashpot model (LSD) was chosen as the soft-sphere contact model in this study. In the LSD model, the normal (subscript *N*) and tangential (subscript *T*) contact forces are given by

$$\vec{F}_{C,N}^{i,j} = -k_N \delta_N \hat{u}_N^{i,j} - \eta_N \frac{d\delta_N}{dt} \hat{u}_N^{i,j} \tag{2-3}$$

$$\vec{F}_{C,T}^{i,j} = \begin{cases} -k_T \delta_T \hat{u}_T^{i,j} - \eta_T \dfrac{d\delta_T}{dt} \hat{u}_T^{i,j}, & \left|\vec{F}_{C,T}^{i,j}\right| < \mu \left|\vec{F}_{C,N}^{i,j}\right| \\ -\mu \left|\vec{F}_{C,N}^{i,j}\right| \hat{u}_T^{i,j}, & otherwise \end{cases} \tag{2-4}$$

where k is the spring constant; η the dashpot coefficient; δ the overlap for pair i,j; μ the sliding (kinetic) friction coefficient; and $\hat{u}_N^{i,j}$ and $\hat{u}_T^{i,j}$ the unit vectors along and perpendicular to the i,j line of contact, respectively. The normal dashpot coefficient η_N is related to the normal coefficient of restitution e_N by

$$\eta_N = \frac{2\sqrt{k_N m_{eff}}|ln e_N|}{\sqrt{\pi^2 + ln^2 e_N}} \tag{2-5}$$

where $m_{eff} = \frac{m_i m_j}{m_i + m_j}$ is the effective mass of the i, j pair. The relationships between tangential and normal spring constants $\left({}^{k_T}/_{k_N}\right)$ and dashpot coefficients $\left({}^{\eta_T}/_{\eta_N}\right)$ are typically set to a constant value of ${}^{2}/_{7}$ and ${}^{1}/_{2}$ in the linear spring-dashpot model, respectively.

The van der Waals cohesive force $\sum_k \vec{F}_{vdW}^{i,k}$ is determined using the Rumpf adhesion model. This model accounts for surface roughness through asperity height and requires fewer inputs than more complex expressions like the Rabinovich model[32].

$$\vec{F}_{vdW}^{i,k} = \frac{AR_i}{6s^2}\left(\frac{r_i}{r_i + R_i} + \frac{1}{\left(1 + \frac{r_i}{s}\right)^2}\right)\hat{u}_N^{i,j} \tag{2-6}$$

Here, A represents the Hamaker coefficient, s the separation distance of the adhesive pair, and r_i the asperity height. To avoid an infinite adhesive force at zero separation, an inner cutoff value is chosen equal to the typical minimum intermolecular distance (0.3 nm).

2.3.2 Simulation Setup

For particle flow modeling, we chose the widely used open-source code MFIX[33]. This multiphase flow package features many gas-solid flow modeling frameworks, a flexible guided user interface, and easy implementation of user-defined functions. The discrete element method (MFIX-DEM) allows for easy particle tracking and explicit treatment of material properties such as friction coefficient and particle-particle stiffness. Simulations were performed using distributed memory parallelization on the RMACC Summit supercomputing cluster at the University of Colorado[34].

The conveyor was moved kinematically using accelerometer data. This approach allows us to shrink our simulation size by using a periodic box model, providing flexibility in computational expense. The reactor kinematics can be incorporated as a position, velocity, or acceleration condition in a periodic box model. A hybrid condition with a fluctuating wall Y-velocity and fluctuating gravitational acceleration[35] was chosen for highest accuracy without the complexity of programming a moving mesh. These modifications were implemented using Fortran user-defined subroutines in the MFIX source code.

Soda-lime glass microspheres (GL0191B4, 45-63 μm) from Mo-Sci Corporation were chosen as the substrate material in this study (**Figure 2.2**). These microspheres are an ideal material due to their well-characterized properties[36, 37] and predictable flow behavior as mildly cohesive Geldart A powder. Ultrafine Geldart C powders (<20 μm) are also used as substrates in CVR-ALD but present a much higher computational expense in DEM and additional interparticle forces such as hydrogen bridging[38], wet cohesion, and electrostatic charging[39] become non-negligible at these small sizes. The particle-particle (P-P) Hamaker constant A_{pp}, the P-P friction coefficient μ_{pp} and the P-P restitution coefficient e_{pp} were chosen based on experimental measurements for soda lime glass spheres [36, 40]. An asperity height of 1 nm was selected to match experimental observations of pull-off force for 50 μm soda lime glass microspheres[37]. The particle-wall (P-W) Hamaker constant is calculated as the geometric mean from the interacting materials, $A_{pw} = \left(A_p A_w\right)^{1/2}$[41]. Other material properties relevant to particle-wall (P-W) interactions were taken from manufacturer data sheets or literature[36, 40, 42-45] (**Table**

2.1). The dimensionless granular P-P Bond number (Bo_{pp}^*) is also included in **Table 2.1** to quantify the intensity of cohesive forces for 50 μm soda lime glass spheres.

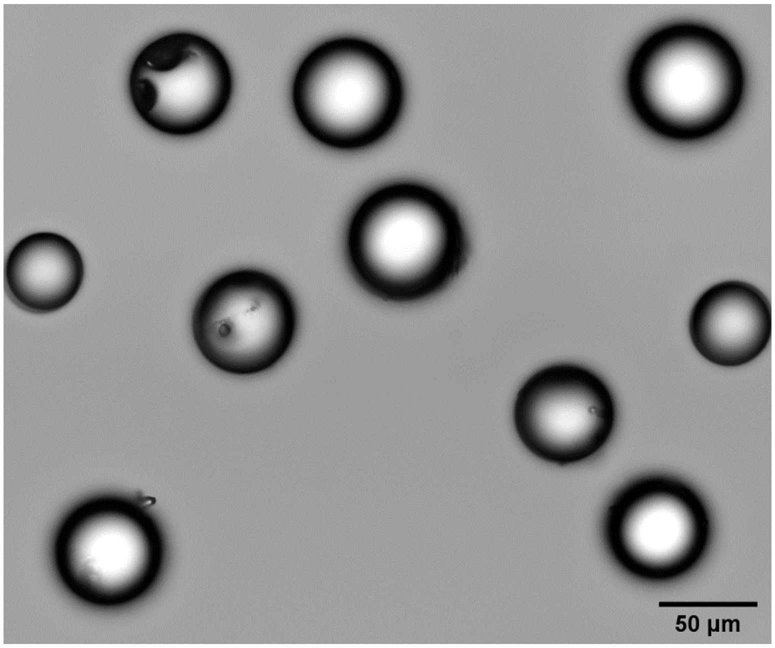

Figure 2.2. Optical microscope image of 45-63 μm soda lime glass microspheres.

Table 2.1. Properties used in DEM simulations to simulate Mo-Sci glass microspheres on a porous stainless surface

Parameter	**Value**
Mechanical properties	
Particle diameter, d_p	$50\ \mu m$
Particle density, ρ_p	$2500\ kg/m^3$
P-P friction coefficient, μ_{pp}	0.273
P-W friction coefficient, μ_{pw}	0.4
P-P restitution coefficient, e_{pp}	0.97
P-W restitution coefficient, e_{pw}	0.83
Particle Young's modulus, E_p	$73\ GPa$
Wall Young's modulus, E_w	$22\ GPa$
Particle Poison's ratio, ν_p	0.22
Wall Poison's ratio, ν_w	0.07
Cohesive properties	

P-P Hamaker constant, A_{pp}	$3.1 \times 10^{-20}\,J$
P-W Hamaker constant, A_{pw}	$6.2 \times 10^{-20}\,J$
Asperities	$1\,nm$
Outer cutoff (for $F_{van\ der\ Waals}$)	$10\,nm$
Inner cutoff (for $F_{van\ der\ Waals}$)	$0.3\,nm$
$Bo_{pp}^{*} = F_{cohesion}^{max}/m_p g$	24

2.3.3 Experimental Setup

Experiments were conducted using an in-house continuous vibrating bed reactor (Forge Nano Inc., Colorado, **Figure 2.3**). A pair of fiberglass leaf springs support the stainless steel reactor housing vibrated by a pneumatic linear actuator (Martin NTK 25 AL). Particles travel through the reactor on top of a 1/16” thick sintered stainless frit from Mott Corporation with a mean pore size of 10 μm to allow for purge gas and precursor gas flow during ALD. The gas flow was turned off ($v_g = 0$) for all experiments in this work. Oscillation frequency and amplitude can be controlled independently by adjusting the supplied air pressure and the outlet metering valve position (SMC ASN2-03) to the pneumatic actuator, respectively. A Mide Slam Stick X tri-axial piezoelectric accelerometer (±16 g DC response MEMS, 1600 Hz sampling rate) was attached to the top of the reactor to measure conveyor acceleration. Powder convection velocity was determined by timing the powder’s travel between two lines on the reactor with a stopwatch. Flow tests were performed at atmospheric pressure (626 Torr) and low pressure (2 Torr) using a vacuum pump. A camera mounted on a tripod captured top-view and side-view videos of powder flow behavior. The stainless upper chamber of the reactor was replaced with a transparent acrylic chamber during imaging tests. Stainless steel shim tape was placed over the inner walls of the acrylic to mimic the stainless walls of the upper reactor chamber.

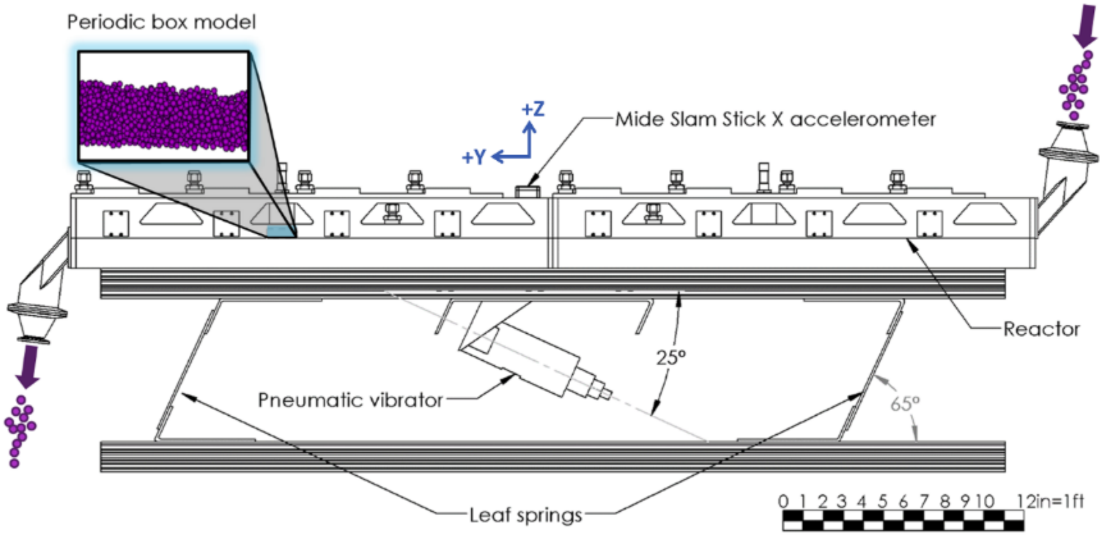

Figure 2.3. Computer-aided design (CAD) model of the continuous vibrating bed reactor. CAD models of the pneumatic vibrator and accelerometer were obtained from GrabCAD. Exploded inset provides context for the approximate region simulated by the periodic box model

A continuous function describing the reactor oscillations can be developed by reconstructing the accelerometer signal using the three largest-amplitude harmonics from Fast Fourier Transform decomposition (the "FFT model"). By summing the cosine waves of each m^{th} component with frequency f_m, phase angle ϕ_m, and amplitude A_m, the FFT model for acceleration $\ddot{x}$ in the k^{th} direction can be described by the equation

$$\ddot{x}_k(t) = \sum_m A_m \cos(2\pi f_m t - \phi_m) \tag{2-7}$$

This method requires a well-conditioned input data set with 2^n data points, where n is any integer, for accurate amplitude and phase angle extraction. One challenge hindering accurate amplitude extraction is the slight irregularity in accelerometer sampling interval. Time step irregularities were corrected by resampling at a constant interval. Some amplitude loss was encountered during FFT signal decomposition, so the FFT model amplitude was magnified slightly through multiplication by a constant "mod factor" based on the maximum amplitude of the low pass filtered signal. Finally, a numerical fitting procedure was applied to the phase angles, which are not well determined from FFT, using MATLAB's *fmincon* function. With an FFT model in place, the signal is integrated once to determine velocity $\dot{x}_k$ and twice to determine position x_k as described by

$$\dot{x}_k(t) = \sum_m \frac{A_m}{2\pi f_m} \sin(2\pi f_m t - \phi_m) \tag{2-8}$$

$$x_k(t) = \sum_m \frac{-A_m}{(2\pi f_m)^2} \cos(2\pi f_m t - \phi_m) \tag{2-9}$$

2.4 Results and Discussion

2.4.1 Characterizing Vibratory Convection

We need frequency and amplitude data to describe the reactor vibration as inputs to the vibrating bed DEM simulation. Y and Z-acceleration data (**Figures 2.4A, 2.4C**) were obtained for an inlet pressure of 60 psi at maximum amplitude (100% open throttle) and used as the baseline case. A Fast Fourier Transform was performed on the Y/Z-acceleration in MATLAB using the built in *fft* function to reveal the underlying frequencies (**Figures 2.4B, 2.4D**). For the purposes of this discussion, the +Y axis lies along the primary flow direction (reactor long axis) and -Z axis lines up with gravitational acceleration (**Figure 2.3**). X acceleration was disregarded as noise and omitted due to X-direction constraints by the reactor walls and lack of X-motion observed experimentally. Accelerations are normalized by Earth's gravity through the acceleration ratio $\ddot{x}_k/g$. A conveyor acceleration equal to gravity, $\ddot{x}_k = 9.81\ m/s^2$, corresponds to a normalized "g-force" of 1g.

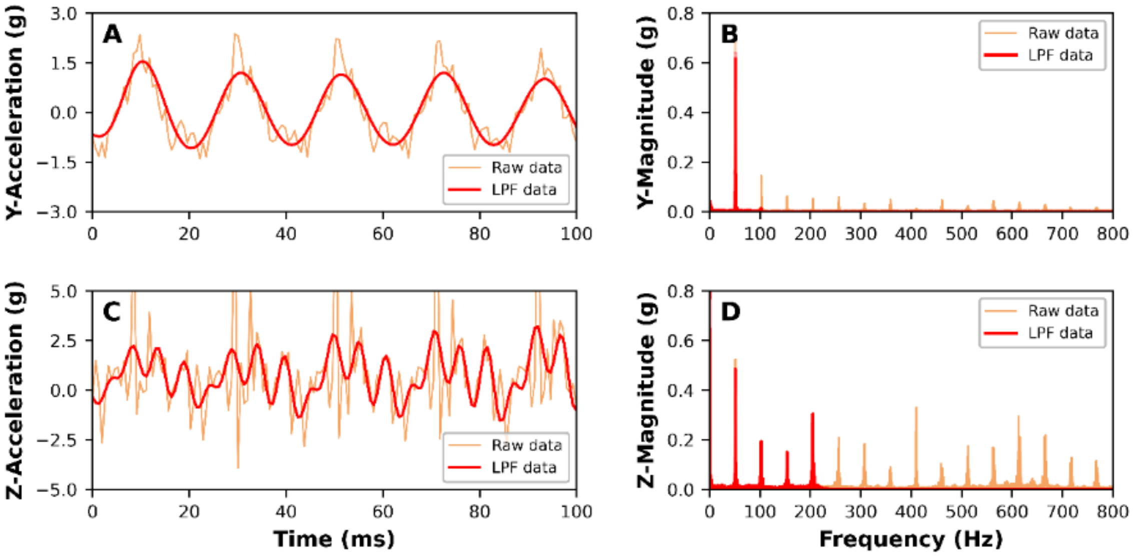

Figure 2.4. Plots of raw time-domain (A, C) and frequency-domain (B, D) accelerometer results. Low-pass filtered ("LPF") data are overlaid to emphasize the relative magnitude of low-frequency components

Both the principal (Y) and gravity (Z) directions are characterized by high-g total acceleration. Despite strong differences in high-frequency content, both directions have similar g-forces at low frequencies. The dominant frequency in the FFT results matches the base actuator frequency of 48 Hz, so although reactor displacement is only submillimeter, maximum accelerations are >1g in both Y and Z-directions. Another interesting feature is the strong presence of integer multiples of the fundamental frequency, also called "harmonics". Both directions have strong harmonics, but the Z direction shows significantly stronger resonance than the Y direction. The bolts holding the top and bottom halves of the assembly together may be acting as nodes along the reactor body, allowing small standing waves to form between anchor points in the unconstrained Z-direction. The resonance behavior of steel, which makes up most of the reactor body, has been correlated with microstructural properties such as alloy composition, material hardness, fracturetoughness, and the presence of nonmetallic inclusions[46, 47]. Rigidity and composition of the support can be tuned to produce the desired harmonic response, enabling harmonic intensity to be treated as a degree of freedom. The influence of resonance on powder flow behavior is investigated further in Section 2.4.3. Details on the waveform characteristics (amplitude, frequency, and phase for **Figure 2.5** data) can be found in **Table 2.2.**

Table 2.2. Sample waveform characteristics from FFT model fitting.

	1Y	**1Z**	**2Z**	**3Z**
Amplitude, A_m $[{}^{m}/_{s^2}]$	10.581	10.273	10.114	9.154
Frequency, f_m $[Hz]$	48	48	192	167
Phase, ϕ_m $[rad]$	3.08	3.08	-2.66	-1.38

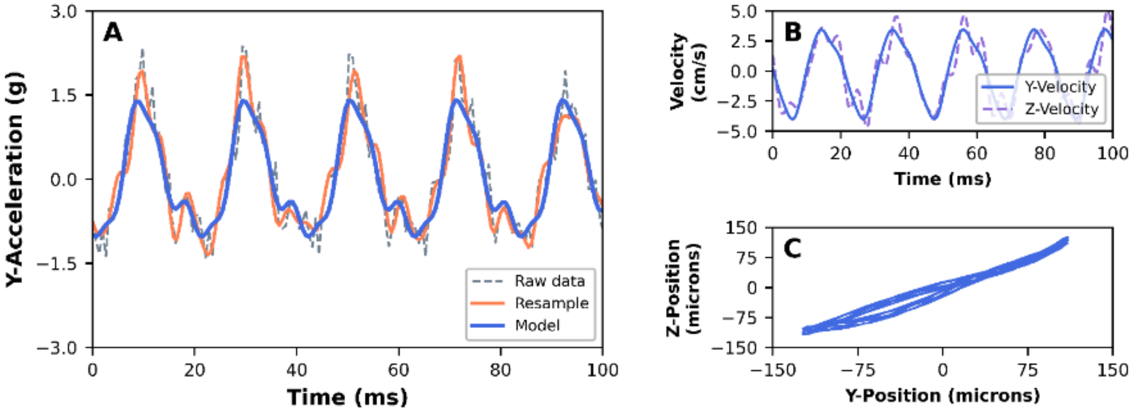

Figure 2.5. (A) Raw accelerometer data with resampled waveform and FFT model overlaid. Velocity (B) and position (C) were determined by integrating the FFT acceleration model

The presence of frequency f_m in the coefficient denominators causes high-frequency components to drop out upon integration, so Y and Z-position are similar even though Y and Z-acceleration are not. The Y and Z-positions form two in-phase sinusoids of similar magnitude, consistent with the “forward and upward” extension and “backward and downward” retraction mechanism. Under these conditions, many modes of motion are available to the particles, including no-slip conveyor contacting, forward sliding, backward sliding and hopping[48]. There are two mechanisms that could explain the bulk convection of powder in a CVR-ALD reactor. Mechanism 1 is a no-slip/slip mechanism or “continuous contact” conveying and is common for non-sinusoidal conveyors[49]. Continuous contacting assumes the particles maintain some contact with the conveyor during extension but slide on the conveyor during retraction, giving net-forward motion. Mechanism 2 is a throw or hopping mechanism, the most common method discussed in literature[48]. Here, the particles once again maintain contact with the conveyor during extension but then lose contact or “lift off” from the conveyor during retraction, producing net-forward motion. In addition to conveyor design and operating conditions, we expect that particle properties such as friction coefficient, Hamaker constant, and coefficient of restitution will determine which convection mechanism dominates. To the authors’ knowledge, there has been no investigation into the possibility of a hybrid slide-throw mechanism. For certain fine powders with low P-W friction or high Y-acceleration, conveyors may operate in a hybrid state, where some micro-slipping occurs for bottom-layer particles at the conveyor-particle interface and some liftoff occurs in the powder bulk during frit retraction. The cutoff between hopping and sliding is difficult to distinguish experimentally, but we can investigate the contact behavior at the particle-wall interface under vibratory convection through DEM simulations.

2.4.2 Modeling Particle Convection with DEM

Simulations were run using the conditions defined in **Table 2.3**. A detailed explanation for these simulation parameters can be found in **Supplemental Material B**. To aid in discussion of the results, we will define several theoretical limits for powder convection based on the reactor kinematics and idealized hopping trajectories (**Figure 2.6**).

First, we will use the “straight drop” solution to define a lower limit on ideal convection. This trajectory assumes that the particle travels with the conveyor on the extension stroke and separates or “lifts off” at the start of the retraction stroke. In this case, the conveyor imparts the minimum forward velocity possible (zero) to the particle during the flight stage, leading to no forward motion during the retraction stage and a time-averaged convection velocity of $\frac{\left(A_1/_{2\pi f_1^2}\right)}{T} = \frac{226\ \mu m}{20.83\ ms} = 1.08\ cm/s$. At the other extreme, we have the “perfect flight” solution, where particles travel at the maximum conveyor velocity of 3.51 cm/s and only briefly contact the frit before being launched again. It is worth noting that perfect flight conditions, which correspond to vibro-fluidization, require high conveyor accelerations >3g[50]. This speed can also be theoretically achieved through a slip/slip ‘sealskin’ convection mechanism if the particles slide forward on a frit material with a high extension friction coefficient and low retraction friction coefficient[51]. The true velocity profile of the powder bed will depend on the particle-particle and particle-wall dynamics which determine exactly when liftoff or sliding occurs. Here, any real convection velocity between the perfect flight and straight drop solutions will be referred to as “ideal” convection, and any below the straight drop solution as “partial” convection. Neither straight drop nor perfect flight are fully achievable in practice but can still be used to benchmark conveying efficiency.

Table 2.3. Simulation geometry and parameters

Parameter	Value
Periodic box depth	0.25 mm/5d_p
Periodic box width	5 mm/100d_p
Static bed height	0.75 mm/15d_p
Simulated P-P spring constant, k_{pp}	2500 N/m

Simulated P-W spring constant, k_{pw}	1562.5 N/m

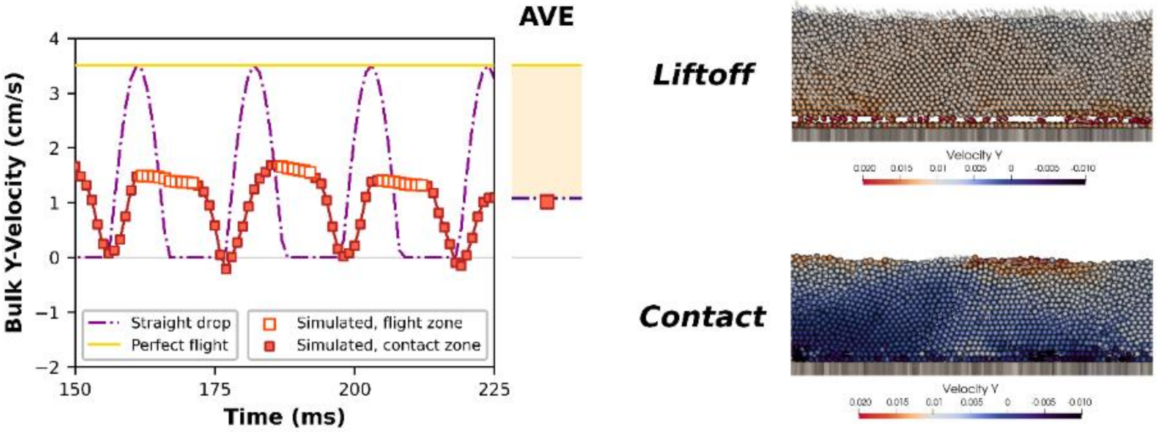

Figure 2.6. Simulated powder convection velocity compared to limiting behavior under straight drop and perfect flight conditions. Time average for the simulated profile (square point) relative to the time averages from the analytical solutions (straight and dash-dot lines) is displayed in **AVE**. Yellow shading spans the range of time-averaged velocities corresponding to ideal convection

The simulated powder velocity profile includes features of the straight drop and perfect flight limiting behaviors. As in the straight drop approximation, the powder follows a quasi-sinusoidal forward trajectory during frit extension but lifts off before the extension stroke is complete. The point when liftoff begins varies from cycle to cycle but is typically near the middle of the extension stroke, at maximum frit velocity. During liftoff, the particles travel under free flight as indicated by the plateau in convection velocity. This trajectory is analogous to the constant horizontal velocity imparted on a projectile in the absence of drag. The particles then recontact the frit around the middle of the retraction stroke and undergo a deceleration period before establishing no-slip contact with the frit. A lack of particle-wall sliding in the simulations indicates that a pure hopping mechanism, not a hybrid sliding-hopping mechanism, is dominant for 50 μm glass microspheres.

Qualitatively, both the simulated and experimental results show nearly ideal plug flow behavior (**Figure 2.7**). Individual microspheres are difficult to distinguish during reactor vibration, so a row of microspheres was colored with Jacquard Piñata Color glass dye to track particle movement during the stopwatch tests. Simulated particles were also colored to aid in side-by-side comparisons with the tracer tests from the experimental setup. Side views of the simulation results show a clear front of particles with nearly uniform powder velocities in the bulk and lower, nonzero convection velocities at the particle-frit interface. Dispersion can be observed in the bottom particle layer due to cohesive particle-frit interactions impeding forward convection. Top views from both the experimental and simulated results show smooth, consistent fronts of tracer particles. Significant changes in particle-wall stickiness or friction, which can occur with a new substrate material or deposited film chemistry, will likely affect the shape of this convection profile. It is also worth noting that the periodic box model, by virtue of being periodic, assumes reactor-depth-independent flow behavior. Here, where wall-to-wall deviations from ideal plug flow are relatively small, the periodicity approach was able to produce realistic results. Powders other than soda lime glass may not exhibit ideal plug flow experimentally, so the validity of a periodic box for vibrating bed reactor modeling should be verified on a case-by-case basis.

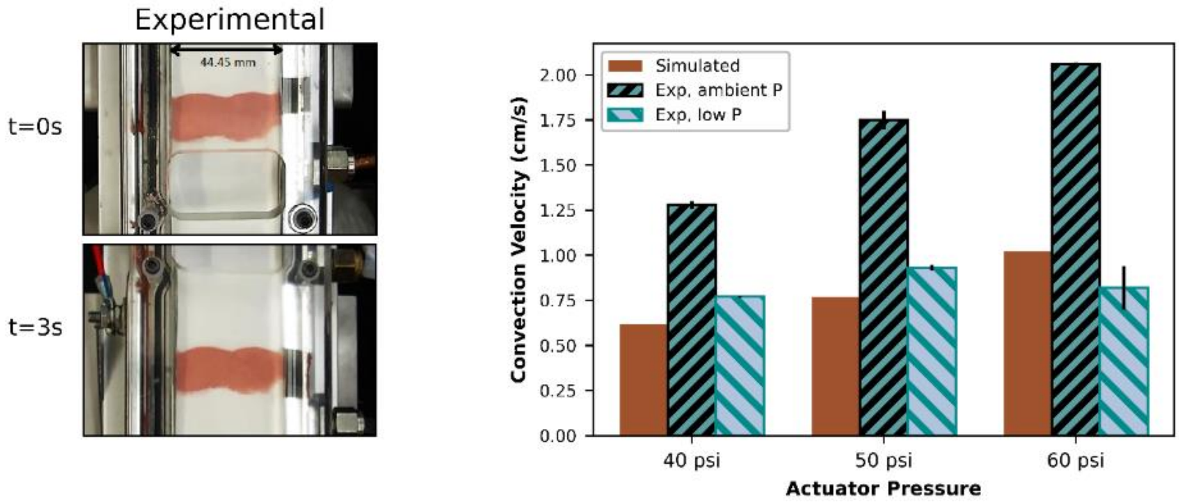

Figure 2.7. Snapshots from experimental tracer tests at two different points in time illustrating the solids flow behavior. Time-averaged convection velocity from the simulations is compared to the experimentally determined convection velocities at ambient pressure (626 Torr) and low pressure (2 Torr). Errors bars represent the calculated standard deviation from 3 replicates at each actuator pressure

Differences in mean convection velocity between ambient pressure and low-pressure tests indicate that drag effects play a role in the low Knudsen number regime at all three actuator conditions tested (**Figure 2.7**). Even a stationary background gas phase would lead to noticeable Stokes drag in a porous vibratory conveyor, where maximum reactor Z-velocities are comparable to the minimum fluidization velocity of the powder. The low-pressure condition shows closer agreement to the DEM results than tests at ambient pressure. At room temperature and 2 Torr, the mean free path of nitrogen molecules is around 25 microns, half of the mean particle diameter. Dense, highly coordinated particle regions further confine the gas flow to small interstitial spaces between particles. Slip-flow or free molecular flow may be occurring in the interstitial gaps, reducing the effective drag force and leading to improved agreement between experimental and simulated results at low pressure. The remaining disagreement between experimental and simulated results at 2 Torr may also be due to imperfect determination of the frit excitation amplitude. All assemblies have finite rigidities and measured acceleration is known to vary with accelerometer placement[52]. The channel containing the thin reactor frit, which is too shallow for accelerometer placement, may be experiencing higher accelerations than the thick and rigid reactor upper chamber where the accelerometer is mounted. The accelerometer sensor's signal-to-noise ratio and the FFT signal decomposition process also have finite resolutions that limit their accuracy. Jump discontinuities in the accelerometer data lead to ringing artifacts such as Gibbs phenomenon during signal processing[53]. Further studies will be needed to explore gas-phase effects in the low Knudsen number regime.

2.4.3 The Role of High-Frequency Excitation

The rigidity of the reactor support plays a role in the solids flow behavior through amplification or attenuation of conveyor resonance. To illustrate this, accelerometer results (**Figure 2.8**) are provided for two different conveyor support structures at the same actuator conditions (60 psi, 100% open throttle). The "no flow" conveyor support had a smaller leaf spring separation and less rigid base than the improved "flow" conveyor support structure from **Figure 2.3**. There are two noticeable changes from the no flow to the flow scenario. The first is an increase in the amplitude of the first harmonic. The second is the magnification of higher resonant frequencies. Resonance caused by operating frequencies near the conveyor's natural frequency are hazardous, generating dangerously large deflections and high stresses that compromise mechanical integrity of the entire structure[54]. However, low amplitude resonance of individual components such as the frit may improve powder agitation and flow. Conveyor resonance characteristics are a key component in resonance-based vibratory feeders but often ignored in brute force driving mechanisms like the pneumatic actuator in this study. Either, or both, of these factors could explain the transition to steady powder flow. Although the beneficial effects of increasing the first harmonic amplitude have been documented for low-g conveyors[7], the superposition of resonant frequencies and their effects on powder flow behavior in brute force vibratory convection remain unreported.

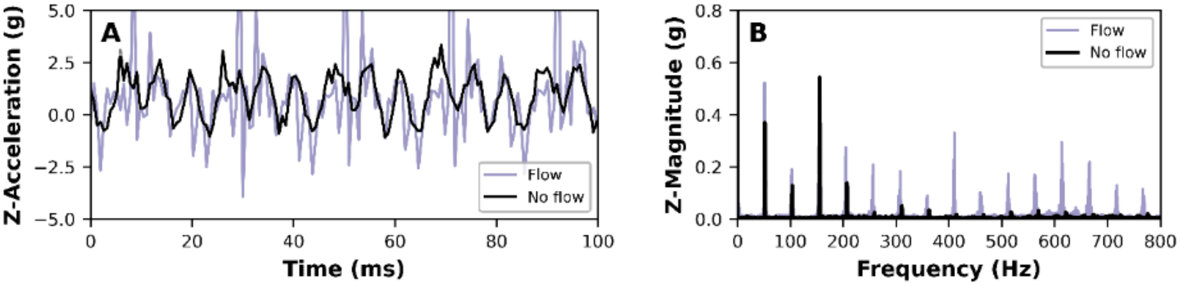

Figure 2.8. Raw time-domain (A) and frequency-domain (B) acceleration data when powder "flow" and powder "no flow" was observed

To support the notion that resonant frequencies play a role in hopping convection, FFT models are presented at near-1g conditions (**Figure 2.9**). Shading corresponds to favorable periods for liftoff when the net force due to gravity and vibration is <0g and results in momentary particle weightlessness. The importance of weightlessness in hopping convection has been discussed by other researchers in the vibratory conveying field[7]. Considering only the first harmonic ("1f" in **Figure 2.9**), a <1g case will always remain above the 0g threshold. Ensuring hopping convection of bottom layer particles impeded by downward-acting contact forces will require a net force due to vibration and gravity <0g. A first harmonic of 1.05g (**Table 2.2**) leads to some instances of weightlessness, but they are small and short-lived. After incorporating the two strongest resonant frequencies ("3f"), the number and magnitude of weightlessness instances greatly increases. This increase in <0g occurrences with resonance can be seen in the raw accelerometer data between the no flow and flow cases (**Figure 2.8**). Thus, Z resonance can be considered a tunable parameter to increase the duration of <0g events without changing Y acceleration.

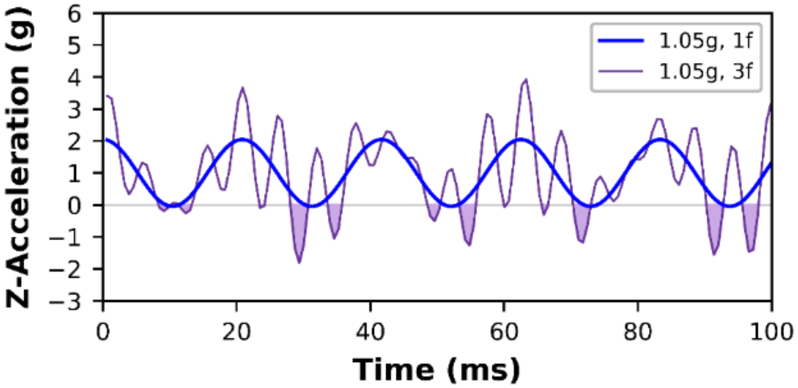

Figure 2.9. FFT model acceleration with regions <0g shaded to highlight instances of weightlessness

2.4.4 Optimizing Convection Efficiency

Another implication of this frequency sensitivity is the opportunity for optimizing the excitation waveform. Alternatives to the simple sinusoidal waveform, from out-of-phase sinusoids[55] to non-sinusoidal excitation[18, 49], provide another avenue for improving powder flow behavior in vibratory convection. Excitation modifications may be needed in cases where increasing total acceleration amplitude to drive powder flow comes with undesirable side effects. Y and Z are geometrically linked by the leaf spring setup such that we cannot independently vary the Y and Z excitations without making support modifications. This geometric constraint limits the minimum steady powder convection velocity that can be achieved under hopping convection in a horizontal conveyor, which requires >0.5g Z accelerations[48]. Lower convection velocities corresponding to <0.5g in the Y direction may be desirable in CVR-ALD for ultrafine powders that easily elutriate at >1g or slow chemistries that require longer dose times. Changes to the vibration waveform or superposition of resonant frequencies by using stiffer metal support structures, which introduces randomness to the agitation, may be more effective at separating cohesive particle-wall contacts and promoting steady powder flow than increasing the first harmonic amplitude.

We will investigate an excitation waveform that enables lower convection velocities of highly cohesive fine powders in CVR-ALD. In both the continuous contact and hopping mechanisms, we want to optimize particle translation during extension. Lower speeds on the extension stroke should decrease particle backward slipping during convection. To discourage sticking during retraction, which reverses forward progress made during the extension stroke, higher retraction speeds are desired. Here, we propose a reactor position profile that follows a sawtooth waveform to minimize extension-backsliding and retraction-sticking tendencies.

To approximate a sawtooth, we use a piecewise sinusoid with low-frequency extension and high-frequency retraction. The maximum displacement of this pseudo-saw is set equal to the baseline sinusoid (113 μm) for comparison purposes, so that the lower velocity limits as defined by straight drop convection are the same. The piecewise function is defined using relative time $t^* = mod(t/T_1)$ with respect to the period of the baseline sinusoid T_1. The constraints for a continuous piecewise sinusoid with the same amplitude and total period as the baseline sinusoid are

$$1/f_a + 1/f_b = 2/f_1 \tag{2-10}$$

$$\sin(2\pi f_a t_{crit} - \phi_1) = \sin(2\pi f_b t_{crit} - \phi_b) \qquad where\ t_{crit} = \frac{1}{4f_a} + \frac{\phi_1}{2\pi f_a} \tag{2-11}$$

where t_{crit} refers to the transition point between half sines a and b, when the first half sine is at its maximum. For simplicity, we have chosen $f_a = {}^{2}/_{3}\, f_1$ in this study. ϕ_b is solved for numerically using the constraint defined in equation 2-11. Combining these relationships results in a piecewise function as described by equations 2-12a and 2-12b.

$$x(t^*) = \begin{cases} \dfrac{A_1}{(2\pi f_1)^2}\sin(2\pi f_a t^* - \phi_1)\,, & t^* < t_{crit} \\ \dfrac{A_1}{(2\pi f_1)^2}\sin(2\pi f_b t^* - \phi_b)\,, & otherwise \end{cases} \tag{2-12}$$

The pseudo-saw waveform results in higher convection velocities than the sinusoidal waveform (**Figure 2.10**). Although the pseudo-saw travels slower on extension, giving a lower perfect flight maximum of 2.27 cm/s than the baseline sine from **Figure 2.6**, the hopping convection cycle is more effective, giving a higher time-averaged velocity of 1.57 cm/s. Particles under this excitation remain in liftoff during the full retraction phase, avoiding the low or even backwards velocities observed under pure sinusoidal excitation. observed under pure sinusoidal excitation.

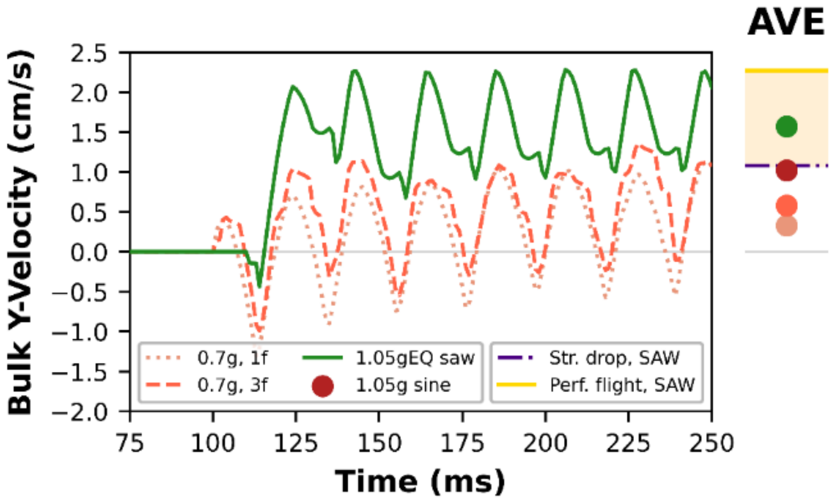

Figure 2.10. Spatially averaged powder y-velocity for the baseline case from **Figure 2.6** (1.05g sine) versus low-amplitude cases (0.7g, 1f and 0.7g, 3f) and optimized sawtooth waveform with an "effective" average acceleration equal to the baseline case (1.05gEQ saw). Time average for the simulated sawtooth profile is compared to averages for the simulated sine waves (AVE)

Simulations incorporating higher resonant frequencies were also performed to verify the role of resonance proposed in Section 3.3. As expected, the time-averaged convection velocity increased from 0.33 cm/s to 0.58 cm/s when the next two resonant frequencies were added to a bed excited at 0.7g (**Figure 2.10**). Liftoff plateaus appeared once higher frequency content was included, indicating an improvement in convection behavior. Smaller dips in the bulk velocity profile also demonstrate a decrease in backflow for the three-frequency case. Higher amplitude excitations (>0.9g) at the same fundamental frequency showed little to no change when additional frequencies were incorporated, indicating that resonance improves convection through promotion of weightlessness when the first harmonic is <1g. Thus, high-frequency Z resonance contributes to achieving the weightlessness necessary for powder liftoff in sub-1g conveyors.

The robustness of the pseudo-saw waveform is best demonstrated with a highly cohesive substrate. Large Hamaker coefficients of $A_{pp} = A_{pw} = 4 \times 10^{-19}\,J$ were used to describe a highly cohesive powder, increasing the Bo_{pp}^{*} number from 24 to 307. Hamaker constants or Bo_{pp}^{*} numbers of this magnitude can be expected among metallic substrates[41] or particles in high humidity environments based on pull-off force measurements[56] and have been used by other researchers to simulate micron-size cohesive powders[57]. Effective acceleration for the sawtooth waveform, which has a piecewise varying acceleration, refers to acceleration based on the displacement equalization procedure described in equations 2-11 and 2-12a,b. A regular basis must be defined for comparisons since the sawtooth waveform has a lower maximum extension velocity at each effective acceleration than the sinusoidal waveform. Here, we normalize the results by defining a convection velocity efficiency η_{cv} based on the time-averaged simulated particle velocity $v_{p,ave}$ and maximum frit extension velocity $v_{w,max}$:

$$\eta_{cv} = \left| \frac{v_{p,ave}}{v_{w,max}} \right| \tag{2-13}$$

As expected, the sawtooth waveform produces higher convection velocities and more consistent convection efficiencies than the sinusoidal waveform at sub-2g input accelerations (**Figure 2.11**). The sinusoidal waveform is unable to produce consistent and measurable powder convection until >1.4g acceleration, indicating a failure to break cohesive particle-wall bonds during frit retraction. The 1.4g to 2g input region is also marked by severe fluctuations in bulk velocity and hopping suppression. Consistent powder flow behavior is not observed until at least 2.2g, when the sinusoidal waveform stabilizes at around 38% convection efficiency. The 2.2g cutoff corresponds to a minimum convection velocity of 2.84 cm/s that can be reliably achieved with this sinusoidal excitation, higher than the <2 cm/s velocities ideal for adequate precursor exposure in typical CVR-ALD reactors. By contrast, the sawtooth waveform demonstrates stable powder convection for velocities as low as 0.33 cm/s with clear and consistent liftoff regions for all accelerations >0.4g and stable convection efficiencies around 34% for >0.8g accelerations. When cohesive particle-wall interactions prevent powder convection, sinusoidal excitation can be replaced with an optimized sawtooth waveform to achieve slow, steady powder flow.

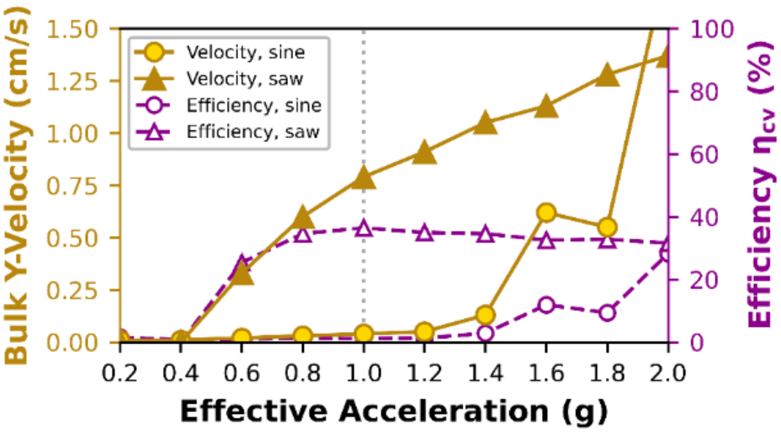

Figure 2.11. Convection velocity and efficiency comparisons for the sawtooth and sinusoidal waveforms

2.5 Conclusions

The solids flow behavior of fine cohesive powder in a vibrating bed reactor was studied using the discrete element method. Bulk simulated velocity results revealed clear liftoff plateaus typical of a hopping convection mechanism. In experimental and simulated tracer tests, the powder bed exhibited nearly ideal plug flow behavior. For the pure DEM approach taken in this work, close agreement between experiments and simulations can only be expected in the high Knudsen number regime where gas-particle drag is negligible. With gas manifolds turned off, particles moving through a quiescent background gas phase at ambient pressure travel at conveyor velocities close to the minimum fluidization of fine Geldart A powders, generating appreciable drag forces. Tests at high and low reactor pressures corresponding to particle Knudsen numbers in the continuum and slip-flow regimes, respectively, confirmed that only the low-pressure case achieved quantitative and qualitative results that were comparable with the experimentally observed solids flow behavior.

FFT decomposition of the reactor acceleration revealed the importance of high-frequency excitation for horizontal conveyors at low-g accelerations. Adjustments to the excitation waveform or the resonance behavior provide another avenue for improving powder flow behavior. Flow improvements under the novel sawtooth waveform demonstrate the importance of high-g retraction for convection of highly cohesive fine powders at low flow velocities. If steady powder flow is not possible under simple sinusoidal excitation, the waveform can be optimized by tuning half-wave frequency and amplitude. Future work will incorporate the gas phase in a CFD-DEM model for investigations into the gas-solid coupling and its effects on flow behavior.

Acknowledgements

The authors are grateful for the support of the National Science Foundation [NSF GOALI #1852824]. This work utilized the RMACC Summit supercomputer, which is supported by the National Science Foundation (awards ACI-1532235 and ACI-1532236), the University of Colorado Boulder, and Colorado State University. The Summit supercomputer is a joint effort of the University of Colorado Boulder and Colorado State University. The Summit supercomputer is a joint effort of the University of Colorado Boulder and Colorado State University. The authors also thank Forge Nano for providing the CVR-ALD reactor and Jay Valuet at Martin Vibration Systems for helpful discussions and feedback on upgrading the vibratory convection setup.

Supplemental Material A. Estimating Maximum Forces

The maximum force estimates in **Figure 2.1** were determined using CVR-ALD reactor conditions and equations from literature. The cohesive force was calculated using equation 2-6 for a single contact (single-particle) and five contacts (multi-particle) at a minimum separation of 0.3 nm, a Hamaker constant of $A = 3.1 \times 10^{-20} J$ and a surface roughness of 1 nm. Drag forces were determined using the single-particle drag expression

$$F_D = \frac{1}{2}\rho_g\left(u_p - v_g\right)^2 C_d \frac{\pi}{4} {d_p}^2 \qquad (2.a.1)$$

where ρ_g is the gas density; u_p the particle velocity; v_g the gas velocity; C_d the drag coefficient; and d_p the particle diameter. A maximum relative velocity of ~2 cm/s was chosen for 50-micron soda lime glass microspheres based on minimum fluidization velocity and tested actuator conditions. Stokes drag ($C_D = \frac{24}{Re}$) was used in **Figure 2.1** due to the low characteristic Reynolds numbers $\left(Re = \frac{\rho_g |u_p - v_g| d_p}{\mu_g} < 0.1\right)$ at CVR-ALD reactor conditions. For multi-particle drag, an estimate based on the Ergun drag coefficient correlation

$$C_D = \frac{a}{Re}\frac{1-\varepsilon}{\varepsilon^2} + \frac{B}{\varepsilon^2} \qquad (2.a.2)$$

with $a = 180$, $b = 1.8$, and $\varepsilon = 0.50$ was used[58]. The single-particle Knudsen drag correction from Loth at $Kn = 1$,

$$C_{D,Kn,Re} = \frac{\frac{24}{Re}\left(1 + 0.15Re^{0.637}\right)}{\left(1 + \left(2.514 + 0.8e^{\frac{-0.55}{Kn}}\right)Kn\right)} \qquad (2.a.3)$$

was used for the Knudsen estimate in **Figure 2.1** [59]. The presence of nearby particles is known to increase the drag force, and while multi-particle correlations for high-Knudsen aka “rarefied” flows are lacking in literature, an approximate magnification factor was applied in **Figure 2.1** using Lattice Boltzmann simulation data on multi-particle arrays in boundary-slip flows at low Re[60]. The chosen magnification factor (8) is likely an overestimate for $Kn = 1$ and thus a conservative guess for maximum multi-particle Knudsen drag. As the Knudsen number increases (*i.e.* lower reactor pressures) the relative influence of drag will continue to decrease.

Supplemental Material B. Choosing Simulation Conditions

The domain size and simulated P-P/P-W stiffness in a periodic box model must be chosen carefully. At a minimum, the periodic box must be large enough that further increases in the box size do not affect the simulation results. Domain sensitivity tests revealed the need for periodic box sizes ≥75 particle diameters wide and ≥5 particle diameters deep for system-size independent results based on trends in the spatially averaged ("bulk") powder velocity (**Figures B.1A, B.1B**).

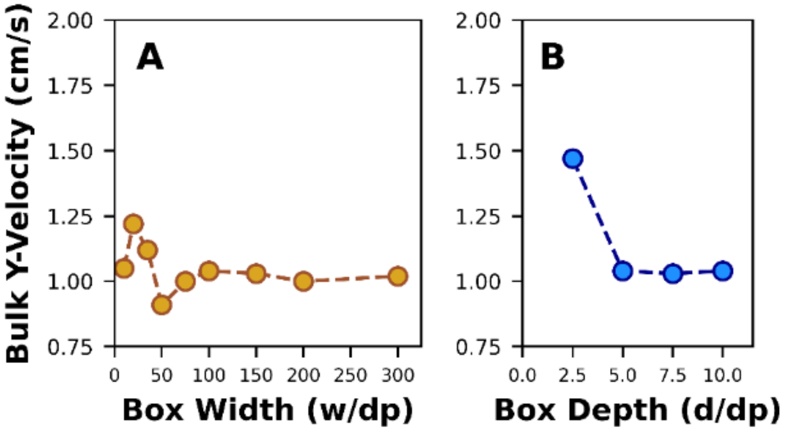

Figure B.1. (A,B) Sensitivity tests on periodic box size. Box dimensions are specified in terms of number of particle diameters

Simulations using a nonlinear (Hertzian) spring-dashpot model were performed to verify the accuracy of a linear spring-dashpot model for low-g vibratory convection. The Hertzian model is based on the linear theory of elasticity and is highly accurate for low-strain collisions of elastic spheres[61]. The linear spring-dashpot model provides a computationally efficient linearization to Hertzian contact mechanics and, for near-elastic behavior ($e_{pp} > 0.8$), has been shown to agree with experimental results fairly well[62]. Both models predict similar forces for collisions involving small deformations and low impact velocities. Since no

DEM simulations have been performed on CVR-ALD, it was important to test the validity of the LSD model against the Hertzian results.

The Hertzian contact model utilizes a nonlinear relationship between overlap δ and contact force as described by

$$\vec{F}_{C,N}^{i,j} = -\frac{4}{3}E_{eff}\sqrt{R_{eff}}\delta_N{}^{\frac{3}{2}}\hat{u}_N^{i,j} - \eta_N\frac{d\delta_N}{dt}\hat{u}_N^{i,j} \qquad (2.b.1)$$

$$\vec{F}_{C,T}^{i,j} = \begin{cases} -\frac{16}{3}G_{eff}\sqrt{R_{eff}}\delta_N{}^{\frac{1}{2}}\delta_T\hat{u}_T^{i,j} - \eta_T\frac{d\delta_T}{dt}\hat{u}_T^{i,j}, & \left|\vec{F}_{C,T}^{i,j}\right| < \mu\left|\vec{F}_{C,N}^{i,j}\right| \\ -\mu\left|\vec{F}_{C,N}^{i,j}\right|\hat{u}_T^{i,j}, & otherwise \end{cases} \qquad (2.b.2)$$

In the Hertzian model, both the tangential and normal contact forces are dependent on normal overlap δ_N, and the material properties of interest are the effective Young's Modulus, $E_{eff} = \left(\frac{\left(1-\nu^{i^2}\right)}{E^i} + \frac{\left(1-\nu^{j^2}\right)}{E^j}\right)^{-1}$ and an effective Shear Modulus, $G_{eff} = \frac{E_{eff}}{2+2\nu_{eff}}$, for each i,j pair. The effective radius of the colliding pair, $R_{eff} = \frac{R_iR_j}{R_i+R_j}$, also plays a role in the resulting force. The normal damping coefficient η_N can be related to the normal coefficient of restitution e_N by the relationship

$$\eta_N = \frac{-2\sqrt{15}R_{eff}{}^{\frac{1}{4}}\sqrt{m_{eff}E_{eff}}\ln e_N}{3\sqrt{\pi^2 + \ln^2 e_N}}\delta_N{}^{\frac{1}{4}} \qquad (2.b.3)$$

Unlike in the LSD model, the Hertzian dashpot coefficient depends on normal overlap δ_N. Typically, the tangential damping coefficient η_T is assumed equal to the normal damping coefficient η_N[63].

In the LSD model, material stiffness is described by the spring constant k. The Hertzian model uses Young's modulus E for stiffness. To make direct comparisons between both models, Hertzian stiffness can be recast as a linearized spring constant[64] $k_{n,eff}$ through the equation

$$k_{n,eff} = k_{n,Hertz}\sqrt{\delta_n} = \frac{4}{3}E_{eff}\sqrt{r_{eff}\delta_n} \qquad (2.b.4)$$

Linearized spring constants based on collisional velocity[64, 65] and/or overlap[64] gave similar results of around 1000-4000 N/m for the material spring stiffness. Particle behavior was dominated by enduring, multiparticle contacts rather than binary collisions, so the value based on average overlap (2500 N/m) was chosen as the true linear spring stiffness in this study.

Reduced stiffnesses are often used to keep the computational expense low when modeling gas-solid systems. For cohesive particle modeling, care must be taken to avoid choosing an excessively reduced spring constant. Previous studies have shown that a reduced stiffness can artificially increase the area of contact and lead to overprediction of the cohesive force if an appropriate scaling law is not implemented[66]. Kobayashi et. al. demonstrated the need for spring constants ≥1000 N/m to obtain fluidized bed bubbling patterns that match experimental results for mildly-cohesive 60 μm soda lime glass spheres[65]. When using reduced stiffnesses, a reduced Hamaker constant of A_r should also be chosen relative to the material Hamaker constant $A_m$using the correlation $A_r = A_m\left({E_R}/{E_m}\right)^{2/5}$ for a Hertzian model with material Young's modulus E_m and reduced Young's modulus E_R or the correlation $A_r = A_m\left({k_R}/{k_m}\right)^{1/2}$ for a linear spring dashpot model with material spring constant k_m and reduced spring constant k_R [66].

Stiffness sensitivity of our powder bed was tested using 2D LSD and Hertzian simulations up to the material Young's modulus (73 GPa). A consistent correlation between the Young's modulus and the linearized spring stiffness was observed (**Figures B.2A, B.2B**). Similar to the approach by Kobayashi et. al., trends in the spatially averaged particle-particle coordination number were used to quantify the effects of a reduced stiffness and cohesive force on vibratory convection flow behavior,

$$CN_{pp} = \frac{N_{j,PP}}{2N} \tag{2.b.5}$$

where $N_{j,PP}$ is the number of overlapping particle-particle pairs (neighbors within a radial distance $r = R_i$ of each particle i) and N is the total number of particles in the system. As observed with fluidized bed simulations[65, 66], the coordination behavior of vibrated mildly-cohesive soda lime microspheres changes with spring stiffness when a reduced Hamaker constant is not used (**Figure B.3A**). “Hard” particles near the material stiffness of 73 GPa were characterized by low average coordination numbers CN_{pp} and uncoordinated flight periods. By contrast, “soft” particles with stiffnesses under 1.8 GPa (effective spring constants of ~200 N/m or less) were characterized by continuous particle-particle contact ($CN_{pp} > 0$). By contrast, when a reduced spring stiffness is employed with an appropriately reduced Hamaker constant, the coordination network remains relatively insensitive to spring stiffness down to at least $k = 3\ N/m$ or $E = 0.018\ GPa$ (**Figure B.3B**). Particle-wall coordination numbers CN_{pw} exhibited similar trends with increasing spring stiffness.

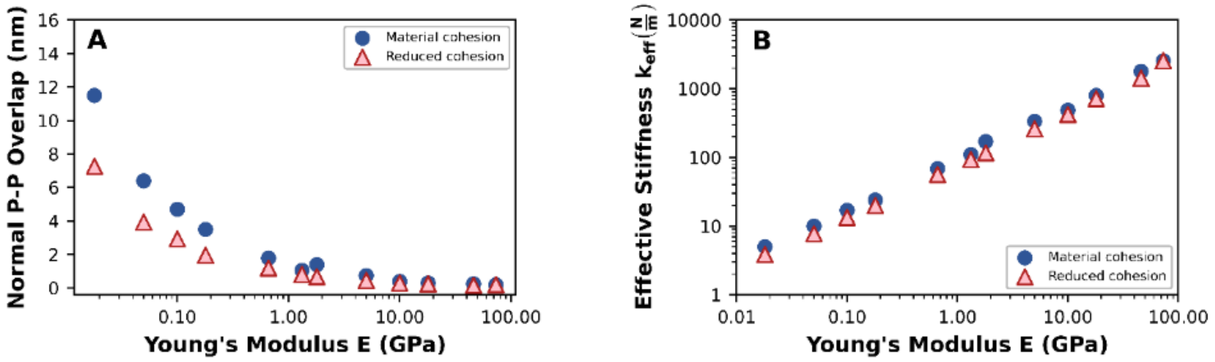

Figure B.2. (A) Relationship between time-averaged normal overlap and simulated Hertzian stiffness using a fixed material Hamaker constant versus a stiffness-scaled Hamaker constant (“reduced cohesion”). (B) Relationship between simulated stiffness in the Hertzian model (Young’s modulus) and calculated stiffness for the LSD model (effective spring constant) with and without reduced cohesion

To ensure all features of vibrated soda lime glass microspheres are captured accurately, the LSD model at the true material stiffness was used in all remaining simulations (**Table 2.3**). LSD model simulations gave similar results to the Hertzian model but with larger time steps, enabling a faster solution, so the LSD model was chosen for modeling fine powder vibratory convection. The small overlap observed in these simulations (below 17 nm or <0.03% of the particle diameter) is commonly accepted as a valid regime for the linear spring-dashpot model.

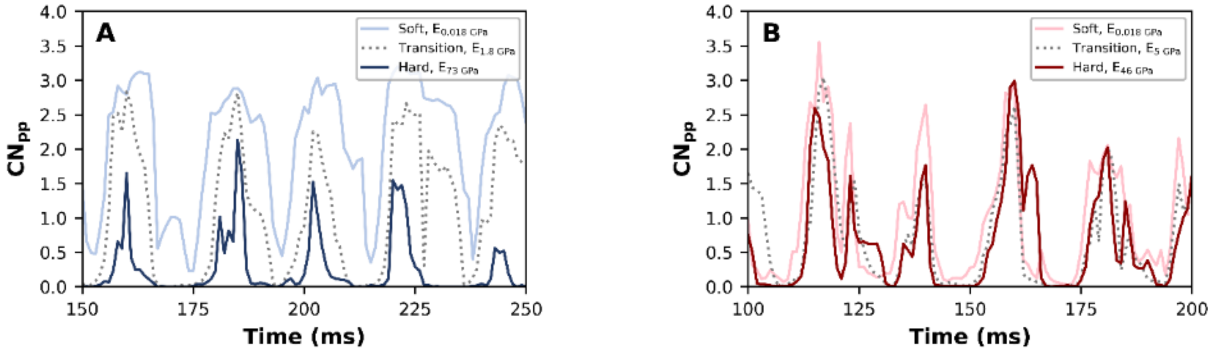

Figure B.3. Time evolution of spatially averaged particle-particle coordination number at different reduced spring stiffnesses without reduced cohesion (A) and with reduced cohesion (B)

References

[1] J. Duran, Sands, powders, and grains: an introduction to the physics of granular materials, Springer Science & Business Media2012.

[2] S. Limtrakul, W. Rotjanavijit, T. Vatanatham, Lagrangian modeling and simulation of effect of vibration on cohesive particle movement in a fluidized bed, Chemical Engineering Science, 62 (2007) 232-245.

[3] H. Wang, T. Zhou, J.S. Yang, J.J. Wang, H. Kage, Y. Mawatari, Model for Calculation of Agglomerate Sizes of Nanoparticles in a Vibro-fluidized Bed, Chemical Engineering & Technology: Industrial Chemistry-Plant Equipment-Process Engineering-Biotechnology, 33 (2010) 388-394.

[4] Y. Mawatari, M. Tsunekawa, Y. Tatemoto, K. Noda, Favorable vibrated fluidization conditions for cohesive fine particles, Powder technology, 154 (2005) 54-60.

[5] C.H. Nam, R. Pfeffer, R.N. Dave, S. Sundaresan, Aerated vibrofluidization of silica nanoparticles, AIChE journal, 50 (2004) 1776-1785.

[6] D. Longrie, D. Deduytsche, C. Detavernier, Reactor concepts for atomic layer deposition on agitated particles: A review, Journal of Vacuum Science & Technology A: Vacuum, Surfaces, and Films, 32 (2014) 010802.

[7] C. Woodcock, J. Mason, Bulk solids handling: an introduction to the practice and technology, Springer Science & Business Media2012.

[8] D. Barletta, M. Poletto, Aggregation phenomena in fluidization of cohesive powders assisted by mechanical vibrations, Powder Technology, 225 (2012) 93-100.

[9] L.F. Hakim, J.L. Portman, M.D. Casper, A.W. Weimer, Aggregation behavior of nanoparticles in fluidized beds, Powder Technology, 160 (2005) 149-160.

[10] J.M. Valverde, A. Castellanos, Effect of vibration on agglomerate particulate fluidization, AIChE journal, 52 (2006) 1705-1714.

[11] P. Poodt, D.C. Cameron, E. Dickey, S.M. George, V. Kuznetsov, G.N. Parsons, F. Roozeboom, G. Sundaram, A. Vermeer, Spatial atomic layer deposition: A route towards further industrialization of atomic layer deposition, Journal of Vacuum Science & Technology A: Vacuum, Surfaces, and Films, 30 (2012) 010802.

[12] W. Cong, Z. Li, K. Cao, G. Feng, R. Chen, Transient analysis and process optimization of the spatial atomic layer deposition using the dynamic mesh method, Chemical Engineering Science, 217 (2020) 115513.

[13] M.B.M. Mousa, J.S. Ovental, A.H. Brozena, C.J. Oldham, G.N. Parsons, Modeling and experimental demonstration of high-throughput flow-through spatial atomic layer deposition of Al2O3 coatings on textiles at atmospheric pressure, Journal of Vacuum Science & Technology A: Vacuum, Surfaces, and Films, 36 (2018) 031517.

[14] D. Pan, Numerical study on the effectiveness of precursor isolation using N2 as gas barrier in spatial atomic layer deposition, International Journal of Heat and Mass Transfer, 144 (2019) 118642.

[15] I.J.A. Spencer, R.A. Hall, Continuous spatial atomic layer deposition process and apparatus for applying films on particles, Google Patents, 2018.

[16] J.R. van Ommen, D. Kooijman, M.d. Niet, M. Talebi, A. Goulas, Continuous production of nanostructured particles using spatial atomic layer deposition, Journal of Vacuum Science & Technology A: Vacuum, Surfaces, and Films, 33 (2015) 021513.

[17] J. Booth, H. McCallion, On predicting the mean conveying velocity of a vibratory conveyor, Proceedings of the Institution of Mechanical Engineers, 178 (1963) 521-532.

[18] K. Srinath, R. Karmakar, Vibratory conveying by non-sinusoidal excitation, Proceedings of the Institution of Mechanical Engineers, Part C: Journal of Mechanical Engineering Science, 202 (1988) 405-408.

[19] K. Lonie, A practical model for sub-resonant vibratory feeders, Bulk Solids Handling, 3 (1983) 741-746.

[20] S. MacDonald, B. Stone, An investigation of vibratory feeders, Proceedings of international conference of noise and vibration, 1989, pp. 12-26.

[21] G. Lim, On the conveying velocity of a vibratory feeder, Computers & structures, 62 (1997) 197-203.

[22] E. Sloot, N.P. Kruyt, Theoretical and experimental study of the transport of granular materials by inclined vibratory conveyors, Powder Technology, 87 (1996) 203-210.

[23] J. Li, C. Webb, S.S. Pandiella, G.M. Campbell, Discrete particle motion on sieves—a numerical study using the DEM simulation, Powder technology, 133 (2003) 190-202.

[24] M. Jahani, A. Farzanegan, M. Noaparast, Investigation of screening performance of banana screens using LIGGGHTS DEM solver, Powder Technology, 283 (2015) 32-47.

[25] H. Ashrafizadeh, S. Ziaei-Rad, A numerical 2D simulation of part motion in vibratory bowl feeders by discrete element method, Journal of Sound and Vibration, 332 (2013) 3303-3314.

[26] C. Hogue, D. Newland, Efficient computer simulation of moving granular particles, Powder Technology, 78 (1994) 51-66.

[27] G. Uryadov, A. Katterfeld, F. Krause, DEM Simulation of the Bulk Solid Reaction on Vibratory Conveyors, Bulk Europe, (2008).

[28] S. Ganapathy, M. Parameswaran, Effect of material loading on the starting and transition over resonance of a vibratory conveyor, Mechanism and Machine Theory, 22 (1987) 169-176.

[29] E. Simsek, S. Wirtz, V. Scherer, H. Kruggel-Emden, R. Grochowski, P. Walzel, An experimental and numerical study of transversal dispersion of granular material on a vibrating conveyor, Particulate Science and Technology, 26 (2008) 177-196.

[30] J.M.V. Millán, Fluidization of fine powders: cohesive versus dynamical aggregation, Springer Science & Business Media2012.

[31] M.F. Llop, F. Madrid, J. Arnaldos, J. Casal, Fluidization at vacuum conditions. A generalized equation for the prediction of minimum fluidization velocity, Chemical Engineering Science, 51 (1996) 5149-5157.

[32] Y.I. Rabinovich, J.J. Adler, A. Ata, R.K. Singh, B.M. Moudgil, Adhesion between nanoscale rough surfaces: I. Role of asperity geometry, Journal of colloid and interface science, 232 (2000) 10-16.

[33] M. Syamlal, W. Rogers, T.J. OBrien, MFIX documentation theory guide, USDOE Morgantown Energy Technology Center, WV (United States), 1993.

[34] J. Anderson, P.J. Burns, D. Milroy, P. Ruprecht, T. Hauser, H.J. Siegel, Deploying RMACC Summit: an HPC resource for the Rocky Mountain region, Proceedings of the Practice and Experience in Advanced Research Computing 2017 on Sustainability, Success and Impact2017, pp. 1-7.

[35] P. Liu, T. Brown, W.D. Fullmer, T. Hauser, C. Hrenya, R. Grout, H. Sitaraman, Comprehensive Benchmark Suite for Simulation of Particle Laden Flows Using the Discrete Element Method with Performance Profiles from the Multiphase Flow with Interface eXchanges (MFiX) Code, National Renewable Energy Lab.(NREL), Golden, CO (United States), 2016.

[36] C. LaMarche, P. Liu, K. Kellogg, C. Hrenya, Fluidized-bed measurements of carefully-characterized, mildly-cohesive (Group A) particles, Chemical Engineering Journal, 310 (2017) 259-271.

[37] C.Q. LaMarche, S. Leadley, P. Liu, K.M. Kellogg, C.M. Hrenya, Method of quantifying surface roughness for accurate adhesive force predictions, Chemical Engineering Science, 158 (2017) 140-153.

[38] M. Tahmasebpoor, L. de Martín, M. Talebi, N. Mostoufi, J.R. van Ommen, The role of the hydrogen bond in dense nanoparticle–gas suspensions, Physical Chemistry Chemical Physics, 15 (2013) 5788-5793.

[39] J.P.K. Seville, C.D. Willett, P.C. Knight, Interparticle forces in fluidisation: a review, Powder Technology, 113 (2000) 261-268.

[40] J. Dickinson, R. Hariadi, L. Scudiero, S. Langford, A scanning force microscope study of detachment of nanometer-sized particles from glass surfaces, Tribology Letters, 7 (1999) 113-119.

[41] J.N. Israelachvili, Intermolecular and surface forces, Academic press2011.

[42] S.F. Foerster, M.Y. Louge, H. Chang, K. Allia, Measurements of the collision properties of small spheres, Physics of Fluids, 6 (1994) 1108-1115.

[43] P. Liu, C.M. Hrenya, Challenges of DEM: I. Competing bottlenecks in parallelization of gas–solid flows, Powder technology, 264 (2014) 620-626.

[44] J. Kováčik, Correlation between Young's modulus and porosity in porous materials, Journal of materials science letters, 18 (1999) 1007-1010.

[45] J. Kováčik, Correlation between shear modulus and porosity in porous materials, Journal of materials science letters, 20 (2001) 1953-1955.

[46] I. Mészáros, Magnetic characterisation of duplex stainless steel, Physica B: Condensed Matter, 372 (2006) 181-184.

[47] K. Kawashima, T. Ito, Y. Nagata, Detection and imaging of nonmetallic inclusions in continuously cast steel plates by higher harmonics, Japanese Journal of Applied Physics, 49 (2010) 07HC11.

[48] A. Redford, G. Boothroyd, Vibratory feeding, Proceedings of the Institution of Mechanical Engineers, 182 (1967) 135-152.

[49] S. Okabe, Y. Kamiya, K. Tsujikado, Y. Yokoyama, Vibratory feeding by nonsinusoidal vibration— optimum wave form, (1985).

[50] S. Nadler, O. Bonnefoy, J.-M. Chaix, G. Thomas, J.-L. Gelet, Parametric study of horizontally vibrated grain packings, The European Physical Journal E, 34 (2011) 1-10.
[51] G. Winkler, Analysing the vibrating conveyor, International Journal of Mechanical Sciences, 20 (1978) 561-570.
[52] D.C. Kammer, M.L. Tinker, Optimal placement of triaxial accelerometers for modal vibration tests, Mechanical systems and signal processing, 18 (2004) 29-41.
[53] A.J. Jerri, The Gibbs phenomenon in Fourier analysis, splines and wavelet approximations, Springer Science & Business Media2013.
[54] M.L. Chandravanshi, A.K. Mukhopadhyay, Dynamic analysis of vibratory feeder and their effect on feed particle speed on conveying surface, Measurement, 101 (2017) 145-156.
[55] R. Schofield, M. Yousuf, The design of a linear “out of phase” vibratory conveyor, (1973).
[56] A. Fukunishi, Y. Mori, Adhesion force between particles and substrate in a humid atmosphere studied by atomic force microscopy, Advanced Powder Technology, 17 (2006) 567-580.
[57] Y. Gu, A. Ozel, J. Kolehmainen, S. Sundaresan, Computationally generated constitutive models for particle phase rheology in gas-fluidized suspensions, Journal of Fluid Mechanics, 860 (2019) 318-349.
[58] J.M. Parker, A Baseline Drag Force Correlation for CFD Simulations of Gas-Solid Systems, 2016 NETL Workshop on Multiphase Flow ScienceMorgantown, WV, 2016.
[59] E. Loth, Compressibility and rarefaction effects on drag of a spherical particle, AIAA journal, 46 (2008) 2219-2228.
[60] K.J. Berger, On the Role of Collisions in the Ejection of Lunar Regolith during Spacecraft Landing, University of Colorado at Boulder, 2016.
[61] E. Dintwa, E. Tijskens, H. Ramon, On the accuracy of the Hertz model to describe the normal contact of soft elastic spheres, Granular Matter, 10 (2008) 209-221.
[62] H.P. Kuo, P.C. Knight, D.J. Parker, Y. Tsuji, M.J. Adams, J.P.K. Seville, The influence of DEM simulation parameters on the particle behaviour in a V-mixer, Chemical Engineering Science, 57 (2002) 3621-3638.
[63] Y. Tsuji, T. Tanaka, T. Ishida, Lagrangian numerical simulation of plug flow of cohesionless particles in a horizontal pipe, Powder technology, 71 (1992) 239-250.
[64] H.A. Navarro, M.P. de Souza Braun, Determination of the normal spring stiffness coefficient in the linear spring–dashpot contact model of discrete element method, Powder technology, 246 (2013) 707-722.
[65] T. Kobayashi, T. Tanaka, N. Shimada, T. Kawaguchi, DEM–CFD analysis of fluidization behavior of Geldart Group A particles using a dynamic adhesion force model, Powder technology, 248 (2013) 143-152.
[66] Y. Gu, A. Ozel, S. Sundaresan, A modified cohesion model for CFD–DEM simulations of fluidization, Powder technology, 296 (2016) 17-28.

CHAPTER 3

AERATION AND COHESION EFFECTS

3.1 Abstract

A CFD-DEM model for aerated vibratory convection was developed to explore the coupled gas-solid interactions governing bulk powder bed dynamics. Each simulation was prepared by carefully characterizing the rough, porous conveyor baseplate and four candidate particle sizes representative of typical powder beds. Trends in the vibratory convection of particles between 20 and 250 microns in diameter could be explained by considering each powder's minimum fluidization velocity and the magnitude of van der Waals cohesive forces. Simulations of fine powders under high cohesive forces exhibited competing effects from drag and cohesion; drag promotes powder-frit liftoff while cohesion suppresses contact separation. Experimental convection velocities were observed to be in good agreement with the simulated mean powder velocity for throw numbers between 0.25 and 0.50.

3.2 Introduction

Vibratory convection has been used in bowl feeders, spiral elevators, and linear conveying trays since the early 1900s to transport components down industrial product lines[1, 2]. Oscillations are produced by a pneumatic, piezoelectric, or electromagnetic drive and can be broken up into extension phases, when the conveyor is moving towards the feed outlet, and retraction phases. All vibratory feeders use a shaking mechanism to propel objects forward, but how these mechanisms induce flow depends on the design of the conveyor and properties of the material being fed. Hopping, jumping, or throwing conveyors[2-5] use high acceleration vibrations to throw components during conveyor extension. Stick-slip[6], sliding, sealskin or jerk conveyors[7-9] rely on forward sliding between the conveyor and component to drive forward flow. Under certain conditions, a hybrid slide-throw convection mechanism has been observed[10]. The vibration waveform can be pure sinusoidal, out-of-phase[7, 11], or non-sinusoidal[12], and conveyors can be run at an inclination or a declination[13]. Because of their simple construction, versatility and easy operation[14], vibratory conveyors have seen widespread adoption in many applications such as the mining, packaging, agricultural[14], and pharmaceutical industries.

One emerging application for vibratory convection is in reacting powder systems. Several unique features of vibratory conveyors make these systems appealing as fine powder reactors. When combined with aeration, studies have shown that vibration can improve flowability and break up agglomerates of cohesive fine powders[15-17]. Vibratory conveyor surfaces are also free of moving machinery, minimizing the contamination and flow jamming challenges seen with screw feeder and conveyor belt systems. High-temperature compatibility[2] and ease of cleaning[18] are further advantages of vibratory conveyors for reacting particle flows. By replacing the open conveyor tray with an enclosed housing, dosing manifolds, and a porous baseplate, gas can be fed in through the bottom in an "aerated" vibratory conveyor setup. The authors are particularly interested in the application of aerated vibratory conveyors to particle atomic layer deposition (ALD)[19] in a process called continuous spatial particle ALD. For conciseness and to be consistent with prior literature, continuous spatial particle ALD reactors will hereafter be referred to using the acronym CVR-ALD which abbreviates continuous vibrating reactor for atomic layer deposition. CVR-ALD reactors introduce gases through a porous baseplate at velocities below fluidization, using vibratory convection to transport particles through alternating regions of precursor and purge gas. Particle ALD frequently involves fine powder feedstocks <50 micron in diameter and elevated temperatures >100°C but vibratory conveyor studies under these conditions are lacking in the literature.

Many open questions remain about the gas-solids flow behavior in an aerated vibratory conveyor setup. The small and light nature of fine powders results in high bed expansion under large aeration velocities and heightened sensitivity to cohesive forces[20]. Even in the absence of forced convection, gas flow induced by particle movement can have a measurable impact on solids flow behavior[21]. Previous studies on vibratory convection have found that air pressure differences between top and bottom layers of granular material adversely affect hopping convection when an impermeable tray is used[22, 23]. However, the porous baseplate in an aerated conveyor design imposes a different set of constraints on the gas phase. The impact of gas-particle drag on particle flow over a porous baseplate has not yet been reported. Particles on vibrating surfaces interact in complex ways, forming spatiotemporal bed patterns[24-27] and conveying at speeds that differ from the behavior of a single isolated particle under vibratory excitation[28]. There is no consensus in the literature over whether a velocity gradient exists through the depth of the material heap being conveyed[23, 29], and the magnitude and direction of these variations likely depend on the excitation and material characteristics.

Another poorly understood aspect of aerated vibratory conveyors relevant to continuous spatial particle ALD is the role of cohesion. The fine powders used frequently in particle ALD reactors are susceptible to high van der Waals cohesive forces which depend on particle size, asperity size[30], and the material's Hamaker constant. Higher cohesive forces can lead to a transition in Geldart classification from Group A to Group C[31] and highly coordinated particle bed regions that alter bulk powder flow structures[32, 33]. The cohesive nature of particle ALD powders is also expected to change over the course of multiple ALD cycles. In alumina atomic layer deposition, particles passing through alternating precursor zones will oscillate between hydroxylated and methylated surface terminations, leading to gas-particle suspensions with varying degrees of hydrogen bridging[34]. Changes in hydrogen bridging have been correlated with differences in bulk powder characteristics such as fluidization behavior[35] and powder flowability[36]. If water is used as one of the ALD precursors, spatial differences in relative humidity may result in wet cohesive effects due to liquid bridging or capillary condensation[37]. Changes to interparticle cohesion have been linked to a looser packing structure[38] with stress networks that resist tensile deformation[39] and could have consequences for bulk powder flow in a vibratory conveyor, where motion is propagated through force chains.

This study aims to better understand how cohesion and gas-solid interactions influence powder flow in aerated vibratory conveyors. Computational fluid dynamics (CFD) was used to simulate the gas phase with discrete element method (DEM) modeling for the solids phase. First, results from careful characterization of the particles and a porous reactor baseplate were used to inform a CFD-DEM model of the aerated vibratory conveyor. Simulations were then performed to probe the effects of conveyor acceleration and particle-

particle cohesion on bulk powder flow characteristics. Comparisons between modeling outputs and experimental results provided model validation and a multiscale perspective on the key driving forces from bulk flow trends down to the level of particle-particle and gas-particle interactions.

3.3 Methods

3.3.1 Materials Characterization

Three sizes of glass beads (Mo-Sci Corporation, class IV industrial grade) and one size of stainless-steel beads (Next Advance) were chosen for the powder feedstocks in this study. These materials represent two powder classes of interest (Geldart A and B) but require further characterization for use as DEM modeling inputs. The size distribution of each powder was evaluated using a Malvern Panalytical Mastersizer 2000 Particle Size Analyzer. In the Mastersizer, particles dispersed in DI water are pumped through a flow cell where they pass through a laser beam. The light scattering pattern is then captured and used to quantify particle size from three to five replicate measurements. Particle samples were also placed on glass slides in an inverted widefield optical microscope (Olympus IX81) and imaged for sphericity quantification. The particle images were segmented and converted to approximate sphericity values in ImageJ, a free image analysis program, by squaring the perimeter-based circularity measurement[40]. At least 40 particles, the minimum sample size at which the mean sphericity deviated by <1% with additional particles, were used to calculate the average value for each particle size.

The porous baseplate (Mott Corporation sintered stainless, 10-micron mean pore size) and particle-baseplate interaction were also characterized for use in the DEM model. Surface profilometry tests (Dektak 3000 surface profilometer, 12.5 µm stylus) were carried out to quantify the micron-scale surface roughness of 50-mm samples from the porous baseplate. Valleys in the profilometer data were identified by inverting the signal and using MATLAB's findpeaks algorithm. An Anton Paar MCR-302 air-bearing rheometer (**Figure 3.1**) equipped with an annular powder wall friction accessory and a convection temperature device (CTD 180) was used to perform the wall friction tests at room temperature (25°C) and elevated temperature (200°C)[41]. Air bearing rheometers in conjunction with powder accessories have recently been used in a host of different powder characterization studies[42-47]. Wall friction tests in the form of a wall yield locus were used to quantify the friction factor and adhesion between the powder bed and porous baseplate. The tests were performed by attaching a disc sample of the porous baseplate to the wall friction accessory (Part #PSC43-21-0) with JB Weld high temperature adhesive epoxy. Wall yield locus measurements were performed at 25°C and 200°C by consolidating the powder bed with this custom-made disc at five defined decreasing normal stresses and measuring the corresponding steady state shear stresses at 0.05 rpm. The porous baseplate surface was conditioned by completing four runs before recording the steady state stress values in the fifth run. Before every measurement, the measuring disc was cleaned with water and then ethanol and was allowed to dry completely. Kinematic wall friction values are then calculated from the normal and shear stress values. The above obtained shear stress values are then plotted as a function of the applied normal stresses and a linear regression fit is used to obtain the adhesion between the base plate and the powder studied. The shear stress at the point where the wall yield locus intersects the shear stress axis at zero normal stress is called the adhesion. Each test was repeated two to three times to obtain an average at each stress and temperature state.

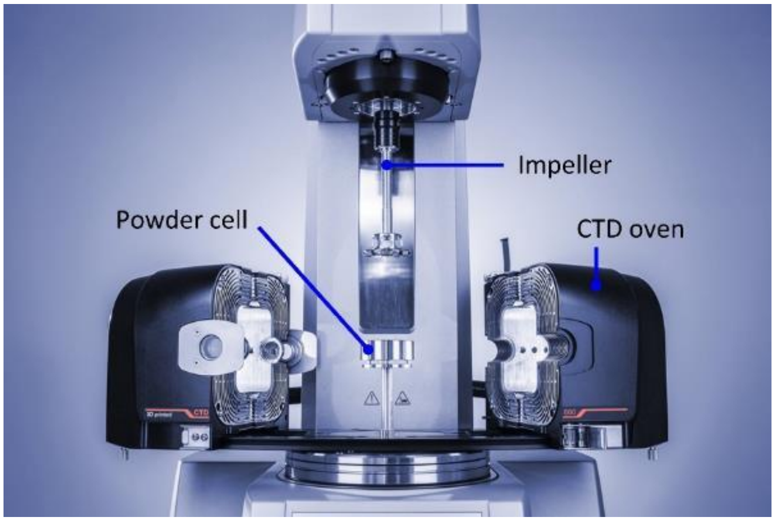

Figure 3.1. Photograph of the Anton Paar MCR-302 air-bearing powder rheometer. The impeller, powder cell, and CTD oven are labeled. For wall friction tests, the impeller shown is replaced with a wall friction impeller attached to the custom wall friction coupon

3.3.2 Experimental Setup

Before running aerated convection tests, the fluidization behavior of each powder was measured in a 50-mm diameter fluidization test stand (**Figure 3.2**). Air was delivered into the chamber through a porous distributor plate by a mass flow controller (Omega FMA series), and the resulting pressure drop was measured with a differential pressure transducer (Halstrup-Walcher PU series). For each particle size, the fluidization chamber was filled with powder to a height equal to the diameter of the tube and fluidized well above the minimum fluidization velocity for about ten seconds before settling and starting the gas velocity ramp. A custom LabVIEW program was developed to increase the flowrate from zero to twice the expected minimum fluidization velocity in 15 increments, holding each step for 30- to 45 seconds until the pressure signal reached a statistically steady state. Measurements at each constant gas velocity were averaged to produce an increasing fluidization curve. The flow rate was then decreased in the same manner to produce a defluidization curve. All fluidization tests were performed at room temperature.

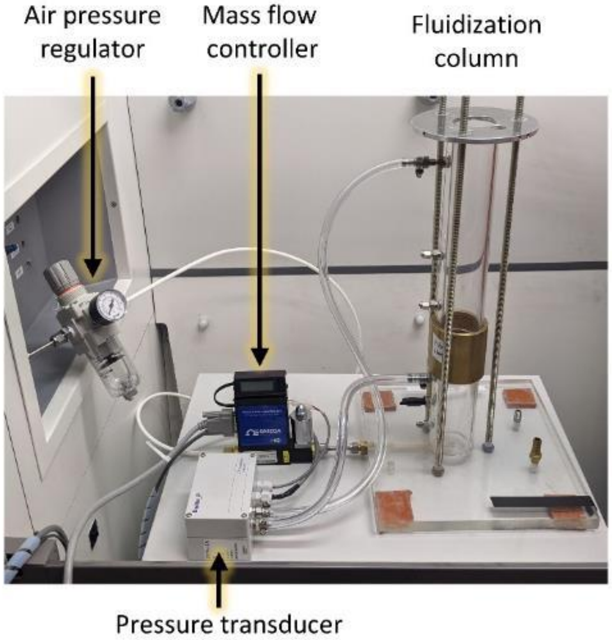

Figure 3.2. Experimental fluidization test stand. Air pressure to the mass flow controller is maintained constant using a pressure regulator. The mass flow controller delivers air to the fluidization column at a flow rate assigned by the LabVIEW program. A differential pressure transducer measures the pressure drop at each flow rate

The mean convection velocity of each powder was evaluated at different accelerations with an in-house aerated vibratory conveyor setup (**Figure 3.3**). Powder was fed from a hopper through a feed tube into the acrylic viewing chamber. The height of the bed was controlled by adjusting the gate valve position in the hopper feed line. During operation, the powder passed over several gas dosing regions before dropping into a catch pan. Gas velocity, $\boldsymbol{u_g}$, was controlled by a panel of flow meters (Omega FL3288-ST) and set to values relevant to particle ALD ($0 < \boldsymbol{u_g} < 1\ cm/s$). By adjusting air pressure to the pneumatic drive unit (Martin Vibration Systems NTK 25 AL), the vibration intensity can be tuned to obtain the desired powder bed convection speed. A Mide Slam Stick X accelerometer was used to record the chamber acceleration. The bed speed was measured by recording the traverse time between two demarcations on the viewing chamber surface with a stopwatch. To aid in powder tracking, colored tracer particles were added to the powder bed surface. Each tracer was made from the same material but one sieve size larger than the bed particles to enable separation and recovery after the tests.

Figure 3.3. Experimental setup for powder convection tests. Powder travels through an acrylic chamber and over a porous baseplate during vibratory convection. Gas feed to the chamber is controlled by a series of rotameters

3.3.3 Governing Equations

Simulations were also conducted to explore specific gas-solid interactions during vibration. In these simulations, the gas-phase behavior is resolved using CFD. All variables used in the equations below and throughout this paper can be found in the section labeled Nomenclature. The CFD code solves the Reynolds-averaged Navier-Stokes (RANS) equations for fluid mass and momentum[48, 49], which are

$$\frac{\partial}{\partial t}\left(\varepsilon_g \rho_g\right) + \nabla \cdot \left(\varepsilon_g \rho_g \boldsymbol{u_g}\right) = 0 \tag{3-1}$$

$$\frac{\partial}{\partial t}\left(\varepsilon_g \rho_g \boldsymbol{u_g}\right) + \nabla \cdot \left(\varepsilon_g \rho_g \boldsymbol{u_g} \boldsymbol{u_g}\right) = -\varepsilon_g \nabla P_g + \nabla \cdot \boldsymbol{\tau_g} + \varepsilon_g \rho_g \boldsymbol{g} - \boldsymbol{I_{gs}} \tag{3-2}$$

After discretization over a control volume, the gas-solids interaction term, $\boldsymbol{I_{gs}} = \beta(\boldsymbol{u_p} - \boldsymbol{u_g})$, is determined by summing up individual contributions for each DEM particle i in CFD cell m [50] and takes the form

$$\boldsymbol{I_{gs}} = \frac{1}{V_m} \sum_i \frac{\phi_m^i V_p^i \beta}{1 - \varepsilon_g} (\boldsymbol{u_p^i} - \boldsymbol{u_g}) \tag{3-3}$$

In this work, the gas-solids interaction coefficient, β, is based on the Gidaspow drag law[51] which includes the single particle drag coefficient, C_D, particle Reynolds number, $Re = \frac{\rho_g \varepsilon_g |\boldsymbol{u_p} - \boldsymbol{u_g}| d_p}{\mu_g}$, and empirically derived factors A and B (150 and 1.75 by default),

$$\beta = \begin{cases} \frac{3}{4} C_D \frac{\rho_g \varepsilon_g \varepsilon_s |\boldsymbol{u_p} - \boldsymbol{u_g}|}{\varphi d_p} \varepsilon_g^{-2.65}, & \varepsilon_g \geq 0.8 \\ \frac{A(1 - \varepsilon_g)\varepsilon_s \mu_g}{\varepsilon_g (\varphi d_p)^2} + \frac{B \rho_g \varepsilon_s |\boldsymbol{u_p} - \boldsymbol{u_g}|}{\varphi d_p}, & \varepsilon_g < 0.8 \end{cases} \tag{3-4}$$

$$C_D = \begin{cases} \frac{24}{Re}(1 + 0.15 Re^{0.687}), & Re < 1000 \\ 0.44, & Re \geq 1000 \end{cases} \tag{3-5}$$

The default Gidaspow drag law was modified to account for particle sphericity φ as shown in equation 3-4. Studies on particle fluidization have shown that particle shape can have a significant impact on gas-solid drag[52]. Given the previously observed sensitivity of vibratory powder convection to gas-phase effects[53], sphericity was incorporated to provide more realistic drag predictions.

The movement of individual particles is tracked by solving Newton's equations of motion[54, 55]. These are

$$m_p \frac{d\boldsymbol{u_p}}{dt} = \sum \boldsymbol{f}^i = m_p \boldsymbol{g} + \sum_j \boldsymbol{f}_C^j + \sum_k \boldsymbol{f}_{vdW}^k + \boldsymbol{f}_{gp} \tag{3-6}$$

$$I_p \frac{d\boldsymbol{\omega_p}}{dt} = \sum \boldsymbol{t}^i = \sum_j \boldsymbol{r}^j \times \boldsymbol{f}_C^j \tag{3-7}$$

The contact force, $\boldsymbol{f}_C$, for all j particle-particle and particle-wall contact pairs is calculated using the linear spring-dashpot model[54]. The only cohesive force considered in this study is van der Waals cohesion, $\boldsymbol{f}_{vdW}$, and is based on a Rumpf cohesion model with asperity radius r_a for k particle-particle and particle-wall cohesion pairs[38] as in

$$\boldsymbol{f}_{vdW} = \frac{A_{ij}R_{ij}}{6s^2}\left(\frac{r_a}{r_a + R_{ij}} + \frac{1}{\left(1 + \frac{r_a}{s}\right)^2}\right)\hat{\boldsymbol{u}}_N^{i,j} \tag{3-8}$$

A_{ij} and R_{ij} refer to the particle-particle (A_{pp}/R_{pp}) or particle-wall (A_{pw}/R_{pw}) effective Hamaker constant and average radius, respectively. The gas-particle interaction force, $\boldsymbol{f}_{gp}$, is given by[50]

$$\boldsymbol{f}_{gp} = -V_p\nabla P_g - \frac{V_p\beta}{1-\varepsilon_g}(\boldsymbol{u_p} - \boldsymbol{u_g}) \tag{3-9}$$

All CFD-DEM simulations in this work were conducted using the open-source code MFIX[49]. Further details on the CFD-DEM model are provided in the MFIX documentation[56]. The MFIX solver uses an incompressible formulation for the gas phase and solves the RANS equations with finite-volume spatial discretization. Documented verification and validation studies for the code can also be found on the MFIX website.

3.3.4 Simulation Conditions

3D cylindrical fluidized bed simulations were performed with the dimensions described in **Table 3.1** and compared with each experimental fluidization curve to validate the chosen drag model. Following a similar procedure to the experimental setup, a pressure drop versus increasing superficial gas velocity curve was produced by averaging the simulated pressure at multiple gas velocities below and above minimum fluidization. The particle-particle Hamaker constant A_{pp} was selected from experimental measurements for soda lime glass spheres [57, 58]. Frictionless and cohesionless walls were modeled in all fluidization simulations except the smallest 29-micron glass beads, where an overshoot in experimental pressure drop was observed due to wall effects. In this instance, values of particle-wall friction coefficient, $\mu_{pw} = 0.1$, and particle-wall Hamaker constant, $A_{pw} = 8.0 \times 10^{-21}\ J$, were used to model the particle-wall interaction. Simulated column diameters and heights were chosen based on particle diameter to avoid a bed-size-dependent minimum fluidization velocity[52]. A mesh cell size of $2.5d_p$ was selected based on recommendations for proper resolution of near-grid-scale gas features when fluidizing Geldart A powders[59].

Table 3.1. Properties used in DEM simulations to simulate Mo-Sci glass microspheres on a porous stainless surface

Fluidized bed geometry		
Column height	114-168d_p	
Column diameter	38-50d_p	
Powder bed height	38-50d_p	
Number of particles in simulation	24,394-102,702	
CFD grid size	2.5d_p	
Periodic box geometry		
Box width, W	100-250d_p	
Box height, H	65-130d_p	
Box depth, D	5-10d_p	
Powder bed height, Hbed	15-30d_p	
Number of particles in simulation	12,085-40,000	
CFD grid size	2.5d_p	
Gas properties		
Viscosity, μ_g	18 μPa·s	
Molecular weight	29 kg/kmol	
Solid properties	**Glass**	**Stainless**

Mean diameter, d_p	29, 56 & 223 μm	231 μm
Material density, ρ_p	2500 kg/m^3	7500 kg/m^3
Particle-particle Hamaker constant, A_{pp}	3.1×10^{-20} J	-
Particle-wall Hamaker constant, A_{pw}	6.2×10^{-20} J	-
Asperity height, r_a	1 nm	-

Powder bed convection was simulated using a 3D rectangular periodic box model (**Figure 3.4**). In this model, each vertical plane boundary is assigned a periodic boundary condition. Gas is dosed in through the bottom of the box and exits through the top plane. Rather than vibrating the entire simulation domain, vibration was incorporated by kinematically driving a horizontal plane of "frit particles" that approximate the porous baseplate. The vibrating frit particles interact with the bed particles via collisions to induce vibratory convection, capturing the particle-frit interaction more directly than the fluctuating gravity approach[53, 60, 61]. This technique has been used by others to model vibrating containers in molecular dynamics[62] or moving DEM boundaries[63, 64] and enables chamber vibration to be incorporated without the complexity of programming a moving mesh. Vertical vibration amplitude, A_v, and frequency, f, were determined from a Fast Fourier Transform (FFT) decomposition of the accelerometer results. Frit particle vibration was set to a frequency of 18.5 Hz. Vibration strength or "throw number", $\Gamma = A_v/g$, was varied from 0.20 to 0.60 to investigate the effects of conveyor acceleration on powder convection. To set up the simulations, bed particles were initialized at locations chosen by the Box-Muller random sampling method. Frit particles were placed beneath the bed particles in a monolayer with simple cubic packing. At the start of each simulation, bed particles were allowed to settle before vibration begins.

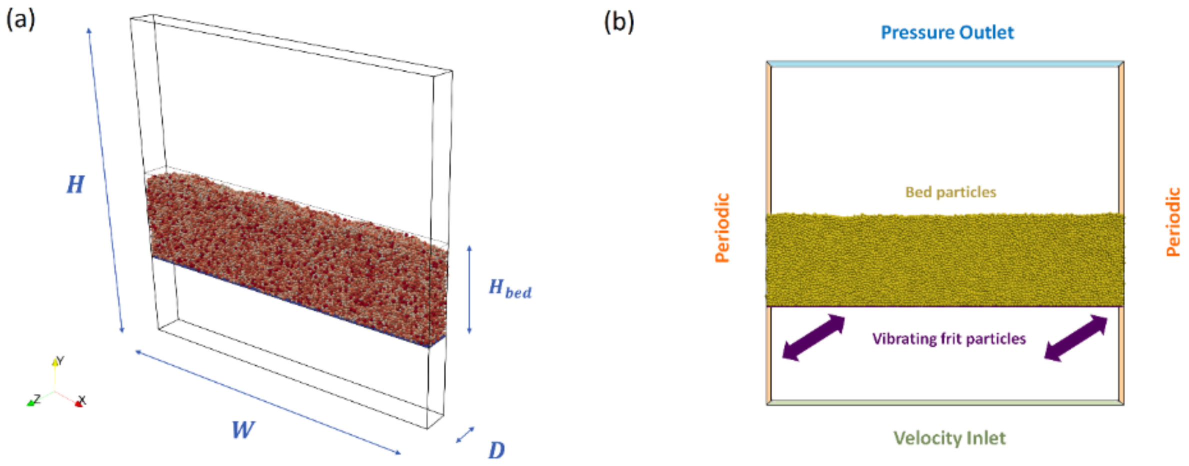

Figure 3.4. (a) Periodic box model geometry labeled with box height, H, box width, W, box depth, D, and powder bed height, H_{bed}. (b) Illustration of periodic box model approach and boundary conditions. Vibrating frit particles (purple) and powder bed particles (gold) are also shown

All particle-particle DEM properties in the fluidization simulations and the aerated convection simulations were set to the same values. Particle-wall (P-W) Hamaker constant in the vibratory convection simulations is described by $A_{pw} = \left(A_p A_w\right)^{1/2}$ which gives the geometric mean between particle material Hamaker constant A_p and wall material Hamaker constant $A_w = 1.25 \times 10^{-19}\,J$ [65, 66]. Cohesion from van der Waals forces was found to be negligible for the 223-micron glass beads and the 231-micron stainless-steel beads; as such, cohesion modeling was turned off for those simulations. The methods used to select appropriate periodic box dimensions and all remaining DEM inputs are described in our previous publication[53].

3.4 Results and Discussion

3.4.1 Particle-Particle and Particle-Wall Characterization

To develop a better understanding of the powder geometry, each material was characterized for sphericity and size distribution. Based on laser diffraction analysis, all powders in this study are polydisperse (**Figure 3.5**) with Gaussian-like distributions and standard deviations from 8.1 to 64.2 microns. For the remainder of this discussion, each material will be referred to by its mean diameter and material class: GL29 (29-micron glass), GL56, GL223 and SS231 (231-micron stainless steel). Two of the powder samples, GL29 and GL56, fall under the Geldart A "aeratable" classification, whereas the remaining larger powder sizes (GL223 and SS231) are classified as light and heavy "bubbling" Geldart B powders, respectively. The glass and stainless-steel powders exhibited sphericities between 0.78 and 0.81 as calculated from 2D circularity measurements in ImageJ (**Figure 6**). Factors such as erosion or pitting, ellipticity, and the presence of small, <10-micron surface asperities contribute to non-spherical particle shape in these substrates. Average values for the mean particle diameter, size distribution standard deviation, and sphericity were selected and used in the polydisperse CFD-DEM model (**Table 3.2**).

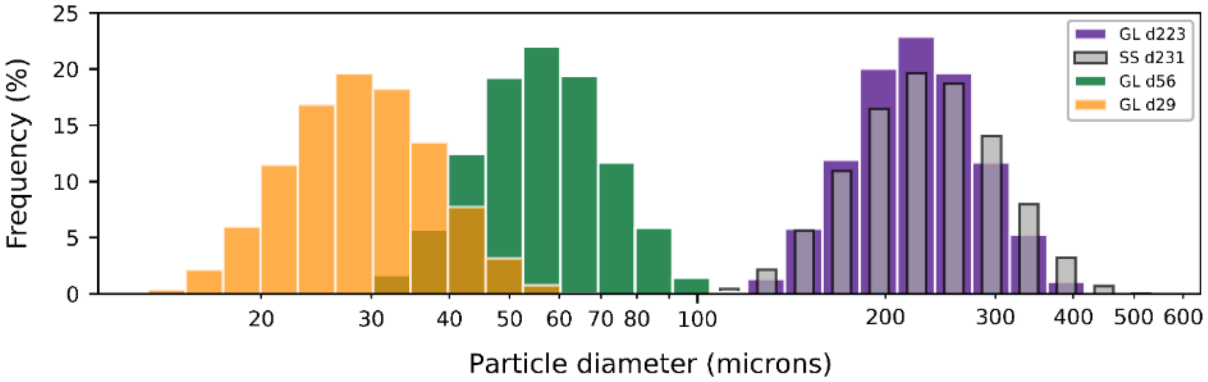

Figure 3.5. Particle size distributions for all four powders tested. The first two characters indicate material type (GL=glass, SS=stainless steel) and the number indicates mean diameter in microns

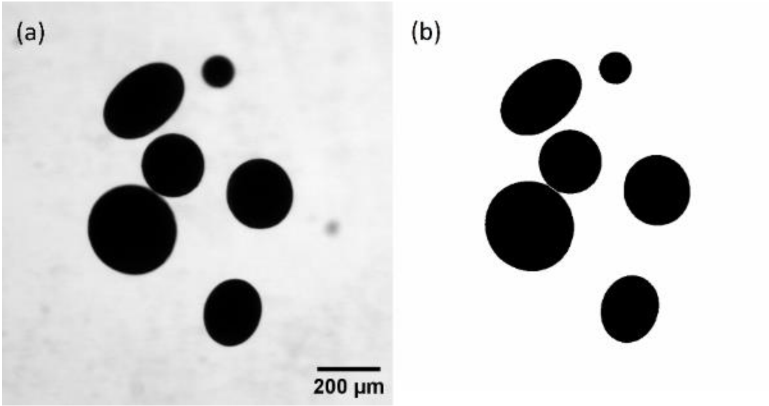

Figure 3.6. Sample raw (a) and segmented (b) microscopy images used to calculate particle sphericities

Table 3.2. Powder characterization values used in CFD-DEM simulations

Powder Type	Mean Diameter (µm)	Standard Deviation (µm)	Sphericity
GL29	29	8.1	0.78
GL56	56	13.9	0.79
GL223	223	53.5	0.80
SS231	231	64.2	0.81

The porous baseplate also has distinct geometric features because of the manufacturing process (**Figure 3.7**). Surface roughness depends on the sintering process and the powder size used to produce the final part[67]. In the aerated vibratory conveyor used for this study, particles interact with frit roughness elements characterized by trough widths and depths up to 50 microns. Although the frit mean pore size is sufficient to prevent passage of >10-micron particles, fine <50-micron particles are still small enough to occupy surface cavities in the porous baseplate, creating a quasistatic intermediate layer between the sintered frit and the moving powder bed during convection. By contrast, typical nonporous vibratory conveyor trays are made with metal forming techniques and characterized by lower surface roughness down to <1 micron for electropolished parts. Fine powders in an aerated vibratory conveyor setup exhibit a more complex relationship with the conveyor surface than traditional vibratory conveyor setups through the development of a heterogeneous powder-frit interface.

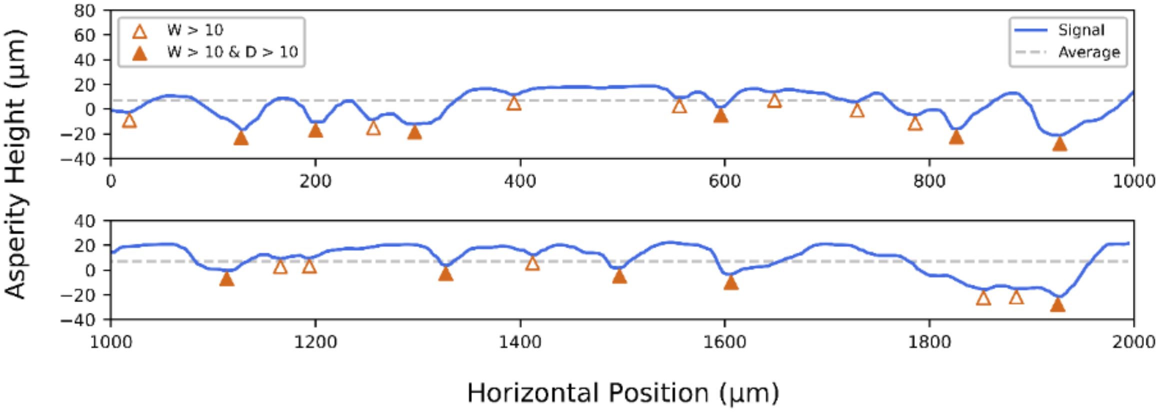

Figure 3.7. Surface profilometry results (solid line) for the porous stainless-steel frit material. Labeled points indicate “shallow” valleys at least 10 microns wide (empty triangles) and “deep” valleys at least 10 microns wide and 10 microns deep (filled triangles)

The resulting interfacial layer introduces additional complexities when modeling the particle-baseplate interaction. Variations in the contact network within the intermediate layer can lead to spatially varying properties such as static friction coefficient, which is highly dependent on the stress distribution at the particle-frit interface[68]. Each contact point on a heterogeneous surface can reach its slipping threshold at a different instant, resulting in complex interfacial flow behavior. An intermediate region packed with fines may act at times like a granular lubrication layer, effectively diminishing the friction force between the powder bulk and the frit[68]. In cases where particle-particle friction coefficient is greater than the particle-baseplate friction coefficient, a trapped layer of particles can increase the effective friction over a rough baseplate[69]. Highly rough materials with large asperities or irregular topography can also prohibit flow through mechanical interlocking of the mating surfaces, leading to higher particle-baseplate friction.

To investigate the role of conveyor baseplate roughness, the frit surface topography was modeled using a vibrating simple cubic packing of frit particles with varying particle size. Simulation results indicate that at the conditions tested in this paper (throw numbers of $\Gamma = 0.20 - 0.60$), the convection behavior of 50- to 250-micron glass powders is insensitive to frit macroroughness elements between 12.5 and 50 microns in diameter. Changes in powder convection velocity due to frit particle size were not observed to be significant relative to the periodic variation in bed properties caused by vibration. A frit particle size equal to the mean asperity height in the surface profilometry results (25 microns) was deemed sufficient to describe the local frit topography and used for the remaining fine powder simulations (GL29 and GL56). For the coarse powder simulations (GL223 and SS231), frit particle sizes of 25 and 125 microns gave similar results; thus, a frit particle size of 125 microns was chosen for computational efficiency.

Temperature-controlled air-bearing powder rheometry was used to investigate the frictional and cohesive characteristics of the particle-baseplate interaction at room temperature, 25°C, and typical ALD process conditions, 200°C (**Figures 3.8** and **3.9**). Particle size is seen to have an inverse scaling relationship with wall friction factor, decreasing from 0.44–0.52 for GL29 to 0.29–0.38 for GL223 (**Figure 3.8**). Powder beds of small glass beads have more contact points with the frit surface than coarse powder beds and have been correlated with an increase in the angle of internal friction[45, 70, 71]. Smaller particles are also able to fill some cavities in the porous baseplate, increasing the friction as particle-particle interactions dominate over particle-wall interactions due to particles passing over other trapped particles during shear[69]. All sizes exhibited a decrease in friction factor with wall normal stress, a trend which has been observed for other powdered substances[45, 72]. All powders also exhibited larger variations between tests in friction factor at higher temperatures. Some variation in values between replicate runs is to be expected[73], particularly on rough surfaces[69], and larger deviations with temperature may be explained by changes in thermomechanical behavior such as the prevalence of stick-slip friction. However, the influence of temperature on friction factor magnitude varied with particle size and type. The smallest glass bead size tested (GL29) exhibited a slight decrease in friction factor from 25°C to 200°C, with the largest change being from 0.52 to 0.48 at 1800 Pa normal stress. Van der Waals cohesion is reported to decrease with temperature[74] and likely contributed to the trends in GL29 which, as the finest powder tested, is most sensitive to changes in cohesion. By contrast, the coarser glass powders (GL56 and GL223) did not have a significant change in friction factor with temperature under the normal stresses tested. The SS231 stainless-steel powder exhibited the opposite trend to GL29 as a function of temperature, with an increase in friction factor of around 0.07 at each normal stress condition. This may be explained by a greater tendency for galling or plastic deformation at higher temperatures over the frit-powder bed interface[75]. Galling is a prevalent adhesive wear phenomenon among stainless steels and other metal alloys at elevated temperatures[76] but is not recognized as a common failure mode for soda lime glass.

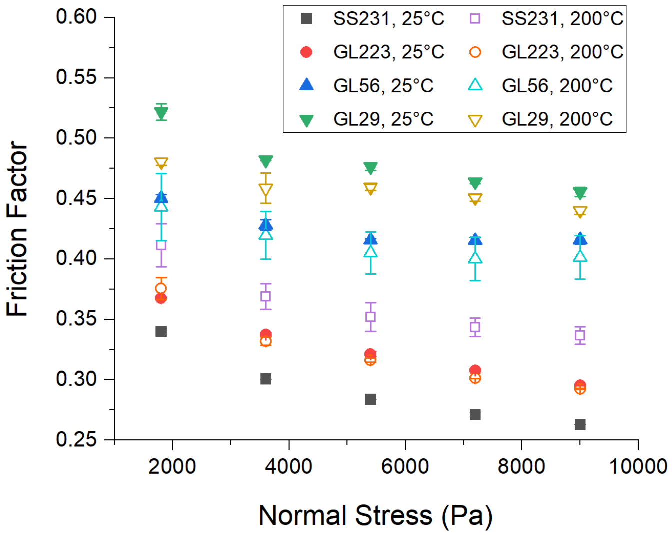

Figure 3.8. Wall friction test results for all four powders at room temperature (25°C) and an elevated temperature (200°C) representative of reactor conditions. Error bars represent standard error of the mean from three measurements

Adhesion derived from the wall yield loci revealed the adhesive interaction between the powder and the baseplate at 25°C and 200°C (**Figure 3.9**). Adhesion varied from 72 Pa for GL56 at 25°C up to 208 Pa for GL223 at 200°C. Only the GL29 powder exhibited a significant decrease in average adhesion from 157 to 103 Pa with temperature. A drop in van der Waals cohesion is expected at higher temperatures as discussed earlier[74]. Based on the adhesion results, the coarser powders (GL56, GL223 and SS231) are not sensitive to the temperature dependence of van der Waals cohesion between 25°C and 200°C. Low results for adhesion also indicate that cohesive forces, namely van der Waals forces, are small relative to each powder's size. Other attractive interparticle forces such as wet cohesion and hydrogen bridging are not expected to be significant for the dry conditions and particle sizes tested.

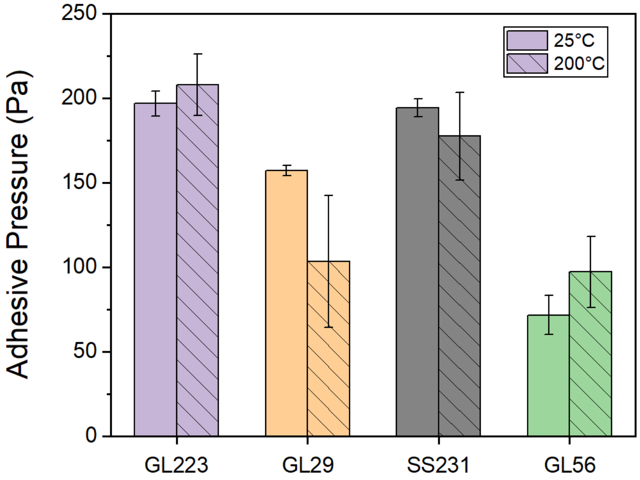

Figure 3.9. Adhesion values derived from wall yield locus tests at two different temperatures (25°C, 200°C)

3.4.2 Fluidization Characteristics

Each powder was fluidized to evaluate its relative permeability and minimum fluidization velocity. Fluidization curves exhibited the expected homogeneous fluidization and bubbling characteristics based on each powder's Geldart classification (**Figure 3.10**). The two smallest powders, GL29 and GL56, fluidized smoothly beyond their minimum fluidization velocities, u_{mf}, of around 0.175 cm/s and 0.35 cm/s, respectively. With further increases in superficial gas velocity, small bubbles began to appear in the bed, leading to small fluctuations around the average pressure drop at the highest gas velocities. Each powder also exhibited hysteretic trends, with the defluidization curves lying below the fluidization curves, as is typical for cohesive powders[38].

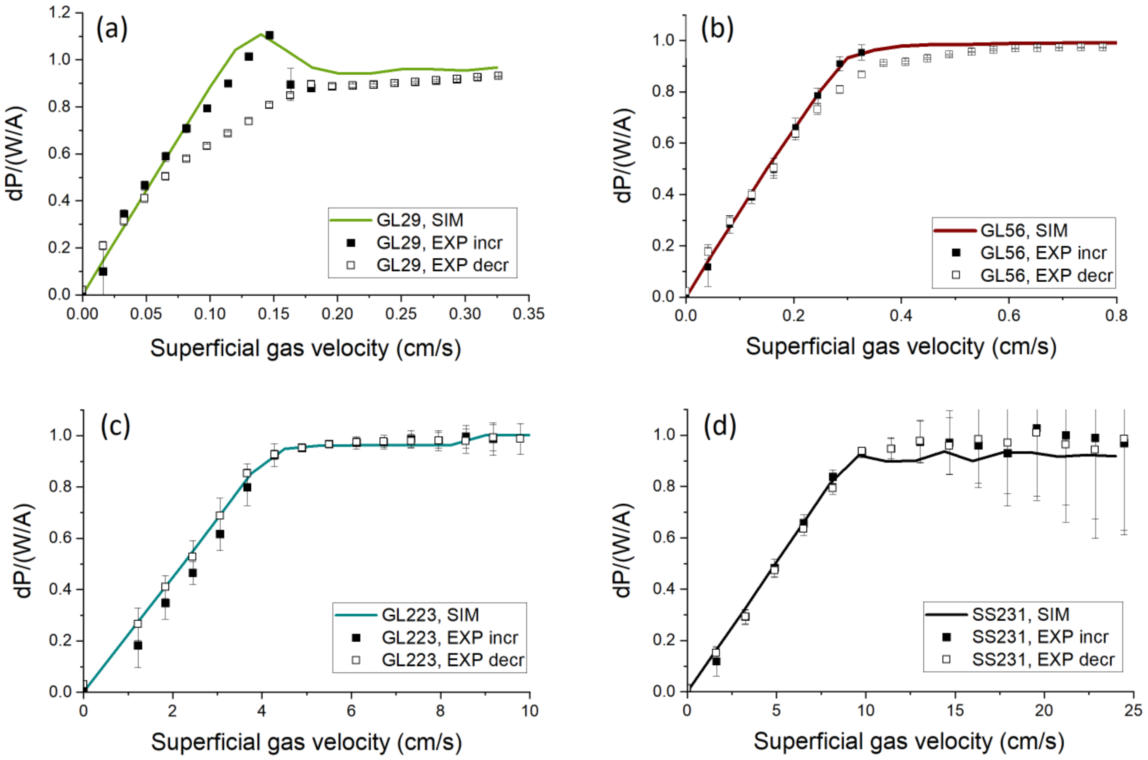

Figure 3.10. Simulated and experimental fluidization curves during increasing gas velocity (incr) and defluidization (decr). The pressure drop, dP, is normalized by the bed pressure due to gravity (weight/area or W/A)

Only the GL29 substrate exhibited a significant overshoot during increasing fluidization. Overshoots have typically been associated with high cohesive or friction forces[38, 52]. Particle-wall friction factor on rough wall materials has been observed to increase as glass bead particle size shrinks[69], but the walls of the acrylic chamber are relatively smooth. For a fine powder like GL29, which is close to the Geldart A/highly cohesive Geldart C powder classification dividing line, cohesion is likely to dominate the overshoot behavior. Test simulations with particle-wall friction coefficients of $\mu_{pw} = 0.1 - 0.4$ and Hamaker constants from zero to $A_{pw} = 3.1 \times 10^{-20}\,J$ revealed that the overshoot in GL29 is primarily due to particle-wall cohesion.

The coarser substrates, GL223 and SS231, exhibited much higher minimum fluidization velocities of around 5 cm/s and 10 cm/s, respectively. Minimum bubbling velocity is less than or equal to the minimum fluidization velocity for Geldart B powders[77], so bubbling commences immediately at u_{mf}. As the gas velocity increases, the bubbles grow in size, leading to increasing fluctuations around the steady pressure drop as indicated by the growing error bars. This is particularly evident for the heaviest material, SS231. Fluidization of this material produced large bubbles and vigorous solids mixing. At the highest velocities, the fluidization stand was observed to shake as the powder's center of mass shifted with the passage of each bubble.

After accounting for sphericity, close agreement was obtained between the simulated and experimental fluidization curves. All glass bead simulations used the default Ergun drag law values (A=150, B=1.75). Only the stainless-steel simulations required modifications to the default coefficients to match experimental pressure drop data (A=248, B=1.75). Values for drag coefficient A have been reported in this range even after accounting for sphericity[78]. Low sphericity values in the stainless-steel bead packs were dominated by elliptical particles such as the upper left particle in **Figure 3.6**. The glass particles were primarily non-spherical due to pitting and large surface asperities. Sphericity may not be enough to account for the contribution of elliptical particles to pressure drop with flow through the stainless-steel bead pack, giving higher A values than in the glass bead pack. It is also worth noting that the perimeter-based sphericity calculation used in this work is a 2D approximation. True sphericity is a 3D metric that requires knowledge of the actual particle's surface area[78] which is not directly available from 2D optical microscopy. Ignoring the effects of sphericity resulted in packed-bed permeability predictions up to 33% higher and minimum fluidization velocities up to 43% larger than the true experimental values. The high sensitivity of fluidized bed simulation accuracy to sphericity has also been reported by other researchers[52].

3.4.3 Aerated Powder Convection

Experiments were performed to evaluate the relationship between the dimensionless vertical acceleration of the conveyor, Γ, the aeration velocity, $\boldsymbol{u_g}$, the powder size, d_p, and the mean convection velocity of each powder, $\bar{v}_{pb}$. All powders conveyed at faster speeds as the vertical acceleration was increased (**Figure 3.11**), which is consistent with the behavior of other objects transported by vibratory convection[3]. Repeatable convection speeds of 1.0 cm/s to 3.5 cm/s were obtained for throw numbers between 0.25 and 0.60. Lower throw numbers <0.25 resulted in irregular or halted powder bed convection velocities. Discrepancies between the simulated and experimental results, particularly at high convection velocities of the SS231 powder, are likely because of simplifications made in the modeling approach. The static velocity inlet only approximately replicates the experimental gas-phase boundary condition. Each dosing gas inlet vibrates with the conveyor and requires a moving boundary to treat exactly. Velocity underprediction may also occur due to stick-slip phenomena between particle layers or at the particle-frit interface[79, 80]. The mechanics of stick-slip are not accounted for in the DEM model and require complex contact treatment beyond the scope of this study. Overall, experiments with the GL56 powder demonstrated a nearly linear increase in convection velocity with throw number whereas the GL223 and SS231 powder velocities increased monotonically with throw number. These trends reflect transitions in the convection velocity mechanism and will be investigated further in the following discussion.

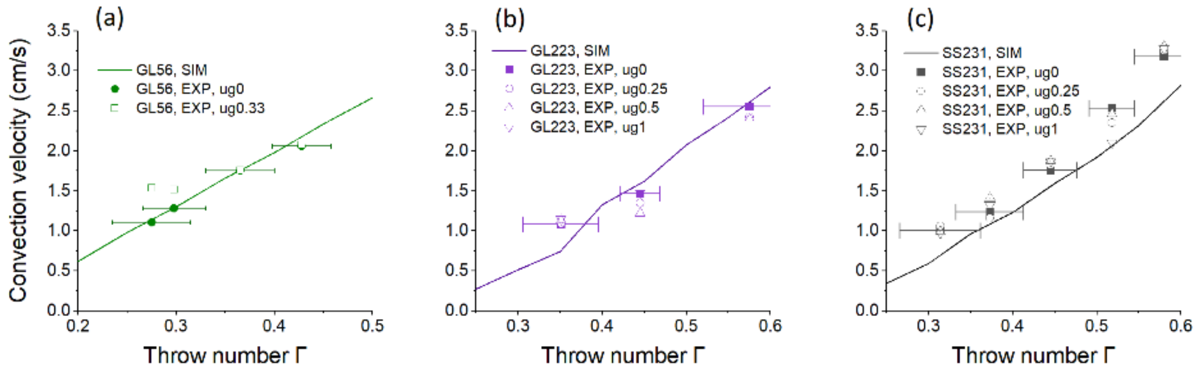

Figure 3.11. Experimental (EXP) and simulated (SIM) powder convection velocity versus throw number Γ at each gas velocity in cm/s (ug0.5 means 0.5 cm/s). Error bars correspond to one standard deviation of the FFT acceleration amplitude from three replicate measurements. To minimize clutter, error bars are only shown for the $\boldsymbol{u_g} = 0\ cm/s$ case in each subplot

For gas velocities between $\boldsymbol{u_g} = 0$ and $1\ cm/s$, the effect of aeration on convection velocity appears to depend on particle size and can be explained by the powder's Geldart classification. At high throw numbers ($\Gamma > 0.35$), increases in gas velocity do not produce a consistent effect on the mean powder speed. For example, a gas flow of 1.0 cm/s causes the mean convection speed of SS231 to increase by 0.1 cm/s at $\Gamma = 0.58$ but then decrease by 0.4 cm/s at $\Gamma = 0.53$. In this regime, collisional forces and powder bed dynamics dominate the convection behavior relative to gas-solids drag. The Geldart B powders, GL223 and SS231, have fluidization velocities around 5 cm/s and 10 cm/s respectively, which meet or exceed the maximum vertical conveyor velocity at $\Gamma = 0.60$. With vertical accelerations significantly less than $1\boldsymbol{g}$, the GL223 and SS231 powders cannot be thrown into a hopping convection cycle without the aid of gas-solids drag. Gas velocities up to 1.0 cm/s are not sufficient to fluidize these particles during conveyor retraction; thus, no aeration effects are observed when $\Gamma < 0.60$.

By contrast, at low throw numbers ($\Gamma < 0.35$), the GL56 powder experienced enhanced convection speeds when the gas velocity increased from 0 to 0.33 cm/s, approximately the minimum fluidization velocity of the powder. At gas velocities >0.33 cm/s (not shown), chaotic powder flow and mixing patterns were observed as the powder bed lost contact with the porous baseplate. No consistent relationship between conveyor acceleration and convection speed could be determined at velocities above u_{mf}. The increase in convection speed for gas velocities <0.33 cm/s can be explained by the role of fluidization during or just before the retraction stroke of conveyor vibration. Easily fluidized powders like GL56 have a u_{mf} less than the maximum vertical conveyor velocity, $v_{c,max}$. When $0.20 < \Gamma < 0.35$, the presence of gas appears to cushion powder liftoff during the retraction phase, resulting in higher convection velocities than observed during vibratory convection of objects[3] and that predicted by models ignoring drag[7]. Higher convection velocities at atmospheric pressure than under vacuum conditions were also observed in our previous work[53], supporting this conclusion. At higher accelerations, liftoff occurs even before the conveyor begins to retract, indicating that powder-frit separation is dominated by vibration-induced particle bed dynamics or “throwing” by the conveyor rather than gas cushioning during retraction.

Liftoff timing can be further explained by examining the simulated mean convection velocity over a single vibration cycle (**Figure 3.12**). Several vibration cycles are plotted at each acceleration versus “relative” time, which begins at the middle of each retraction stroke. The difference between liftoff-dominated convection and shearing-dominated convection is particularly apparent in the transient powder convection profiles. Both the GL56 and GL29 profiles exhibit clear regions corresponding to liftoff and contact. During liftoff, the powder bed separates from the frit and travels at a constant velocity (horizontal line segment in **Figure 3.12**). The contact phase is dominated by sinusoidal behavior as the bed follows the fluctuating velocity of the frit. As acceleration is increased from 0.30$\boldsymbol{g}$ to

0.50$\boldsymbol{g}$, the powder bed lifts off from the frit at earlier relative times, leading to higher flight-phase velocities. The sinusoidal contact phase also increases in magnitude to match the increase in vertical conveyor acceleration. The GL223 and SS231 powders, on the other hand, follow vastly different transient profiles. The 223-micron glass is less cohesive than the 56- and 29-micron glass, resulting in more relative motion between horizontal layers within the powder bed. Unlike GL29 and GL56, the >200-micron powders maintain contact with the frit during extension and retraction cycles. Instead of hopping, convection is induced by shearing between horizontal layers, leading to a broad sawtooth-like wave profile that matches the sinusoidal conveyor velocity in amplitude but not in shape. As acceleration increases, the wave profile shifts to higher convection speeds, but the peak-to-peak amplitude stays relatively constant. Larger accelerations are observed to promote sliding and rolling contact between the bottom powder layer and the frit. Shearing action in the bulk of the bed also increases with acceleration but to a lesser degree than powder-frit sliding.

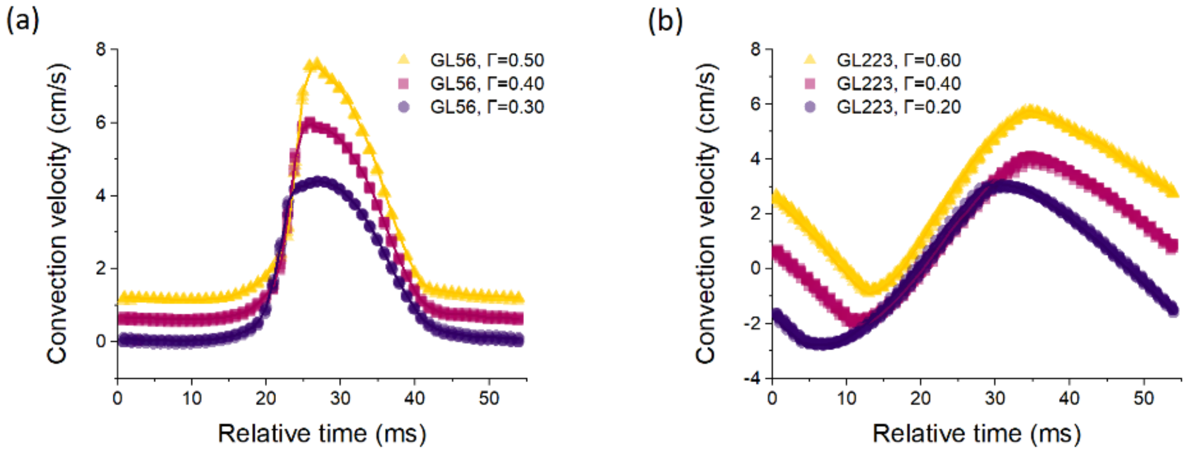

Figure 3.12. Simulated mean velocity trajectories for (a) GL56 and (b) GL223 with changes in acceleration

Another effect of particle size is to change the instantaneous velocity distribution (**Figure 3.13**). Particles such as GL56, with moderate cohesion and a u_{mf} less than $v_{c,max}$, exhibit a tight velocity distribution. During frit contact, bed particles travel with the conveyor. Relative motion between particles is minimal due to the stable coordination network maintained by interparticle cohesion. As the frit retracts, particles in the bottom layers of the bed begin to separate and lift off from the frit. The uncoordinated bottommost layer falls faster than the remainder of the bed, which continues traveling forward in a packed-bed configuration. At all stages during vibration extension and retraction, the majority of GL56 particles travel as a unified mass with small gradients in velocity through the bed thickness. Similar trends were observed in the spatiotemporal simulation data for GL29. The GL223 and SS231 materials, on the other hand, do not exhibit liftoff. As a result, bed convection is driven by a shearing cycle, with the top and bottom layers of particles leading and lagging the mean convection velocity in an alternating fashion. Particles in this convection mode exhibit larger instantaneous velocity distributions than particles transported by liftoff, as demonstrated in **Figure 3.13**.

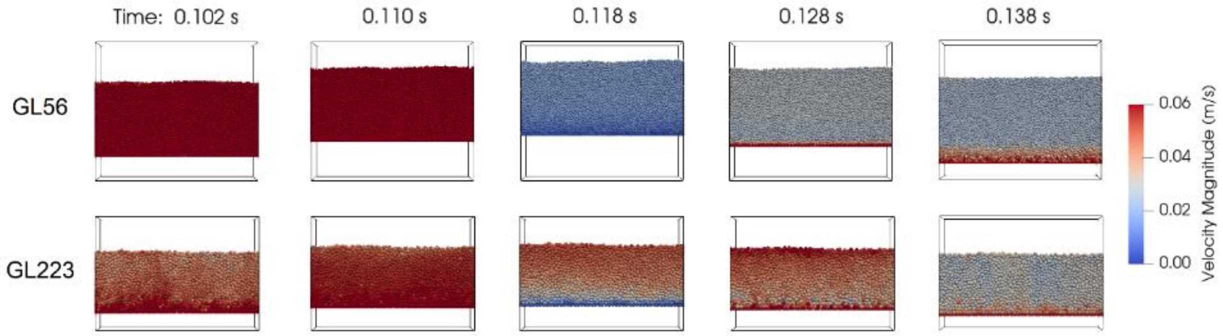

Figure 3.13. Side view simulation snapshots at high acceleration (Γ=0.50) for GL56 and GL223

The coordination networks of each powder bed exhibit different patterns during extension and retraction. For fine powders GL56 and GL29, the powder bed is highly coordinated during the contact phase (**Figure 3.14**). Particle pairs remain in contact with minimal changes to their neighbor networks during frit extension. As the frit retracts, the bed begins to fluidize and the bottom layer of particles separate, forming a loosely coordinated lower region at all accelerations tested. The emergence of poorly coordinated and uncoordinated particles with retraction can be seen in the histograms of **Figures 3.14a** and **3.14b**. During fluidization, the upper portion of the bed mostly maintains the coordination network from the extension phase as lower layers separate from the powder bulk. Upon recontacting the frit, the powder bed compresses, and some neighboring pairs rearrange to produce a coordination network for the next extension phase. The coarse substrates (GL223 and SS231) exhibit self-similar coordination structures through the bed thickness at all accelerations tested, but due to interlayer motion, coordination pairs are seen breaking and forming during extension and retraction. These coordination networks are not stabilized by cohesion and experience constant rearrangement during vibration.

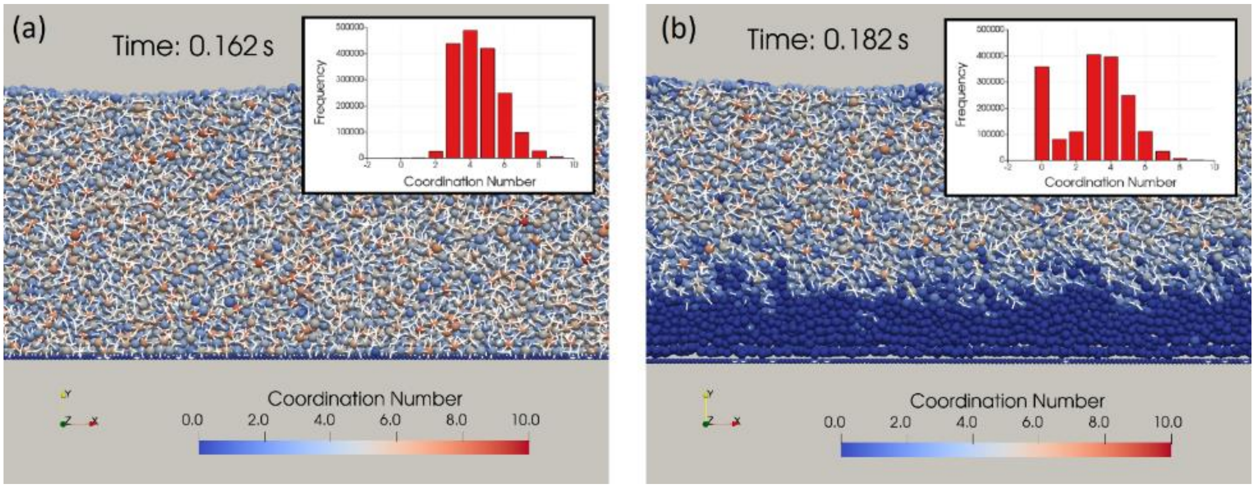

Figure 3.14. Side views of powder bed coordination network during (a) contact and (b) liftoff for GL56 at Γ=0.40. Insets display the coordination number histogram at the chosen points in time. Throughout this paper, coordination number refers to the number of particle contacts (overlap>0)

At low accelerations, the cohesive powders GL56 and GL29 travel forward while maintaining many particle-particle contacts. The packed-bed structure of the powder during vibration can be visualized by averaging the voidage distribution along fixed vertical lines through the simulation domain (**Figure 3.15**). For GL56, typical mesh-cell void fractions within the powder bulk varied between 0.42 and 0.62. Some spatial variations in voidage result due to the polydisperse nature of the powder bed, but the porosity is mostly constant through the bed thickness, as illustrated in **Figure 3.15**. Even as the bed vibrates, bed density remains relatively constant, with a slight dilation region visible near the frit surface as the conveyor retracts from $t = 118$ to $145\ ms$ and again from $t = 172$ to $199\ ms$. The dilation region expands as acceleration increases for the cohesive GL56 and GL29 powders, but voidage in the bulk of the bed remains relatively constant.

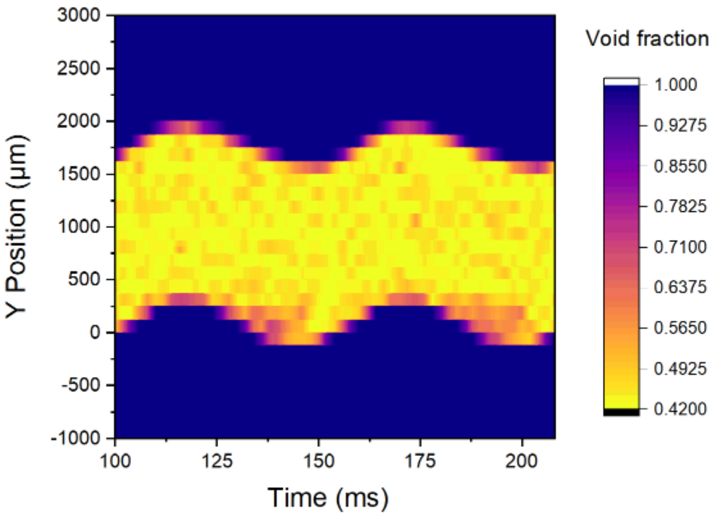

Figure 3.15. Simulated mean void fraction vs time over two cycles of vibration for GL56 at $\Gamma = 0.30$. Y position is measured relative to the top of the frit at time $t = 100\ ms$

3.4.4 Cohesive Effects on Powder Flow

Powder bed flow characteristics during vibratory convection depend on more than excitation magnitude and particle size alone. Material properties also play a role through changes in the interparticle cohesion force. As particle size decreases, the magnitude of van der Waals forces increases relative to particle weight and can lead to changes in bulk powder flow behavior[33]. Cohesive effects can be observed in the GL29 simulations through slower and occasionally backwards travel during the flight phase when compared to the GL56 simulations. While the conveyor retracts, the more cohesive GL29 particles remain in contact with the frit surface, lifting off at negative convection velocities. In cases of high cohesion, liftoff suppression could impede powder bed convection entirely. Both particle-particle and particle-baseplate cohesion influence powder bed convection; therefore, simulations were conducted to understand the effects of each type of cohesion separately.

Simulations of GL56 and GL29 under varying degrees of cohesion revealed the coupling between interparticle forces and powder bed dynamics during vibratory convection. Particle-particle Hamaker constants were set to values between $A_{pp} = 3.1 \times 10^{-21}\,J$ and $7.75 \times 10^{-19}\,J$ to alter the interparticle cohesion (**Table 3.3**). Particle-wall Hamaker constants were also modified from $A_{pw} = 6.2 \times 10^{-21}\,J$ to $1.55 \times 10^{-18}\,J$. The resulting powder bed dynamics can be quantified in terms of the average coordination number and liftoff timing. Liftoff delay is defined as the time, in milliseconds, after the middle of the extension stroke when the average particle velocity deviated measurably from sinusoidal contact (i.e., $\left|\frac{\partial \bar{v}_{pb}}{\partial t} - \frac{\partial v_{conveyor}}{\partial t}\right| > 1\ m/s^2$). Each cohesion simulation can be compared in terms of particle-particle and particle-wall granular Bond numbers, Bo_g, which relate the maximum cohesive force for a single cohesive bond at minimum separation $(F_{c,max})$ to the particle weight, $Bo_g = \frac{F_{c,max}}{m_p g}$ [81]. As expected, powder convection speed was inhibited by higher cohesion. Simulation results for coordination number and liftoff timing are shown in **Figures 3.16-3.18** and will be discussed further in the following paragraphs.

Table 3.3. Particle-particle and particle-wall Hamaker constants used in cohesion simulations. "Base" Hamaker constants are the values used in all previous simulations (**Table 3.1**)

Test Label	**Hamaker constant** (J)	**Magnification factor,** A_{ppn}/A_{pp2}	**GL56 Bond number,** $\boldsymbol{Bo_g}$
Particle-particle cohesion			
A_{pp1}	3.1×10^{-21}	0.1	1.9
(base) A_{pp2}	3.1×10^{-20}	1	19
A_{pp3}	1.55×10^{-19}	5	95
A_{pp4}	7.75×10^{-19}	25	475
Particle-wall cohesion			
A_{pw1}	6.2×10^{-21}	0.1	7.6
(base) A_{pw2}	6.2×10^{-20}	1	76
A_{pw3}	3.1×10^{-19}	5	380
A_{pw4}	1.55×10^{-18}	25	1900

Several regimes emerged when varying the maximum GL56 particle-particle and particle-wall cohesive force magnitudes under a low vibration strength of $\Gamma = 0.25$ (**Figure 3.16**). Low values of particle-particle cohesion ($Bo_{g,pp} = 1.9$) were characterized by highly uncoordinated retraction phases (**Figure 3.17**). Loose coordination of the bottom particle layers allowed the powder bed to separate from the frit, resulting in short liftoff delays and reliable hopping convection. No effect of increasing particle-wall cohesion was observed in this regime. High particle-wall cohesion with low particle-particle cohesion caused some particles to stick to the frit but did not significantly impact the overall bed convection characteristics. As particle-particle Hamaker constant was increased to $3.1 \times 10^{-20}\ J$ ($Bo_{g,pp} = 19$), liftoff delays and average coordination number during liftoff increased. Higher particle-particle cohesion maintains a tighter coordination network, preventing lower particle layers from separating as the frit retracts. Coordination networks during retraction continued to grow as particle-particle cohesion was increased to $Bo_{g,pp} = 95$. Under these conditions, inconsistent liftoff times and significant powder bed-frit sticking were observed due to the formation of stable particle-frit force chains with increasing $Bo_{g,pw}$. At the highest particle-particle cohesion value tested ($Bo_{g,pp} = 475$), powder bed convection was irregular or completely impeded as indicated by a liftoff delay equal to the full vibration cycle (54.1 ms). For $Bo_{g,pp} = 475$ and $Bo_{g,pw} \geq 380$, all particles stuck to the frit and no relative motion between particle layers was observed.

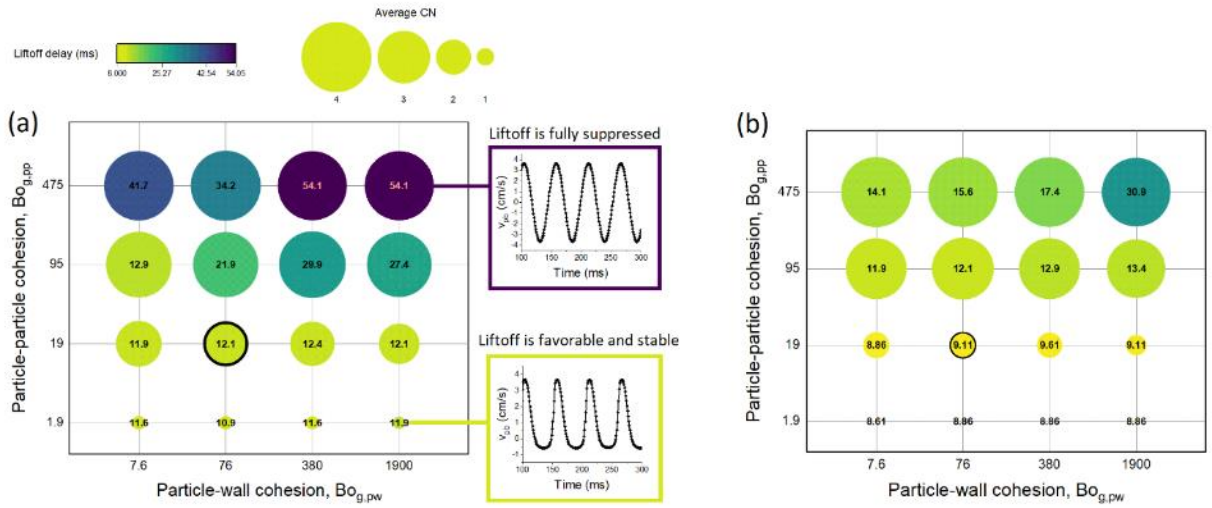

Figure 3.16. Quantifying sticking behavior of GL56 beads at a low throw number, $\Gamma = 0.25$ (a) and a high throw number, $\Gamma = 0.50$ (b) using liftoff delay time (color bar) and average coordination number during frit retraction (bubble size). Base cohesion simulations with Hamaker constants equal to the experimental values from **Table 3.1** are circled in black

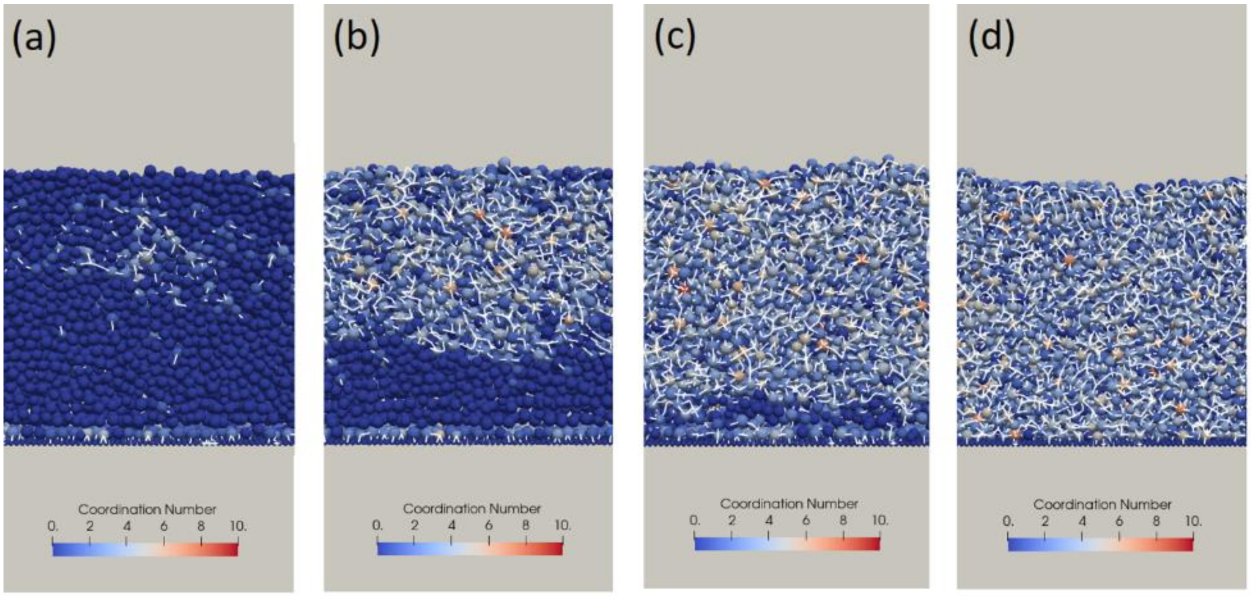

Figure 3.17. Side view of the GL56 particle-particle coordination networks during frit retraction ($t = 190\ ms$) with $\Gamma = 0.25$ and $Bo_{g,pw} = 1900$ when varying particle-particle cohesion from (a) $Bo_{g,pp} = 1.9$, (b) $Bo_{g,pp} = 19$, (c) $Bo_{g,pp} = 95$ and (d) $Bo_{g,pp} = 475$

To determine whether liftoff failure can be overcome by higher conveyor accelerations, simulations were also run at a higher throw number ($\Gamma = 0.50$, **Figure 3.16b**). Liftoff delay and average coordination number exhibited similar trends with cohesion at $\Gamma = 0.50$ as with $\Gamma = 0.25$ but were marked by earlier liftoff times and lower coordination numbers during frit retraction. Liftoff failure was no longer observed at the highest cohesion values and liftoff times remained consistent without significant powder bed-frit sticking up to particle-particle Bond numbers of 475. Average coordination number was once again found insensitive to particle-wall cohesion but depended strongly on particle-particle cohesion, indicating that the packed-bed structure is determined primarily by particle-particle interactions rather than particle-wall interactions.

Compared to the GL56 simulations, GL29 particles were generally characterized by longer liftoff delays and higher mean coordination numbers for the same material Hamaker constants (**Figure 3.18**). Smaller particles stuck to the frit with higher cohesive forces relative to particle weight, delaying liftoff relative to GL56 under the same acceleration conditions. Despite these higher cohesive forces, complete liftoff failure was not observed until granular Bond numbers over 1000. Competing effects driving the powder bed dynamics can be seen for GL29, particularly at moderate cohesion conditions ($Bo_{g,pp} = 354$) where liftoff delays increased with higher particle-wall cohesion except for the highest value of $Bo_{g,pw} = 7086$. Higher cohesive forces cause particles to stick to the frit during retraction but are counteracted by GL29's low u_{mf} of around 0.175 cm/s which promotes powder-frit separation. Partway through retraction when $Bo_{g,pp} = 354$, bottom layer particles maintained adhesive contact with the frit while the remainder of the powder bed lifted off. As cohesion was increased further to $Bo_{g,pp} = 1772$, high values of particle-wall cohesion $Bo_{g,pw} \geq 1417$ forced the entire bed to adhere to the frit and forward convection was halted completely. Convection speed was improved as throw number increased from 0.25 to 0.50 for all simulations except the most cohesive case ($Bo_{g,pp} = 1772$ and $Bo_{g,pw} = 7086$). Under these conditions, a throw number of 0.50 was still not sufficient to induce flow. Additional sources of energy, such as increasing the gas flow, would be needed to drive powder convection in this case.

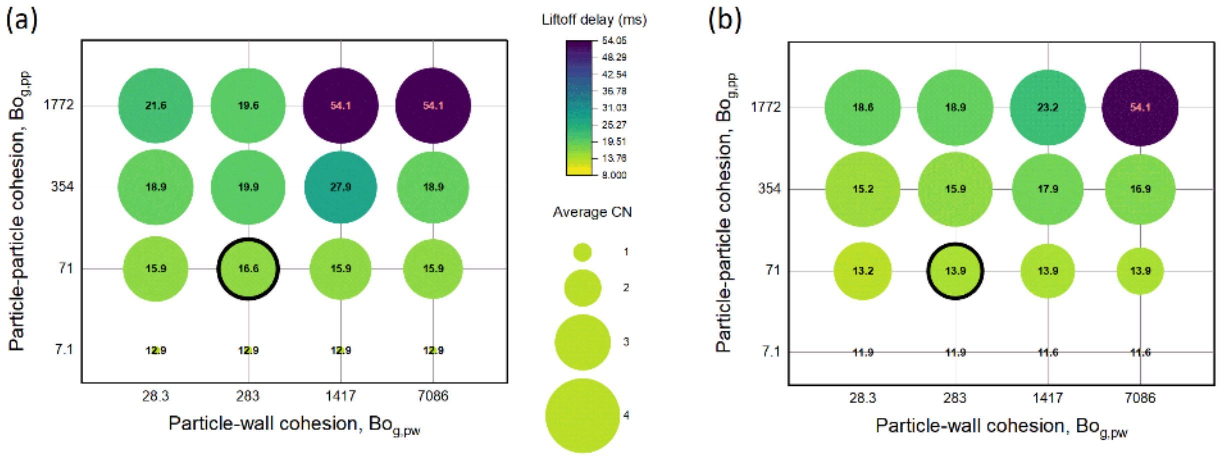

Figure 3.18. Quantifying sticking behavior of GL29 beads at a low throw number, Γ = 0.25 (a) and a high throw number, Γ = 0.50 (b) using liftoff delay time (color bar) and average coordination number during frit retraction (bubble size). Base cohesion simulations with Hamaker constants equal to the experimental values from **Table 3.1** are circled in black

3.5 Conclusions

CFD-DEM simulations were performed at different accelerations and cohesion conditions to investigate the gas-solids flow behavior of a powder bed under vibratory convection. Each simulation setup was guided by materials characterization data for the powder feedstocks and porous baseplate, exposing particle-particle, gas-particle, and particle-wall characteristics relevant to aerated vibratory convection. The combined experimental and modeling campaign was conducted to take advantage of each setup's relative strengths. Experiments confirmed the bulk convection and fluidization behavior of each powder while simulations revealed aspects of the spatial and temporal particle velocities that are not easily seen or measured in the experimental setup.

In summary,

(1) Porous baseplates for use in aerated vibratory conveyors have different surface topography than their smooth nonporous counterparts. Local topography of the frit should be considered when modeling the convection of

fine powders which may interact with frit roughness elements in complex ways.

(2) Under sufficient conveyor acceleration, particles with minimum fluidization velocities less than the maximum conveyor speed will fluidize intermittently during each retraction stroke of the vibration. Air entrainment during powder bed liftoff appears to cushion particles in free fall, resulting in higher mean convection velocities.

(3) Higher throw numbers lead to faster convection speeds for all powders tested but through different convection mechanisms. Increases in conveyor acceleration advance the liftoff timing for fine powders that fluidize during vibration. Coarser powders, which do not fluidize during vibration, experience increased shearing and rolling/sliding between the frit surface and the powder bed as acceleration increases.

(4) Cohesion is attributed to the preservation of stable particle-particle coordination networks during vibratory convection. Powders with higher cohesive forces maintained packed-bed-like structures, and in cases of extreme cohesion $\left(Bo_{g,pp} \gg 100\right)$ convection was completely suppressed in the simulations.

3.6 Nomenclature

ε_g	Gas-phase volume fraction
ρ_g	Gas-phase density
$\boldsymbol{u_g}$	Gas-phase velocity
P_g	Gas-phase pressure
$\boldsymbol{\tau_g}$	Gas-phase shear stress tensor
$\boldsymbol{g}$	Gravitational constant

$\boldsymbol{I_{gs}}$	Gas-solids interaction term
ϕ_m	Drag force interpolation factor
V_m	CFD mesh cell volume
β	Gas-solids interaction coefficient
C_D	Single particle drag coefficient
d_p	Particle diameter
φ	Particle sphericity
Re	Particle Reynolds number
A	Empirical drag model factor, viscous term
B	Empirical drag model factor, inertial term
ε_s	Solids-phase volume fraction
μ_g	Gas-phase viscosity
m_p	Particle mass
$\boldsymbol{u_p}$	Particle translational velocity
$\boldsymbol{\omega_p}$	Particle angular velocity
$\boldsymbol{f}_C$	Particle contact force
$\boldsymbol{f}_{gp}$	Gas-particle interaction term
$\boldsymbol{f}_{vdW}$	Particle van der Waals cohesión
A_{pp}	Particle-particle Hamaker constant
A_{pw}	Particle-wall Hamaker constant
r_a	Asperity height
s	Separation distance of an adhesive pair
$\boldsymbol{\hat{u}}_N$	Unit vector pointing between centers of a particle-particle pair
I_p	Particle moment of inertia
$\boldsymbol{t}$	Particle torque
$\boldsymbol{r}$	Displacement vector between centers of a particle-particle pair
V_p	Particle volume
W	Periodic box width
H	Periodic box height
D	Periodic box depth
H_{bed}	Powder bed height
μ_{pw}	Particle-wall friction coefficient
ρ_p	Particle material density
A_v	Vertical vibration amplitude
f	Vibration frequency
Γ	Throw number
u_{mf}	Minimum fluidization velocity
$v_{c,max}$	Maximum conveyor velocity
$\bar{v}_{pb}$	Average particle bed velocity
$Bo_{g,pp}$	Particle-particle granular Bond number
$Bo_{g,pp}$	Particle-wall granular Bond number

Acknowledgements

The authors are grateful for the support of the National Science Foundation [NSF GOALI #1852824]. This work utilized the RMACC Summit supercomputer, which is supported by the National Science Foundation (awards ACI-1532235 and ACI-1532236), the University of Colorado Boulder, and Colorado State University. The Summit supercomputer is a joint effort of the University of Colorado Boulder and Colorado State University. Surface profilometry work was made possible by the Colorado Shared Instrumentation in Nanofabrication and Characterization (COSINC) facility. The authors also thank Ipsita Mishra and Aaron Lattanzi for helpful discussions about the CFD-DEM model as well as Sarah Arpin and Victoria Kravets from the Laboratory for Interdisciplinary Statistical Analysis (LISA) for feedback on data visualization.

References

[1] M.T. Sgriccia, Feeder bowl, Google Patents, 1953.
[2] M. Parameswaran, S. Ganapathy, Vibratory conveying—Analysis and design: A review, Mechanism and Machine Theory, 14 (1979) 89-97.
[3] A. Redford, G. Boothroyd, Vibratory feeding, Proceedings of the Institution of Mechanical Engineers, 182 (1967) 135-152.
[4] G. Winkler, Analysing the hopping conveyor, International Journal of Mechanical Sciences, 21 (1979) 651-658.
[5] C. Woodcock, J. Mason, Bulk solids handling: an introduction to the practice and technology, Springer Science & Business Media2012.
[6] D. Schulze, Powders and bulk solids, Behaviour, characterization, storage and flow. Springer, 22 (2008).
[7] G. Winkler, Analysing the vibrating conveyor, International Journal of Mechanical Sciences, 20 (1978) 561-570.
[8] S. Okabe, Y. Yokoyama, G. Boothroyd, Analysis of vibratory feeding where the track has directional friction characteristics, The International Journal of Advanced Manufacturing Technology, 3 (1988) 73-85.
[9] W. Mansour, M. Massoud, W. Morcos, C. Lauzier, The mechanism of conveyance with bristled tracks, (1975).
[10] B. Balaji, R. Gupta Burela, G. Ponniah, Dynamics of part motion on a linear vibratory feeder, Proceedings of the Institution of Mechanical Engineers, Part C: Journal of Mechanical Engineering Science, 236 (2022) 886-893.
[11] R. Schofield, M. Yousuf, The design of a linear "out of phase" vibratory conveyor, (1973).
[12] S. Okabe, Y. Kamiya, K. Tsujikado, Y. Yokoyama, Vibratory feeding by nonsinusoidal vibration—optimum wave form, (1985).
[13] E. Sloot, N.P. Kruyt, Theoretical and experimental study of the transport of granular materials by inclined vibratory conveyors, Powder Technology, 87 (1996) 203-210.

[14] C.E. Schertz, Motion of granular material on an oscillating conveyor, Iowa State University1962.

[15] G. Wes, S. Stemerding, D. van Zuilichem, Control of flow of cohesive powders by means of simultaneous aeration, and vibration, Powder technology, 61 (1990) 39-49.

[16] E. Marring, A. Hoffmann, L. Janssen, The effect of vibration on the fluidization behaviour of some cohesive powders, Powder technology, 79 (1994) 1-10.

[17] D. Barletta, M. Poletto, Aggregation phenomena in fluidization of cohesive powders assisted by mechanical vibrations, Powder Technology, 225 (2012) 93-100.

[18] L. Moskowitz, Vibratory feeding and conveying, Automation, 6 (1959) 78-82.

[19] A.W. Weimer, Particle atomic layer deposition, Journal of Nanoparticle Research, 21 (2019) 9.

[20] A.R. Abrahamsen, D. Geldart, Behaviour of gas-fluidized beds of fine powders part I. Homogeneous expansion, Powder Technology, 26 (1980) 35-46.

[21] S. Benyahia, Simulating the Formation of Granular Jets, Industrial & Engineering Chemistry Research, 59 (2020) 8416-8425.

[22] W. Kroll, Über das Verhalten von Schüttgut in lotrechi schwingenden Gefäßen, Forschung auf dem Gebiet des Ingenieurwesens A, 20 (1954) 2-15.

[23] S. Bottcher, Contribution to the problem of conveying materials by oscillating conveyors, Foerdern und Heben (3), (1958) 127-131.

[24] S. Douady, S. Fauve, C. Laroche, Subharmonic instabilities and defects in a granular layer under vertical vibrations, EPL (Europhysics Letters), 8 (1989) 621.

[25] H. Pak, R. Behringer, Surface waves in vertically vibrated granular materials, Physical review letters, 71 (1993) 1832.

[26] T.H. Metcalf, J.B. Knight, H.M. Jaeger, Standing wave patterns in shallow beds of vibrated granular material, Physica A: Statistical Mechanics and its Applications, 236 (1997) 202-210.

[27] G. Straßburger, I. Rehberg, Crystallization in a horizontally vibrated monolayer of spheres, Physical Review E, 62 (2000) 2517.

[28] R. Grochowski, P. Walzel, M. Rouijaa, C.A. Kruelle, I. Rehberg, Reversing granular flow on a vibratory conveyor, Applied physics letters, 84 (2004) 1019-1021.

[29] P. Berry, Basic theory of low acceleration oscillating conveyors, (1959).

[30] Y.I. Rabinovich, J.J. Adler, A. Ata, R.K. Singh, B.M. Moudgil, Adhesion between nanoscale rough surfaces: I. Role of asperity geometry, Journal of colloid and interface science, 232 (2000) 10-16.

[31] O. Molerus, Interpretation of Geldart's type A, B, C and D powders by taking into account interparticle cohesion forces, Powder technology, 33 (1982) 81-87.

[32] T. Kobayashi, T. Tanaka, N. Shimada, T. Kawaguchi, DEM–CFD analysis of fluidization behavior of Geldart Group A particles using a dynamic adhesion force model, Powder technology, 248 (2013) 143-152.

[33] Y. Gu, A. Ozel, S. Sundaresan, A modified cohesion model for CFD–DEM simulations of fluidization, Powder technology, 296 (2016) 17-28.

[34] R.L. Puurunen, Surface chemistry of atomic layer deposition: A case study for the trimethylaluminum/water process, Journal of applied physics, 97 (2005) 9.

[35] M. Tahmasebpoor, L. de Martín, M. Talebi, N. Mostoufi, J.R. van Ommen, The role of the hydrogen bond in dense nanoparticle–gas suspensions, Physical Chemistry Chemical Physics, 15 (2013) 5788-5793.

[36] C. Hirschberg, N.S. Jensen, J. Boetker, A.Ø. Madsen, T.O. Kääriäinen, M.-L. Kääriäinen, P. Hoppu, S.M. George, M. Murtomaa, C.C. Sun, Improving Powder Characteristics by Surface Modification Using Atomic Layer Deposition, Organic Process Research & Development, 23 (2019) 2362-2368.

[37] A. Fukunishi, Y. Mori, Adhesion force between particles and substrate in a humid atmosphere studied by atomic force microscopy, Advanced Powder Technology, 17 (2006) 567-580.

[38] J.E. Galvin, S. Benyahia, The effect of cohesive forces on the fluidization of aeratable powders, AIChE Journal, 60 (2014) 473-484.

[39] R. Yang, R. Zou, A. Yu, S. Choi, Characterization of interparticle forces in the packing of cohesive fine particles, Physical Review E, 78 (2008) 031302.
[40] M.D. Abràmoff, P.J. Magalhães, S.J. Ram, Image processing with ImageJ, Biophotonics international, 11 (2004) 36-42.
[41] Digital Asset Library, Anton Paar, 2022.
[42] I. Mishra, P. Liu, A. Shetty, C.M. Hrenya, On the use of a powder rheometer to probe defluidization of cohesive particles, Chemical Engineering Science, 214 (2020) 115422.
[43] A. Iams, M. Gao, A. Shetty, T. Palmer, Influence of particle size on powder rheology and effects on mass flow during directed energy deposition additive manufacturing, Powder Technology, 396 (2022) 316-326.
[44] C.G. Jange, P. Taku, S. Peng, M.P. Dixon, A. Shetty, R.K. Ambrose, Cohesivity assessment of semi-crystalline and crystalline powders using a Warren Springs cohesion tester, Powder Technology, 371 (2020) 96-105.
[45] Y. Zhao, P. Phalswal, A. Shetty, K.A. RP, Effects of Powder Vibration and Time Consolidation on Soft and Hard Wheat Flour Properties, KONA Powder and Particle Journal, (2021) 2021007.
[46] S.-Y. Chang, S.W. Li, K. Kowsari, A. Shetty, L. Sorrells, K. Sen, K. Nagapudi, B. Chaudhuri, A.W. Ma, Binder-jet 3D printing of indomethacin-laden pharmaceutical dosage forms, Journal of Pharmaceutical Sciences, 109 (2020) 3054-3063.
[47] I. Mishra, M.J. Molnar, M.Y. Hwang, A. Shetty, C.M. Hrenya, Experimental validation of the extraction of a particle-particle cohesion model (square-force) from simple bulk measurements (defluidization in a rheometer), Chemical Engineering Science, (2022) 117782.
[48] T.B. Anderson, R. Jackson, Fluid mechanical description of fluidized beds. Equations of motion, Industrial & Engineering Chemistry Fundamentals, 6 (1967) 527-539.
[49] M. Syamlal, W. Rogers, T.J. OBrien, MFIX documentation theory guide, USDOE Morgantown Energy Technology Center, WV (United States), 1993.
[50] G. Johnson, K.R. Rajagopal, M. Massoudi, A review of interaction mechanisms in fluid-solid flows, (1990).
[51] D. Gidaspow, Hydrodynamics of fiuidizatlon and heat transfer: Supercomputer modeling, (1986).
[52] C.Q. LaMarche, P. Liu, K.M. Kellogg, A.W. Weimer, C.M. Hrenya, A system-size independent validation of CFD-DEM for noncohesive particles, AIChE Journal, 61 (2015) 4051-4058.
[53] J. Hartig, H.C. Howard, T.J. Stelmach, A.W. Weimer, DEM modeling of fine powder convection in a continuous vibrating bed reactor, Powder Technology, (2021).
[54] P.A. Cundall, O.D. Strack, A discrete numerical model for granular assemblies, geotechnique, 29 (1979) 47-65.
[55] Y. Tsuji, T. Kawaguchi, T. Tanaka, Discrete particle simulation of two-dimensional fluidized bed, Powder technology, 77 (1993) 79-87.
[56] R. Garg, J. Galvin, T. Li, S. Pannala, Open-source MFIX-DEM software for gas–solids flows: Part I—Verification studies, Powder Technology, 220 (2012) 122-137.
[57] J. Dickinson, R. Hariadi, L. Scudiero, S. Langford, A scanning force microscope study of detachment of nanometer-sized particles from glass surfaces, Tribology Letters, 7 (1999) 113-119.
[58] C. LaMarche, P. Liu, K. Kellogg, C. Hrenya, Fluidized-bed measurements of carefully-characterized, mildly-cohesive (Group A) particles, Chemical Engineering Journal, 310 (2017) 259-271.
[59] J. Wang, M.A. van der Hoef, J. Kuipers, CFD study of the minimum bubbling velocity of Geldart A particles in gas-fluidized beds, Chemical Engineering Science, 65 (2010) 3772-3785.
[60] Q. Guo, Y. Zhang, C. Vazquez, K. Xi, C.M. Boyce, Multi-Fluid Model Simulations of Gravitational Instabilities in Fluidized Binary Granular Materials, AIChE Journal, (2022) e17714.
[61] Q. Guo, C.M. Boyce, Structured bubbling in layered gas-fluidized beds subject to vibration: A CFD-DEM study, AIChE Journal, (2022) e17709.

[62] J.A. Gallas, H.J. Herrmann, T. Pöschel, S. Sokołowski, Molecular dynamics simulation of size segregation in three dimensions, Journal of Statistical Physics, 82 (1996) 443-450.
[63] B.C. Eric, F. Luke, D. Josef, T. Michael, F.-N. Alberto, D. Jean-François, Investigating the rheology of fluidized and non-fluidized gas-particle beds: implications for the dynamics of geophysical flows and substrate entrainment, Granular Matter, 24 (2022) 1-25.
[64] Y. Xu, J. Musser, T. Li, J.T. Padding, W.A. Rogers, Particles climbing along a vertically vibrating tube: numerical simulation using the Discrete Element Method (DEM), Powder Technology, 320 (2017) 304-312.
[65] J.N. Israelachvili, Intermolecular and surface forces, Academic press2011.
[66] J. Visser, On Hamaker constants: A comparison between Hamaker constants and Lifshitz-van der Waals constants, Advances in colloid and interface science, 3 (1972) 331-363.
[67] P. Tyagi, T. Goulet, C. Riso, F. Garcia-Moreno, Reducing surface roughness by chemical polishing of additively manufactured 3D printed 316 stainless steel components, The International Journal of Advanced Manufacturing Technology, 100 (2019) 2895-2900.
[68] A. Vakis, V. Yastrebov, J. Scheibert, L. Nicola, D. Dini, C. Minfray, A. Almqvist, M. Paggi, S. Lee, G. Limbert, Modeling and simulation in tribology across scales: An overview, Tribology International, 125 (2018) 169-199.
[69] D.B. Hastie, W.G. Halford, Preliminary observations of the effect of plate roughness and particle size on the determination of wall friction, (2016).
[70] F. Podczeck, Y. Mia, The influence of particle size and shape on the angle of internal friction and the flow factor of unlubricated and lubricated powders, International Journal of Pharmaceutics, 144 (1996) 187-194.
[71] S. Tan, J. Newton, Powder flowability as an indication of capsule filling performance, International Journal of Pharmaceutics, 61 (1990) 145-155.
[72] B.C. Hancock, The wall friction properties of pharmaceutical powders, blends, and granulations, Journal of pharmaceutical sciences, 108 (2019) 457-463.
[73] W. Halford, C. Lawler, A.P. Grima, P.C. Arnold, Some influences on wall friction measurements-a preliminary investigation, (2013).
[74] A. Pinon, M. Wierez-Kien, A. Craciun, N. Beyer, J. Gallani, M. Rastei, Thermal effects on van der Waals adhesive forces, Physical Review B, 93 (2016) 035424.
[75] A. Harsha, P. Limaye, R. Tyagi, A. Gupta, Effect of Temperature on Galling Behavior of SS 316, 316 L and 416 Under Self-Mated Condition, Journal of Materials Engineering and Performance, 25 (2016) 4980-4987.
[76] S.R. Rogers, D. Bowden, R. Unnikrishnan, F. Scenini, M. Preuss, D. Stewart, D. Dini, D. Dye, The interaction of galling and oxidation in 316L stainless steel, Wear, 450 (2020) 203234.
[77] D. Geldart, Types of gas fluidization, Powder technology, 7 (1973) 285-292.
[78] I. Macdonald, M. El-Sayed, K. Mow, F. Dullien, Flow through porous media-the Ergun equation revisited, Industrial & Engineering Chemistry Fundamentals, 18 (1979) 199-208.
[79] D. Schulze, Time-and Velocity-Dependent Properties of Powders Effecting Slip-Stick Oscillations, Chemical Engineering & Technology: Industrial Chemistry-Plant Equipment-Process Engineering-Biotechnology, 26 (2003) 1047-1051.
[80] G. Capone, V. D'Agostino, S. Della Valle, D. Guida, Influence of the variation between static and kinetic friction on stick-slip instability, Wear, 161 (1993) 121-126.
[81] M. Capece, R. Ho, J. Strong, P. Gao, Prediction of powder flow performance using a multi-component granular Bond number, Powder Technology, 286 (2015) 561-571.

CHAPTER 4

POWDER MIXING AND SELF-DIFFUSION

4.1 Abstract

This paper presents particle image velocimetry (PIV) and computational fluid dynamics discrete element method modeling (CFD-DEM) results for powder flow in a continuous vibrating reactor for particle atomic layer deposition (CVR-ALD). Three frit baffle designs were investigated to improve powder mixing for 50-micron glass, 225-micron glass, and 225-micron stainless steel beads in the reactor purge zones. Mixing rates were enhanced by an order of magnitude with frit baffles as quantified by self-diffusion coefficient. Tracer particles were used to evaluate mixing quality in experimental and simulation snapshots. Powder flow in the presence of frit baffles was characterized by funneling between flow obstructions and bed thinning over sawtooth features. Particles on the bed surface flow faster over a sawtooth frit baffle than particles at the bottom of the bed. Higher bed declination angles up to 9 degrees improved the mixture homogeneity.

4.2 Introduction

Vibratory conveyors use 2D excitation to transport material along a feeding tray and can be found in a variety of styles. Some conveyors are designed with mechanisms to dislodge adhered material[1], promote tray-powder separation[2], or induce particle mixing[3-6]. The bed may be aerated to suspend particles as they are thrown off the conveyor surface[7] or de-aerated to compact fluffy feedstocks and increase the conveying capacity[3, 8]. Some studies have been performed to investigate the mixing quality of specialized conveyor-mixers[9] or the transverse dispersion of glass beads under vibration[10], but the mechanics and quality of powder mixing during aerated vibratory convection remain uninvestigated or, at a minimum, unpublished.

Recently, interest in vibratory convection and mixing has been renewed with the development of continuous vibrating reactors for particle atomic layer deposition (CVR-ALD)[11]. Also known as a continuous spatial particle ALD reactor, CVR-ALD reactors transport powders through alternating regions of precursor gas using vibratory convection. Gas is fed into the enclosed conveyor housing through a porous baseplate and reacts with particle surface functional groups to build a film with Angstrom-level thickness control. Self-diffusion, which describes the mixing of particles amongst themselves, is desired in any particle ALD process to minimize agglomerate formation and coating nonuniformities[12]. The need for self-diffusion is particularly pronounced in CVR-ALD where gases are dosed through the bottom of the bed. In the absence of top-bottom mixing, particles at the top of the bed located far from the dosing zone will see a lower precursor concentration than particles at the bottom. Residence time differences due to powder bed shearing from top to bottom could lead to film nonuniformities due to insufficient precursor exposure of the top particles. As the powder flows through the reactor, bed characteristics such as surface roughness[13], hydrogen bridging strength[14] and overall flowability[15] may also change as a result of ALD, further complicating the self-mixing process. Mixing has been demonstrated in fluidized bed particle ALD reactors[16] under normal operation but not yet for CVR-ALD reactors. Understanding and improving the mixing behavior is a key step in guaranteeing surface titration uniformity for all material properties and operating conditions encountered in CVR-ALD reactors.

Many mechanical methods have been developed to induce powder mixing. Examples of mixing devices include Kenics mixers, V-blenders and v-blade mixers[17], ribbon mixers, rotating drums with or without baffles[18], orbiting screw/Nauta mixers, and paddle mixers[19]. The underlying principle behind stepwise mixing of granular materials is the "pastry-maker technique", which involves splitting the flow, layering the flow, and repeating until the desired mixture homogeneity is achieved[20]. Powder mixing can be divided into larger-scale "advective mixing" (relative motion between particle parcels) and smaller-scale "diffusive mixing" (relative motion between particles)[19, 21]. An ideal mixing process produces a random distribution of particles within the bed[19, 22]. Studies on the mixing devices described above have found that interparticle cohesion[23, 24], bed height[25], baffle or mixer geometry[26] and operating conditions such as shaft speed[27] impact mixing efficacy. Mixing quality can be impeded by segregation effects due to variations in particle size, density and shape, or by agglomeration from interparticle cohesion[19]. Rocking[17] or vibration can promote mixing, but care must be taken to avoid agitation-induced segregation effects[28, 29]. Granular mixtures of dissimilar materials tend to segregate, not mix, when vibrated[30]. Any design which integrates standard mixing geometries with a CVR-ALD reactor should take these observations into consideration.

Traditionally, the homogeneity of a solid mixture has been quantified using a metric that evaluates the transition from a fully segregated (M=0) to a fully mixed state (M=1). Mixing indices[31] are based on statistical variations between the sample to be analyzed and a fully segregated and/or fully mixed state. One of the most well-known metrics, Lacey's index[32], uses the difference in variance between the sample and perfectly segregated/perfectly random systems to quantify mixedness. Other mixing indices have been developed over the years and can be found in the reviews by Fan et. al.[33, 34]. Relative standard error (RSE) or relative standard deviation (RSD)[35] of the particle concentration, particle-scale mixing index (PSMI)[36], deviations in particle velocity[37] or particle position[38] and coordination-number-based mixing indices from discrete element method (DEM) data[39, 40] are just a few of the many alternative metrics available. Many of these measures are based on the batch mixing of two discrete granular materials and are not easily evaluated in a continuous self-mixing process like CVR-ALD. Mixing indices are sensitive to the size and number of samples analyzed, making cross-comparison between studies difficult[33]. Extrapolation to continuous powder flow applications, where the sample size is not fixed, is also not straightforward. In a continuous feed setup, the rate of mixing provides a more direct measure of the process's mixing efficacy than mixing index of the outlet stream[41], which depends on the length of the mixing device. Rate-based parameters such as instantaneous particle diffusivity and Peclet number[25, 42] provide a means to evaluate mixing quality in a continuously flowing powder and can be calculated from transient DEM data.

We propose analysis of computational fluid dynamics-discrete element method (CFD-DEM) simulations coupled with experimental particle image velocimetry (PIV)[43] data to quantify particle mixing in a CVR-ALD reactor. Cross-correlation PIV is an optical measurement technique that provides instantaneous velocity fields from particle displacement calculations between successive image frames. The PIV setup enables visualization of horizontal mixing between tracer particles and bed particles for powders 50- to 225-microns in diameter. Several porous baseplate geometries with mixing baffles were developed and evaluated using PIV for mixing efficacy. CFD-DEM simulations augment the PIV results by providing details on particle-level interactions and vertical (top-bottom) mixing over a sawtooth baffle below the resolution of our imaging equipment for PIV.

4.3 Methods

4.3.1 CVR-ALD Setup

Powder mixing geometries were integrated into our existing in-house CVR-ALD reactor (**Figure 4.1**). Each powder (50-micron glass, 225-micron glass and 225-micron stainless steel from Mo-Sci Corporation and Next Advance) was seeded with dyed tracer particles of the same material to improve visualization of the mixing behavior. During operation, particles leave a gravity-feed hopper, pass through a feed tube, and enter the reactor. As the bed vibrates, particles travel over the porous reactor baseplate through multiple gas dosing zones before exiting the reactor. A panel of flow meters (Omega FL3288-ST) control the gas velocity into the chamber from $v_g = 0$ to $v_g = 1\ cm/s$ for the 225-micron beads or $v_g = 0.2\ cm/s$ for the 50-micron beads. Air pressure to the pneumatic drive unit (Martin Vibration Systems NTK 25 AL) regulates the oscillation frequency and amplitude. All tests were performed at the same acceleration condition by setting the actuator air pressure to P=45 psi (vertical vibration strength Γ=0.50, where Γ is the vertical conveyor acceleration normalized by gravitational acceleration g). A camcorder (Sony HXR-NX80) mounted to a stand of two-by-fours above the reactor captured top-down 1920×1080-

pixel high-speed videos of the powder flow during vibratory convection. Camera settings were chosen to maximize clarity and brightness during vibration (manual focus, shutter speed 350, iris F6.2, iso/gain 18dB, S&Q motion with 120 fps, no ND filter). At high shutter speeds, ambient light was not sufficient to provide high image contrast and remove shadows cast by the reactor walls; a ring light attached to the two-by-four stand was added to further illuminate the imaging area. Files were recorded with the recommended HD format (XAVC S HD). To provide optical clarity of the powder inside, the transparent acrylic upper chamber was sanded down to 3000 grit and polished with the Novus 7100 Plastic Polish Kit.

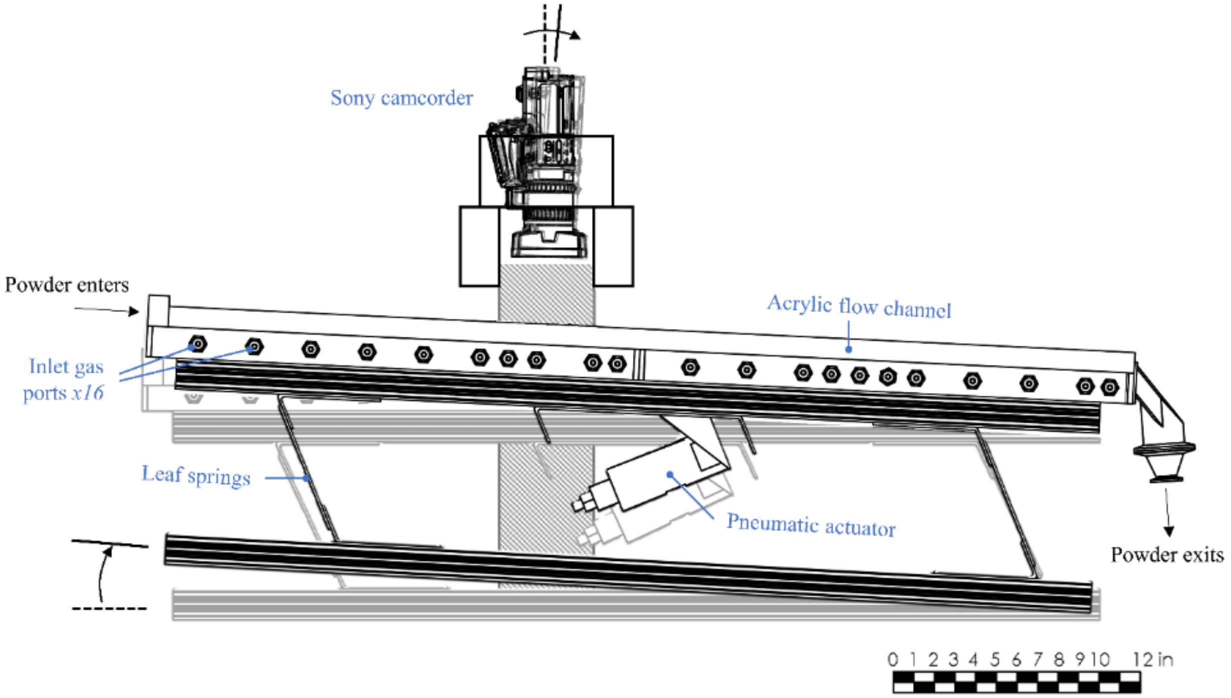

Figure 4.1. Imaging setup for CVR-ALD reactor. Gas is fed through the inlet gas ports from a panel of flow meters. Conveyor acceleration is controlled by air pressure to the pneumatic actuator. Declination angle can be changed by elevating one end of the suspension, as shown. Generic Sony camcorder and pneumatic actuator models were obtained from GrabCAD

Frits with mixing baffles were prepared from 10-micron, 2-ply sintered stainless-steel mesh (TWP Inc). The 2-ply mesh sheet was cut to fit within the frit cavity and laid over the existing porous baseplate. The fine mesh side was placed face up, preventing the passage of >10-micron particles, while the coarse mesh underlayer provides structural integrity to the frit baffles. 2D profiles defining the baffle edges were cut out on all but one side using a waterjet and bent to form a flow obstruction (**Figure 4.2**). A triangular insert bridging the gap between the bent baffle faces was attached using JB Weld high-temperature epoxy for mating metal surfaces.

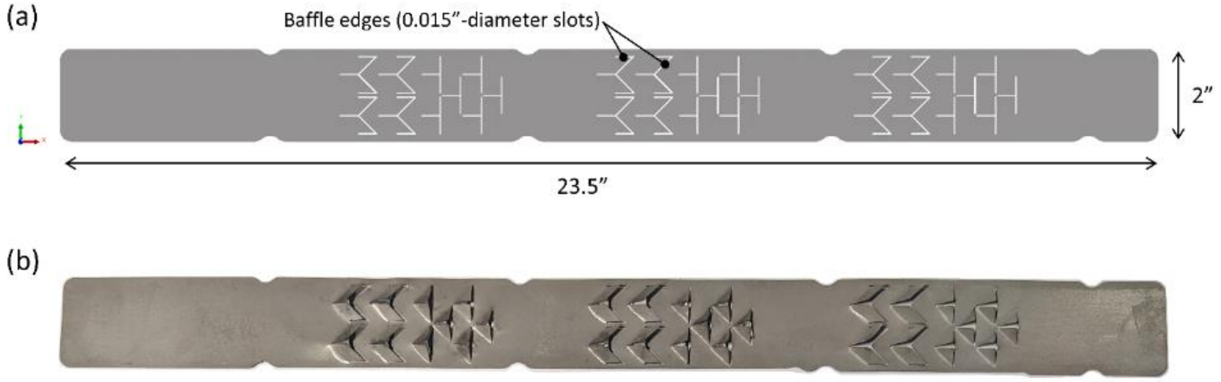

Figure 4.2. (a) Sample 2-inch by 23.5-inch 2D CAD geometry describing frit features for waterjet. (b) Photograph of completed frit prototype. Baffles are cut out of a 2-ply mesh sheet and bent to form 3D flow obstructions as shown

4.3.2 Image Processing in PIVlab

Lateral powder mixing in frames from the CVR-ALD reactor tests were analyzed in MATLAB using PIVlab v2.56. The PIVlab software has a wide user base with extensive algorithmic evaluation[44, 45] and has been successfully applied to study flows of granular media[46-48]. It should be noted that the PIV software does not track individual particles as in particle tracking velocimetry (PTV)[49]; instead, particle ensembles or parcels are followed by correlating intensity distributions between the image frames. Each video was analyzed using the same procedure. First, 120 frames were imported from the 120-fps slow motion video. A rectangular region of interest (ROI) ~40 mm wide and 80 mm long was selected to fall within the chamber edges and the halo produced by the ring light. Each frame was preprocessed with the standard settings (contrast limited adaptive histogram equalization or CLAHE with a 64 px window size, auto contrast stretch enabled). An FFT window deformation algorithm with three passes (64-pixel, 32-pixel, and 16-pixel square interrogation areas, respectively) and Gauss 2x3-point sub-pixel estimator with standard correlation robustness were selected to analyze each frame. After processing, the calibration distance was set based on center-to-center distance between two bolts in the frame (148 mm). Velocity limits from -10 to 10 cm/s in y and -10 to 12 cm/s in x were applied to remove invalid velocity vectors. These limits were chosen to give a 10 cm/s buffer around the average powder velocity (0 cm/s in y and 1-2 cm/s in x). At a frame rate of 120 fps, a 12 cm/s upper velocity limit maintains maximum frame-to-frame displacement within 11 pixels. Frames from several tests were exported to the VTK file format for further analysis in ParaView.

4.3.3 Governing Equations

We simulated particle flow over a sawtooth to analyze top-bottom mixing during vibration. Gas phase modeling in CFD takes the Eulerian approach by solving a set of Navier-Stokes equations for fluid mass and momentum,

$$\frac{\partial}{\partial t}\left(\varepsilon_g \rho_g\right) + \nabla \cdot \left(\varepsilon_g \rho_g \vec{v}_g^i\right) = 0 \tag{4-1}$$

$$\frac{\partial}{\partial t}\left(\varepsilon_g \rho_g \vec{v}_g^i\right) + \nabla \cdot \left(\varepsilon_g \rho_g \vec{v}_g^i \vec{v}_g^i\right) = -\varepsilon_g \nabla P_g + \nabla \cdot \vec{\tau}_g^{i,j} + \varepsilon_g \rho_g \vec{g}^i - \vec{I}_{gs}^i \tag{4-2}$$

where ε_g is the gas volume fraction; ρ_g is the gas density; $\vec{v}_g^i$ is the gas velocity; P_g is the gas pressure; $\vec{\tau}_g^{i,j}$ is the gas stress tensor; $\vec{g}$ is the gravity vector; and $\vec{I}_{gs}^i$ is the gas-solids interaction term. Air is a Newtonian fluid with the viscous stress tensor $\vec{\tau}_g^{i,j}$ described as in

$$\vec{\tau}_g^{i,j} = \mu_g \varepsilon_g \left(\nabla \vec{v}_g^i + \left(\nabla \vec{v}_g^i\right)^T\right) - \frac{2}{3}\mu_g \varepsilon_g \left(\nabla \cdot \vec{v}_g^i\right) \vec{I}_k^{i,j} \tag{4-3}$$

where μ_g is the dynamic gas viscosity and $\vec{I}_k^{i,j}$ is the unit tensor.

In DEM, particle dynamics are described by Newton's equations of motion. The forces, $\vec{F}^i$, and torques, $\vec{T}^i$, on a particle are used to solve for linear velocity $\vec{u}_p^i$ and angular velocity $\vec{\omega}_p^i$. These are

$$m_p^i \frac{\partial \vec{u}_p^i}{\partial t} = \sum \vec{F}^i = m_p^i \vec{g}^i + \sum_j \vec{F}_C^{i,j} + \vec{F}_{gp}^i \tag{4-4}$$

$$I_p^i \frac{\partial \vec{\omega}_p^i}{\partial t} = \sum \vec{T}^i = \sum_j \vec{r}^{i,j} \times \vec{F}_C^{i,j} \tag{4-5}$$

where m_p^i is the particle mass; $\vec{u}_p^i$ is the particle velocity; $\vec{F}_C^{i,j}$ is the contact force; $\vec{F}_{gp}^i$ is the gas-particle interaction force; I_p^i is the particle's moment of inertia; and $\vec{r}^{i,j}$ is a displacement vector between the centers of particles i and j. Contact force is calculated using the soft sphere approach with a linear spring-dashpot model[50]. Detailed expressions for the force and torque terms can be found elsewhere[51].

All CFD-DEM simulations in this work were conducted using the open-source code MFIX[52]. The MFIX solver treats the gas phase as incompressible with a control volume discretization as described by Patankar[53]. Further details on the CFD-DEM model with verification studies are provided in the MFIX documentation[54].

4.3.4 Simulation Setup

Top-bottom mixing induced by a sawtooth feature was evaluated using CFD-DEM periodic box model simulations in the open-source code MFIX (**Figure 4.3**)[52]. The vibrating powder bed is approximated using a thin “2.5D” slice with periodic boundaries on all vertical planes (front, back, left, and right). The periodic box approach implies an infinitely long and wide chute[55]. This approximation was considered sufficient for CVR-ALD where reactor dimensions are at least hundreds of particles wide and thousands of particles long. The sawtooth baseplate was constructed by “gluing” 125-micron particles together and kinematically driving them along a sinusoidal trajectory corresponding to the reactor vibration. This glued particles approach is often used to describe boundaries in DEM that move or contain features below the CFD grid resolution[56, 57]. Baseplate particle vibration was assigned a frequency of 16 Hz and amplitudes of $0.30g$ and $0.50g$ based on typical CVR-ALD vibration conditions. Particle input files describing a sawtooth with 15-, 30-, 45-, or 60-degree inclinations and 2- or 4-mm in height were generated using a custom Matlab code. These sawtooth heights correspond to approximately 40% and 80% of the powder bed height, respectively. Where applicable, bed declinations of 3-, 6- and 9-degrees were simulated by rotating the gravity vector in MFIX. The x- and y-axes (directions i and j) in declination simulations refer to axes parallel and perpendicular to the frit surface, not the horizontal and vertical planes. By rotating the frame of reference, x-and y-values of interest such as bed convection speed can be compared directly between declined and flat simulations.

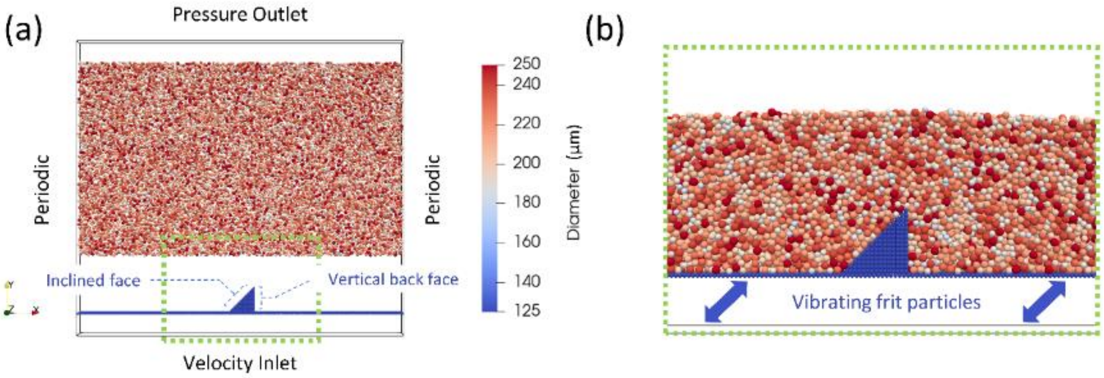

Figure 4.3. Side-view snapshots of (a) simulation initialization and (b) the zoomed-in settled bed starting condition for a typical sawtooth vibration simulation. Simulation boundary conditions and sawtooth faces are also labeled in (a)

Simulation conditions were set to the values in **Table 4.1**. At the start of each simulation, polydisperse glass particles 180-250 microns in diameter were initialized at random positions above the sawtooth. Bed particles were allowed to settle for 50 to 200 ms before the vibration intensity and declination angle were assigned. At each simulation time step, particle self-diffusivity D_{ij} and Peclet number Pe_{ij} were evaluated. Self-diffusivity was calculated using the equation $D_{ij} = (\Delta x_i - \overline{\Delta x_i})(\Delta x_j - \overline{\Delta x_j})/(2\Delta t)$ where Δx_i and Δx_j are changes in the particle position in directions i and j, respectively; $\overline{\Delta x_i}$ and $\overline{\Delta x_j}$ are changes in the mean powder position as defined by the mean bed convection speed in the i and j directions; and Δt is the DEM time step. Peclet number was determined with the equation $Pe_{ij} = \frac{\bar{u}_i L_i}{D_{ij}}$ where $\bar{u}_i$ is the average particle velocity in the i^{th} direction and L_i is the periodic box length. Further details on the equations used and simulation parameter choices can be found in the MFIX documentation[52] and our previous work[51, 58]. All simulations were conducted on the RMACC Summit supercomputer at the University of Colorado[59]. Data visualization and exploration was performed in the open-source application ParaView.

Table 4.1. Simulation inputs

Geometry	
Box width	25 mm
Box height	22.5 mm
Box depth	1.25 mm
Bed height	5 mm
Particle count	18,520-26,490
CFD grid size	0.625 mm
CFD properties	
Viscosity	18 µPa·s
Molecular weight	29 kg/kmol
DEM properties	
Mean diameter	223 µm
Material density	2500 kg/m^3
Material stiffness, bed-bed collisions	100 N/m
Material stiffness, bed-sawtooth collisions	65 N/m
Restitution coefficient, bed-bed collisions	0.97
Restitution coefficient, bed-sawtooth collisions	0.83
Friction coefficient, bed-bed collisions	0.273
Friction coefficient, bed-sawtooth collisions	0.42

4.4 Results and Discussion

4.4.1 Horizontal Mixing

Considerations specific to particle ALD reactors constrain the frit baffle designs suitable for CVR-ALD. The baseplate must be porous to allow precursor and purge gas flow. Baffle designs requiring machining techniques which plug the frit pores should be avoided.

The baffle design must also be easy to clean. Over many cycles, particle ALD baseplates become clogged with fines and must be cleaned periodically to maintain low pressure drops and high usable porosity. In general, rotating or moving parts should also be avoided; high contact pressures between the mixing surface and powder bed could result in breakage and introduce contaminants to the final product. Some powder feedstocks are more friable than others so a universal powder mixing design should minimize breakage risks.

Taking these considerations into account, principles governing the design of traditional mixing devices[20] and mixing vibratory conveyors[3, 6] were integrated into a porous frit design for CVR-ALD. Inspired by farming implements like the plough, mesh frit baffles were designed with a wedge-shaped leading edge and a sawtooth lip for splitting and layering the powder bed, respectively (**Figure 4.4**). The first design utilizes sawtooth baffles in a symmetrical zigzag or chevron profile. The second design uses alternating tetrahedron-shaped baffles with a vertical back face. It is worth noting that both frit baffle styles have a sawtooth cross-section along the powder flow direction. These “v-saws” and “tets” can also be combined in a hybrid third design (**Figure 4.4**). Each design was placed in the reactor and evaluated for mixing efficacy using tracer tests and PIV results.

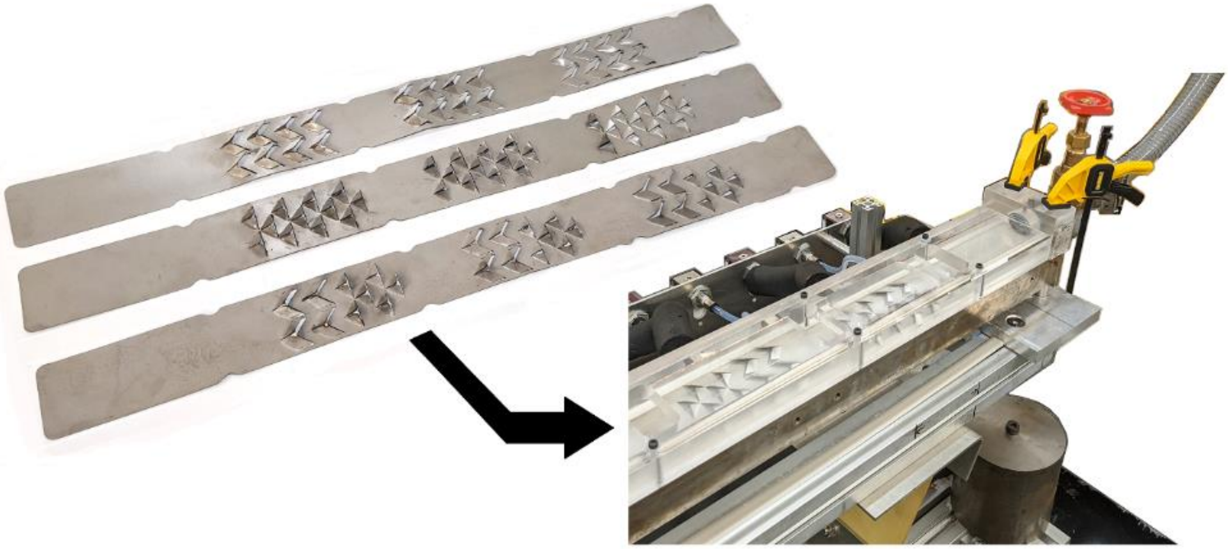

Figure 4.4. Three candidate frit geometries tested in the reactor: a frit with vee-shaped sawtooth features in a chevron pattern or “vsaws” (top), alternating tetrahedron-shaped baffles or “tets” (middle), and a hybrid of the vsaws and tets (bottom). The empty reactor (no powder) assembled with one of the frit baffle geometries is shown to the right, for reference

During vibration, large fluctuations in the instantaneous particle velocity were observed. The speed and direction of powder flow around sawtooth features varied substantially with time. As the frit extends, powder is pushed over the tips of sawtooth features and funneled through low-elevation frit zones. In the v-saws geometry, the frit centerline and outer edges form the lowest-lying areas. In the tets geometry, flat triangular gaps between the tetrahedrons facilitate flow. The hybrid design takes advantage of this behavior to funnel powder through the low regions of the v-saws into the leading edge of the tets, splitting and layering the flow multiple times per purge zone. Powder flow over each sawtooth is most pronounced towards the end of the extension stroke when the reactor is decelerating faster than the powder bed. During frit retraction, powder continues to flow over the sawtooth edge as it approaches the velocity of the conveyor.

Over many vibration cycles, a quasi-steady flow pattern emerges (**Figure 4.5**). The average velocity vector fields indicate that powder convection speed and direction change in the vicinity of a frit baffle. Velocities are high at the lip of the v-saws where bed heights are low. Particles cascading over the sawtooth edge can be seen decelerating and occasionally stagnating as they reach the deep, slow-flowing region beyond the sawtooth lip. In the tets geometry, surface velocities are highest near the leading edge of the tet baffles. Flow is diverted between tet features to form a snake-like velocity flow field. Stagnation zones can be seen near the vertical back face of the tetrahedrons. Particle velocity magnitude over and around frit baffles was observed to depend on particle size and density, but qualitative velocity trends were similar for all three powders (**Figure 4.5**).

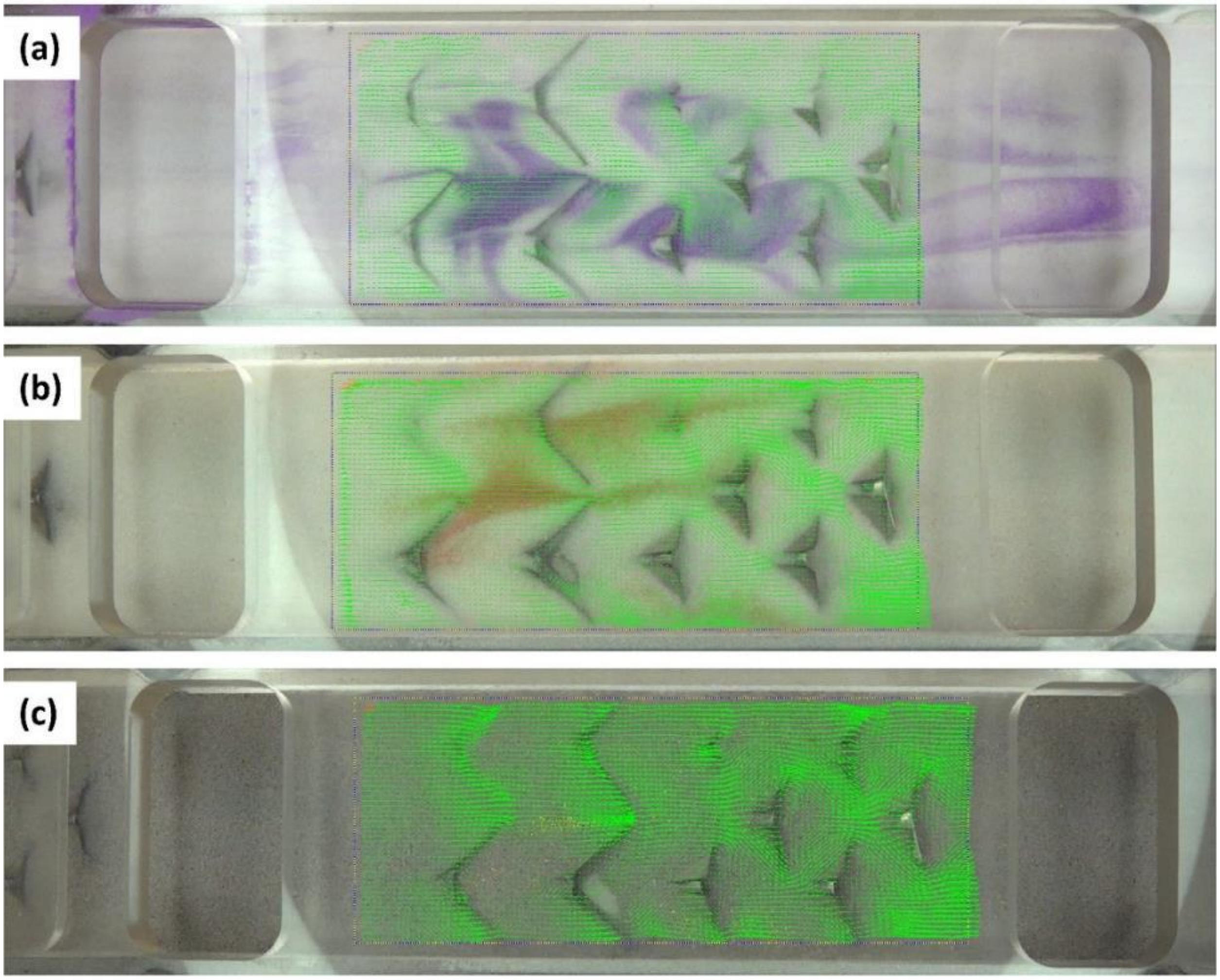

Figure 4.5. Average velocity vector fields over the hybrid frit baffles for (a) 50-micron glass, (b) 225-micron glass, and (c) 225-micron stainless steel beads at a 3-degree declination and a gas velocity of $0\ cm/s$. Mean powder convection speeds for the tests depicted are (a) 0.63, (b) 0.96 and (c) 1.41 cm/s

The enhancement in lateral powder motion with frit baffles can be visualized by comparing streamlines between the time-averaged velocity fields for each frit design (**Figure 4.6**). In the absence of frit baffles, powder flows from inlet to outlet with minimal spatial variation in frit velocity. The incorporation of v-saw baffles introduces slow-flowing regions and additional lateral motion (**Figure 4.6b**). The high velocities from inlet to outlet over sawtooth edges and low velocities between v-saw features from **Figure 4.5** can also be seen in the streamlines. The weight of the gas dosing manifold pulls asymmetrically on the reactor during vibration, leading to slightly lower streamline velocities and larger stagnation zones in the bottom half of **Figures 4.6a-6d**. The snakelike flow pattern around tetrahedron-shaped baffles can be seen in the streamlines from **Figure 4.6c**. Powder velocities are highest near the corners of each tet baffle and lowest in the stagnation zones trailing tet baffles. When both geometries are combined in the hybrid design, the streamlines follow patterns bridging the first half of **Figure 4.6b** and the second half of **Figure 4.6c** with a transition region between the v-saw and tet zones.

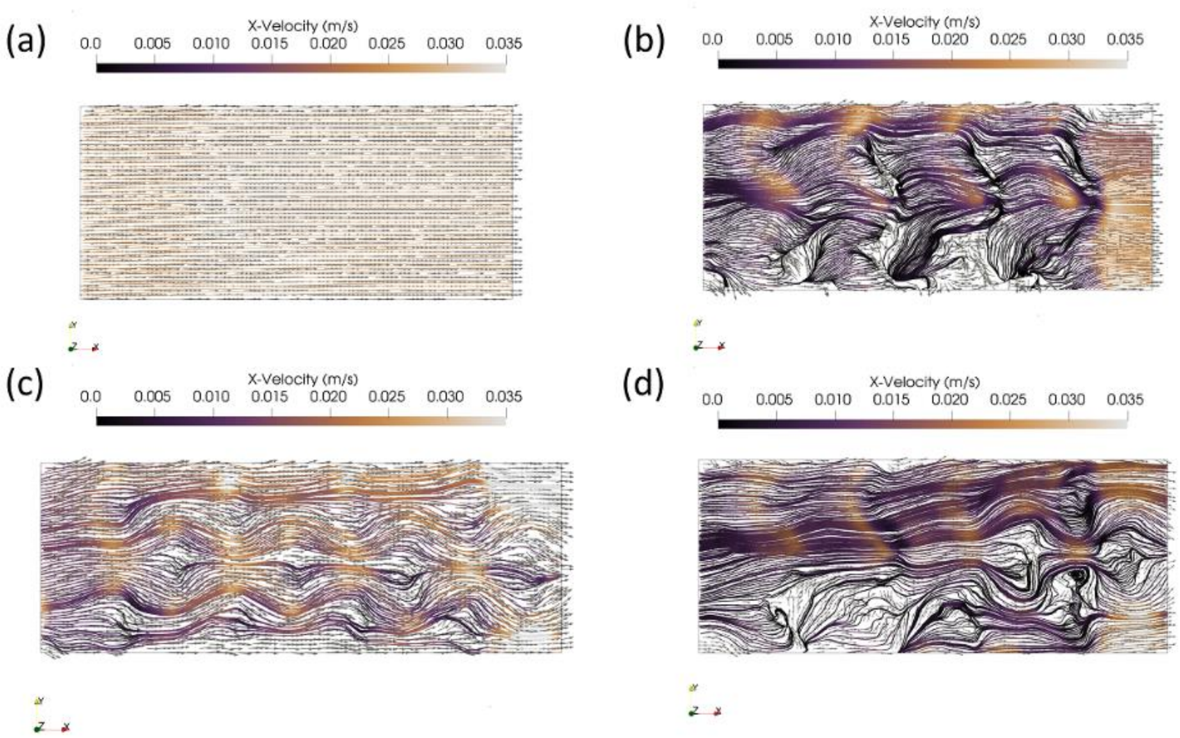

Figure 4.6. Time-averaged streamlines colored by x-velocity magnitude for (a) base case with no frit baffles, (b) v-saw baffles, (c) tet baffles and (d) hybrid baffles. Data shown is for 225-micron glass at a 3-degree declination and gas velocity of 1 cm/s

Operating conditions and frit baffle design also influence the mean convection velocity of the powder surface (**Figure 4.7**). For all three powders, mean flow over a flat or "base" frit surface is higher than powder flow in the presence of frit baffles, as expected. All else held constant, baffles constrain the motion of particles and force more tortuous, uphill paths, leading to flow velocities around 0.7-1.3 cm/s lower for 50-micron glass or 1.2-2.0 cm/s lower for 225-micron glass and stainless-steel particles. Bed heights in baffle-containing zones were around two times deeper than in baffle-free zones as fast-moving inlet particles rearrange in the slow-moving baffle zones. Gas velocity was not found to have a significant effect on powder flow velocity. Qualitative surface flow patterns did not exhibit detectable differences between no aeration ($v_g = 0\ cm/s$) and moderate aeration conditions ($v_g = 0.2\ cm/s$ for 50-micron particles or $v_g = 1\ cm/s$ for 225-micron particles). Mean powder convection velocities were also not observed to change with aeration velocity. By contrast, bed declination produced a substantial speedup effect. Increasing the angle from 0 to 3 degrees has the most effect on a flat frit design, magnifying the surface flow velocity by 0.5-0.6 cm/s for the 50-micron particles to 0.9-1.6 cm/s for the 225-micron particles. Less-pronounced speedups of 0.2-0.5 cm/s are observed in the frit baffle cases due to bed declination.

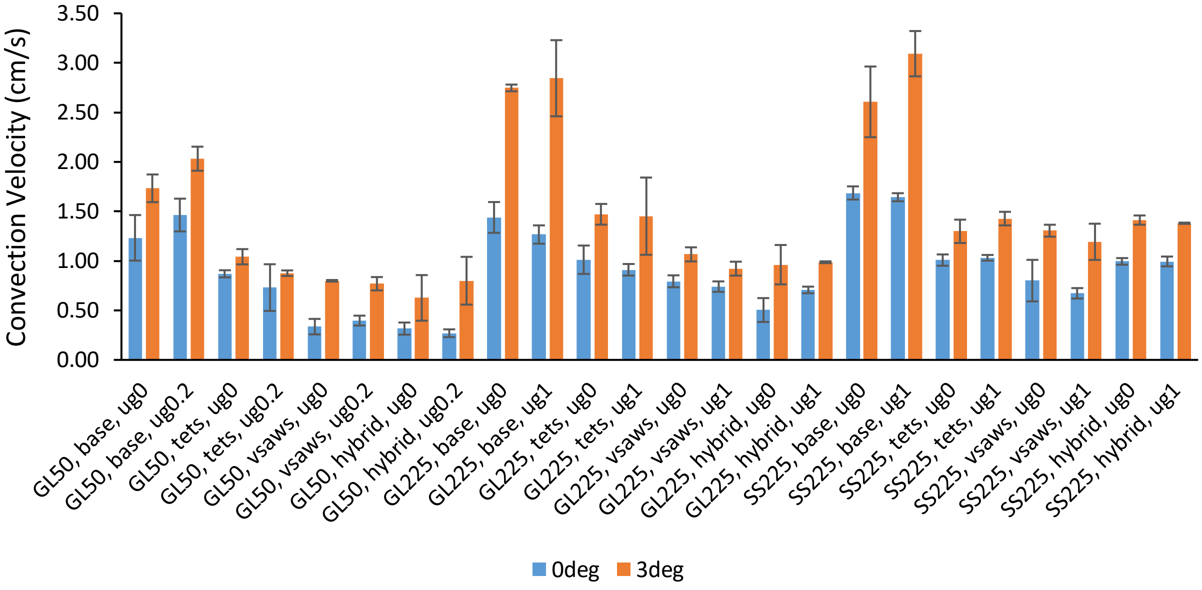

Figure 4.7. Mean convection velocity of powder surface under all tested conditions. Error bars correspond to the standard deviation from PIV analysis of three different videos at the same operating conditions

Enhanced lateral motion alone does not guarantee mixing; single-phase laminar flow through a winding channel or shearing parallel plates can be two-dimensional without inducing significant relative motion between layers of flow media. To evaluate whether the frit baffles are generating mixing, stripes of different color tracer particles were added to the powder surface (**Figure 4.8**). Stripes in the no-baffle case maintain a similar structure from inlet to outlet. Some stretching of the tracer plug can be observed along the reactor axis but boundaries between stripes of color remain sharp and straight. Color intensity is also well preserved, indicating that particles are not being displaced by neighboring undyed particles next to or beneath the dyed layer. In the tet baffle geometry, tracer powder forms serpentine patterns around flow obstructions. Some mixing occurs along the serpentine flow paths where the streams of color meet, but the outlet feed maintains substantial segregation between the orange and purple stripes. In the vsaw baffle geometry, dyed particles can be seen mixing as they pass over sawtooth features and into recirculation zones just below the sawtooth lip. The funnel zone along the bed centerline also guides the purple and orange tracer particles into mixing contact. As the bed is conveyed, the tracer particle plug becomes highly dispersed. Color intensity at the mixing outlet is substantially reduced compared to the inlet concentration. These results contrast with **Figures 4.8a** and **4.8b** where high color intensity was observed at the outlet. Additional tests with a tracer layer beneath the powder surface indicate that some top-bottom mixing is occurring during flow over a sawtooth. Buried tracer particles can be seen surfacing as the bed traverses the baffle zone. A combination of the tet baffle and vsaw baffle behaviors is seen in the hybrid geometry tests (**Figure 4.8d**). Tracer powder becomes disperse over the vsaws segment followed by mixing along the serpentine flow paths between tet baffles. Powder leaving the hybrid baffle zone appears more evenly mixed than the outlet feed from **Figures 4.8b** and **4.8c**.

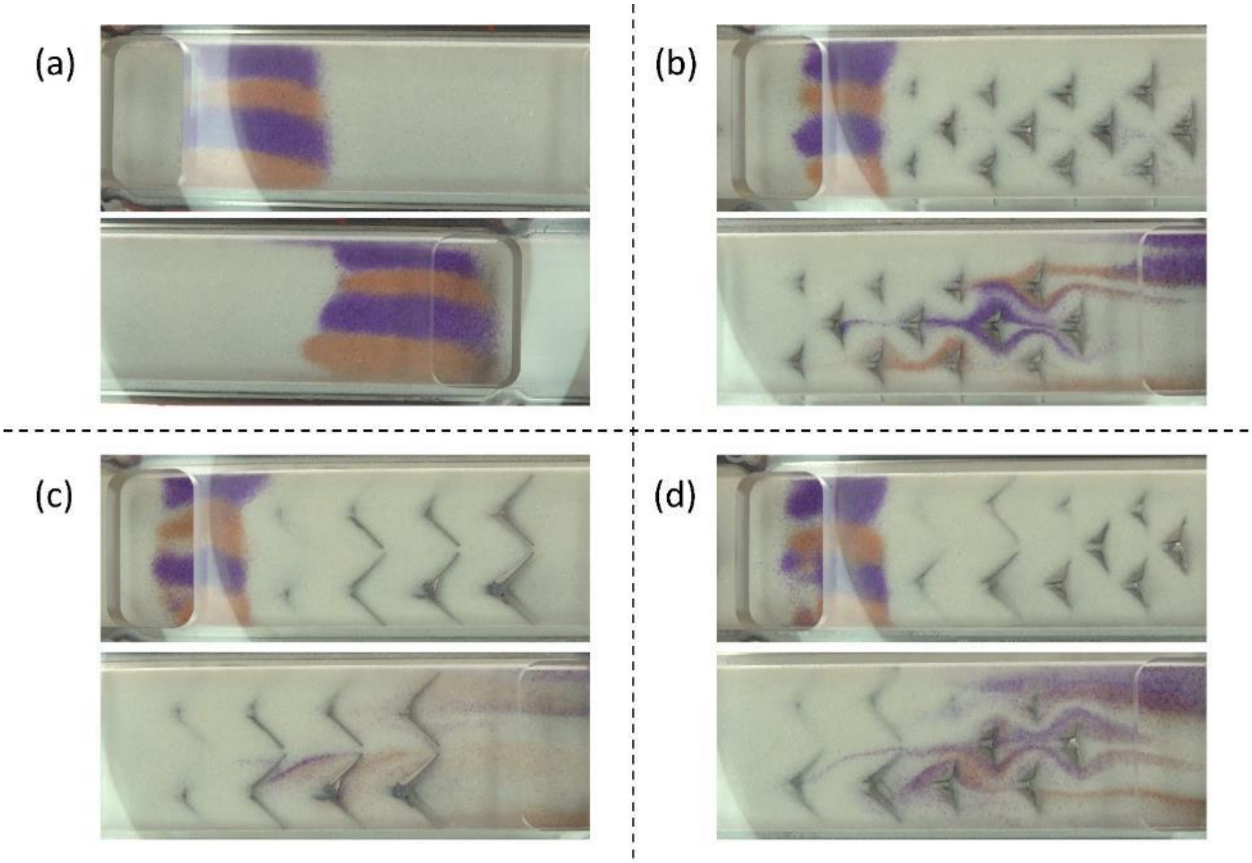

Figure 4.8. Snapshots of tracer particle mixing before (top) and after (bottom) passing over several frit baffles for (a) base case with no frit baffles, (b) tet baffles, (c) v-saw baffles, and (d) hybrid baffles. Test conditions are 225-micron glass, 3-degree declination, and a gas velocity of 1 cm/s

As previously mentioned, in both the 225-micron glass and stainless-steel bead tests, some tracer particles could be observed disappearing below the top surface of powder after passage over a sawtooth feature. The connection between dispersion of top-layer particles and top-bottom mixing cannot be easily confirmed with the PIV data. Our PIV setup only measures surface flow; details of flow through the bed depth are not resolved. Even with a particle tracking velocimetry setup, fine glass powder particles have poor edge contrast under soft lighting and are difficult to distinguish in image analysis. Rather than measuring mixing through the bed depth experimentally, vertical mixing can be explored with a particle tracking simulation technique like CFD-DEM. The following sections are devoted to better understanding top-bottom mixing in vibratory conveyors through numerical simulation.

4.4.2 Vertical Mixing, No Declination

CFD-DEM simulations were performed to investigate top-bottom mixing with and without a sawtooth flow obstruction. Previous simulations of 225-micron glass beads[58] indicate that minimal top-bottom mixing occurs in the absence of baffles under typical vibratory convection conditions (**Figure 4.9**). These results are consistent with the snapshots from **Figure 4.8a** showing poor tracer mixing over a flat frit surface. Over the time corresponding to one purge zone, horizontal layers maintain similar vertical centroids and do not mix considerably. At $\Gamma = 0.30$, self-diffusivity of the powder bed is highest in the horizontal flow direction with an average value of $D_{xx} = 1.6 \times 10^{-11}\ m^2/s$, followed by a vertical mixing rate D_{yy} around 2 times lower than D_{xx} and a D_{zz} value nearly 10 times lower than D_{xx} (**Figure 4.9a**). These self-diffusion coefficients are many orders of magnitude lower than those in mixing devices for mm-diameter particles[25, 42] and the self-diffusion of common liquids and gases at atmospheric conditions[60] which are around 1×10^{-7} to $1 \times 10^{-3}\ m^2/s$. Quantitative mixing rates increase with an increase in conveyor acceleration from $\Gamma = 0.30$ to $\Gamma = 0.50$ but all cases exhibit the qualitative lack of top-bottom mixing from **Figures 4.9b** and **4.9c**.

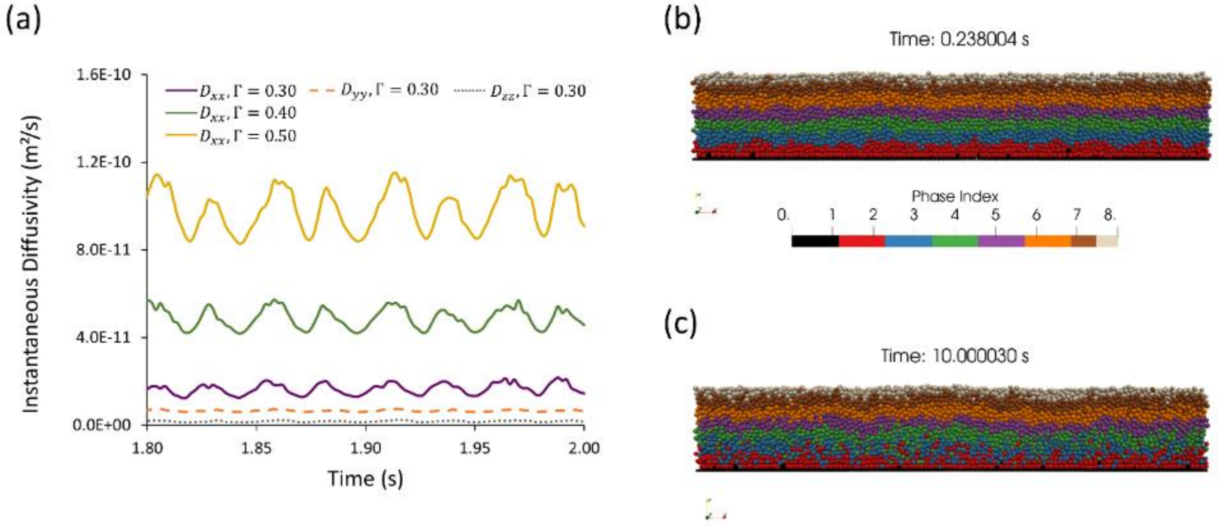

Figure 4.9. (a) Instantaneous self-diffusivity of 225-micron glass over time with no frit baffles at different acceleration conditions: $\Gamma = 0.30$, $\Gamma = 0.40$ and $\Gamma = 0.50$. (b, c) Snapshots of top-bottom mixing for $\Gamma = 0.50$ after (b) three vibration cycles and (c) 160 vibration cycles. For reference, the 225-micron glass powder bed traverses 14 cm (the length of a purge zone) in about 7 seconds when $\Gamma = 0.50$

Mixing rates can also be quantified by considering characteristic convective and diffusive time scales. When $\Gamma = 0.30$, powder travels at an average convection velocity of $0.58\ cm/s$. At this speed, powder traverses the 22.5-mm long periodic box in 3.88 seconds. It would take approximately 45 days for top-layer particles to diffuse 5 mm to the bottom of the bed with an average vertical diffusion coefficient of $D_{xx} = 6.5 \times 10^{-12}\ m^2/s$. The ratio of diffusion time to convection time is 9.9×10^5, indicating a highly convection-dominated system. When $\Gamma = 0.50$, the characteristic convection time decreases to 1.11 seconds without a substantial increase in y-diffusivity ($D_{yy} = 7.3 \times 10^{-12}\ m^2/s$). The ratio of diffusion time to convection time grows to 3.07×10^6. Baffles were incorporated to increase self-diffusion coefficients and decrease convection speeds, lowering the diffusion-convection ratio.

Vertical particle flow patterns were altered substantially in the presence of a 2-mm tall sawtooth (**Figure 4.10**). During frit extension, particles move forward with some shearing from top to bottom as in the flat frit case. When the frit retracts, particles at the bottom of the bed move back and down with the frit. A quasistatic region forms on the inclined surface of the sawtooth and near the vertical back face. The size and shape of the quasistatic region depends on the conveyor acceleration (for $\Gamma = 0.30$ to $\Gamma = 0.50$) and sawtooth angle (from 15- to 60-degrees). The topmost layer of particles flow in a heap over the falling edge of the sawtooth during frit retraction, inducing relative motion between particle layers. Falling particles fill the void formed at the sawtooth back face. Heaping wave convection continues over many vibration cycles to drive fast-flowing surface particles over slow-flowing bottom layer particles. Mixing extent advances with time but segregation persists between the top half and bottom half of the bed (**Figure 4.10d**). With this geometry, bottom-layer particles would not displace the surface layer over time scales relevant to a single purge zone (*i.e.* less than 8 seconds).

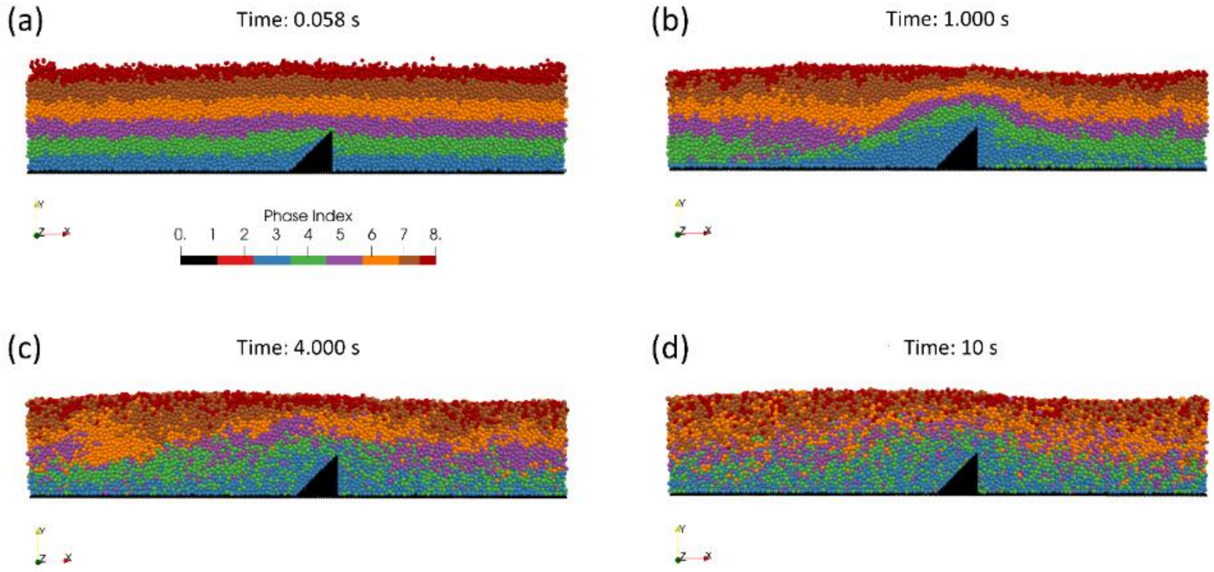

Figure 4.10. Snapshots of 225-micron powder flow over a 2-mm wide, 2-mm tall sawtooth (a) at the start of vibration and after traversing the periodic box approximately (b) one time, (c) four times, and (d) ten times. Simulation conditions include a 0-degree declination and $\Gamma = 0.50$

The 4-mm tall sawtooth features produced more exaggerated heaping convection patterns, accelerating the mixing process (**Figure 4.11**). Frit retraction pinches the thin powder surface layer, driving fast cascading flow over the sawtooth. A larger void opens at the sawtooth back face than with the 2-mm tall sawtooth. Particles flow to fill the void in a rolling pattern over the sawtooth edge. The 4-mm sawtooth provides more resistance to flow than a 2-mm sawtooth, leading to lower mean convection velocities but with higher mixing rates. After traversing the periodic box one and four times, particles exhibit greater mixing extent than over comparable traverse distances from **Figures 4.10b** and **4.10c**. Phases do not reach perfect mixedness after traversing the periodic box four times (**Figure 4.11c**). Low phase indices remain most concentrated at the bottom of the bed but are better mixed with the 4-mm sawtooth than after the same period with the 2-mm sawtooth (**Figures 4.10d** and **4.11d**).

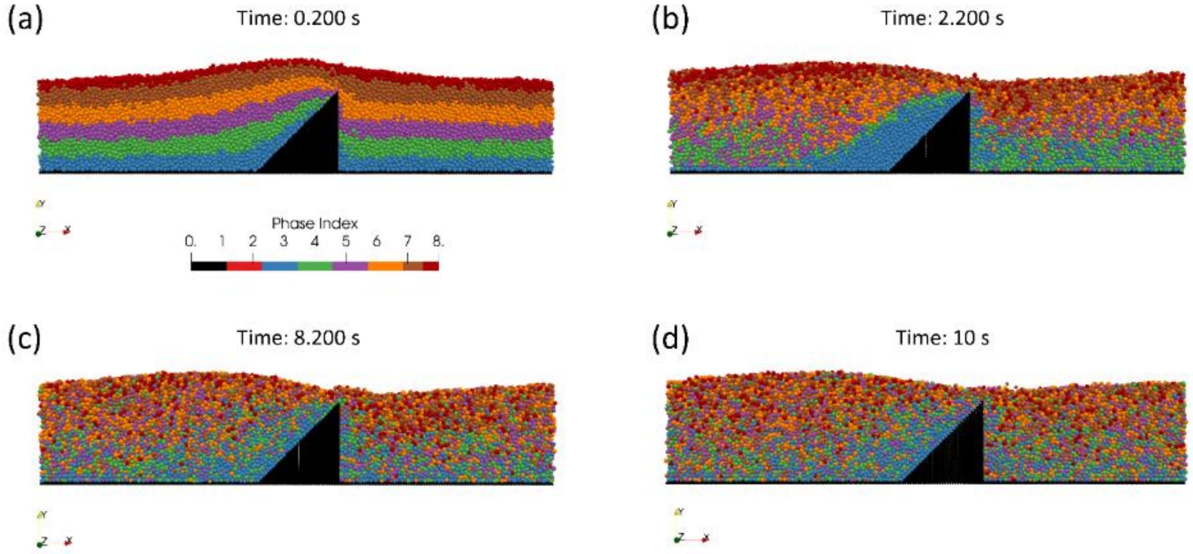

Figure 4.11. Snapshots of 225-micron powder flow over a 4-mm wide, 4-mm tall sawtooth (a) at the start of vibration, (b) after traversing the periodic box once, (c) after traversing the periodic box four

times, and (d) at ten seconds for direct comparison to **Figure 4.10d**. Simulation conditions include a 0-degree declination and $\Gamma = 0.50$

For both 2-mm tall and 4-mm tall sawtooth features, sawtooth angles between 15 and 60 degrees were not observed to significantly alter the extent or rate of mixing (**Table 4.2**). 2-mm sawtooth features exhibited horizontal mixing diffusivities between $4.2 \times 10^{-10}\ m^2/s$ and $4.7 \times 10^{-10}\ m^2/s$ with vertical mixing diffusivities between $9.5 \times 10^{-11}\ m^2/s$ and $9.9 \times 10^{-11}\ m^2/s$. Sawtooth height had a larger effect on mixing than sawtooth width in the range investigated with a 1.25x average magnitude increase in D_{xx} and a 2.3x average magnitude increase in D_{yy}. All 4-mm sawtooth features between 15 and 60 degrees in declination produced more mixing after 10 seconds than any of the 2-mm sawtooth features. For some of the steepest sawtooth features (*i.e.* 60-degree inclination angle), larger quasistatic regions appeared along the inclined surface of the sawtooth, particularly at low conveyor accelerations. Heap and void formation during frit retraction were less severe for shallow sawtooth features (*i.e.,* 15-degree inclination angle) but the same mixing patterns and primary flow features discussed with **Figures 4.10** and **4.11** were retained for all sawtooth angles. Unless otherwise noted, subsequent discussions refer to sawtooth features with a 45-degree declination only (*i.e.,* 2-mm tall and 2-mm wide or 4-mm tall and 4-mm wide only).

Table 4.2. Average self-diffusivities in the horizontal (D_{xx}) and vertical (D_{yy}) directions for different geometries with 0-degree bed declination and $\Gamma = 0.50$. The first and second number indicate height and width, respectively ($h2w3.46$ means a 2-mm tall, 3.46-mm wide sawtooth)

D_{xx} (m^2/s)						
$h2w1.15$	$h2w2$	$h2w3.46$	$h2w7.46$	$h4w2.31$	$h4w4$	$h4w6.93$
4.68×10^{-10}	4.19×10^{-10}	4.46×10^{-10}	4.77×10^{-10}	5.82×10^{-10}	5.32×10^{-10}	5.83×10^{-10}
D_{yy} (m^2/s)						
$h2w1.15$	$h2w2$	$h2w3.46$	$h2w7.46$	$h4w2.31$	$h4w4$	$h4w6.93$

9.94×10^{-11}	9.66×10^{-11}	9.92×10^{-11}	9.50×10^{-11}	2.24×10^{-10}	2.38×10^{-10}	2.13×10^{-10}

The most notable changes in powder mixing with lower accelerations were lower convective powder transport rates and enhanced interlayer diffusion (**Figure 4.12**). It takes around 9.8 seconds after vibration has commenced with a conveyor acceleration of $\Gamma = 0.30$ to transport powder an average distance of 15 mm over a 4-mm tall sawtooth. The same average distance is covered in 1.4 seconds with a conveyor acceleration of $\Gamma = 0.50$. Interfaces between powder layers after passage over the sawtooth edge are less sharp in the low-acceleration case, indicating more boundary diffusion. The quasistatic layer along the inclined sawtooth face is also larger at lower accelerations. The number of particles with enough energy to climb the sawtooth decreases when $\Gamma = 0.30$ compared to when $\Gamma = 0.50$. If lower convection speeds can be tolerated, low accelerations can be used to enhance diffusive mixing at the expense of larger “frozen” powder zones on the inclined sawtooth face.

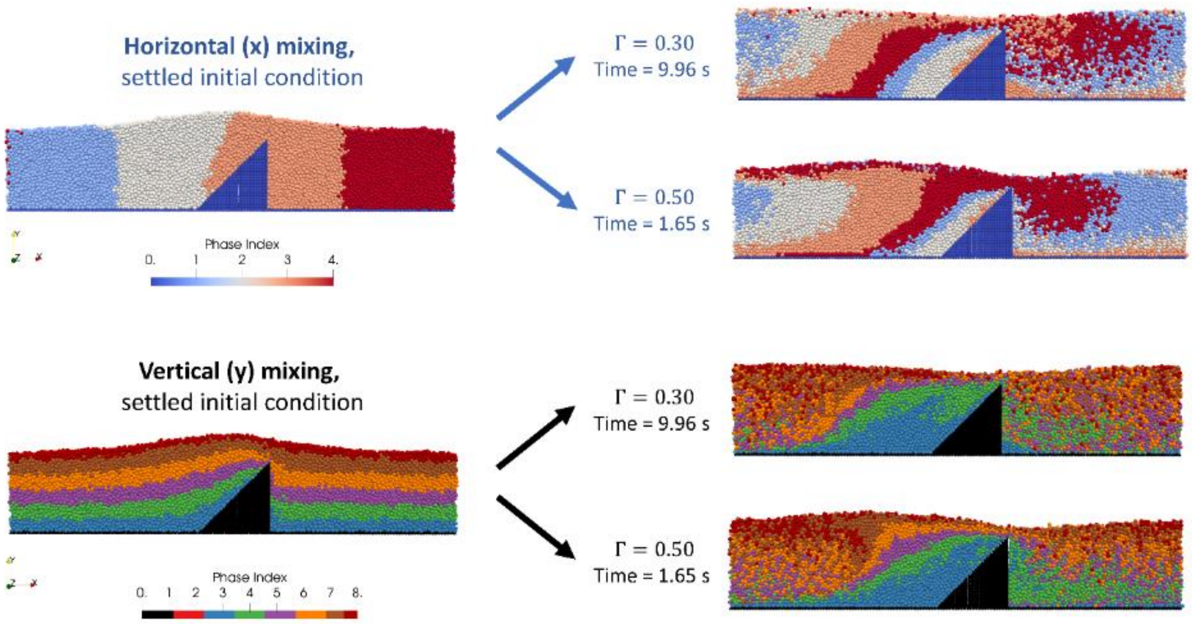

Figure 4.12. Snapshots of 225-micron powder flow over a 4-mm-tall sawtooth at a low acceleration (Γ = 0.30) and a high acceleration (Γ = 0.50). Particles are colored in vertical and horizontal stripes to highlight self-similar mixing patterns at low and high accelerations

4.4.3 Vertical Mixing, Declined Plane

All previous simulations have focused on powder flow over a sawtooth on a horizontal baseplate (0-degree frit declination). Conveyor declination may be used in applications where a maximum acceleration of Γ = 0.50 is not sufficient to transport powder. To determine whether conveyor declination affects the mixing process, simulations were performed at several declination angles. Mixing extent improved with an increase in declination angle up to 9 degrees (**Figure 4.13**). Higher angles contribute to a larger void space along the sawtooth back face during frit retraction and a faster flowing top layer which penetrates deeper into the powder bed after passing over the sawtooth edge. Particles rush to fill the larger triangular void and form a zigzag pattern over many vibration cycles as shown in **Figure 4.13b**. Over time, top layer particles pierce through the bottom layer, leading to higher mixing extents with a 9-degree declination angle than a 0-degree declination angle (**Figure 4.10d**). As in the no declination case, flow over a 2-mm sawtooth was not as well mixed as with the 4-mm sawtooth at a 9-degree declination. Some top-bottom segregation remained even after ten seconds of vibration.

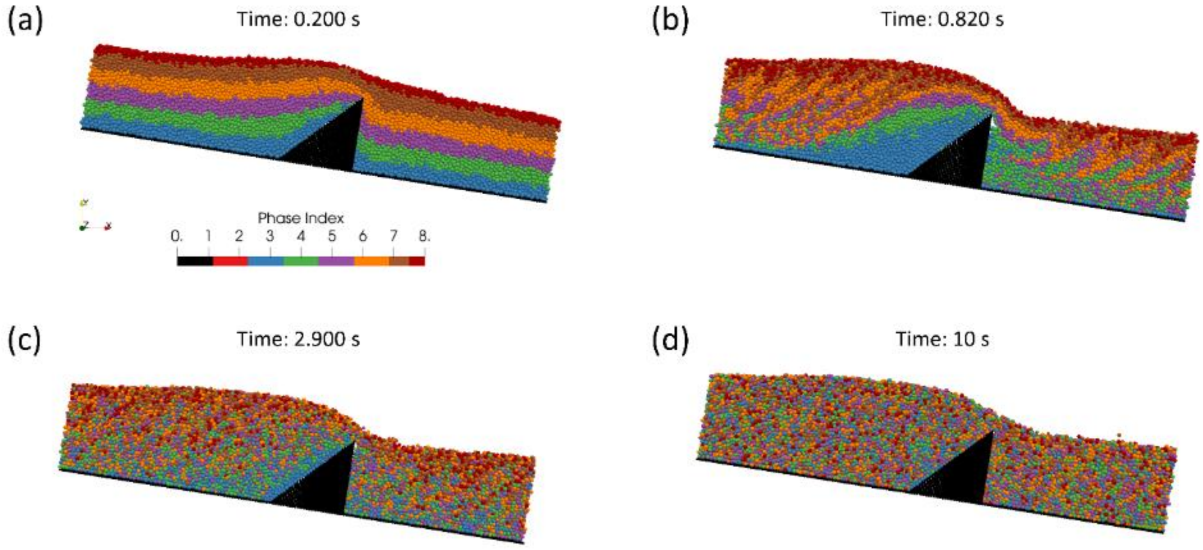

Figure 4.13. Snapshots of 225-micron powder flow over a 4-mm wide, 4-mm tall sawtooth with a 9-degree decline (a) at the start of vibration, (b) after traversing the periodic box approximately once, (c) after traversing the periodic box approximately four times, and (d) at ten seconds for mixing rate comparison with **Figures 4.10d** and **4.11d**. Simulation were performed with $\Gamma = 0.50$

Mixing rate changes with declination angle can be quantified by comparing self-diffusivity coefficients (**Figure 4.14**). Self-diffusivity values increased with the incorporation of frit baffles by around 5x for D_{xx} with a 2-mm sawtooth when $\Gamma = 0.50$ to as much as 37x for D_{yy} with a 4-mm sawtooth when $\Gamma = 0.50$. The most noticeable change in the visualizations of simulation phase index occurs for vertical mixing. Without frit baffles, the improvement in D_{yy} when $\Gamma = 0.50$ from $7.3 \times 10^{-12}\ m^2/s$ at a 0-degree declination to $1.2 \times 10^{-11}\ m^2/s$ at a 9-degree declination does not result in noticeable improvements to top-bottom mixing. As in **Figure 4.9c**, the bottommost powder layers exhibit some mixing but horizontal layers in the top half of the powder bed maintain distinct boundaries between phase indices. In all cases, self-diffusion coefficients were higher for flow over a 4-mm tall sawtooth than over a 2-mm tall sawtooth, aligning with the improved top-bottom mixing observations from the simulation visualizations.

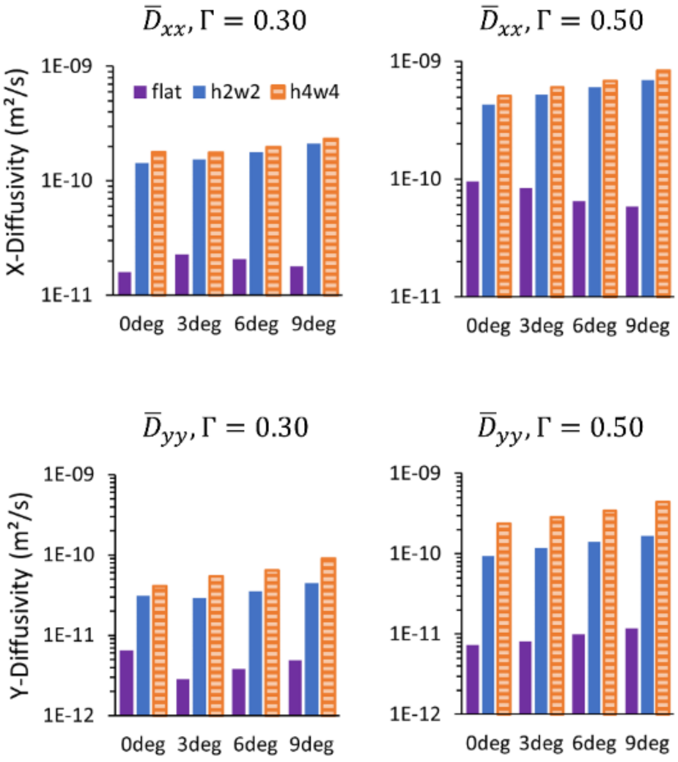

Figure 4.14. Average self-diffusivity in the horizontal direction (D_{xx}) and the vertical direction (D_{yy}) for conveyor declinations from 0 degrees to 9 degrees and three frit geometries: a baffle-free frit (flat), a 2-mm tall, 2-mm wide sawtooth (h2w2), and a 4-mm tall, 4-mm wide sawtooth (h4w4)

When considering a mixing enhancement for particle ALD, the potential impact on coating behavior must also be examined. Convection velocity influences the particle residence time in a continuous flow reactor. High horizontal velocities indicate lower residence times. As conveyor declination increased from 0 degrees to 9 degrees, mean convection velocities increased from 2.1 to 4.7 cm/s over the 2-mm sawtooth and from 1.0 to 3.0 cm/s over the 4-mm sawtooth when $\Gamma = 0.50$. Increased declination angles also broaden the particle velocity distribution (**Figure 4.15**). Particles on the powder bed surface travel faster than particles in contact with the frit. At the end of frit retraction, gravity pulls particles over the sawtooth edge and down the 9-degree declined frit (**Figure 4.15c**). In the 0-degree declination case, gravity acts perpendicular to the frit surface and particles decelerate with the frit rather than continuing to flow. The x-velocity gradient through the bed thickness grows at steeper declinations.

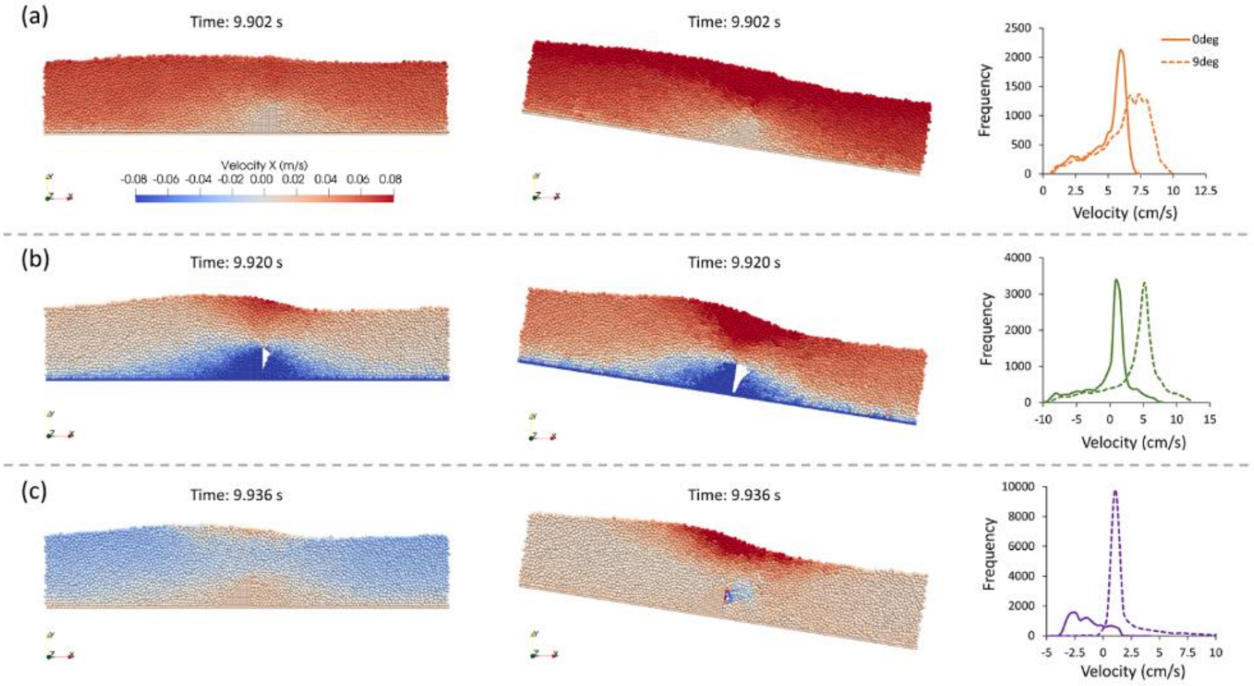

Figure 4.15. Instantaneous particle velocities over a 2-mm tall, 2-mm wide sawtooth with no declination (left) and 9-degree declination (center) at several representative times: (a) the start of retraction, when $t = 9.902s$; (b) the middle of retraction, when $t = 9.920s$; and (c) the end of retraction, when $t = 9.936s$. Horizontal velocity histograms are also shown (right) to highlight the enhanced shearing effect due to declination angle

Residence time distributions were also analyzed by tracking the average time for each particle to traverse the periodic box over many vibration cycles (**Figure 4.16b**). Several trajectories are shown for sample particles traveling over the 2-mm sawtooth with a 9-degree declination at $\Gamma = 0.50$ (**Figure 4.16a**). Particle residence times were characterized by unimodal distributions with a long tail towards high residence times for slow-moving bottom-layer particles (**Figure 4.16b**). Bed surface particles traverse the periodic box fastest while some particles stagnate or even travel backwards over several vibration cycles, particularly at low accelerations and close to the inclination surface of steep sawtooth features. As declination angle increased, mean residence time decreased for both the 2-mm sawtooth and the 4-mm sawtooth (**Figure 4.16b**). From a 0-degree declination to a 9-degree declination, the average residence time decreased from 1.3 ms to 0.6 ms over the 2-mm sawtooth. The standard deviation of the distribution also decreased from 0.6 to 0.3 ms for the 2-mm sawtooth. Fewer particles stagnate over the inclined sawtooth surface with increased declination angle, leading to tighter residence time distributions. Larger declinations angles also allow top-layer particles to penetrate bottom-layer particles more effectively and prevent residence time segregation between top-layer and bottom-layer particles. Similar residence time trends were observed in the 4-mm sawtooth simulations for $\Gamma = 0.50$ but with higher standard deviations and mean residence times (**Figure 4.16b**). An increase in declination angle from 0 degrees to 9 degrees lowered the mean residence time from 2.1 ms to 0.9 ms and the standard deviation from 0.9 ms to 0.5 ms.

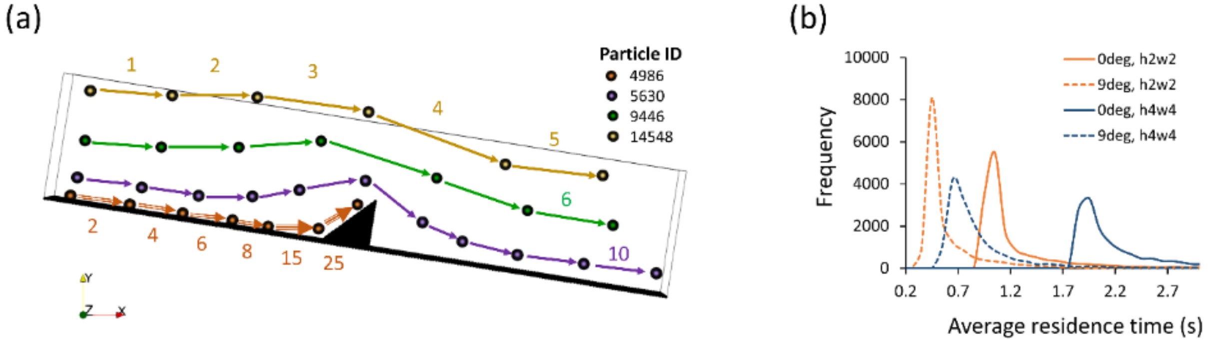

Figure 4.16. (a) Four sample particle trajectories were tracked for up to 25 vibration cycles with $\Gamma = 0.50$ over a 2-mm sawtooth and a 9-degree declination. Arrows mark interpolated travel paths between vibration cycles. Box outline shows the average bounds of the powder bed. Arrow labels indicate the number of vibration cycles since the beginning of tracking at $t = 8.238\,s$. (b) Residence time distributions at $t = 8.000\,s$ for two different declination angles (0 degrees, 9 degrees) and two sawtooth geometries (2-mm tall, 2-mm wide and 4-mm tall, 4-mm wide)

4.5 Conclusions

The mixing quality of vibrating powder flow over frit baffles in a CVR-ALD reactor was evaluated using PIV analysis and CFD-DEM simulations. PIV provided details on the surface flow characteristics of vibratory powder convection over 3D frit baffle shapes. CFD-DEM simulations enabled particle tracking and top-bottom flow visualization over simple sawtooth baffles. The effects of particle size, baffle shape, baffle size, gas velocity, and bed declination angle on the mixing process were investigated. Key findings in this study are summarized below.

- All three baffle designs were observed to promote mixing relative to a flat, baffle-free conveyor surface. The tetrahedron-shaped baffles diverted flow around wedge-shaped obstructions, leading to enhanced lateral motion. The v-saw baffles promoted top-bottom mixing by forcing flow over a sawtooth-shaped drop-off, causing particles to cascade in a rolling wave and mix from top to bottom. The hybrid geometry combined these features to give high rates of vertical and horizontal mixing.

- Some parameters did not significantly impact powder flow behavior over the ranges tested. In the PIV experiments, gas velocities of 0 and 0.2 cm/s for 50-micron particles or 0 and 1 cm/s for 225-micron particles produced the same mean powder convection velocities. Serpentine flow patterns around tet baffles and cascading powder flow over v-saw baffles shared the same qualitative features for 50-micron glass, 225-micron glass and 225-micron stainless-steel beads. In the CFD-DEM simulations, sawtooth angles between 15 and 60 degrees gave similar top-bottom mixing extents.
- Bed declination was observed to improve mixing extent and broaden the instantaneous particle velocity distribution during frit retraction. The highest mixing rate was achieved over a 4-mm wide, 4-mm tall baffle with a 9-degree bed declination and vibration acceleration of $\Gamma = 0.50$. Longer purge zones could be designed to accommodate a minimum residence time for declined beds.

Acknowledgements

The authors are grateful for the financial support provided by the National Science Foundation GOALI program [award #1852824]. This work utilized the RMACC Summit supercomputer, which is supported by the National Science Foundation (awards ACI-1532235 and ACI-1532236), the University of Colorado Boulder, and Colorado State University. The Summit supercomputer is a joint effort of the University of Colorado Boulder and Colorado State University. The authors also thank Alex Weaver and Dragan Meijic for mesh frit manufacturing suggestions and Professor Richard Lueptow at Northwestern University for general advice on powder mixing.

References

[1] J.F. Sullivan, J.D. White, Apparatus and method for conveying material, Google Patents, 1988.

[2] R.W. Evans, J.M. Morris, Method and apparatus for moving pulverulent materials, Google Patents, 1962.

[3] J.R.M. Carrier, Conveyor for mixing and de-aerating, Google Patents, 1958.

[4] E.A. Wahl, Vibratory conveyor-mixer apparatus, Google Patents, 1967.

[5] R.A. Krynock, Vibratory blender/conveyor, Google Patents, 1993.

[6] R.L. Opila, A.P. Oleson, Method for modifying a carbohydrate material, Google Patents, 1963.

[7] R.W. Evans, Means for aerating granular and pulverulent materials, Google Patents, 1963.

[8] J.R.M. Carrier, J.M. Morris, De-aerating conveyor, Google Patents, 1956.

[9] T. Tupolskikh, N. Gucheva, O. Kirishiev, Simulation of the process of movement of bulk material in a vibrating conveyor-mixer, MATEC Web of Conferences, EDP Sciences, 2018, pp. 05021.

[10] E. Simsek, S. Wirtz, V. Scherer, H. Kruggel-Emden, R. Grochowski, P. Walzel, An experimental and numerical study of transversal dispersion of granular material on a vibrating conveyor, Particulate Science and Technology, 26 (2008) 177-196.

[11] I.J.A. Spencer, R.A. Hall, Continuous spatial atomic layer deposition process and apparatus for applying films on particles, Google Patents, 2018.

[12] A.W. Weimer, Particle atomic layer deposition, Journal of Nanoparticle Research, 21 (2019) 9.

[13] D. Valdesueiro, H. Hettinga, J.P. Drijfhout, P. Lips, G.M. Meesters, M.T. Kreutzer, J.R. Van Ommen, Tuning roughness and gloss of powder coating paint by encapsulating the coating particles with thin Al2O3 films, Powder Technology, 318 (2017) 401-410.

[14] M. Tahmasebpoor, L. de Martín, M. Talebi, N. Mostoufi, J.R. van Ommen, The role of the hydrogen bond in dense nanoparticle–gas suspensions, Physical Chemistry Chemical Physics, 15 (2013) 5788-5793.

[15] C. Hirschberg, N.S. Jensen, J. Boetker, A.Ø. Madsen, T.O. Kääriäinen, M.-L. Kääriäinen, P. Hoppu, S.M. George, M. Murtomaa, C.C. Sun, Improving Powder Characteristics by Surface Modification Using Atomic Layer Deposition, Organic Process Research & Development, 23 (2019) 2362-2368.

[16] L.F. Hakim, J.L. Portman, M.D. Casper, A.W. Weimer, Aggregation behavior of nanoparticles in fluidized beds, Powder Technology, 160 (2005) 149-160.

[17] D. Brone, C. Wightman, K. Connor, A. Alexander, F. Muzzio, P. Robinson, Using flow perturbations to enhance mixing of dry powders in V-blenders, Powder Technology, 91 (1997) 165-172.

[18] M. Jiang, Y. Zhao, G. Liu, J. Zheng, Enhancing mixing of particles by baffles in a rotating drum mixer, Particuology, 9 (2011) 270-278.

[19] M. Poux, P. Fayolle, J. Bertrand, D. Bridoux, J. Bousquet, Powder mixing: some practical rules applied to agitated systems, Powder Technology, 68 (1991) 213-234.

[20] J. Duran, Sands, powders, and grains: an introduction to the physics of granular materials, Springer Science & Business Media2012.

[21] P.B. Umbanhowar, R.M. Lueptow, J.M. Ottino, Modeling segregation in granular flows, Annual Review of Chemical and Biomolecular Engineering, 10 (2019) 129-153.

[22] S.S. Weidenbaum, Mixing of solids, Advances in Chemical Engineering, Elsevier1958, pp. 209-324.

[23] M. Halidan, G.R. Chandratilleke, K. Dong, A. Yu, The effect of interparticle cohesion on powder mixing in a ribbon mixer, AIChE Journal, 62 (2016) 1023-1037.

[24] A. Elajnaf, P. Carter, G. Rowley, Electrostatic characterisation of inhaled powders: effect of contact surface and relative humidity, European journal of pharmaceutical sciences, 29 (2006) 375-384.

[25] B. Remy, B.J. Glasser, J.G. Khinast, The effect of mixer properties and fill level on granular flow in a bladed mixer, AIChE journal, 56 (2010) 336-353.

[26] D. Cahn, T. Healy, D. Fuerstenau, Blender geometry in mixing of solids, Industrial & Engineering Chemistry Process Design and Development, 4 (1965) 318-322.
[27] G.R. Chandratilleke, Y. Zhou, A. Yu, J. Bridgwater, Effect of blade speed on granular flow and mixing in a cylindrical mixer, Industrial & engineering chemistry research, 49 (2010) 5467-5478.
[28] K. Hashemnia, S. Pourandi, Study the effect of vibration frequency and amplitude on the quality of fluidization of a vibrated granular flow using discrete element method, Powder technology, 327 (2018) 335-345.
[29] J.N. Staniforth, Determination and handling of total mixes in pharmaceutical systems, Powder Technology, 33 (1982) 147-159.
[30] J. Ottino, D. Khakhar, Mixing and segregation of granular materials, Annual review of fluid mechanics, 32 (2000) 55-91.
[31] J. Bridgwater, Fundamental powder mixing mechanisms, Powder Technology, 15 (1976) 215-236.
[32] P.M.C. Lacey, Developments in the theory of particle mixing, Journal of applied chemistry, 4 (1954) 257-268.
[33] L. Fan, S. Chen, C. Watson, Annual review solids mixing, Industrial & Engineering Chemistry, 62 (1970) 53-69.
[34] L. Fan, Y.-M. Chen, F. Lai, Recent developments in solids mixing, Powder Technology, 61 (1990) 255-287.
[35] F. Boukouvala, Y. Gao, F. Muzzio, M.G. Ierapetritou, Reduced-order discrete element method modeling, Chemical Engineering Science, 95 (2013) 12-26.
[36] G.R. Chandratilleke, A. Yu, J. Bridgwater, K. Shinohara, A particle-scale index in the quantification of mixing of particles, AIChE Journal, 58 (2012) 1099-1118.
[37] H. Kruggel-Emden, E. Simsek, S. Wirtz, V. Scherer, A comparative numerical study of particle mixing on different grate designs through the discrete element method, Journal of Pressure Vessel Technology, 129 (2007) 593-600.
[38] B. Asmar, P. Langston, A. Matchett, A generalised mixing index in distinct element method simulation of vibrated particulate beds, Granular Matter, 4 (2002) 129-138.
[39] Y. Akao, H. Kunisawa, L. Fan, F. Lai, R. Wang, Degree of mixedness and contact number A study on the mixture of particulate solids and the structure of solid mixtures, Powder technology, 15 (1976) 267-277.
[40] P. Bhalode, M. Ierapetritou, A review of existing mixing indices in solid-based continuous blending operations, Powder Technology, 373 (2020) 195-209.
[41] P.M. Portillo, M.G. Ierapetritou, F.J. Muzzio, Characterization of continuous convective powder mixing processes, Powder Technology, 182 (2008) 368-378.
[42] A. Yaraghi, M. Ebrahimi, F. Ein-Mozaffari, A. Lohi, Mixing assessment of non-cohesive particles in a paddle mixer through experiments and discrete element method (DEM), Advanced Powder Technology, 29 (2018) 2693-2706.
[43] Y. Zhang, E.W.C. Lim, C.-H. Wang, Pneumatic transport of granular materials in an inclined conveying pipe: Comparison of computational fluid dynamics− discrete element method (CFD− DEM), electrical capacitance tomography (ECT), and particle image Velocimetry (PIV) results, Industrial & engineering chemistry research, 46 (2007) 6066-6083.
[44] W. Thielicke, The flapping flight of birds, Diss. University of Groningen, (2014).
[45] W. Thielicke, E. Stamhuis, PIVlab–towards user-friendly, affordable and accurate digital particle image velocimetry in MATLAB, Journal of open research software, 2 (2014).
[46] M.J. Sandlin, Experimental verification of numerical models of granular flow through wire mesh screens, Georgia Institute of Technology, 2017.

[47] L. Sarno, A. Carravetta, Y.C. Tai, R. Martino, M.N. Papa, C.Y. Kuo, Measuring the velocity fields of granular flows – Employment of a multi-pass two-dimensional particle image velocimetry (2D-PIV) approach, Advanced Powder Technology, 29 (2018) 3107-3123.
[48] D. Mori, G. Ishigami, Excavation model of soil sampling device based on particle image velocimetry, Journal of Terramechanics, 62 (2015) 19-29.
[49] T. Hagemeier, M. Börner, A. Bück, E. Tsotsas, A comparative study on optical techniques for the estimation of granular flow velocities, Chemical Engineering Science, 131 (2015) 63-75.
[50] Y. Tsuji, T. Tanaka, T. Ishida, Lagrangian numerical simulation of plug flow of cohesionless particles in a horizontal pipe, Powder technology, 71 (1992) 239-250.
[51] J. Hartig, H.C. Howard, T.J. Stelmach, A.W. Weimer, DEM modeling of fine powder convection in a continuous vibrating bed reactor, Powder Technology, (2021).
[52] M. Syamlal, W. Rogers, T.J. OBrien, MFIX documentation theory guide, USDOE Morgantown Energy Technology Center, WV (United States), 1993.
[53] S.V. Patankar, Numerical heat transfer and fluid flow, CRC press2018.
[54] R. Garg, J. Galvin, T. Li, S. Pannala, Open-source MFIX-DEM software for gas–solids flows: Part I—Verification studies, Powder Technology, 220 (2012) 122-137.
[55] L.E. Silbert, D. Ertaş, G.S. Grest, T.C. Halsey, D. Levine, S.J. Plimpton, Granular flow down an inclined plane: Bagnold scaling and rheology, Physical Review E, 64 (2001) 051302.
[56] C.S. Campbell, Boundary interactions for two-dimensional granular flows. Part 2. Roughened boundaries, Journal of Fluid Mechanics, 247 (1993) 137-156.
[57] Y. Chung, H. Liao, S. Hsiau, Convection behavior of non-spherical particles in a vibrating bed: Discrete element modeling and experimental validation, Powder technology, 237 (2013) 53-66.
[58] J. Hartig, A. Shetty, D.R. Conklin, A.W. Weimer, Aeration and cohesive effects on flowability in a vibrating powder conveyor, Powder Technology, 408 (2022) 117724.
[59] J. Anderson, P.J. Burns, D. Milroy, P. Ruprecht, T. Hauser, H.J. Siegel, Deploying RMACC Summit: an HPC resource for the Rocky Mountain region, Proceedings of the Practice and Experience in Advanced Research Computing 2017 on Sustainability, Success and Impact2017, pp. 1-7.
[60] R.C. Reid, J.M. Prausnitz, B.E. Poling, The properties of gases and liquids, (1987).

CHAPTER 5

A MOVING POROUS MEDIA MODEL

5.1 Abstract

A moving porous media (MPM) modeling methodology was developed for reactor-scale CFD simulations of continuous spatial particle ALD. The continuous vibrating reactor process for particle atomic layer deposition (CVR-ALD) is modeled by treating the powder bed as a porous media which conveys as a sliding and layering dynamic mesh zone inside the vibrating reactor zone. Candidate porous reactor baseplates were experimentally characterized using x-ray computed tomography (XRCT), porometry, porosimetry, and atomic force microscopy (AFM) before permeabilities from flow tests were used as inputs to the MPM model. Parameter sweeps over vibration magnitude, powder bed convection speed, and precursor mass fraction revealed the dependence of surface titration uniformity and residual gas breakthrough on operating conditions and powder properties. Parasitic chemical vapor deposition (CVD) reactions were observed in the first precursor zone when dose start times and inlet gas compositions were not optimized.

5.2 Introduction

Atomic layer deposition (ALD) is a coating technique used to produce thin films with atomic-level thickness control. In ALD, self-limited reactions between the substrate surface and gaseous precursors enable the synthesis of highly conformal and precise nanofilms. Simulations and modeling from the atomic level to the continuum scale have contributed to our multiscale understanding of the behavior inside ALD reactors. Investigations into the atomic and mesoscales include density functional theory (DFT) and molecular dynamics simulations[1], growth mode deposition models[2], and ballistic transport models[3]. Monte Carlo methods discretize the surface to be coated and use probabilistic trajectories to identify reaction sites and track surface coverage[4, 5]. Continuum models for deposition provide clarity on the reactive transport of species to and from the substrate surface. These vary in complexity from solving the diffusion equation with surface reactions[6, 7] to highly coupled computational fluid dynamics (CFD) solvers of the reactor cavity[8-15]. Reaction kinetic expressions may be derived from Langmuir's equation[7, 16], kinetic theory[17] or kinetic Monte Carlo models[10, 18]. Physics-based analytical expressions have also been developed to describe spatial atomic layer deposition on moving substrates[19, 20].

Particle ALD refers to an ALD film on a particle substrate and uses different reactor configurations than the systems from existing CFD modeling studies on planar substrates. ALD films can be deposited on batches of particles using fixed-bed[21], fluidized-bed[22], or rotary-drum[23, 24] reactors. In high-throughput manufacturing environments, continuous particle processing methods have also been employed[25, 26]. A continuous vibrating reactor for spatial particle atomic layer deposition (CVR-ALD)[27] was recently developed for large-scale particle ALD. CVR-ALD reactors use linear vibration to continuously transport particles through alternating regions of inert purge gas and dilute precursor in a carrier gas. Purge zones are needed to prevent precursor gases from coming into contact and forming solid nanoparticles through chemical vapor deposition (CVD) reactions, which may deposit on the substrate to produce porous, non-self-limited films. Vibration is known to promote gas-solid contact and film uniformity in batch particle ALD systems[28] but its effect on the gas-phase diffusion of dilute ALD precursors through an inert carrier gas has not yet been quantified. Non-self-limited CVD reactions between precursor gases become more difficult to avoid during concurrent dosing and will depend on diffusion extent of the ALD precursor front.

Capital cost and desired operating conditions also influence the CVR-ALD system design for specific film and substrate chemistry combinations. The minimum purge zone size required to keep CVD byproducts below experimental targets will be process dependent. High precursor utilization can be achieved in particle ALD[22, 29] but is challenging to monitor downstream in CVR-ALD, where precursor and product gases have been significantly diluted by purge gas. Surface titration uniformity, which refers to the sterically hindered final film coverage after one ALD cycle and may be less than one monolayer[2, 30], requires saturating doses of often expensive precursor gases[8, 29]. How to maximize surface titration uniformity while minimizing precursor utilization and other questions about reactive transport behavior can be investigated in a continuum-scale CFD model for CVR-ALD.

Continuum approaches to the gas phase have been well-documented and well-validated for many gases in the literature[31]. Continuum treatments of the solids phase and gas-solid interactions, on the other hand, are more restrictive and require justification[32, 33]. Packed-bed-like solids flow behavior was observed in the CVR-ALD reactor at low vibration intensities in our previous work[26] and enables the powder bed to be treated as a porous media[34-36] characterized by viscous and inertial resistances[37] under the appropriate conditions. Viscous resistance, or inverse permeability from Darcy's law, depends on the powder bed's porosity, packing orientation, and particle shape[38]. A reacting moving porous media (MPM) model can explore how powder bed properties such a specific surface area and site density lead to changes in the residual gas concentration and bed surface titration uniformity.

The permeability of a porous medium depends on geometric properties of the fluid channels forming flow paths in the solid skeleton. Many permeability correlations contain empirical fitting factors relating to aspects of pore networks that are difficult to measure experimentally such as shape and interconnectivity. The original Carman-Kozeny or Kozeny-Carman equation[39, 40] is often referred to as the simplest permeability equation and calculates permeability α from the void fraction ε and the pore surface area per unit total volume S as

$$\alpha = \frac{1}{c_0} \frac{\varepsilon^3}{S^2} \tag{5-1}$$

where c_0 is the Kozeny or Kozeny-Carman (KC) constant and generally assigned a value of five[41]. Specific surface area in the Kozeny-Carman equation can also be written in terms of solid volume, $s_v = S/(1 - \varepsilon)$, as[41]

$$\alpha = \frac{1}{c_0} \frac{\varepsilon^3}{(1 - \varepsilon)^2 {s_v}^2} \tag{5-2}$$

For an unconsolidated bed of spheres, the specific surface area can be replaced with $s_v = 6/d_{eff}$ where d_{eff} is the effective particle diameter[42]. The Kozeny-Carman equation for spherical packings is commonly written with the d_{eff} substitution for specific surface area[43] as

$$\alpha = \frac{d_{eff}^2}{36} \frac{\varepsilon^3}{c_0 (1 - \varepsilon)^2} \tag{5-3}$$

The Kozeny constant corrects for differences in pore connectivity between materials with the same specific surface area and porosity. Some studies have used the expression $c\tau^2$ for c_0 where c is a pore shape factor (equivalent to $b/16$ from the capillary form of the equations[44]) and τ is the tortuosity, a ratio between the effective pore path length and the shortest distance from pore inlet to outlet (*i.e.* the material thickness L)[45]: L_e/L. Tortuosity values range from one for the shortest path from point A to point B (*i.e.,* a line) to high numbers for long, circuitous pore paths. The $c_0 = 5$ value mentioned previously comes from assuming a shape factor $c = 2.5$ and a tortuosity $\tau = \sqrt{2}$ [46]. The definition of the dimensionless parameter tortuosity varies between publications and has been discussed in several reviews[44, 47]. Studies can be found defining tortuosity as a path length ratio[39, 48], L_e/L, or as a "tortuosity factor"[49-51] using the square of this path length ratio, $(L_e/L)^2$. Throughout this paper, tortuosity will refer to the ratio of the path lengths, not the tortuosity factor: $\tau \equiv (L_e/L)$.

In this work, we propose a reacting MPM model in ANSYS Fluent to capture the reacting multiphase flow behavior inside CVR-ALD reactors. The powder bed is approximated as a porous media which conveys as a sliding and layering dynamic mesh zone inside the vibrating (2D rigid body translation) reactor dynamic mesh zone. The porous baseplate or "frit" is also included as a porous media zone which moves with the reactor. Heterogeneous half-reactions (ALD) and homogeneous volume reactions (CVD) are modeled using first-order Arrhenius kinetics. Inputs to the MPM model such as frit and packed bed permeability, porosity, and velocity are derived from pressure drop versus gas velocity curves and previously acquired DEM data[52].

5.3 Methods

5.3.1 Materials

The CVR-ALD reactor has two key components which change in composition depending on the application: the porous frit and powder substrate. In this study, soda lime glass beads (45-63 micron in diameter, from Mo-Sci Corporation) were chosen as an ideal, mildly cohesive Geldart A particle bed. Powders of this size fluidize intermittently during vibratory convection, exhibiting clear distinctions between liftoff and contact that can be applied as a piecewise velocity profile in the porous media dynamic meshing model[52]. Three inert frit materials with sieve diameters ~10 microns were also selected: a sintered stainless steel powder sheet (Mott Corporation, part number 1100-10-40-.062-10-A SHEET 316LSS), a sintered stainless-steel felt and a sintered stainless-steel mesh (TWP-Inc, part number MIC10TL5). The 5-ply mesh material consists of two coarse layers (12x64 mesh size), two fine layers (100 mesh) and one ultrafine layer (165x1400 mesh). These frits represent porous materials with varying pore geometry that may be suitable for a particle ALD reactor. The sintered mesh and powder materials are approximately 1.6 mm thick and can be placed directly in the reactor frit cavity. The felt material is only 0.5 mm thick; several felt layers were stacked to match the sintered mesh and powder material thicknesses.

5.3.2 Porous Media Analysis

To better understand how the porous baseplate geometry affects gas transport behavior, each of the three candidate frit materials were characterized by tomography, porometry, and porosimetry. X-ray computed tomography (XRCT) images of the porous baseplate samples were obtained using a Zeiss Xradia 520 Versa CT microscope at the University of Colorado's Materials Instrumentation and Multimodal Imaging Core Facility

(MIMIC, RRID:SCR_019307). Square samples 2- to 6-mm in length were scanned using 140 kV and the settings shown in **Table 5.1**. Voxel resolutions were chosen to maximize the field of view while resolving the minimum characteristic feature size (1.05 μm, 1.05 μm and 5.97 μm for the powder, felt and mesh, respectively). After scanning, each image stack was processed and visualized in the 3D data analysis application Dragonfly (Object Research Systems/ORS). Image stacks were segmented into pore space and stainless-steel skeleton regions of interest (ROIs) using the Otsu threshold method. The pore space ROI was used to develop a pore network model with the default settings in OpenPNM, an open-source plugin for pore size analysis hosted in Dragonfly ($\sigma = 0.4$, $R\,\text{max} = 4$, edge tolerance = 0.10%, and trim isolated pores enabled). Permeability values for each material were determined from fluidization data in our prior publication[52].

Table 5.1. List of CT microscope settings

Sample Name	**Projections**	**Binning**	**Power** (W)	**Objective**	**Exposure** (s)	**Resolution** (microns)	**Image size** L x W (pixels)
Powder	1996	1	9.94	4X	2	1.06	2026x1976
Felt	2401	1	10.08	4X	0.5	1.06	2026x2026
Mesh	2401	2	10.08	4X	0.6	5.97	1013x1013

Frit samples 25-mm and 5-mm in diameter were then prepared for capillary flow porometry (CFP) and mercury intrusion porosimetry (MIP), respectively. These methods were chosen to compare the number of through-pores from CFP to the number of all open pores, which includes through-pores and dead-end pores, from MIP. Both techniques relate the fluid injection pressure P to the equivalent cylindrical pore size d_s through the Washburn equation,

$$d_s = -\frac{4\gamma_l \cos\theta_l}{P} \tag{5-4}$$

where γ_l is the liquid surface tension and θ_l is the contact angle between the solid skeleton and intruded liquid. In MIP, the volume change of mercury intruded into the sample is monitored with a capacitance sensor to give a pore volume versus pressure curve. In CFP, pores are filled with wetting liquid and flow rate is monitored as the pores are emptied. The pore number density can be derived from the Hagen-Poiseuille equation,

$$Q = -\frac{n_{d_s}\pi {d_s}^4 \Delta P}{128\eta l} \tag{5-5}$$

where Q is the fluid flow rate; n_{d_s} is the number density of pores with diameter d_s; ΔP is the fluid pressure drop; η is the fluid viscosity; and l is the sample thickness.

Capillary flow tests were performed in a Quantachrome (brand of Anton Paar) 3Gzh Porometer. During flow tests, pressure drop across the sample was increased from zero to 0.2 bar to drive Porofil fluid (density=1.85 g/cm^3 surface tension=16 dyn/cm) through the solid skeleton. Both dry and wet curves were analyzed. MIP tests were conducted using a Quantachrome Poremaster 60 GT in low- and high-pressure modes (pressure range 0-60 psi) after running a vacuum to remove sample moisture and contaminants.

Tortuosity of the porous media samples was derived from the segmented tomography image stacks using the free MATLAB application TauFactor. TauFactor performs a numerical diffusion simulation, using voxels from the tomography data as mesh cell elements, to compare steady-state diffusive flow through the tomography-derived pore network to that of a perfectly dense control volume. The ratio of these flows gives the tortuosity of the porous media sample through the equation,

$$D^{eff} = D\frac{\varepsilon}{\tau} \tag{5-6}$$

where D is the intrinsic diffusivity of the void space. When applicable, tomography data sets were cropped to fall within a 1000-pixel cube (**Table 5.2**) to keep diffusion simulations under the 64 GB memory capacity of our lab workstation. TauFactor simulations were performed using the "(D:D) w/ Mirror" option. More details on the TauFactor algorithm and numerical implementation can be found in the software documentation[53].

Table 5.2. Dimensions, in pixels, of TauFactor image samples

Sample Name	Pixels in x	Pixels in y	Pixels in z
Powder	1000	1000	1000
Felt	1001	1001	292
Mesh	900	900	302

All three frit materials are constructed of the same material (stainless steel), but powder flow may also be affected by differences in local surface topography or the presence of surface species. Short-range cohesive forces are known to be particularly sensitive to surface properties such as nanoscale roughness[54-56] and chemical composition[57, 58]. To evaluate whether powder-baseplate interactions are altered by the presence of an ALD-grown alumina film, 50 cycles of alumina were deposited on frit sample squares (~0.25" x 0.25") and compared against uncoated frit samples.

Flat ALD was performed in a 2-inch stainless steel reactor tube with a porous distributor plate. Nitrogen was used as the inert carrier gas and maintained at a flow rate of around 10 sccm. A vacuum pump held the reactor outlet pressure at 0.7 Torr. Liquid precursors trimethylaluminum (TMA, Sigma-Aldrich) and DI water were delivered as gaseous reactants from a vapor draw precursor delivery manifold held at 80°C. Precursor bottles were maintained at 25°C . After setting the reactor temperature to 200°C, the entire system was allowed to reach thermal equilibrium overnight before starting the ALD sequence. A typical ALD cycle comprised of a 3-minute TMA dose followed by a 50-minute nitrogen purge and a 1-minute water dose followed by a 50-minute nitrogen purge. Reactor control and data acquisition were performed in a custom LabVIEW program. Scanning electron microscopy (SEM) with energy dispersive X-ray spectroscopy (EDS) was performed at the Colorado Shared Instrumentation in Nanofabrication and Characterization (COSINC) facility to confirm an increase in surface aluminum weight percent after 50 ALD cycles.

The powder-baseplate cohesiveness for each frit material sample was analyzed using force-deflection ("pull-off" force) measurements in contact mode on a Bruker Icon atomic force microscope (AFM). A 10-micron-diameter borosilicate colloidal AFM probe (Nanosensors, part number CP-qp-CONT-BSG) was purchased to act as a spherical contact point representing the Mo-Sci glass beads in the powder bed. Before evaluating sample pull-off force, the deflection sensitivity (171.2 nm/V) and spring constant (0.02176 N/m) of the probe were determined by calibrating against fused quartz and using the thermal tune calibration method, respectively. Five sites were measured on each sample and averaged to give a mean adhesive force.

5.3.3 Equations

Both the gas phase – a mixture of precursor, purge, and product gases – and the solid substrate phases for the frit and powder bed are treated as continua in this work. Rather than tracking each particle in the powder bed as a discrete entity, the entire powder bed is treated as a solid skeleton with continuum properties (**Figure 5.1**). Individual particle quantities such as mass m_p, diameter d_p and number of sites $n_{s,p}$ become continuum properties of the packed bed *i.e.* solids density ρ_s, bed porosity γ, surface-to-volume ratio SV_s, site density ρ_{site}, and so on. In a porous media formulation, spatial variations in bed surface titration uniformity and precursor utilization can be tracked without the need to resolve individual particle behavior.

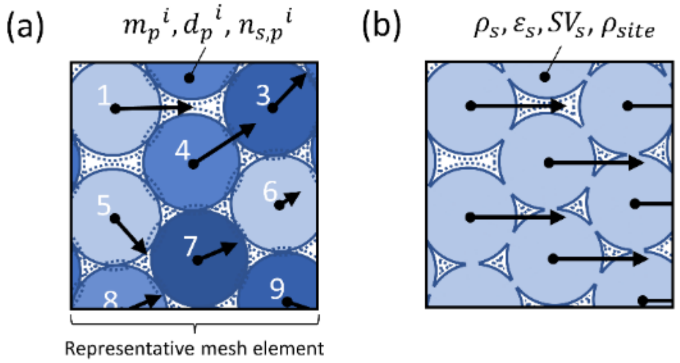

Figure 5.1. (a) Schematic illustration of the traditional Lagrangian approach, where discrete properties of each particle i are tracked. (b) Porous media treatment, where the packed bed of particles is treated as a porous solid skeleton

The reacting MPM model involves solving mass, momentum, (thermal) energy, and species balances. The conservation equations for mass and momentum used in this work are,

$$\frac{\partial \rho_m}{\partial t} + \nabla \cdot (\rho_m \vec{v}_m) = 0 \tag{5-7}$$

$$\frac{\partial}{\partial t}(\rho_m \vec{v}_m) + \nabla \cdot (\rho_m \vec{v}_m \vec{v}_m) = -\nabla P_m + \nabla \cdot (\bar{\bar{\tau}}_m) + \rho_m \vec{g} + \vec{F} \tag{5-8}$$

where ρ_m is the mixture density; $\vec{v}_m$ is the mixture velocity; P_m is the static pressure of the mixture; $\bar{\bar{\tau}}_m$ is the mixture stress tensor; $\vec{g}$ is the gravity vector; and $\vec{F}$ is an external body force term. Laminar flow is assumed due to the low particle Reynolds numbers at typical CVR-ALD conditions (Re_p~1 or less). In porous media zones, porosity of the porous medium γ is added to the transient terms to become $\frac{\partial(\gamma\rho_m)}{\partial t}$ and $\frac{\partial(\gamma\rho_m\vec{v}_m)}{\partial t}$. $\vec{F}$ accounts for the pressure drop due to viscous losses through the porous medium in the k^{th} direction,

$$F_k = -\mu_m C_{v,k} \left| \vec{v}_{m,k} \right| \tag{5-9}$$

where $C_{v,k}$ is the viscous resistance in direction k and $\left|\vec{v}_{m,k}\right|$ is the mixture velocity magnitude in direction k. Viscous resistance is also known as inverse permeability $1/\alpha_k$ with α_k being the permeability in direction k.

The heat transfer equation for the transport of thermal energy is described by,

$$\frac{\partial}{\partial t}\left(\rho_m e_{m,t}\right) + \nabla \cdot \left(\vec{v}_m\left(\rho_m e_{m,t} + P_m\right)\right) = \nabla \cdot \left(k_m \nabla T_m - \sum_j h_j \vec{J_j} + \bar{\bar{\tau}}_m \cdot \vec{v}_m\right) + S_h \tag{5-10}$$

where $e_{m,t}$ is the total energy of the mixture $\left(e_{m,t} = e_m + {V_m}^2/2\right)$; V_m is the scalar mixture velocity; e_m is the mixture internal energy $\left(e_m = C_{v,m} T_m\right)$; $C_{v,m}$ is the constant-volume heat capacity of the mixture; h_m is the mixture enthalpy; k_m is the mixture conductivity; T_m is the mixture temperature; h_j is the sensible heat of species j; $\vec{J_j}$ is the diffusion flux of species j; and S_h is a thermal energy source term accounting for volumetric heat generation from chemical reactions. For low-speed flows, the total energy per unit mass can be related directly to the temperature by neglecting the pressure and kinetic energy $(V^2/2)$ terms. In porous media regions, thermal energy transport takes the form,

$$\frac{\partial}{\partial t}\left(\gamma \rho_m h_m + (1-\gamma)\rho_s h_s\right) + \nabla \cdot \left(\rho_m \vec{v}_m h_m\right) = \nabla \cdot \left(k_{eff} \nabla T_m\right) + S_h \tag{5-11}$$

where ρ_s is the solid material density; h_s is the sensible enthalpy of the porous medium; k_{eff} is the effective thermal conductivity $\left(k_{eff} = \gamma k_m + (1-\gamma) k_s\right)$; and k_s is the solids conductivity.

The transport of chemical species is modeled using the Fickian convection-diffusion equation with volumetric (CVD) and wall surface (ALD) reactions,

$$\frac{\partial}{\partial t}\left(\rho_i Y_i\right) + \nabla \cdot \left(\rho_i \vec{v}_m Y_i\right) = -\nabla \cdot \vec{J}_i + R_i \tag{5-12}$$

where ρ_i is the density of chemical species i; Y_i is the mass fraction of i; $\vec{J}_i$ is the diffusion flux of species i; and R_i is the generation rate of i due to chemical reactions. $N-1$ chemical species transport equations are solved, where N is the number of species; the N^{th} mass fraction is calculated as $1-\sum_j^{N-1} Y_j$. In porous media zones, the transient term includes porosity, becoming $\frac{\partial}{\partial t}(\gamma\rho_i Y_i)$. The diffusion flux is modeled with the dilute approximation,

$$\vec{J}_i = -\rho_i D_{i,m} \nabla Y_i - D_{T,i} \frac{\nabla T_m}{T_m} \tag{5-13}$$

where $D_{i,m}$ is the mass diffusivity of species i and $D_{T,i}$ is the thermal (Soret) diffusivity of i.

Finite-rate kinetics with no turbulence-chemistry interaction (TCI) contribute to the net source of chemical species i, R_i, according to the following relation,

$$R_i = M_{w,i} \sum_1^{N_r} \left(\nu_{f,ir} - \nu_{b,ir}\right) \left(k_{f,r} \sum_1^{N_j} \left(C_j\right)^{\eta_{j,r}} - k_{b,r} \sum_1^{N_j} \left(C_j\right)^{\eta_{j,r}} \right) \tag{5-14}$$

where $M_{w,i}$ is the molecular weight of species i; $\nu_{f,ir}$ and $\nu_{b,ir}$ are the product and reactant stoichiometric coefficients in reaction r; $k_{f,r}$ and $k_{b,r}$ are the forward and reverse rate constants for reaction r; C_j is the molar concentration of species j; and $\eta_{j,r}$ is the rate exponent of species j in reaction r, all summed over N_j chemical species and N_r chemical reactions. Species concentrations in the reaction rate expression above can include gas-phase species and surface-adsorbed site or solid species for heterogeneous ALD reactions.

In this work, the forward reaction rate constant, $k_{f,r}$, is defined using the Arrhenius equation with no temperature term and site coverage dependence,

$$k_{f,r} = A_r e^{-E_{a,r}/(R_g T_m)} \prod_{k_{site}} {Z_k}^{\mu_{k,r}} \tag{5-15}$$

where A_r is the Arrhenius pre-exponential factor or prefactor; $E_{a,r}$ is the activation energy for reaction r; R_g is the universal gas constant; Z_k is the fraction of sites covered by site species k $\left(Z_k = {}^{C_k}/_{\rho_{site}}\right)$; C_k is the concentration of site species k; ρ_{site} is the constant surface site density; and $\mu_{k,r}$ is the site coverage rate exponent. For CVD volume reactions, the surface coverage term drops out ($\mu_{k,r} = 0$). The Arrhenius prefactor for heterogeneous reactions with a first-order dependence on the concentration of gas species i can be calculated using $A_r = \lambda\sqrt{R_g/\left(2\pi M_{w,i}\right)}$ where λ is the sticking coefficient [59].

In moving mesh zones, the integral form of each conservation equation over a control volume V utilizes a relative velocity formulation,

$$\frac{\partial}{\partial t}\int_V \rho_m \phi dV + \int_{\partial V} \rho_m \phi(\vec{v}_m - \vec{v}_{dm}) \cdot d\vec{A} = \int_{\partial V} \Gamma_\phi \nabla\phi \cdot d\vec{A} + \int_V S_\phi dV \tag{5-16}$$

where ϕ is a scalar quantity described by a conservation equation; $\vec{v}_{dm}$ is the moving mesh velocity; Γ_ϕ is the diffusivity of quantity ϕ; and S_ϕ is the total generation rate of ϕ from sources and sinks. Details on the moving mesh numerical implementation can be found in the Fluent theory manual[37].

5.3.4 Reactor Modeling

CFD-DEM simulations have shown that the porosity and coordination structure of the packed bed under vibratory convection do not change significantly when subjected to low vertical accelerations[52]. In this regime, the powder bed can be considered to move as a continuum. The mean powder bed convection velocity at a vertical acceleration of $0.30g$ was approximated as a piecewise velocity profile in this work. The contact region is fit to the sinusoidal conveyor velocity and a constant horizontal liftoff velocity was chosen that gives the same average powder bed velocity as the experimental results, $\bar{u}_{pb} = 1.3\ cm/s$

(**Figure 5.2**). The resulting piecewise velocity is prescribed to the packed bed zone in the MPM model.

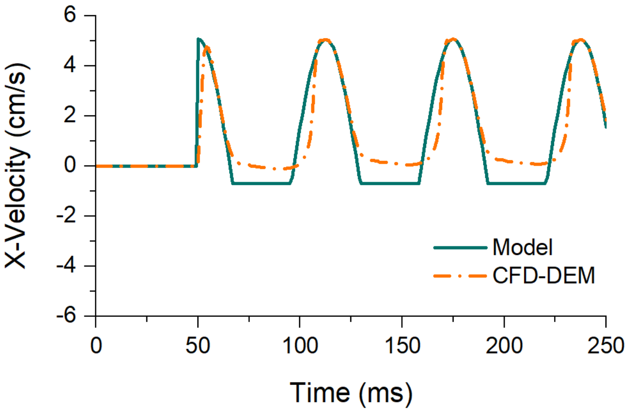

Figure 5.2. Comparison between the CFD-DEM mean powder convection velocity (dash-dot) and the piecewise model approximation with the same average powder bed velocity as the experimental results (solid line)

ANSYS Fluent was chosen to model the CVR-ALD system as one of the few CFD packages with heterogeneous surface reactions, porous media and moving mesh capabilities already built in. A mixture model was applied to the gas phase. Five volumetric (gas) chemical species were considered in this work: (1) the aluminum containing precursor, trimethylaluminum (tma/alme3); (2) the oxidizing precursor, water (h2o); (3) the inert carrier gas, nitrogen (n2); (4) the ALD byproduct, methane (ch4); and (5) the CVD byproduct, aluminum hydroxide (al(oh)3)[60]. Aluminum hydroxide was chosen so that the CVD byproducts could be monitored separately from the ALD-deposited alumina. Two site species (surface hydroxyls, oh, and an alumina intermediate, oal(ch3)2) and one solid film species (alumina, al2o3) were also considered. The mixture model and porous media properties can be found in **Table 5.3**. Standard state enthalpies and entropies were obtained from the NIST chemistry database, when available[61]. Material properties not defined in **Table 5.3** were left at the Fluent Database defaults. Viscous resistances were calculated using the inverse permeability from pressure drop vs. gas velocity fluidization data[52]. Site density was determined assuming a surface site area of $24\,nm^2$ [8]. The remaining porous media properties (surface-to-volume ratio and porosity) were derived from segmented tomography images. All reactions were modeled as irreversible ($k_{b,r} = 0$) with a temperature-independent forward reaction rate constant ($E_{a,r} = 0$). ALD Arrhenius prefactors were calculated by incorporating a constant reactor temperature with a sticking probability $\lambda = 0.01$ (*i.e.*, $A_r = \lambda\sqrt{R_g(473)/(2\pi M_{w,i})}$)[8].

Three reactions were modeled in the CVR-ALD reactor: a TMA half-reaction, a water half-reaction, and a CVD reaction producing aluminum hydroxide. These were described by the following equations,

$$|| - OH \; + \; Al(CH_3)_3 \; = \; CH_4 \; + \; || - OAl(CH_3)_2 \tag{5-17}$$

$$2|| - OAl(CH_3)_2 \; + \; 3H_2O \; = \; 4CH_4 \; + Al_2O_3 + \; 2|| - OH \tag{5-18}$$

$$Al(CH_3)_3 + \; 3H_2O \; = \; 3CH_4 \; + Al(OH)_3 \tag{5-19}$$

The ALD reactions are modeled as first order in concentration and coverage dependence. The CVD reaction is modeled as second order in concentration dependence. All porous materials were assumed to start with fully hydroxylated surfaces ($|| - OH$ site coverage = 1).

Table 5.3. Simulation values

Fluid properties

	TMA	**Water**	**$||$-OAl(CH_3)$_2$**	**$||$-OH**	**Al_2O_3**	**$Al(OH)_3$**
Standard state enthalpy [J/kgmol]	-8.49e+07	-2.42e+08	-1.50e+08	3.90e+07	3.90e+07	2.59e+08
Standard state entropy [J/kgmol-K]	3.50e+05	1.89e+05	5.09e+04	1.84e+05	1.84e+05	1.88e+05

Molecular weight [kg/kmol]	72.09	18.02	73.05	17.00	102.00	78.03

*** Mixture settings were assigned default values** (incompressible ideal gas for density, mixing law specific heat, constant values for thermal conductivity, viscosity and mass diffusivity)

Solid (porous media) properties

	Glass	**Stainless-steel**
Density, ρ_s [kg/m3]	2500	8030
Specific heat, c_p [J/kg-K]	871	503
Thermal conductivity, k_s [W/m-K]	1.3	16.3

Chemical reactions

	TMA half-reaction	**H_2O half-reaction**	**CVD reaction**
Arrhenius prefactor, A_r [1/s]	0.9	1.9	1.0
Species with $\eta_{j,r} = 1$	TMA	H_2O	TMA, H_2O
Species with $\mu_{k,r} = 1$	$\|\| - OH$	$\|\| - OAl(CH_3)_2$	N/A

*** Reaction settings were assigned default values** (heat of surface reactions enabled, diffusion energy source enabled, direct source chemistry solver)

Cell zone and boundary conditions, all

Vibration y-amplitude [g]	0.30
Vibration frequency [Hz]	16
Vibration angle [°]	60
Liftoff y-velocity [cm/s]	-0.40
Precursor velocity [cm/s]	3-4
Precursor mass fraction	0.001
Purge velocity [cm/s]	3-4
Reactor temperature [K]	473

Cell zone conditions, porous zones only

	Packed bed	**Frit**
Surface-to-volume ratio [m^{-1}]	58,000	100,000
Site density [$kgmol/m^2$]	6.92e-11	6.92e-11
Solid material	glass	stainless-steel

Two geometries were used to model the CVR-ALD reactor in this study: a "single zone" model describing the region corresponding to one precursor and a "single cycle" model containing two precursor zones to describe a single cycle of ALD (**Figure 5.3**). The single-zone model only contains three volumetric species (ch4, n2, and alme3 or h2o) while the single-cycle model contains all species from **Table 5.3**. Because only one precursor region is included, CVD reactions are not considered in the single-zone model. In all models, periodic boundary conditions were applied to the left and right boundaries. Inlets and outlets were set to the reactor temperature (473 K). The fluid zones at each outlet were split at the last two rows of mesh cells so that the backflow species mass fractions could be assigned to area-averaged values from the near-outlet cells. As ALD progresses, reaction byproducts begin populating the outlet stream; a time-dependent backflow mass fraction condition more accurately represents the transient composition of the outflowing gas.

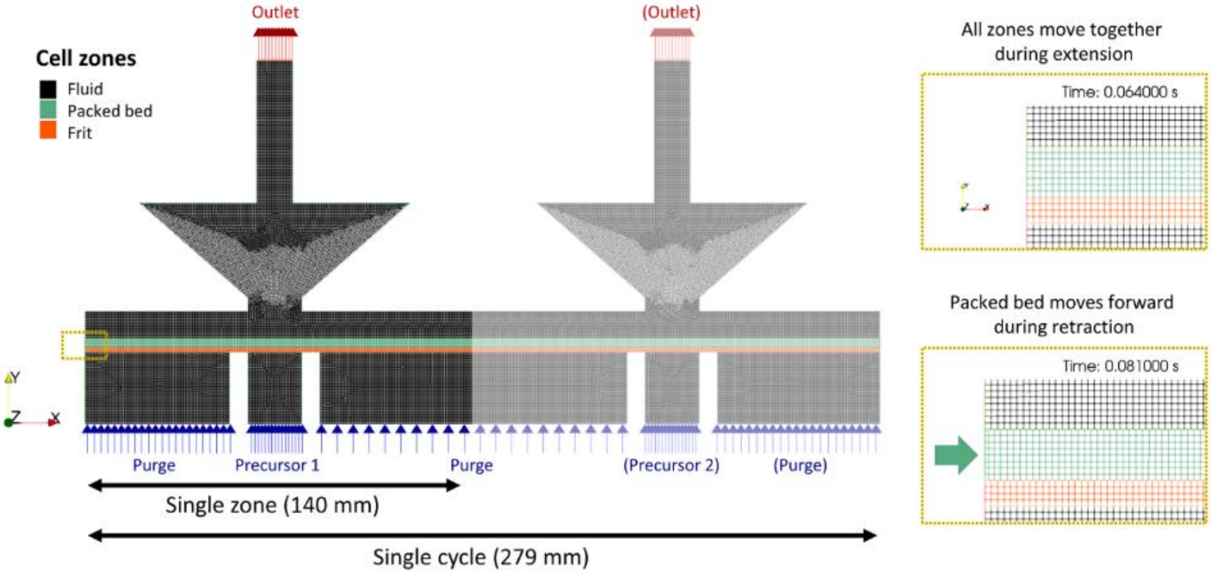

Figure 5.3. Simulation setup (left) for the single-zone model with 49,748 mesh elements and the single-cycle model with 99,432 mesh elements. Insets display sample snapshots of the moving mesh during extension (right, top) and retraction (right, bottom). The frit zone thickness is 1.59 mm and the packed bed zone thickness is 3 mm

Reactor vibration is incorporated through user-defined functions (UDFs). Two DEFINE_ZONE_MOTION UDFs were developed to describe the vibrating reactor and vibrating-conveying packed bed, respectively. These two mesh zones slide across one another in the horizontal direction. Mesh interfaces were created at faces joining the three cell zones (fluid, packed bed, and frit regions). DEFINE_CG_MOTION UDFs at the packed bed inlet and outlet maintain alignment between the packed bed boundaries and the reactor boundaries. Dynamic meshing is only needed at the packed bed inlet and outlet faces, where the mesh cells must be relayered to account for packed bed convection from left to right. Layering was enabled with the recommended settings (height-based, split factor = 0.4, collapse factor = 0.4). Cell height was assigned a value roughly corresponding to the peak-to-peak vibration amplitude (0.00034 m) so that one remeshing step occurs after one period of vibration.

The resulting system of equations was solved using Fluent's transient, pressure-based solver. A converged solution was obtained using the SIMPLE algorithm with pressure-velocity coupling and Rhie-Chow distance-based fluxes. Default values were retained for the under-relaxation factors (0.3 for pressure, 0.7 for momentum, and 1 for all other equations). The gas flow field was allowed to equilibrate for 50 ms before vibration was turned on.

5.4 Results and Discussion

5.4.1 Porous Media Properties

Before running any CVR-ALD simulations, the microstructural characteristics of three candidate frit materials advertised as 10-micron porous media were evaluated. We were interested in how the internal pore structure may affect permeability and the total surface area available for ALD reactions. Tomography data of the frit materials reveals differences in connectivity and pore shape among all three pore networks (**Figure 5.4**). The sintered powder sample is characterized by amorphous, highly interconnected pores (**Figure 5.4a**). Pore path diameters in the pore network model vary from narrow, <10-micron segments to wide 74-micron channels. Pore vertices of varying size are distributed uniformly throughout the porous media with sizes from 67 microns down to <10 microns. The sintered felt sample has similar interconnectivity and size ranges but with different spatial distributions (**Figure 5.4b**). The sintered felt material is functionally graded through the thickness so pore vertices range from 21 microns to <10 microns with larger pores concentrated at the bottom face in **Figure 5.4b**. Pore paths are also narrower and range from <10 microns to 25 microns in diameter. The sintered mesh material exhibits spatial pore network variations and much more noticeable geometric anisotropy than the felt and powder samples (**Figure 5.4c**). Very large pores up to 614 microns in size are visible concentrated at the bottom face in **Figure 5.4c** within the two coarsest mesh layers. The top three mesh layers are dominated by pores <100-micron in size. Pores in the bottom half of the mesh also appear less interconnected than the dense pore networks of **Figures 5.4a** and **5.4b**. Pore paths are also wider, ranging from 601 microns to <20 microns through the finest mesh layer.

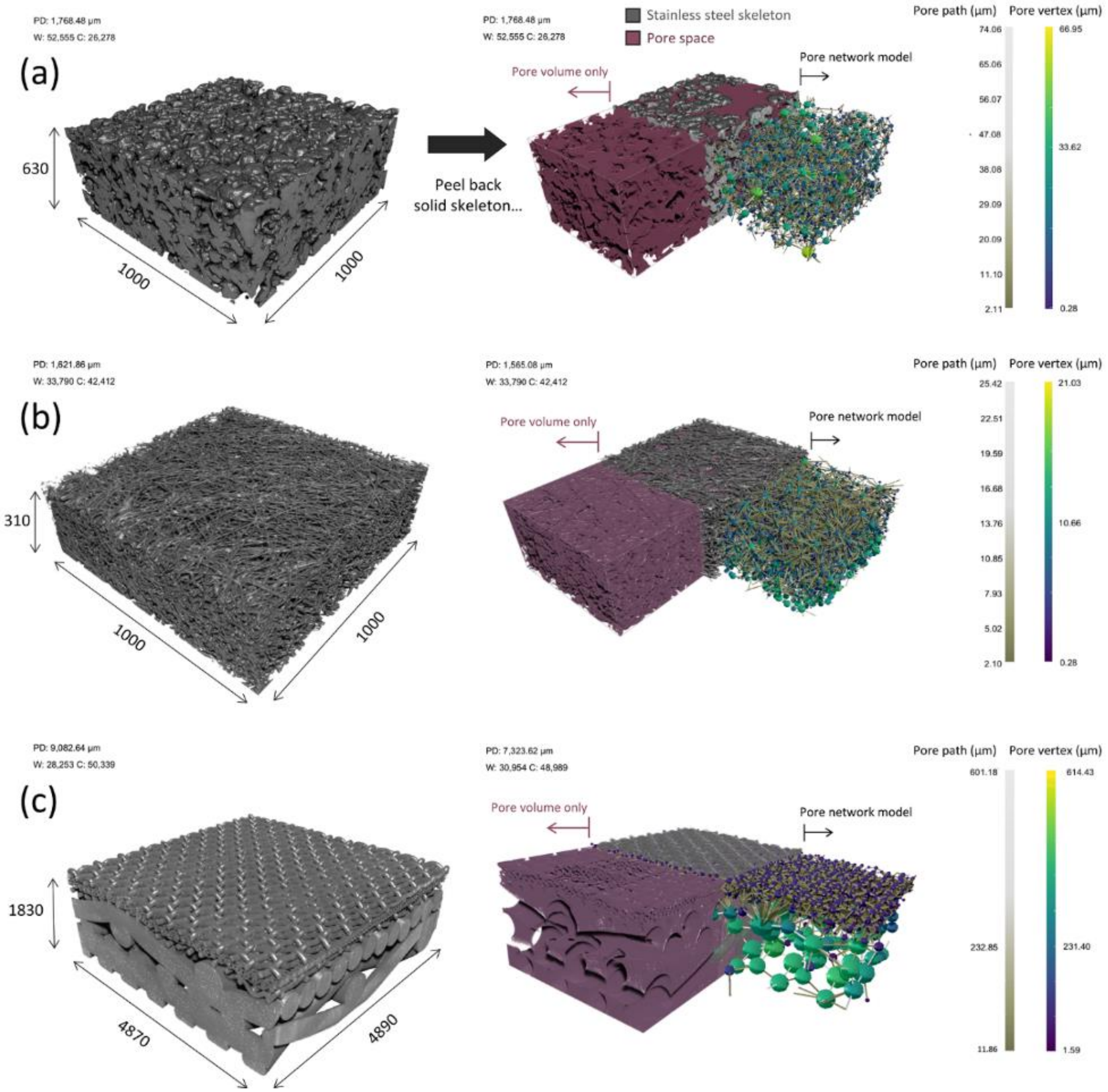

Figure 5.4. XRCT results for three sintered stainless steel baseplate materials: (a) sintered powder, (b) sintered felt, and (c) sintered mesh. 3D visualizations of tomography data display dimensions rounded to the nearest 10 microns (left). The pore volume rendering and pore network model generated by OpenPNM are cropped and revealed by peeling back the solid skeleton (right). Color bars indicate the pore path diameter and pore vertex diameter, in microns, in the pore network model

Similar trends are also observed in the porometry and porosimetry results (**Figure 5.5**). The powder, felt, and mesh sintered samples are characterized by mean through pore sizes of 12.32, 16.08 and 20.12 microns, respectively. The sintered powder has more large open pore spaces than the felt as seen in the MIP results from **Figure 5.5b** and the tomography data from **Figure 5.4a**, but only a fraction of the pore regions constitutes through pores. The mean through pore size, not the average size of all pores, is most relevant to experimental flow measures such as CFP. However, it should be noted that dead end pore spaces still provide additional surface area with reaction sites that can be accessed by ALD precursors through diffusion. The overlap between MIP and CFP results gives a qualitative indication of the dead-end pore frequency. The felt results have the most overlap with only a few small <12-micron and large >25-micron pores observed in the MIP results that were not seen in the CFP results. The powder results overlap mostly for the small pores sizes with a significant number of pores 20-50 microns not seen in the CFP experiments. Many large >50-micron pore spaces can be seen in the mesh MIP results that are not detected in CFP. This is consistent with the tomography data from **Figure 5.4c** indicating that large pores are present in the bottom half of the sintered mesh material, but that flow must pass through small pores in the finest mesh layer before exiting the sample.

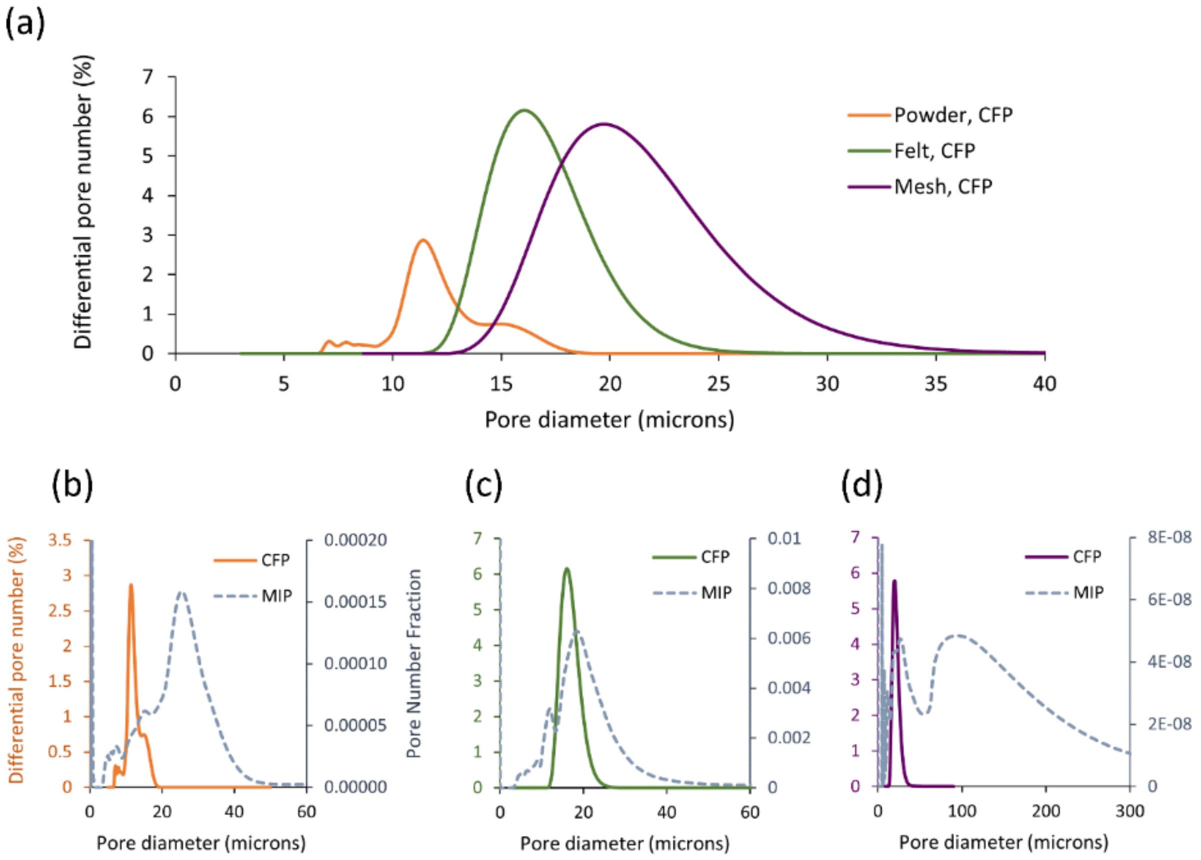

Figure 5.5. Pore size distributions from CFP and MIP. (a) CFP results for the powder, felt and mesh materials indicating through-pore size distributions. (b-d) Comparisons between CFP (left y-axis) and MIP (right y-axis) results for the powder, felt and mesh materials. Non-overlapping regions are indicative of dead-end pores

To better understand how the geometric anisotropy and pore interconnectivity trends observed in **Figure 5.4** affect material permeability, tortuosity factors for in-plane flow ($\tau_1{}^2$ and $\tau_2{}^2$) and through-plane flow ($\tau_3{}^2$) were obtained from TauFactor simulations (**Figure 5.6**). The most highly interconnected pore network from **Figure 5.4** (the sintered powder) had the highest tortuosity factors. The sintered felt material was characterized by the lowest tortuosity factors. Although the sintered felt pore network is also highly interconnected, the porosity is higher, leading to shorter effective pore paths. In general, all materials were only marginally anisotropic in terms of flow resistance – tortuosity factors

$\tau_1{}^2$, $\tau_2{}^2$ and $\tau_3{}^2$ for the sintered powder and sintered felt were within 0.1-0.3 of one another. Tortuosity values typically decreased with increasing porosity, a trend consistent with common tortuosity correlations such as the 2D fiber Tomadakis[62] model and the Bruggeman[63] model. Only the mesh tortuosity results exhibited noticeable anisotropy with a through-plane tortuosity factor $\tau_3{}^2$ around 0.7 lower than the in-plane tortuosity factors $\tau_1{}^2$ and $\tau_2{}^2$.

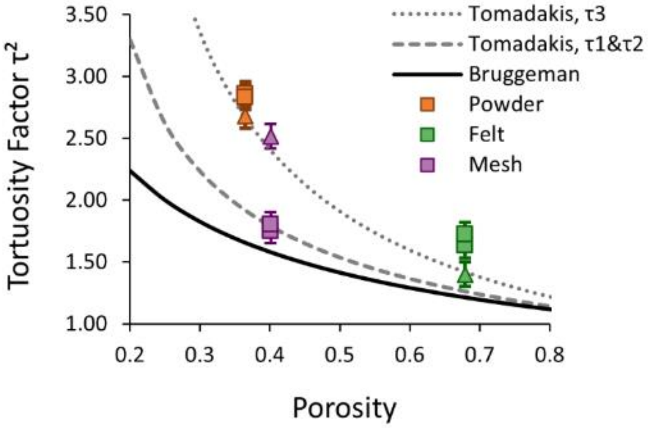

Figure 5.6. Tortuosity factor versus porosity plot for all three sintered materials. Square points designate in-plane tortuosity factors $\tau_1{}^2$ and $\tau_2{}^2$. Triangular points indicate through-plane tortuosity factor $\tau_3{}^2$. The Tomadakis model was fit with parameters $\varepsilon_p = 0.11$ and $\alpha = 0.521$ for in-plane tortuosity or $\alpha = 0.785$ for through-plane tortuosity [62, 64]

The TauFactor and XRCT porous media properties in **Table 5.4** were used with experimental permeability values in equation 5-1 to determine the fitted KC constant c_0. Porosity and specific surface area were calculated from the segmented XRCT images. Approximate porous media properties for the packed bed of 56-micron glass particles are provided for comparison. Permeabilities followed the same order as the mean through-pore size; the sintered powder was the least permeable material, followed by the sintered felt and the sintered mesh. However, the fitted KC constants did not follow the same trend as the through-plane tortuosity factors indicating significant differences in pore shape factor c.

Table 5.4. Porous media characterization results from analysis of fluidized bed data (for permeability) and XRCT images (all others). Specific surface area by total volume (S) and by solid volume (s_v) are included for ease in comparison with other studies

Value	Glass beads	Powder	Felt	Mesh
Porosity, ε	0.46	0.37	0.68	0.40
Tortuosity factor, ${\tau_1}^2$	1.48*	2.86	1.63	1.75
Tortuosity factor, ${\tau_2}^2$	1.48*	2.83	1.72	1.80
Tortuosity factor, ${\tau_3}^2$	1.48*	2.68	1.40	2.52
Specific surface area, s_v $[\mu m^{-1}]$	0.134†	0.097	0.194	0.011
Specific surface area, S $[\mu m^{-1}]$	0.073	0.062	0.062	0.007
Fitted KC constant, c_0	4.2	4.6	22.0	79.9
Permeability, k $[\mu m^{-2}]$	4.25	2.76	3.66	17.93

*Estimate from the Bruggeman correlation, $\tau^2 = \varepsilon^{-0.5}$
†Estimate assuming nearly spherical beads with sphericity $\phi_s = 0.80$ ($s_v = 6/(\phi_s d_s)$)

Several arguments can be made to explain why the KC constants for the sintered felt and sintered mesh samples deviated significantly from the default value of 5[46, 65]. The specific surface areas in **Table 5.4** are calculated from the XRCT images by taking the surface to volume ratio of rectangular prisms forming voxels[53]. This discontinuous, pixelized representation may be a poor approximation of the true, smoother pore surface. Specific surface area has a power law relationship with permeability so any errors in surface area are magnified in the permeability equation. Reported KC constants exceeding 5 are also not uncommon for anisotropic void spaces, particularly as the porosity increases beyond 0.4[41]. Deviations from the Kozeny-Carman model have been attributed to unusable porosity[43, 66] and unresolved complexities in the shape and interconnectivity of pore channels[50]. The Kozeny-Carman relationship assumes that the porous media can be approximated as a collection of sinuous but parallel identical round pipes[39]. For complex pore geometries, this treatment of porous media flow may be an oversimplification. Additional losses not accounted for in the base Kozeny-Carman model can be expected with sudden expansion and contraction of pore capillaries[50] which may explain the lower mesh permeability results.

Porous media surface topography can also influence the cohesive force between the powder bed and frit surface. In this case, no significant differences were detected between the three frit materials or the ALD-coated and uncoated samples (**Figure 5.7b**). AFM pull-off force tests on all three frit materials were characterized by low adhesion values relative to other literature studies[67, 68] from 4.7 to 13.2 nN in magnitude. Standard deviations increased with adhesion force magnitude from 2.1 nN for the ALD-coated mesh to 11.2 nN for the uncoated felt. The large pull-off force variations between replicates can be attributed to site-to-site differences in local surface topography and changes in contact area between the probe and the porous media sample. The presence of TMA-deposited aluminum was confirmed by the 1.2-1.4% weight increase in surface aluminum composition (**Figure 5.7a**). Further tests would be needed to confirm whether particle-frit cohesion is still insensitive to the presence of an ALD film for a thicker coating (>50 cycles alumina).

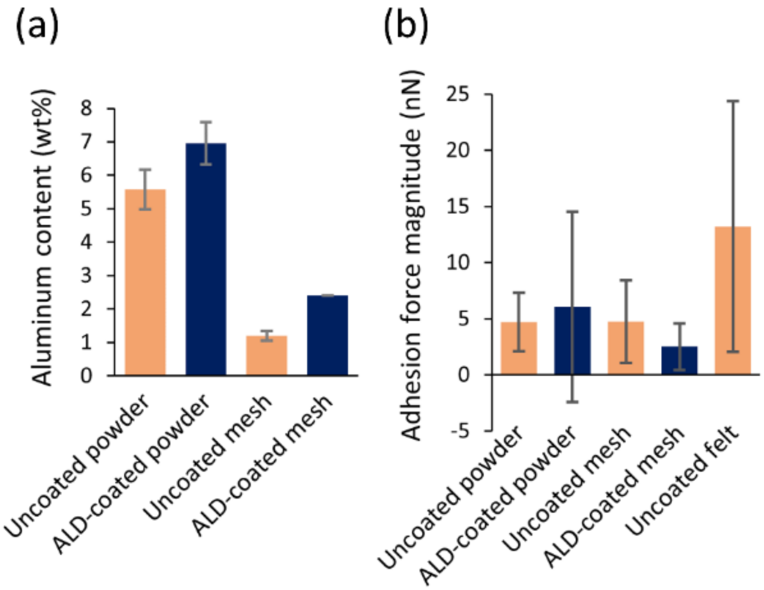

Figure 5.7. (a) EDS aluminum surface weight percent results for coated and uncoated sintered samples. (b) AFM adhesion force magnitude results for coated and uncoated sintered samples

5.4.2 Multiphase Flow Modeling

Reactor-scale CVR-ALD simulations revealed complex multiphase flow behavior during reactor operation. Vibration accelerations produced large, transient fluctuations in the flow streamlines relative to the flow behavior without vibration (**Figure 5.8**). For $\Gamma = 0.30$ to $\Gamma = 0.60$, the reactor vibrates at velocities exceeding the inlet gas velocity. As the extension stroke begins, flow transitions from primarily inlet-to-outlet travel to left-right motion as the fluid moves with the reactor. During retraction, streamlines flip to predominately right-left motion. Some outlet gas is drawn into the reactor during the retraction stroke, but a similar volume of gas is expelled during extension. The symmetric, sinusoidal nature of the vibration prevents outlet gases from propagating into the reactor headspace. Similar behavior is observed between $\Gamma = 0.30$ and $\Gamma = 0.60$ but with larger transient fluctuations and more horizontal streamlines during extension and retraction.

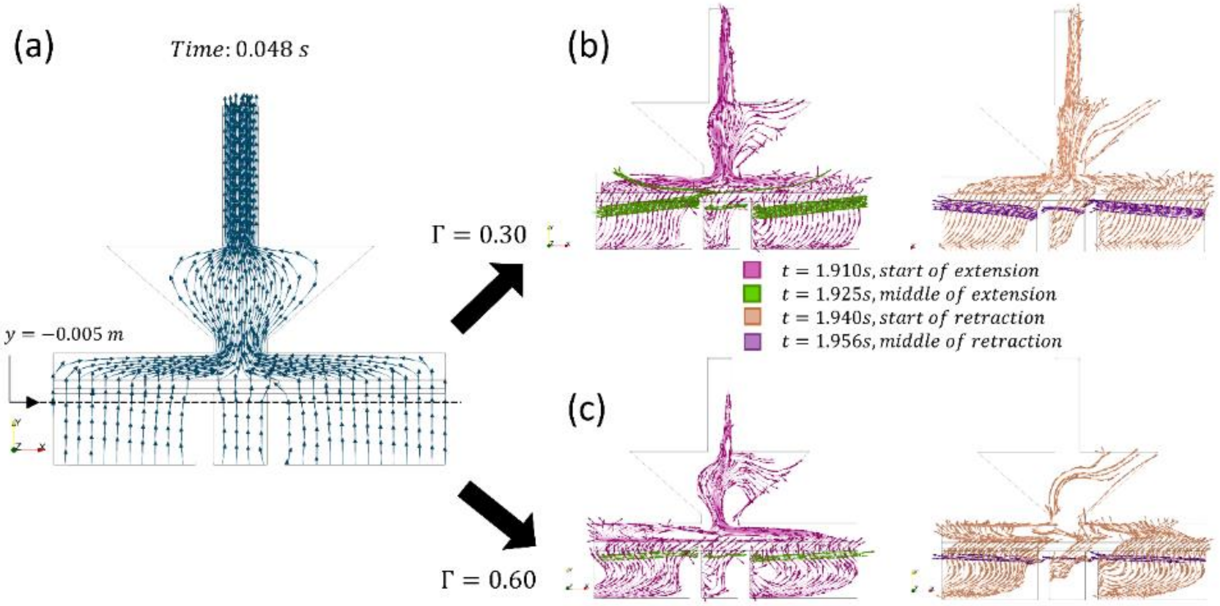

Figure 5.8. (a) Steady streamlines for flow passing through the line $y = -0.005\ m$ (right below the frit, as shown) just before vibration is turned on. (b) Streamlines at select points during vibration when Γ = 0.30. (c) Streamlines at select points during vibration when Γ = 0.60

The net effect of many vibration cycles is to spread out the precursor front (**Figures 5.9a, 5.9b**). Maintaining the average packed bed velocity $\bar{u}_{pb}$ constant, the TMA front can be seen extending farther into the headspace when Γ = 0.60 than when Γ = 0.30. The diffusive effect of vibration magnitude moves the TMA front within the packed bed closer to the packed bed inlet when Γ = 0.60 than when Γ = 0.30. Higher vibration magnitudes lead to a shallower concentration gradient and more spillover into the purge zone headspace. An even more drastic effect is seen when increasing the average packed bed velocity from $\bar{u}_{pb} = 0.5\ cm/s$ to $\bar{u}_{pb} = 3.0\ cm/s$ while maintaining a constant vibration magnitude of Γ = 0.30 (**Figures 5.9c** and **5.9d**). Packed bed convection is observed to have a “dragging” effect on the precursor concentration in both the headspace and the packed bed. The TMA front is pulled towards the outlet as fresh hydroxylated particle surface sites consume the incoming TMA. Vibration magnitude and powder bed convection speed are related[26, 69] but may also depend on particle size and bulk powder bed density so it is important to understand the effects of both factors independently.

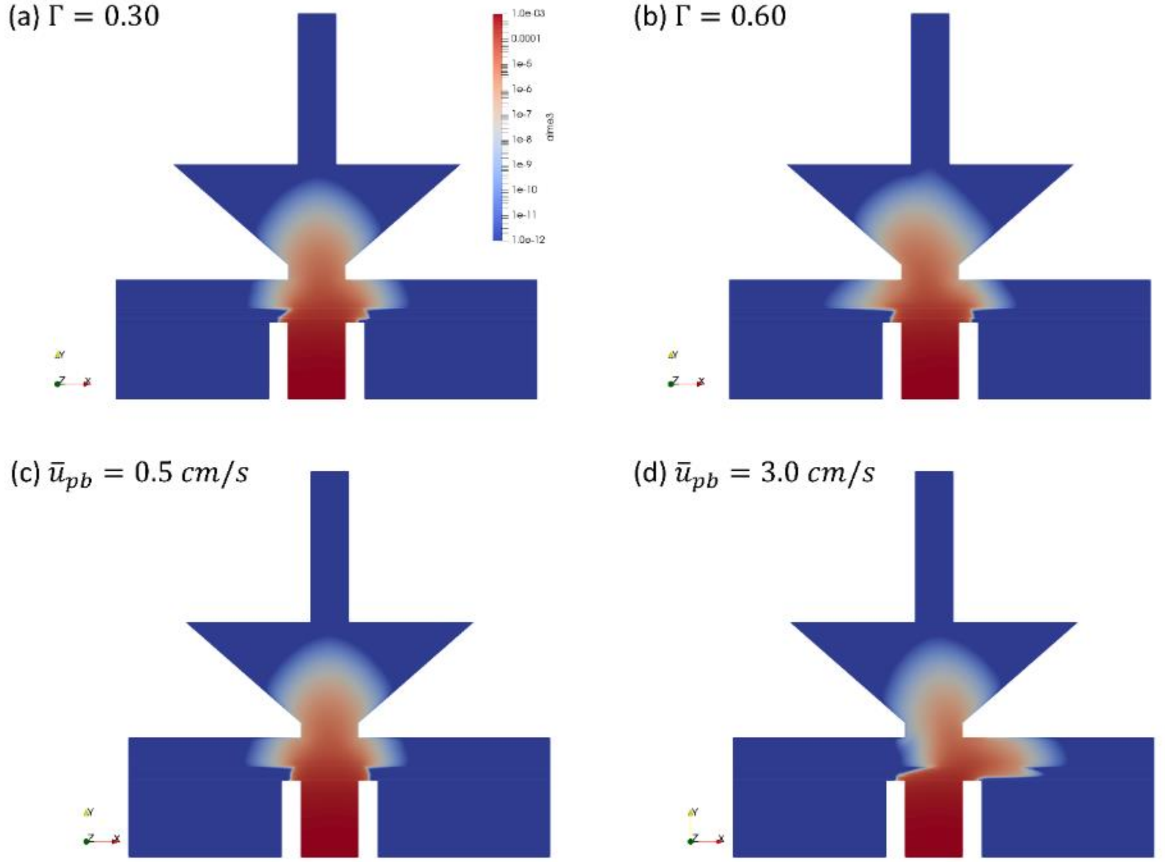

Figure 5.9. TMA concentration profiles at $t = 1.925s$ under different conditions. (a, b) Vibration magnitude Γ is adjusted while keeping the average packed bed velocity, $\bar{u}_{pb}$, constant by adjusting the packed bed liftoff velocity as discussed in **Figure 5.2**. (c,d) Average packed bed velocity $\bar{u}_{pb}$ is adjusted by increasing the liftoff velocity while keeping the vibration magnitude constant at $\Gamma = 0.30$

The trends described in **Figures 5.8** and **5.9** can be quantified by comparing the average surface titration uniformity in the zone leading up to the centerline of the precursor inlet (**Figure 5.10**). The base case corresponding to the convection speed of 56-micron glass particles when $\Gamma = 0.30$ is shown as a black dashed line in **Figure 5.10b**. Higher vibration magnitudes allow the precursor front to spread faster within the packed bed, giving higher average surface titration values. The precursor concentration dragging effect of bed convection velocity can also be seen in the average surface titration results. Faster bed convection pushes incoming TMA towards the packed bed outlet and subsequent water zone, lowering the average surface titration. Purge zones become more necessary at higher packed bed convection speeds and vibration magnitudes to prevent precursors from coming into contact.

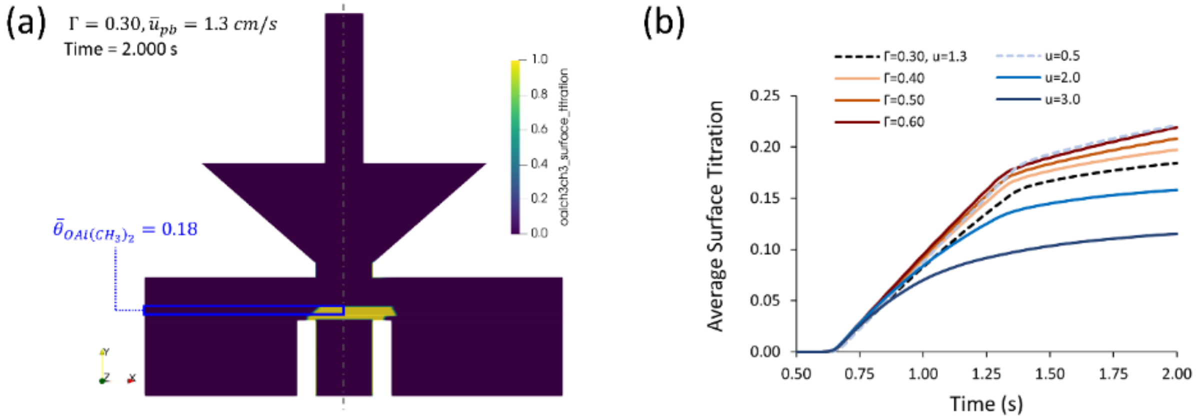

Figure 5.10. (a) Blue boxed region of packed bed used to determine the average surface titration as quantified by the sterically hindered surface coverage of $OAl(CH_3)_2$, $\bar{\theta}_{OAl(CH_3)_2}$. (b) Average surface titration over time for four different vibration intensities ($\Gamma = 0.30, 0.40, 0.50$ & 0.60) and four mean powder bed convection velocities ($\bar{u}_{pb} = 0.5, 1.3, 2.0$ & $3.0\ cm/s$)

Precursor mass fractions spanning two orders of magnitude were tested to evaluate how precursor concentration affects the titration extent of the reaction front (**Figure 5.11**). Only a thin region near the surface of the powder bed in the $Y_{TMA} = 0.0001$ case did not achieve full surface titration before exiting the TMA zone. The fast kinetics of the TMA half-reaction and low surface area of the GL56 powder bed (<1 m^2/g) enable high surface titrations even for mass fractions well below the TMA vapor pressure. Under these conditions, titration uniformity is limited by the number of TMA molecules available for reaction rather than the reaction rate.

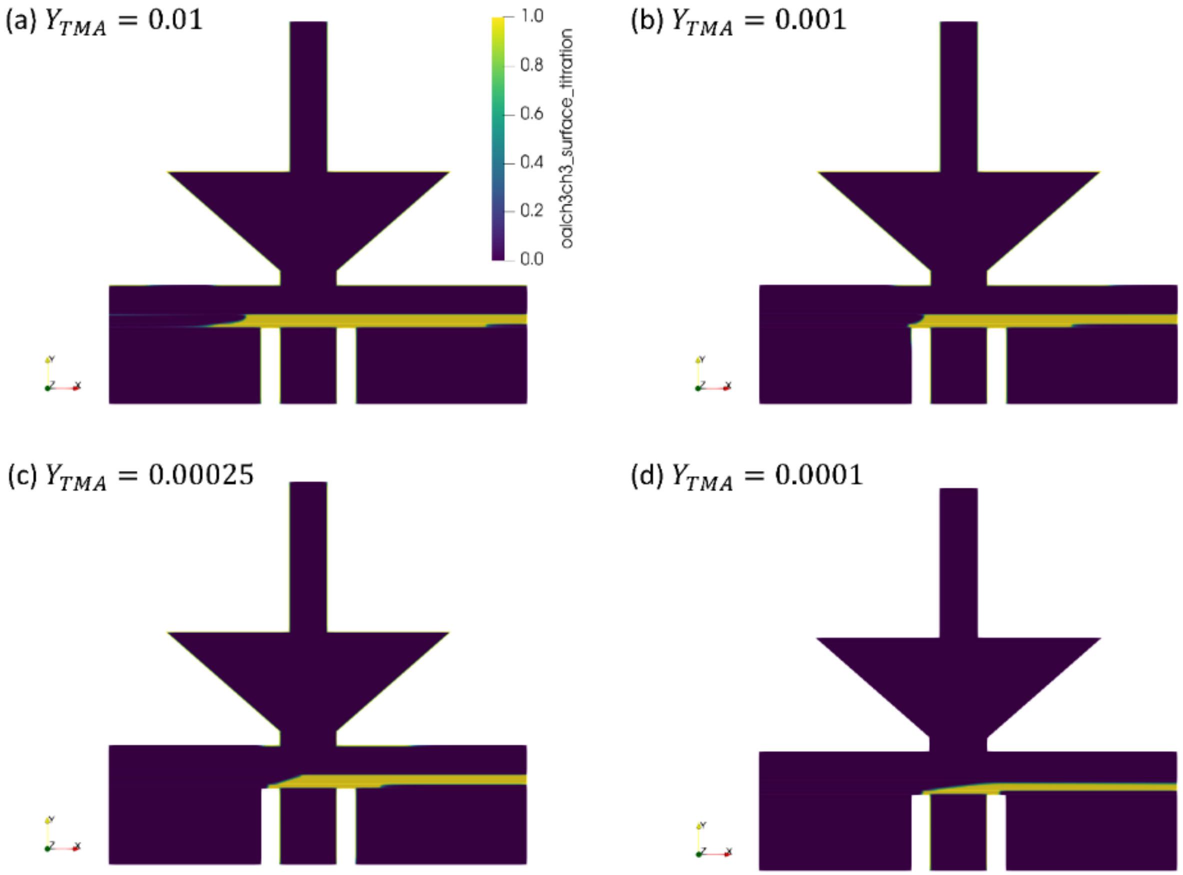

Figure 5.11. Quasi-steady surface titration results for the TMA zone at t = 20 s for different precursor mass fractions

The position and angle of the reaction front are established by a dynamic balance between the precursor flow and the influx of uncoated particles. Excess number γ [70, 71] (a ratio between the number of precursor molecules and the number of surface sites available for ALD) can be used to quantify precursor excess. Redefining excess number on a molar flow rate basis gives

$$\gamma = \frac{\dot{n}_{precursor}}{\dot{n}_{sites}} = \frac{v_g * w_{pr} * n_o * s_0}{\bar{u}_{pb} * h_{pb} * S} \tag{5-20}$$

where v_g is the gas velocity ($|\vec{v}_m|$ from equation 5-7); w_{pr} is the horizontal width of the precursor inlet; n_o is the inlet precursor concentration; s_0 is the surface site area; and

h_{pb} is the height of the packed bed. The precursor inlet width, gas velocity, and inlet precursor concentration control the number of precursor molecules reaching the packed bed zone. High values for v_g, w_{pr}, or n_o increase the precursor excess number. Powder bed convection speed, bed height, powder bed surface area, and surface site area determine the rate of reactive sites available for ALD entering the precursor zone. To keep precursor excess near a desired value, some parameters can be adjusted on the fly (gas velocity, packed bed height, etc.) while others must be considered during the reactor design stage (*i.e.*, precursor inlet width). Additional factors such as vibration amplitude (**Figure 5.9**) and bed permeability influence the position of the reaction front but not the molar balance between flow rates.

The changing position of the reaction front has a complex relationship with the outlet gas composition (**Figure 5.12**). Product gas concentrations are continuously diluted by purge gas as the products travel from the reaction site to the reactor outlet. The outlet stream can be divided into three regions: an initial low signal segment ($t < 2.5s$ in **Figure 5.12b**) when product gases have not had enough time to evolve and propagate to the outlet, a rising signal region ($2.5s < t < 7.5s$ in **Figure 5.12b**) as precursor gas reaches the powder bed and reacts with many available surface sites, and a moderate signal region as the outlet gas composition equilibrates and only sites along the reaction front are continuously producing product gas. An advancing reaction front may be accompanied by an increase in the outlet mole fraction of methane during the rising signal phase (**Figures 5.12a** and **5.12b**). High inlet mass fractions of precursor (i.e., $Y_{TMA} = 0.01$) spread and react quickly to produce a larger spike of methane in the rising signal region compared to slowly-propagating, low inlet mass fractions of precursor. Product gas analysis via mass spectrometry is the most common in-situ diagnostic available in particle ALD systems[22, 28] and provides insight into reaction behavior through changes in the transient outlet gas composition data.

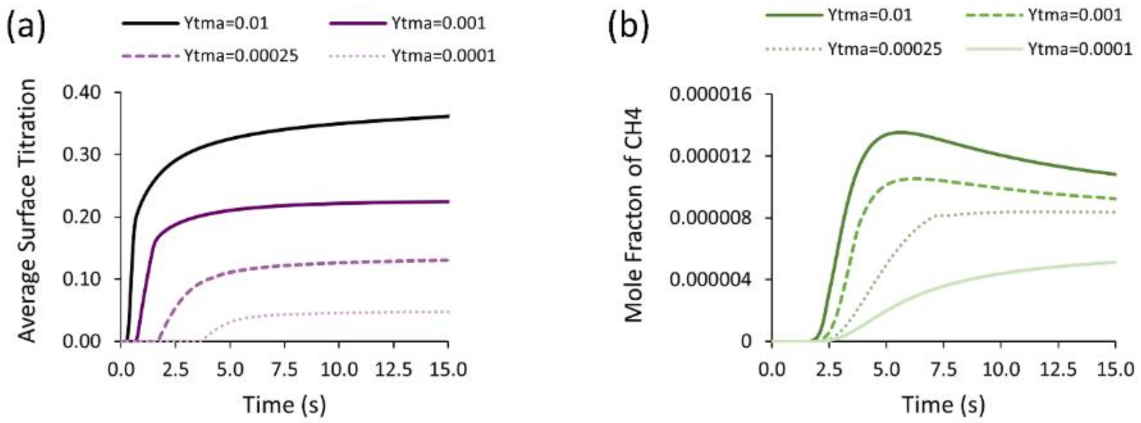

Figure 5.12. (a, b) Average surface titration over the blue boxed region from **Figure 5.10a** and mole fraction of methane at the reactor outlet over time for different precursor mass fractions in the precursor dosing region from **Figure 5.11**.

Single precursor zone models ignore the potential for CVD reactions caused by mixing between precursor zones. High excess numbers indicate unreacted precursor gas is leaving the packed bed zone and can be transported upwards to the reactor outlet or outwards toward the neighboring precursor zones. CVD reactions are not self-limited and can occur wherever both precursors come into contact. Spatially resolved full ALD cycle simulations provide information on the location and severity of parasitic volume reactions.

The full ALD cycle simulations exhibit similarities to the single precursor zone simulations. Quasi-steady surface titration uniformity and outlet gas composition is observed after an equilibration period (**Figure 5.13**). The bed starts with fully hydroxylated surface sites, so the bed is fully titrated in zone 2 ($\bar{\theta}_{OH} = 1$) and incoming water vapor has nothing to react with until methylated sites from the TMA zone are conveyed into the water zone. Both half-reactions are fast and the quasi-steady reaction fronts occur at similar locations relative to the precursor inlet (**Figure 5.14a**), leading to similar average surface titrations after an equilibration period of around 30 seconds. Methane mole fractions in **Figure 5.13b** exhibit the same regions discussed in **Figure 5.12b**. No overshoot is seen in the outlet methane mole fraction for zone 2 because reactions occur at the interface with incoming methylated sites only.

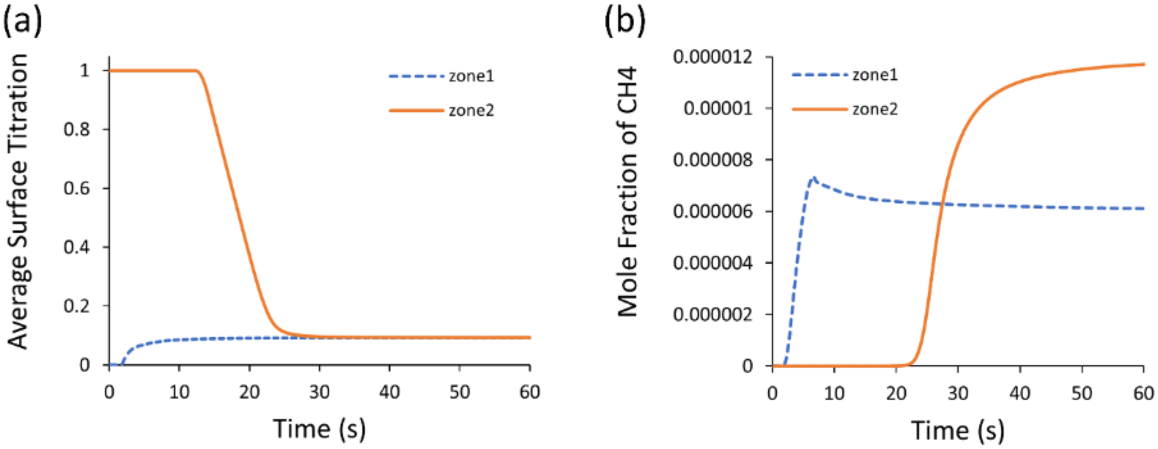

Figure 5.13. Average surface titration over the blue boxed region from **Figure 5.10a** (a) and mole fraction of methane (b) in the outlet gas streams for the first precursor zone and the second precursor zone when $Y_{TMA} = 0.0002$ and $Y_{H_2O} = 0.000075$. Surface titration refers to the sterically hindered coverage of $OAl(CH_3)_2$ for zone 1 or OH for zone 2

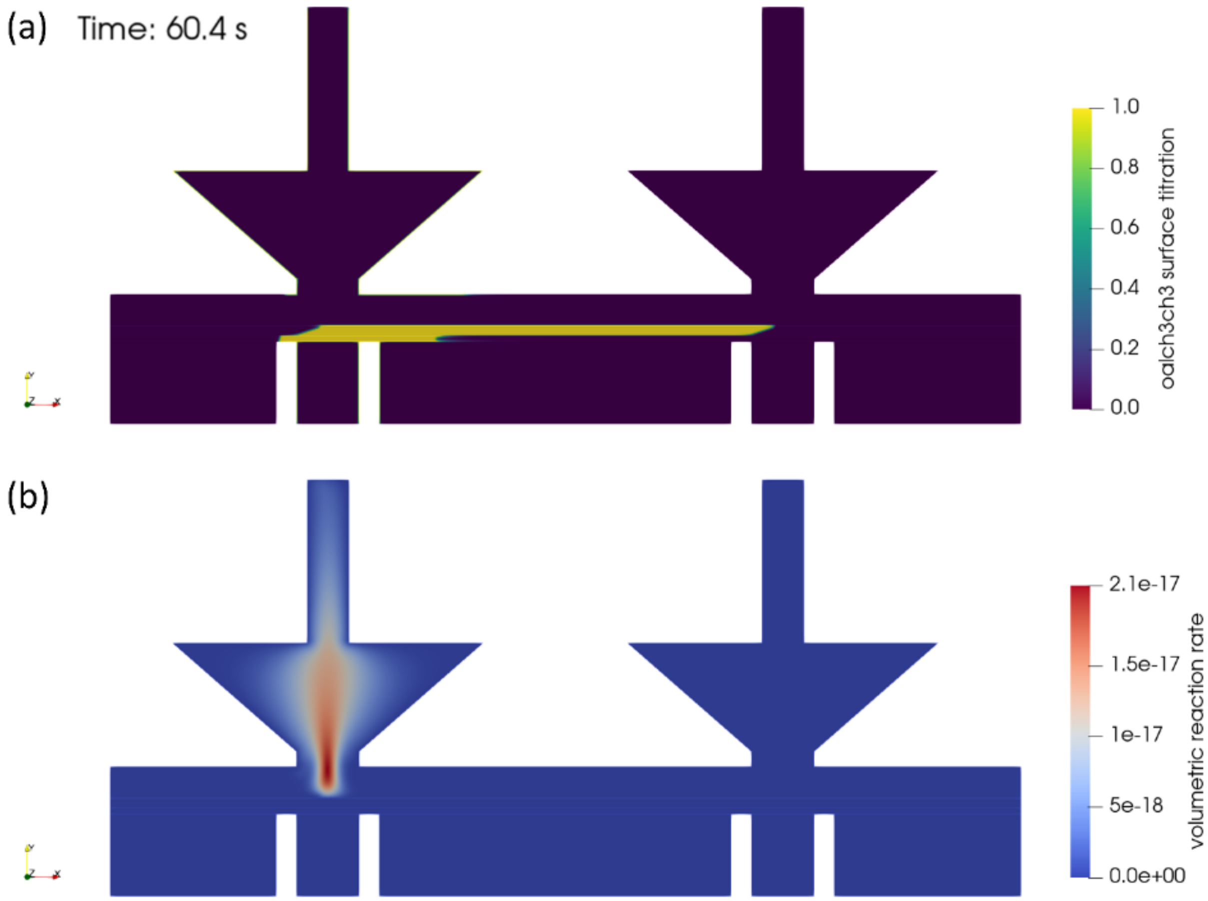

Figure 5.14. Surface plots for surface titration of $OAl(CH_3)_2$ species (a) and CVD reaction rate in kgmol/m^3-s (b) during a stoichiometric TMA/water dose ($Y_{TMA} = 0.0002, Y_{H_2O} = 0.000075$) at time $t = 60.4\ s$

The lack of methylated sites for the water half-reaction results in spillover of water vapor to neighboring TMA zones and subsequent CVD reactions (**Figure 5.14b**). Adjusting inlet mass fractions to give near-unity excess numbers and a stoichiometric TMA/water ratio decreases the magnitude of CVD reactions but does not completely prevent them (**Figure 5.15a**). A pulse delay can be implemented between the start of the TMA dose and the start of the water dose to prevent water vapor spillover. A pulse delay of 15 seconds was observed to eliminate the startup spike in average reaction rate for the stoichiometric case and minimize initial CVD reaction prevalence without impeding average surface titration uniformity (**Figure 5.15**). Excess numbers equal to each half-reaction stoichiometric ratio are needed to prevent CVD reactions entirely.

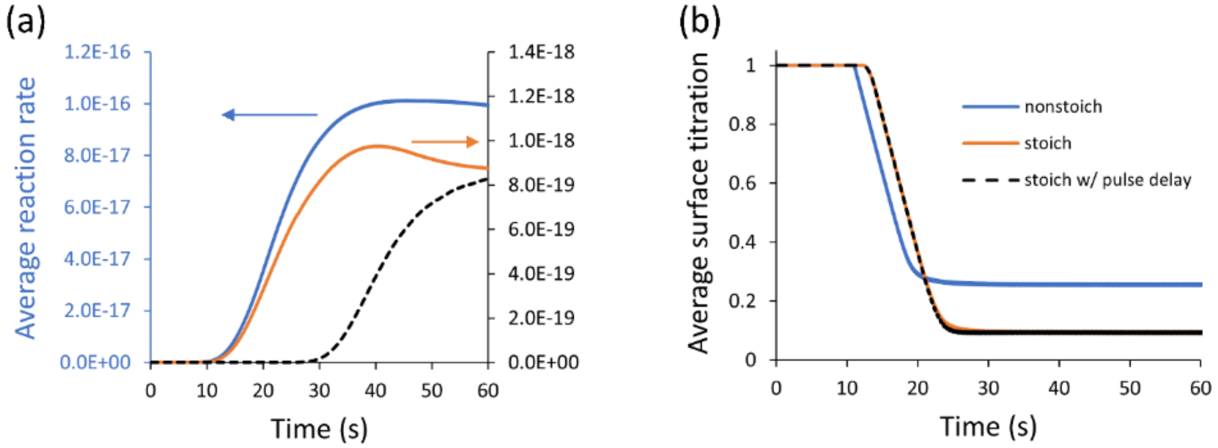

Figure 5.15. Average volumetric reaction rate in kgmol/m^3-s (a) and average surface titration of OH in zone 2 (b). Values are shown for a nonstoichiometric case ($Y_{TMA} = 0.001$ & $Y_{H_2O} = 0.001$), a stoichiometric case ($Y_{TMA} = 0.0002$ & $Y_{H_2O} = 0.000075$), and the same stoichiometric conditions with a 15-second pulse delay between the TMA and H_2O doses. In (a), the blue line reaction rate is labeled on the left vertical axis while the right vertical axis corresponds to the orange and black dashed lines

5.5 Conclusions

A moving porous media model capable of resolving reactor-scale flow behavior in CVR-ALD was presented. This study focused on multiphase flow behavior and operating conditions for TMA/water alumina ALD on ≥20 μm diameter particle beds; future work will be needed to investigate more complex, temperature-dependent ALD kinetics[8, 15, 72] and finer substrate materials[28]. Key findings are included in the summary below.

All three porous media samples were advertised as 10-micron stainless-steel porous materials but differed significantly in mean through-pore size, tortuosity, porosity, and permeability. The mesh material has many large, open pore spaces that do not dictate primary flow channels based on MIP results and visual observations from the XRCT data. The felt and powder materials had tighter MIP pore size distributions with fewer large, open pores than the mesh material. Geometric anisotropies did not always correlate to strong anisotropy in the flow properties. As an example, the felt material had a clear 2D layered structure, but the TauFactor through-thickness tortuosity (1.40) did not differ as expected from the in-plane tortuosities (1.63 and 1.72) predicted by the 2D fiber Tomadakis model.

In the range of attainable operating conditions for our CVR-ALD setup, some parameters were observed to modify bed surface titration and outlet gas streams more than others. Reactor vibration produced large fluctuations in the transient gas flow streamlines. Vibration had a diffusive effect on precursor concentration that increased with vibration magnitudes between $\Gamma = 0.30$ and $\Gamma = 0.60$. An increase in powder bed convection speed skewed the precursor concentration gradient towards the powder bed outlet. The reaction front advanced towards the powder bed inlet with high inlet precursor mass fractions. Qualitative trends in the time evolution of surface titration, outlet product gas mole fraction and outlet precursor mole fraction were similar for all cases studied.

Concurrent dosing of TMA and water in the single ALD cycle simulations led to CVD reactions in the TMA zone. Stoichiometric ratios between the inlet TMA and water dose mole fractions and excess numbers near each half reaction stoichiometry are needed to minimize CVD prevalence. A balance must be struck between optimizing precursor utilization or CVD mitigation (low excess number) and guaranteeing surface titration uniformity (high excess number). Experimentally, water doses exceeding the stoichiometric ratio are often used to compensate for water adsorption on the reactor and tubing walls[73] so comparison to experiments would be necessary to determine the optimal excess number for each half-reaction.

Acknowledgements

Financial support from the National Science Foundation [NSF GOALI #1852824] is gratefully acknowledged. This work was also supported, in part, by the U.S. National Science Foundation (Award No. CBET-1726864). Analyses were performed at the MIMIC center at CU Boulder (RRID:SCR_019307). The authors also thank Sam Cooper from Imperial College London for feedback on preparing datasets for TauFactor and interpreting tortuosity data.

References

[1] M. Shahmohammadi, R. Mukherjee, C. Sukotjo, U.M. Diwekar, C.G. Takoudis, Recent Advances in Theoretical Development of Thermal Atomic Layer Deposition: A Review, Nanomaterials, 12 (2022) 831.
[2] R.L. Puurunen, Random deposition as a growth mode in atomic layer deposition, Chemical Vapor Deposition, 10 (2004) 159-170.
[3] A. Yanguas-Gil, J.W. Elam, A Markov chain approach to simulate atomic layer deposition chemistry and transport inside nanostructured substrates, Theoretical Chemistry Accounts, 133 (2014) 1-13.
[4] J. Elam, D. Routkevitch, P. Mardilovich, S. George, Conformal coating on ultrahigh-aspect-ratio nanopores of anodic alumina by atomic layer deposition, Chemistry of materials, 15 (2003) 3507-3517.
[5] N. Cheimarios, D. To, G. Kokkoris, G. Memos, A.G. Boudouvis, Monte carlo and kinetic monte carlo models for deposition processes: a review of recent works, Front. Phys. 9: 631918. doi: 10.3389/fphy, (2021).
[6] A. Lankhorst, B. Paarhuis, H. Terhorst, P. Simons, C. Kleijn, Transient ALD simulations for a multi-wafer reactor with trenched wafers, Surface and Coatings Technology, 201 (2007) 8842-8848.
[7] M. Ylilammi, O.M. Ylivaara, R.L. Puurunen, Modeling growth kinetics of thin films made by atomic layer deposition in lateral high-aspect-ratio structures, Journal of Applied Physics, 123 (2018) 205301.
[8] A. Yanguas-Gil, J.A. Libera, J.W. Elam, Reactor scale simulations of ALD and ALE: Ideal and non-ideal self-limited processes in a cylindrical and a 300 mm wafer cross-flow reactor, Journal of Vacuum Science & Technology A: Vacuum, Surfaces, and Films, 39 (2021) 062404.
[9] W. Cong, Z. Li, K. Cao, G. Feng, R. Chen, Transient analysis and process optimization of the spatial atomic layer deposition using the dynamic mesh method, Chemical Engineering Science, 217 (2020) 115513.
[10] Y. Zhang, Y. Ding, P.D. Christofides, Multiscale computational fluid dynamics modeling of thermal atomic layer deposition with application to chamber design, Chemical Engineering Research and Design, 147 (2019) 529-544.
[11] Z. Deng, W. He, C. Duan, B. Shan, R. Chen, Atomic layer deposition process optimization by computational fluid dynamics, Vacuum, 123 (2016) 103-110.
[12] G. Gakis, H. Vergnes, E. Scheid, C. Vahlas, B. Caussat, A.G. Boudouvis, Computational fluid dynamics simulation of the ALD of alumina from TMA and H2O in a commercial reactor, Chemical Engineering Research and Design, 132 (2018) 795-811.

[13] D. Pan, T.-C. Jen, C. Yuan, Effects of gap size, temperature and pumping pressure on the fluid dynamics and chemical kinetics of in-line spatial atomic layer deposition of Al2O3, International Journal of Heat and Mass Transfer, 96 (2016) 189-198.

[14] D. Pan, Numerical study on the effectiveness of precursor isolation using N2 as gas barrier in spatial atomic layer deposition, International Journal of Heat and Mass Transfer, 144 (2019) 118642.

[15] M.R. Shaeri, T.-C. Jen, C.Y. Yuan, Reactor scale simulation of an atomic layer deposition process, Chemical Engineering Research and Design, 94 (2015) 584-593.

[16] V. Cremers, R.L. Puurunen, J. Dendooven, Conformality in atomic layer deposition: Current status overview of analysis and modelling, Applied Physics Reviews, 6 (2019) 021302.

[17] R.G. Gordon, D. Hausmann, E. Kim, J. Shepard, A kinetic model for step coverage by atomic layer deposition in narrow holes or trenches, Chemical Vapor Deposition, 9 (2003) 73-78.

[18] V. Dwivedi, R.A. Adomaitis, Multiscale simulation and optimization of an atomic layer deposition process in a nanoporous material, ECS Transactions, 25 (2009) 115.

[19] P.S. Maydannik, T.O. Kaariainen, D.C. Cameron, Continuous atomic layer deposition: Explanation for anomalous growth rate effects, Journal of Vacuum Science & Technology A: Vacuum, Surfaces, and Films, 30 (2012) 01A122.

[20] A. Yanguas-Gil, J.W. Elam, Analytic expressions for atomic layer deposition: Coverage, throughput, and materials utilization in cross-flow, particle coating, and spatial atomic layer deposition, Journal of Vacuum Science & Technology A: Vacuum, Surfaces, and Films, 32 (2014) 031504.

[21] V.E. Strempel, R. Naumann d'Alnoncourt, M. Drieß, F. Rosowski, Atomic layer deposition on porous powders with in situ gravimetric monitoring in a modular fixed bed reactor setup, Review of Scientific Instruments, 88 (2017) 074102.

[22] D.M. King, J.A. Spencer II, X. Liang, L.F. Hakim, A.W. Weimer, Atomic layer deposition on particles using a fluidized bed reactor with in situ mass spectrometry, Surface and Coatings Technology, 201 (2007) 9163-9171.

[23] J. McCormick, B. Cloutier, A. Weimer, S. George, Rotary reactor for atomic layer deposition on large quantities of nanoparticles, Journal of Vacuum Science & Technology A: Vacuum, Surfaces, and Films, 25 (2007) 67-74.

[24] C.-L. Duan, X. Liu, B. Shan, R. Chen, Fluidized bed coupled rotary reactor for nanoparticles coating via atomic layer deposition, Review of Scientific Instruments, 86 (2015) 075101.

[25] J.R. van Ommen, D. Kooijman, M.d. Niet, M. Talebi, A. Goulas, Continuous production of nanostructured particles using spatial atomic layer deposition, Journal of Vacuum Science & Technology A: Vacuum, Surfaces, and Films, 33 (2015) 021513.

[26] J. Hartig, H.C. Howard, T.J. Stelmach, A.W. Weimer, DEM modeling of fine powder convection in a continuous vibrating bed reactor, Powder Technology, (2021).

[27] I.J.A. Spencer, R.A. Hall, Continuous spatial atomic layer deposition process and apparatus for applying films on particles, Google Patents, 2018.

[28] A.W. Weimer, Particle atomic layer deposition, Journal of Nanoparticle Research, 21 (2019) 9.

[29] F. Grillo, M.T. Kreutzer, J.R. van Ommen, Modeling the precursor utilization in atomic layer deposition on nanostructured materials in fluidized bed reactors, Chemical Engineering Journal, 268 (2015) 384-398.

[30] S.M. George, Atomic layer deposition: an overview, Chemical reviews, 110 (2010) 111-131.

[31] E.H. Kennard, Kinetic theory of gases, McGraw-hill New York1938.

[32] M.A. van der Hoef, M. van Sint Annaland, N. Deen, J. Kuipers, Numerical simulation of dense gas-solid fluidized beds: a multiscale modeling strategy, Annu. Rev. Fluid Mech., 40 (2008) 47-70.

[33] J. Wang, Continuum theory for dense gas-solid flow: A state-of-the-art review, Chemical Engineering Science, 215 (2020) 115428.

[34] J. Jänchen, T.H. Herzog, K. Gleichmann, B. Unger, A. Brandt, G. Fischer, H. Richter, Performance of an open thermal adsorption storage system with Linde type A zeolites: Beads versus honeycombs, Microporous and Mesoporous Materials, 207 (2015) 179-184.

[35] H. Choi, A. Mills, Heat and mass transfer in metal hydride beds for heat pump applications, International Journal of Heat and Mass Transfer, 33 (1990) 1281-1288.

[36] B.A. Meyer, D.W. Smith, Flow through porous media: comparison of consolidated and unconsolidated materials, Industrial & engineering chemistry fundamentals, 24 (1985) 360-368.

[37] Ansys, Fluent 17.0 Theory Guide, ANSYS inc, (2015).

[38] D. Beard, P. Weyl, Influence of texture on porosity and permeability of unconsolidated sand, AAPG bulletin, 57 (1973) 349-369.

[39] P.C. Carman, Fluid flow through granular beds, Trans. Inst. Chem. Eng., 15 (1937) 150-166.

[40] A.W. Heijs, C.P. Lowe, Numerical evaluation of the permeability and the Kozeny constant for two types of porous media, Physical Review E, 51 (1995) 4346.

[41] P. Xu, B. Yu, Developing a new form of permeability and Kozeny–Carman constant for homogeneous porous media by means of fractal geometry, Advances in water resources, 31 (2008) 74-81.

[42] C.F. Berg, Permeability description by characteristic length, tortuosity, constriction and porosity, Transport in porous media, 103 (2014) 381-400.

[43] J. Bear, Dynamics of fluids in porous media, Courier Corporation2013.

[44] N. Epstein, On tortuosity and the tortuosity factor in flow and diffusion through porous media, Chemical engineering science, 44 (1989) 777-779.

[45] B. Lu, S. Torquato, Lineal-path function for random heterogeneous materials, Physical Review A, 45 (1992) 922.

[46] M. Kaviany, Principles of heat transfer in porous media, Springer Science & Business Media2012.

[47] L. Shen, Z. Chen, Critical review of the impact of tortuosity on diffusion, Chemical Engineering Science, 62 (2007) 3748-3755.

[48] R. Zhong, M. Xu, R.V. Netto, K. Wille, Influence of pore tortuosity on hydraulic conductivity of pervious concrete: Characterization and modeling, Construction and Building Materials, 125 (2016) 1158-1168.

[49] S.J. Cooper, M. Kishimoto, F. Tariq, R.S. Bradley, A.J. Marquis, N.P. Brandon, J.A. Kilner, P.R. Shearing, Microstructural analysis of an LSCF cathode using in situ tomography and simulation, ECS Transactions, 57 (2013) 2671.

[50] F.A. Dullien, Porous media: fluid transport and pore structure, Academic press2012.

[51] B. Tjaden, S.J. Cooper, D.J. Brett, D. Kramer, P.R. Shearing, On the origin and application of the Bruggeman correlation for analysing transport phenomena in electrochemical systems, Current opinion in chemical engineering, 12 (2016) 44-51.

[52] J. Hartig, A. Shetty, D.R. Conklin, A.W. Weimer, Aeration and cohesive effects on flowability in a vibrating powder conveyor, Powder Technology, 408 (2022) 117724.

[53] S.J. Cooper, A. Bertei, P.R. Shearing, J. Kilner, N.P. Brandon, TauFactor: An open-source application for calculating tortuosity factors from tomographic data, SoftwareX, 5 (2016) 203-210.

[54] C.Q. LaMarche, S. Leadley, P. Liu, K.M. Kellogg, C.M. Hrenya, Method of quantifying surface roughness for accurate adhesive force predictions, Chemical Engineering Science, 158 (2017) 140-153.

[55] J. Katainen, M. Paajanen, E. Ahtola, V. Pore, J. Lahtinen, Adhesion as an interplay between particle size and surface roughness, Journal of Colloid and Interface Science, 304 (2006) 524-529.

[56] Y.I. Rabinovich, J.J. Adler, A. Ata, R.K. Singh, B.M. Moudgil, Adhesion between nanoscale rough surfaces: I. Role of asperity geometry, Journal of colloid and interface science, 232 (2000) 10-16.

[57] M. Tahmasebpoor, L. de Martín, M. Talebi, N. Mostoufi, J.R. van Ommen, The role of the hydrogen bond in dense nanoparticle–gas suspensions, Physical Chemistry Chemical Physics, 15 (2013) 5788-5793.

[58] K. Smith, J. Butterbaugh, S. Beaudoin, Effects of Coating Thickness on Particle Adhesion in Microelectronics-Based Systems, ECS Journal of Solid State Science and Technology, 2 (2013) P488.

[59] ANSYS, #2002733 How are sticking coefficient reactions converted into Arrhenius rate format?, Knowledge Resources: Solutions, 2016.

[60] H. Terao, H. Sunakawa, Effects of oxygen and water vapour introduction during MOCVD growth of GaAlAs, Journal of Crystal Growth, 68 (1984) 157-162.

[61] N.I.o. Standards, Technology, NIST Chemistry WebBook, SRD 69, 2022.

[62] M.M. Tomadakis, T.J. Robertson, Viscous permeability of random fiber structures: comparison of electrical and diffusional estimates with experimental and analytical results, Journal of Composite Materials, 39 (2005) 163-188.

[63] V.D. Bruggeman, Berechnung verschiedener physikalischer Konstanten von heterogenen Substanzen. I. Dielektrizitätskonstanten und Leitfähigkeiten der Mischkörper aus isotropen Substanzen, Annalen der physik, 416 (1935) 636-664.

[64] G. Inoue, K. Yokoyama, J. Ooyama, T. Terao, T. Tokunaga, N. Kubo, M. Kawase, Theoretical examination of effective oxygen diffusion coefficient and electrical conductivity of polymer electrolyte fuel cell porous components, Journal of Power Sources, 327 (2016) 610-621.

[65] M.S. El-Sayed, STUDY OF TRANSPORT PHENOMENA IN SANDSTONE SAMPLES IN RELATION TO THE PORE STRUCTURE, University of Waterloo (Canada), Ann Arbor, 1979, pp. 1.

[66] A. Koponen, M. Kataja, J. Timonen, Permeability and effective porosity of porous media, Physical Review E, 56 (1997) 3319.

[67] R. Jones, H. Pollock, D. Geldart, A. Verlinden, Inter-particle forces in cohesive powders studied by AFM: effects of relative humidity, particle size and wall adhesion, Powder Technology, 132 (2003) 196-210.

[68] M. Ciavarella, J. Joe, A. Papangelo, J. Barber, The role of adhesion in contact mechanics, Journal of the Royal Society Interface, 16 (2019) 20180738.

[69] A. Redford, G. Boothroyd, Vibratory feeding, Proceedings of the Institution of Mechanical Engineers, 182 (1967) 135-152.

[70] A. Yanguas-Gil, J.W. Elam, Self-Limited Reaction-Diffusion in Nanostructured Substrates: Surface Coverage Dynamics and Analytic Approximations to ALD Saturation Times, Chemical Vapor Deposition, 18 (2012) 46-52.

[71] A. Yanguas-Gil, J.W. Elam, Diffusion-Reaction Model of ALD in Nanostructured Substrates: Analytic Approximations to Dose Times as a Function of the Surface Reaction Probability, ECS Transactions, 41 (2011) 169.

[72] R.L. Puurunen, Surface chemistry of atomic layer deposition: A case study for the trimethylaluminum/water process, Journal of applied physics, 97 (2005) 9.

[73] A. Paranjpe, S. Gopinath, T. Omstead, R. Bubber, Atomic layer deposition of AlO x for thin film head gap applications, Journal of the Electrochemical Society, 148 (2001) G465.

CHAPTER 6

CONCLUSIONS AND RECOMMENDATIONS

6.1 Summary of Work Completed

Many aspects of the gas-solid flow behavior in continuous spatial particle ALD reactors have been investigated using experiments and simulations in this thesis. A solids-only discrete element method model was developed with a fluctuating gravity condition to explore bulk powder convection during vibration at low gas pressures. The gas phase was incorporated into a CFD-DEM simulation with a new treatment for vibration (kinematically-driven frit particles) to explore aeration and cohesive effects on powder flow. PIV experiments and CFD-DEM simulations revealed the best frit baffle designs for maximizing powder mixing during vibratory convection through the purge zones. A moving porous media model was developed to explore surface titration uniformity and precursor utilization at the reactor scale. Throughout this thesis, simulations were supported by careful experimental characterization of the powder bed and frit materials through powder rheometry, surface profilometry, optical microscopy, particle size analysis, permeability and fluidization curves, tomography, porometry, and porosimetry. A characterization and modeling pipeline was developed for experimentally informed continuum-scale modeling of CVR-ALD (**Figure 6.1**). Coupling numerical studies with experimental validation provided well-tuned modeling inputs with close agreement between experiments and simulations of the CVR-ALD reactor.

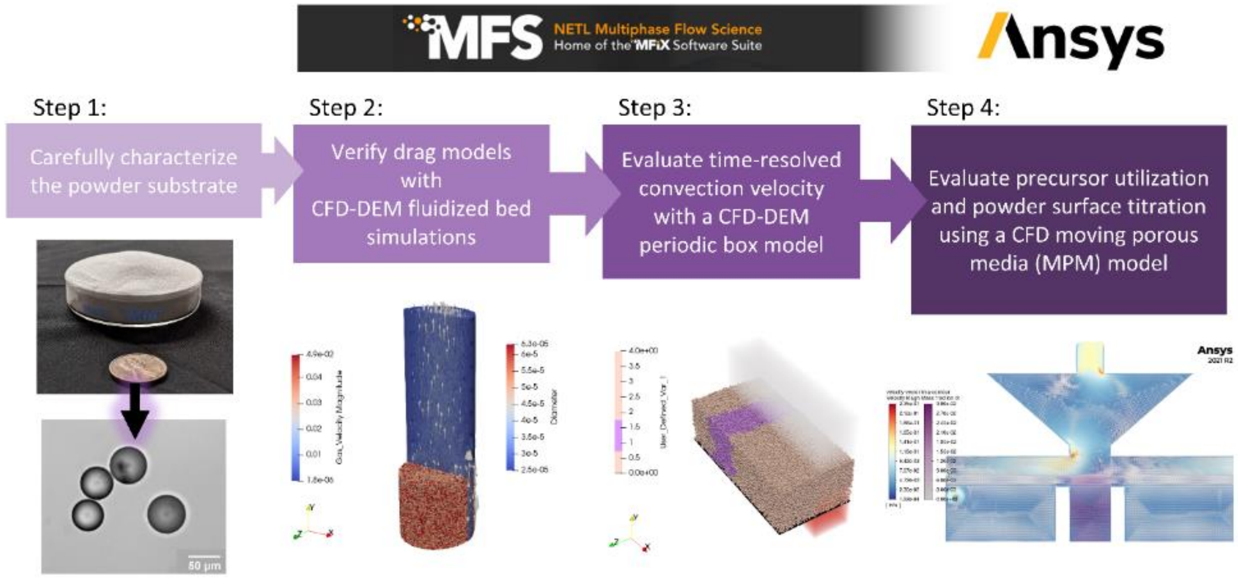

Figure 6.1. Experimental characterization and multiscale modeling workflow pursued in this work

Not all of the CVR-ALD studies produced satisfactory results. Some failed simulations and experiments resulted in teachable moments not explicitly called out in the publications. Limitations of the experimental setup and characterization techniques available had to be examined before modeling efforts were undertaken. The goal of the following section is to address significant challenges encountered during CVR-ALD characterization.

6.2 Primary Challenges

The first hurdle to overcome was achieving reliable powder convection under vibration. The leaf spring support structure and pneumatic actuator received with the CVR-

ALD reactor were originally designed for a much lighter system (**Figure 6.2a**). As a result, the conveyor was significantly underpowered and powder flow could not be achieved unless the reactor was propped at a downward-sloping angle. Declined operation can cause powder bed shearing and exacerbate residence time distributions so steps were undertaken to improve the vibratory conveyor setup. Lengthy discussions with Jay Valuet at Martin Vibration Systems guided the conveyor improvements seen in **Figure 6.2b**. First, the light-duty NTS 350 NF pneumatic actuator was exchanged for an NTK 25-AL linear vibratory with a 1-lb counterweight. The leaf spring bracket base was widened to provide more stability and prevent twisting of the reactor which can lead to powder pooling on one side and poor powder bed convection. Rubber stoppers between the leaf spring bracket and T-slot aluminum frame were also removed to stiffen up the support structure. For reliable powder convection, the base should be heavier and more rigid than the conveyor housing. The original design had a base weight of 93.6 lbs and a stainless steel conveyor housing weight of 103.6 lbs. After adding cylindrical counterweights above the reactor feet and bolting the lower assembly to a welding table (**Figure 6.2b**), at least 100 lbs was added to the base weight and vibration amplitudes were improved significantly. Before conveyor modifications, snakelike flow patterns appeared at many vibration frequencies and stagnating or backwards powder flow zones dominated the convection behavior during horizontal operation (0-degree declination). Steady and consistent hopping powder convection was observed after the conveyor suspension was upgraded.

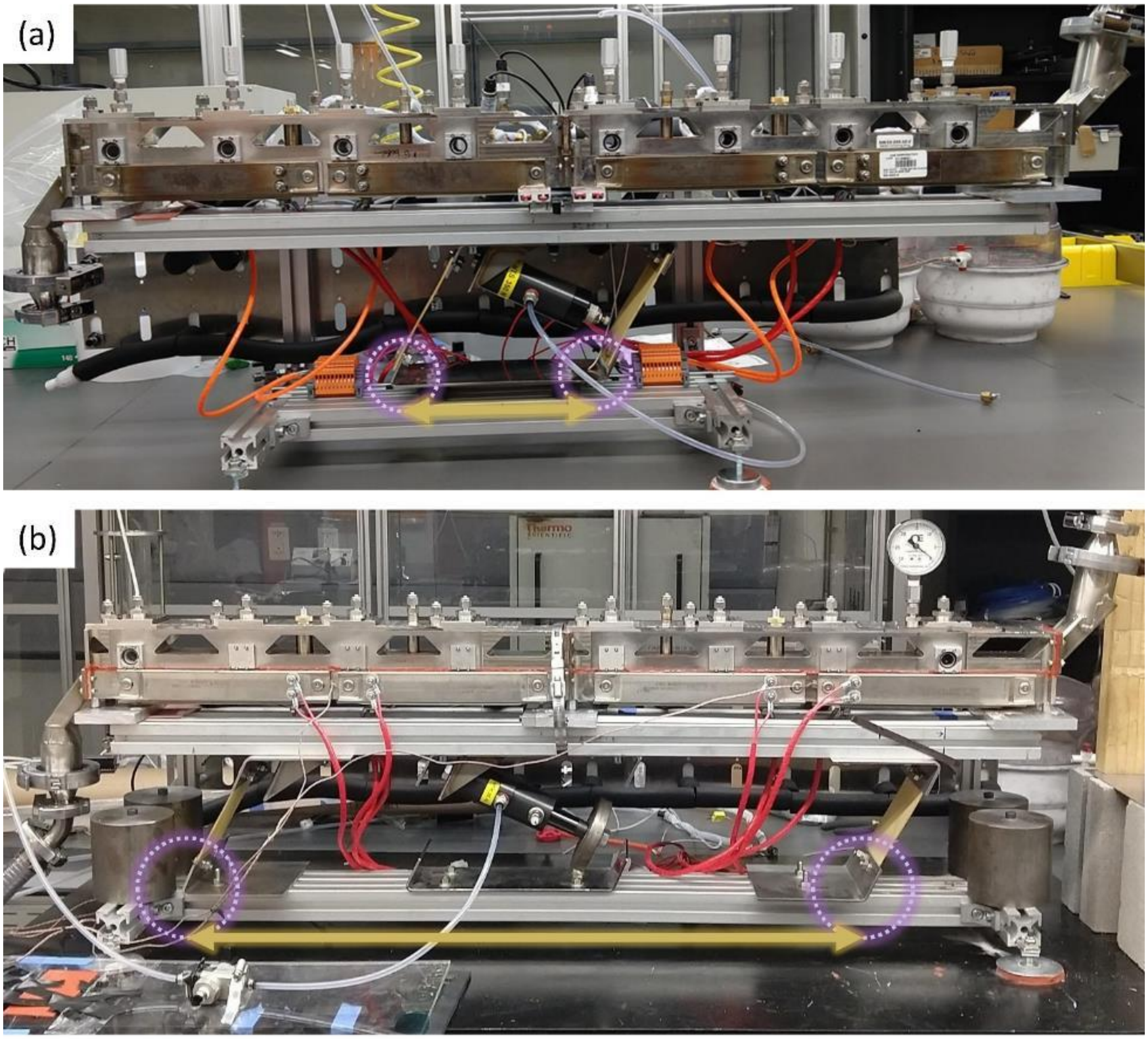

Figure 6.2. (a) Vibratory conveyor suspension as received. (b) Vibratory conveyor suspension after final modifications. The increase in leaf spring separation distance is labeled on the figure

Leak-tight seals were also difficult to achieve with the original reactor design. Mating zones with large surface areas require closely spaced bolts and a smooth o-ring groove with gradual turns. The original design featured deep, discontinuous o-ring grooves and sharp turns around obstacles (**Figure 6.3**). An o-ring groove that is too deep does not compress the o-ring when the assembly is bolted together. Instead, metal-on-metal contact occurs between the mating surfaces. Unless the surfaces in contact are perfectly flat and smooth, gas can flow between roughness elements and wavy segments on the stainless steel surface. Gaps in an o-ring profile also do not prevent gas flow and are unable to seal, especially under vibration. RTV silicone adhesive sealant can be applied to mating surfaces (red rubber lines in **Figure 6.2b**) but must be cleaned off and reapplied every time the reactor is opened. The RTV silicone seals were also not robust to vibration. Several o-ring grooves were also originally machined over a seam between two metal parts (**Figure 6.3a**). Grooves over a seam create a leak point and will not seal. To remedy these issues, seams were welded, surfaces were polished, and grooves were redesigned to provide a more leaktight connection. Despite these modifications, some leaks were still present at certain vibration conditions and under vacuum conditions. A new housing design with thicker walls and closer bolt hole spacing would likely be needed to achieve maximum leak integrity. Time and funding restrictions prevented these changes from taking place over the course of this thesis.

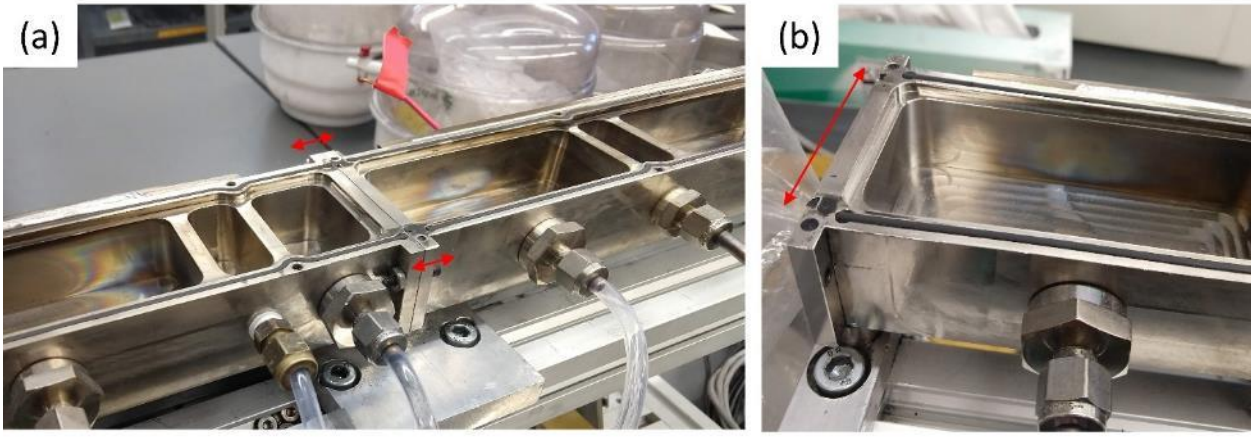

Figure 6.3. Images of discontinuous zones in the o-ring grooves labeled with red arrows. (a) Gap in the o-ring groove when traversing a seam between two mating surfaces. (b) Gap in the o-ring groove at the edge of a part

Several techniques were evaluated as candidates for CVR-ALD reactor modeling before CFD-DEM and moving porous media modeling strategies were selected. The first modeling methodology attempted was the kinetic theory of granular flow (KTGF). KTGF treats the solids phase as a statistical continuum with constitutive models for solids stress[1, 2]. The continuum approach is more computationally efficient for large-scale gas-solid flows than a particle tracking method such as DEM[3]. However, the model was originally developed based on binary collisions and performs poorly for slow flows with high solids packing fractions[1, 4]. KTGF simulations of the CVR-ALD reactor using the dense discrete phase model (DDPM) in ANSYS Fluent produced unphysical powder bed results. Particles in the powder bed would compress and "freeze up" when vibration was turned on in DDPM. Consequently, the KTGF method was disregarded for CVR-ALD reactor modeling. Another low-computational-cost method for dense gas-solid systems is the multiphase particle-in-cell (MP-PIC) approach[5]. MP-PIC maps Lagrangian computational parcels to a grid for approximate particle-particle collision treatment. Friction coefficient at the parcel-wall interface is also not explicitly considered[6]. MP-PIC parcels did not exhibit hopping convection with a fluctuating gravity condition so this method was also abandoned. Other researchers may find success in modeling vibratory powder convection using different constitutive models in KTGF or MP-PIC than were attempted in this thesis.

Advanced microscopy techniques were investigated as a prospect for evaluating particle ALD product uniformity (i.e. surface titration for all particles in a batch). Typical particle ALD film thicknesses are below the diffraction limit of optical microscopes[7], so transmission electron microscopy (TEM) and scanning electroni microscopy (SEM) are needed to visualize film coverage on individual particles. Preparing sample cross-sections for TEM takes anywhere from 30 minutes to hours per particle and is a prohibitively time-consuming method for evaluating large quantities (*i.e.* >100 individual particles) of coated powder. A fluorescence attenuation microscopy technique was attempted for evaluating large powder quantities under an optical microscope based on promising fluorescence quenching results for graphene nanofilms[8]. The idea was to use a fluorescent glass powder, apply an opaque alumina film with ALD, and correlate the amount of fluorescence attenuation to film thickness. However, fluorescence quenching is a special property of graphene caused by photo-induced electron transfer[9, 10]. Alumina nanofilms <300 nm are virtually transparent in the visible spectrum[11] and were not observed to produce a noticeable reduction in the signal from the fluorescent microspheres through attenuation or quenching. Advances in rapid sample preparation or imaging techniques are still needed to enable cost-effective microscopy analysis of coating uniformity in a particle batch.

A key focus in this work was the pursuit of experimentally validated simulations. It is worth noting that multiple experimental techniques may produce different values for the same material property. In particle size analysis, discrepancies in the particle diameter obtained from different techniques, postprocessing algorithms, or even equipment from different manufacturers are widely recognized[12]. Sieve diameter and mean particle diameter from image analysis are not equivalent for nonspherical particles[13]. Careful interpretation of particle size analysis results is needed when using characterization values as modeling inputs. As an example, using laser diffraction mean particle size for CFD-DEM simulations of the finest glass sample (29 micron) was found to give simulated packed bed pressure drops closer to the experimental pressure drop curve than the mean particle size from optical microscopy (19 micron). This trend can be explained by considering how particle diameter is used in CFD calculations. The hydrodynamic mean particle size, which may refer to primary particle or complex agglomerate size, is the value needed for accurate drag calculations in a CFD simulation. For fine particles with high cohesion, the geometric mean particle size may well be lower than the size of a particle agglomerate (i.e. 19 versus

29 microns). This discrepancy was only observed for the finest particle size. Care must be taken in characterizing samples for use as modeling inputs especially as particles get finer and more cohesive.

6.3 Recommendations for Future Work

This thesis presents a first look at modeling continuous spatial particle ALD. The potential avenues for future exploration are too numerous to count. I have provided what I see as the most pressing and promising directions for future work below.

Many substrate powders are more complex than simple glass beads. Nanopowders[14], aspherical particles[15], porous particles[16], polymeric particles[17], and easily broken or highly flexible particles are just a few of the substrate characteristics encountered in particle ALD. Particles with unusual surface morphologies and mechanical properties may require more complex shape handling and contact models for rolling friction or involve interparticle forces beyond van der Waals cohesion. Recent developments in DEM for irregular particle shapes[18-21] provide opportunities to model nonspherical particles with existing software packages. For very fine particles or humid environments, models accounting for additional interparticle forces such as wet cohesion, hydrogen bridging, and electrostatic interactions may need to be incorporated for close agreement with experiments (**Figure 6.4**, adapted from [22-24]). A decrease in particle size is correlated with higher interparticle forces relative to particle weight[25]. Changes in interparticle cohesiveness with surface functionalization between ALD half-cycles may be more significant for finer and lighter substrates. Long-range cohesive interactions can also form multibody particle networks capable of supporting a load, leading to bed cracking and phenomena that require a long-range particle contact model[26, 27].

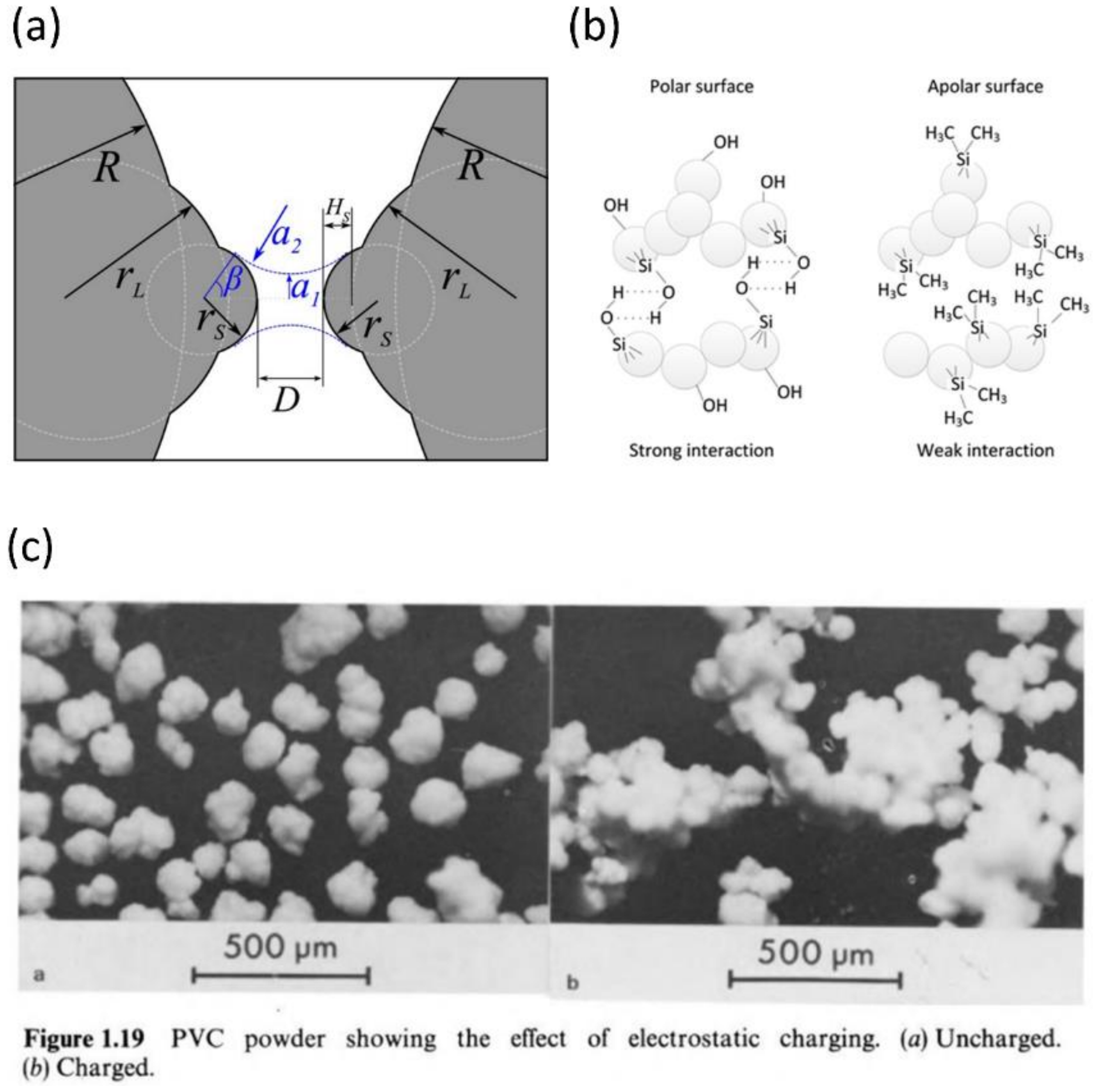

Figure 1.19 PVC powder showing the effect of electrostatic charging. (*a*) Uncharged. (*b*) Charged.

Figure 6.4. Schematic representation of potential cohesive forces. (a) Liquid bridging between spherical particles with asperities. (b) Strong and weak hydrogen bonding between nanoparticles based on surface functionalization (hydroxylated or methylated). (c) Electrostatic attraction between PVC particles

The trimethylaluminum/water alumina ALD chemistry is one of the most extensively studied and "ideal" ALD processes[28]. Other oxides, carbides, nitrides, halides, and pure metals are just a few of the alternative ALD film chemistries. Factors leading to poor film conformality[29] and reproducibility[30] such as nonlinear growth with initial ALD cycles[31], multi-step mechanisms with rate-limiting steps and temperature dependent kinetics, site-blocking by precursor byproducts, soft saturating products, non-self limited and recombination pathways, and "sticky" precursors[32] may limit film conformality in other ALD chemistries but were not considered in this work. Plasma-enhanced ALD has demonstrated great performance benefits for chemistries with high activation energy barriers[33] but relatively few CFD studies exist in this area[34, 35].

A deeper dive into some of the topics covered in this thesis would also be worthwhile. Some powder flow simulations and experiments were performed at low pressures in Chapter 2 but not under high vacuum conditions (<1 Torr). The fluidization and agglomeration behavior of powders in the molecular flow regime may exhibit differences from atmospheric pressure conditions[14, 36]. Experimentally validated drag models for dense particle-laden flows in rarefied regimes are lacking in the literature[37, 38]. The effects of reactor aging such as thermal or mechanical fatigue of the frit material and changing chemical composition of the reactor walls were also not explored in this thesis. Further work is needed to experimentally verify the coating quality produced by continuous spatial particle ALD including comparison to experimental results from fluidized bed particle ALD under the same operating conditions.

The CFD-DEM and MPM models for CVR-ALD were designed to resolve the transient, highly coupled gas-solid flow behavior with explicit vibration treatment. A simpler modeling approach may be appropriate for quasi-steady CVR-ALD flow problems. Based on the results in Chapter 5, vibration promotes diffusion of the gas flow field while powder bed convection produces a dragging on the precursor concentration gradient. By recasting vibration into an effective diffusivity constant and applying momentum sink terms to replicate the bed convection dragging effect, the transient flow simulations from Chapter 5 could be treated as a steady-state flow problem. Whether this simplified treatment could replicate the results of Chapter 5 is beyond the scope of this thesis but poses an interesting question for future investigators.

References

[1] C. Lun, S. Savage, A simple kinetic theory for granular flow of rough, inelastic, spherical particles, (1987).

[2] D. Gidaspow, Hydrodynamics of fiuidizatlon and heat transfer: Supercomputer modeling, (1986).

[3] R. Cocco, W.D. Fullmer, P. Liu, C.M. Hrenya, CFD-DEM: Modeling the small to understand the large, Chemical Engineering Progress, 113 (2017) 38-45.

[4] A. Hashemisohi, L. Wang, A. Shahbazi, Dense discrete phase model coupled with kinetic theory of granular flow to improve predictions of bubbling fluidized bed hydrodynamics, KONA Powder and Particle Journal, 36 (2019) 215-223.

[5] M.J. Andrews, P.J. O'Rourke, The multiphase particle-in-cell (MP-PIC) method for dense particulate flows, International Journal of Multiphase Flow, 22 (1996) 379-402.

[6] M.A. Clarke, J.M. Musser, The mfix particle-in-cell method (mfix-pic) theory guide, National Energy Technology Laboratory (NETL), Pittsburgh, PA, Morgantown, WV …, 2020.

[7] E.H. Stelzer, Beyond the diffraction limit?, Nature, 417 (2002) 806-807.

[8] J. Kim, L.J. Cote, F. Kim, J. Huang, Visualizing graphene based sheets by fluorescence quenching microscopy, Journal of the American Chemical Society, 132 (2010) 260-267.

[9] Y. Wang, Z. Li, J. Wang, J. Li, Y. Lin, Graphene and graphene oxide: biofunctionalization and applications in biotechnology, Trends in biotechnology, 29 (2011) 205-212.

[10] H.R. Matte, K. Subrahmanyam, K.V. Rao, S.J. George, C. Rao, Quenching of fluorescence of aromatic molecules by graphene due to electron transfer, Chemical Physics Letters, 506 (2011) 260-264.

[11] M.M. Aslan, N.A. Webster, C.L. Byard, M.B. Pereira, C.M. Hayes, R.S. Wiederkehr, S.B. Mendes, Low-loss optical waveguides for the near ultra-violet and visible spectral regions with Al2O3 thin films from atomic layer deposition, Thin Solid Films, 518 (2010) 4935-4940.

[12] A. Jillavenkatesa, S.J. Dapkunas, L.-S.H. Lum, Particle size characterization, National Institute of Standards and Technology2001.

[13] J.M. Fernlund, The effect of particle form on sieve analysis: a test by image analysis, Engineering Geology, 50 (1998) 111-124.

[14] L.F. Hakim, J.L. Portman, M.D. Casper, A.W. Weimer, Aggregation behavior of nanoparticles in fluidized beds, Powder Technology, 160 (2005) 149-160.

[15] J.R. Wank, S.M. George, A.W. Weimer, Nanocoating individual cohesive boron nitride particles in a fluidized bed by ALD, Powder Technology, 142 (2004) 59-69.

[16] X. Liang, A.D. Lynn, D.M. King, S.J. Bryant, A.W. Weimer, Biocompatible interface films deposited within porous polymers by atomic layer deposition (ALD), ACS applied materials & interfaces, 1 (2009) 1988-1995.

[17] C. Wilson, J. McCormick, A. Cavanagh, D. Goldstein, A. Weimer, S. George, Tungsten atomic layer deposition on polymers, Thin Solid Films, 516 (2008) 6175-6185.

[18] M. Kodam, R. Bharadwaj, J. Curtis, B. Hancock, C. Wassgren, Force model considerations for glued-sphere discrete element method simulations, Chemical Engineering Science, 64 (2009) 3466-3475.

[19] X. Gao, J. Yu, L. Lu, C. Li, W.A. Rogers, Development and validation of SuperDEM-CFD coupled model for simulating non-spherical particles hydrodynamics in fluidized beds, Chemical Engineering Journal, 420 (2021) 127654.
[20] G. Mollon, J. Zhao, 3D generation of realistic granular samples based on random fields theory and Fourier shape descriptors, Computer Methods in Applied Mechanics and Engineering, 279 (2014) 46-65.
[21] X. Wang, Z. Nie, J. Gong, Z. Liang, Random generation of convex aggregates for DEM study of particle shape effect, Construction and Building Materials, 268 (2021) 121468.
[22] C.Q. LaMarche, A.W. Miller, P. Liu, C.M. Hrenya, Linking micro-scale predictions of capillary forces to macro-scale fluidization experiments in humid environments, AIChE Journal, 62 (2016) 3585-3597.
[23] M. Tahmasebpoor, L. de Martín, M. Talebi, N. Mostoufi, J.R. van Ommen, The role of the hydrogen bond in dense nanoparticle–gas suspensions, Physical Chemistry Chemical Physics, 15 (2013) 5788-5793.
[24] C. Woodcock, J. Mason, Bulk solids handling: an introduction to the practice and technology, Springer Science & Business Media2012.
[25] J.P.K. Seville, C.D. Willett, P.C. Knight, Interparticle forces in fluidisation: a review, Powder Technology, 113 (2000) 261-268.
[26] D. André, M. Jebahi, I. Iordanoff, J.-l. Charles, J. Néauport, Using the discrete element method to simulate brittle fracture in the indentation of a silica glass with a blunt indenter, Computer Methods in Applied Mechanics and Engineering, 265 (2013) 136-147.
[27] B. West, D. O'Connor, M. Parno, M. Krackow, C. Polashenski, Bonded discrete element simulations of sea ice with non-local failure: Applications to Nares Strait, Journal of Advances in Modeling Earth Systems, (2021) e2021MS002614.
[28] R.L. Puurunen, Surface chemistry of atomic layer deposition: A case study for the trimethylaluminum/water process, Journal of applied physics, 97 (2005) 9.
[29] V. Cremers, R.L. Puurunen, J. Dendooven, Conformality in atomic layer deposition: Current status overview of analysis and modelling, Applied Physics Reviews, 6 (2019) 021302.
[30] H.H. Sønsteby, A. Yanguas-Gil, J.W. Elam, Consistency and reproducibility in atomic layer deposition, Journal of Vacuum Science & Technology A: Vacuum, Surfaces, and Films, 38 (2020) 020804.
[31] J. Kim, T.W. Kim, Initial surface reactions of atomic layer deposition, Jom, 61 (2009) 17-22.
[32] A. Yanguas-Gil, J.A. Libera, J.W. Elam, Reactor scale simulations of ALD and ALE: Ideal and non-ideal self-limited processes in a cylindrical and a 300 mm wafer cross-flow reactor, Journal of Vacuum Science & Technology A: Vacuum, Surfaces, and Films, 39 (2021) 062404.
[33] H. Kim, Characteristics and applications of plasma enhanced-atomic layer deposition, Thin Solid Films, 519 (2011) 6639-6644.
[34] M. Crose, W. Zhang, A. Tran, P.D. Christofides, Multiscale three-dimensional CFD modeling for PECVD of amorphous silicon thin films, Computers & Chemical Engineering, 113 (2018) 184-195.
[35] Y. Zhang, Y. Ding, P.D. Christofides, Multiscale computational fluid dynamics modeling and reactor design of plasma-enhanced atomic layer deposition, Computers & Chemical Engineering, 142 (2020) 107066.
[36] J.R. Wank, S.M. George, A.W. Weimer, Vibro-fluidization of fine boron nitride powder at low pressure, Powder Technology, 121 (2001) 195-204.
[37] K.J. Berger, On the Role of Collisions in the Ejection of Lunar Regolith during Spacecraft Landing, University of Colorado at Boulder, 2016.
[38] E. Loth, Compressibility and rarefaction effects on drag of a spherical particle, AIAA journal, 46 (2008) 2219-2228.

COMPLETE BIBLIOGRAPHY

Abrahamsen, A. R., & Geldart, D. (1980). Behaviour of gas-fluidized beds of fine powders part I. Homogeneous expansion. *Powder technology, 26*(1), 35-46. doi:https://doi.org/10.1016/0032-5910(80)85005-4

Abràmoff, M. D., Magalhães, P. J., & Ram, S. J. (2004). Image processing with ImageJ. *Biophotonics international, 11*(7), 36-42.

Adhikari, S., Selvaraj, S., & Kim, D. H. (2018). Progress in powder coating technology using atomic layer deposition. *Advanced Materials Interfaces, 5*(16), 1800581.

Akao, Y., Kunisawa, H., Fan, L., Lai, F., & Wang, R. (1976). Degree of mixedness and contact number A study on the mixture of particulate solids and the structure of solid mixtures. *Powder technology, 15*(2), 267-277.

Anderson, J., Burns, P. J., Milroy, D., Ruprecht, P., Hauser, T., & Siegel, H. J. (2017). Deploying RMACC Summit: an HPC resource for the Rocky Mountain region *Proceedings of the Practice and Experience in Advanced Research Computing 2017 on Sustainability, Success and Impact* (pp. 1-7).

Anderson, T. B., & Jackson, R. (1967). Fluid mechanical description of fluidized beds. Equations of motion. *Industrial & Engineering Chemistry Fundamentals, 6*(4), 527-539.

André, D., Jebahi, M., Iordanoff, I., Charles, J.-l., & Néauport, J. (2013). Using the discrete element method to simulate brittle fracture in the indentation of a silica glass with a blunt indenter. *Computer Methods in Applied Mechanics and Engineering, 265*, 136-147.

Andrews, M. J., & O'Rourke, P. J. (1996). The multiphase particle-in-cell (MP-PIC) method for dense particulate flows. *International journal of multiphase flow, 22*(2), 379-402.

Ansys. (2015). Fluent 17.0 Theory Guide. *ANSYS inc*.

ANSYS (Producer). (2016). #2002733 How are sticking coefficient reactions converted into Arrhenius rate format? *Knowledge Resources: Solutions*. [Resolution Document]

Ashrafizadeh, H., & Ziaei-Rad, S. (2013). A numerical 2D simulation of part motion in vibratory bowl feeders by discrete element method. *Journal of Sound and Vibration, 332*(13), 3303-3314.

Aslan, M. M., Webster, N. A., Byard, C. L., Pereira, M. B., Hayes, C. M., Wiederkehr, R. S., & Mendes, S. B. (2010). Low-loss optical waveguides for the near ultra-violet and visible spectral regions with Al2O3 thin films from atomic layer deposition. *Thin Solid Films, 518*(17), 4935-4940.

Asmar, B., Langston, P., & Matchett, A. (2002). A generalised mixing index in distinct element method simulation of vibrated particulate beds. *Granular Matter, 4*(3), 129-138.

Balaji, B., Gupta Burela, R., & Ponniah, G. (2022). Dynamics of part motion on a linear vibratory feeder. *Proceedings of the Institution of Mechanical Engineers, Part C: Journal of Mechanical Engineering Science, 236*(2), 886-893.

Barletta, D., & Poletto, M. (2012). Aggregation phenomena in fluidization of cohesive powders assisted by mechanical vibrations. *Powder technology, 225*, 93-100.

Barron, A. R. (2020). осаждение атомных слоев. Retrieved from https://thesaurus.rusnano.com/wiki/article1449

Bear, J. (2013). *Dynamics of fluids in porous media*: Courier Corporation.

Beard, D., & Weyl, P. (1973). Influence of texture on porosity and permeability of unconsolidated sand. *AAPG bulletin, 57*(2), 349-369.

Beetstra, R., Lafont, U., Nijenhuis, J., Kelder, E. M., & van Ommen, J. R. (2009). Atmospheric pressure process for coating particles using atomic layer deposition. *Chemical Vapor Deposition, 15*(7-9), 227-233.

Benyahia, S. (2020). Simulating the Formation of Granular Jets. *Industrial & Engineering Chemistry Research, 59*(17), 8416-8425.

Berg, C. F. (2014). Permeability description by characteristic length, tortuosity, constriction and porosity. *Transport in porous media, 103*(3), 381-400.

Berger, K. J. (2016). *On the Role of Collisions in the Ejection of Lunar Regolith during Spacecraft Landing.* University of Colorado at Boulder.

Berry, P. (1959). Basic theory of low acceleration oscillating conveyors.

Bhalode, P., & Ierapetritou, M. (2020). A review of existing mixing indices in solid-based continuous blending operations. *Powder technology, 373*, 195-209.

Booth, J., & McCallion, H. (1963). On predicting the mean conveying velocity of a vibratory conveyor. *Proceedings of the Institution of Mechanical Engineers, 178*(1), 521-532.

Bottcher, S. (1958). Contribution to the problem of conveying materials by oscillating conveyors. *Foerdern und Heben (3)*, 127-131.

Boukouvala, F., Gao, Y., Muzzio, F., & Ierapetritou, M. G. (2013). Reduced-order discrete element method modeling. *Chemical Engineering Science, 95*, 12-26.

Boyce, C. M. (2018). Gas-solid fluidization with liquid bridging: A review from a modeling perspective. *Powder technology, 336*, 12-29.

Bridgwater, J. (1976). Fundamental powder mixing mechanisms. *Powder technology, 15*(2), 215-236.

Brinker, C., Hurd, A., Schunk, P., Frye, G., & Ashley, C. (1992). Review of sol-gel thin film formation. *Journal of Non-Crystalline Solids, 147*, 424-436.

Brone, D., Wightman, C., Connor, K., Alexander, A., Muzzio, F., & Robinson, P. (1997). Using flow perturbations to enhance mixing of dry powders in V-blenders. *Powder technology, 91*(3), 165-172.

Bruggeman, V. D. (1935). Berechnung verschiedener physikalischer Konstanten von heterogenen Substanzen. I. Dielektrizitätskonstanten und Leitfähigkeiten der Mischkörper aus isotropen Substanzen. *Annalen der physik, 416*(7), 636-664.

Cahn, D., Healy, T., & Fuerstenau, D. (1965). Blender geometry in mixing of solids. *Industrial & Engineering Chemistry Process Design and Development, 4*(3), 318-322.

Campbell, C. S. (1993). Boundary interactions for two-dimensional granular flows. Part 2. Roughened boundaries. *Journal of Fluid Mechanics, 247*, 137-156.

Capece, M., Ho, R., Strong, J., & Gao, P. (2015). Prediction of powder flow performance using a multi-component granular Bond number. *Powder technology, 286*, 561-571.

Capone, G., D'Agostino, V., Della Valle, S., & Guida, D. (1993). Influence of the variation between static and kinetic friction on stick-slip instability. *Wear, 161*(1-2), 121-126.

Carman, P. C. (1937). Fluid flow through granular beds. *Trans. Inst. Chem. Eng., 15*, 150-166.

Carrier, J. R. M. (1958). Conveyor for mixing and de-aerating: Google Patents.

Carrier, J. R. M., & Morris, J. M. (1956). De-aerating conveyor: Google Patents.

Chandratilleke, G. R., Yu, A., Bridgwater, J., & Shinohara, K. (2012). A particle-scale index in the quantification of mixing of particles. *AIChE journal, 58*(4), 1099-1118.

Chandratilleke, G. R., Zhou, Y., Yu, A., & Bridgwater, J. (2010). Effect of blade speed on granular flow and mixing in a cylindrical mixer. *Industrial & Engineering Chemistry Research, 49*(11), 5467-5478.

Chandravanshi, M. L., & Mukhopadhyay, A. K. (2017). Dynamic analysis of vibratory feeder and their effect on feed particle speed on conveying surface. *Measurement, 101*, 145-156. doi:https://doi.org/10.1016/j.measurement.2017.01.031

Chang, S.-Y., Li, S. W., Kowsari, K., Shetty, A., Sorrells, L., Sen, K., . . . Ma, A. W. (2020). Binder-jet 3D printing of indomethacin-laden pharmaceutical dosage forms. *Journal of pharmaceutical sciences, 109*(10), 3054-3063.

Cheimarios, N., To, D., Kokkoris, G., Memos, G., & Boudouvis, A. G. (2021). Monte carlo and kinetic monte carlo models for deposition processes: a review of recent works. *Front. Phys. 9: 631918. doi: 10.3389/fphy*.

Choi, H., & Mills, A. (1990). Heat and mass transfer in metal hydride beds for heat pump applications. *International Journal of Heat and Mass Transfer, 33*(6), 1281-1288.

Chung, Y., Liao, H., & Hsiau, S. (2013). Convection behavior of non-spherical particles in a vibrating bed: Discrete element modeling and experimental validation. *Powder technology, 237*, 53-66.

Ciavarella, M., Joe, J., Papangelo, A., & Barber, J. (2019). The role of adhesion in contact mechanics. *Journal of the Royal Society Interface, 16*(151), 20180738.

Clarke, M. A., & Musser, J. M. (2020). *The mfix particle-in-cell method (mfix-pic) theory guide*. Retrieved from

Cocco, R., Fullmer, W. D., Liu, P., & Hrenya, C. M. (2017). CFD-DEM: Modeling the small to understand the large. *Chemical Engineering Progress, 113*(9), 38-45.

Coile, M. W., Young, M. J., Libera, J. A., Mane, A. U., & Elam, J. W. (2020). High-capacity rotary drum for atomic layer deposition onto powders and small mechanical parts in a hot-walled viscous flow reactor. *Journal of Vacuum Science & Technology A: Vacuum, Surfaces, and Films, 38*(5), 052403.

Cong, W., Li, Z., Cao, K., Feng, G., & Chen, R. (2020). Transient analysis and process optimization of the spatial atomic layer deposition using the dynamic mesh method. *Chemical Engineering Science, 217*, 115513. doi:https://doi.org/10.1016/j.ces.2020.115513

Cooper, S. J., Bertei, A., Shearing, P. R., Kilner, J., & Brandon, N. P. (2016). TauFactor: An open-source application for calculating tortuosity factors from tomographic data. *SoftwareX, 5*, 203-210.

Cooper, S. J., Kishimoto, M., Tariq, F., Bradley, R. S., Marquis, A. J., Brandon, N. P., . . . Shearing, P. R. (2013). Microstructural analysis of an LSCF cathode using in situ tomography and simulation. *ECS Transactions, 57*(1), 2671.

Cremers, V., Puurunen, R. L., & Dendooven, J. (2019). Conformality in atomic layer deposition: Current status overview of analysis and modelling. *Applied Physics Reviews, 6*(2), 021302.

Crose, M., Zhang, W., Tran, A., & Christofides, P. D. (2018). Multiscale three-dimensional CFD modeling for PECVD of amorphous silicon thin films. *Computers & Chemical Engineering, 113*, 184-195.

Cundall, P. A., & Strack, O. D. (1979). A discrete numerical model for granular assemblies. *geotechnique, 29*(1), 47-65.

Czok, G. S., & Werther, J. (2006). Liquid spray vs. gaseous precursor injection—its influence on the performance of particle coating by CVD in the fluidized bed. *Powder technology, 162*(2), 100-110.

de Martín, L., Bouwman, W. G., & van Ommen, J. R. (2014). Multidimensional nature of fluidized nanoparticle agglomerates. *Langmuir, 30*(42), 12696-12702.

Deng, Z., He, W., Duan, C., Shan, B., & Chen, R. (2016). Atomic layer deposition process optimization by computational fluid dynamics. *Vacuum, 123*, 103-110.

Dickinson, J., Hariadi, R., Scudiero, L., & Langford, S. (1999). A scanning force microscope study of detachment of nanometer-sized particles from glass surfaces. *Tribology Letters, 7*(2-3), 113-119.

Digital Asset Library. (2022). from Anton Paar https://digitalasset.anton-paar.com/#search-text=POwder&search-assettype=40000&search-info-217=218&details=4172

Dintwa, E., Tijskens, E., & Ramon, H. (2008). On the accuracy of the Hertz model to describe the normal contact of soft elastic spheres. *Granular Matter, 10*(3), 209-221.

Douady, S., Fauve, S., & Laroche, C. (1989). Subharmonic instabilities and defects in a granular layer under vertical vibrations. *EPL (Europhysics Letters), 8*(7), 621.

Duan, C.-L., Deng, Z., Cao, K., Yin, H.-F., Shan, B., & Chen, R. (2016). Surface passivation of Fe3O4 nanoparticles with Al2O3 via atomic layer deposition in a rotating fluidized bed reactor. *Journal of Vacuum Science & Technology A: Vacuum, Surfaces, and Films, 34*(4), 04C103.

Duan, C.-L., Liu, X., Shan, B., & Chen, R. (2015). Fluidized bed coupled rotary reactor for nanoparticles coating via atomic layer deposition. *Review of Scientific Instruments, 86*(7), 075101.

Dullien, F. A. (2012). *Porous media: fluid transport and pore structure*: Academic press.

Duran, J. (2012). *Sands, powders, and grains: an introduction to the physics of granular materials*: Springer Science & Business Media.

Dwivedi, V., & Adomaitis, R. A. (2009). Multiscale simulation and optimization of an atomic layer deposition process in a nanoporous material. *ECS Transactions, 25*(8), 115.

El-Sayed, M. S. (1979). *STUDY OF TRANSPORT PHENOMENA IN SANDSTONE SAMPLES IN RELATION TO THE PORE STRUCTURE.* (NK39858 Ph.D.), University of Waterloo (Canada), Ann Arbor. Retrieved from https://colorado.idm.oclc.org/login?url=https://www.proquest.com/dissertations-theses/study-transport-phenomena-sandstone-samples/docview/302959799/se-2?accountid=14503

http://rp8jq9jy4s.search.serialssolutions.com?ctx_ver=Z39.88-2004&ctx_enc=info:ofi/enc:UTF-8&rfr_id=info:sid/ProQuest+Dissertations+%26+Theses+Global&rft_val_fmt=info:ofi/fmt:kev:mtx:dissertation&rft.genre=dissertations+%26+theses&rft.jtitle=&rft.atitle=&rft.au=EL-SAYED%2C+MOHAMED+SAMIR&rft.aulast=EL-SAYED&rft.aufirst=MOHAMED&rft.date=1979-01-01&rft.volume=&rft.issue=&rft.spage=&rft.isbn=9798660296840&rft.btitle=&rft.title=STUDY+OF+TRANSPORT+PHENOMENA+IN+SANDSTONE+SAMPLES+IN+RELATION+TO+THE+PORE+STRUCTURE.&rft.issn=&rft_id=info:doi/ ProQuest Dissertations & Theses A&I; ProQuest Dissertations & Theses Global database.

Elajnaf, A., Carter, P., & Rowley, G. (2006). Electrostatic characterisation of inhaled powders: effect of contact surface and relative humidity. *European journal of pharmaceutical sciences, 29*(5), 375-384.

Elam, J., Routkevitch, D., Mardilovich, P., & George, S. (2003). Conformal coating on ultrahigh-aspect-ratio nanopores of anodic alumina by atomic layer deposition. *Chemistry of materials, 15*(18), 3507-3517.

Epstein, N. (1989). On tortuosity and the tortuosity factor in flow and diffusion through porous media. *Chemical Engineering Science, 44*(3), 777-779.

Eric, B. C., Luke, F., Josef, D., Michael, T., Alberto, F.-N., & Jean-François, D. (2022). Investigating the rheology of fluidized and non-fluidized gas-particle beds: implications for the dynamics of geophysical flows and substrate entrainment. *Granular Matter, 24*(1), 1-25.

Evans, R. W. (1963). Means for aerating granular and pulverulent materials: Google Patents.

Evans, R. W., & Morris, J. M. (1962). Method and apparatus for moving pulverulent materials: Google Patents.

Fan, L., Chen, S., & Watson, C. (1970). Annual review solids mixing. *Industrial & Engineering Chemistry, 62*(7), 53-69.

Fan, L., Chen, Y.-M., & Lai, F. (1990). Recent developments in solids mixing. *Powder technology, 61*(3), 255-287.

Ferguson, J., Buechler, K., Weimer, A., & George, S. (2005). SnO2 atomic layer deposition on ZrO2 and Al nanoparticles: pathway to enhanced thermite materials. *Powder technology, 156*(2-3), 154-163.

Ferguson, J., Weimer, A., & George, S. (2002). Atomic layer deposition of boron nitride using sequential exposures of BCl3 and NH3. *Thin Solid Films, 413*(1-2), 16-25.

Fernlund, J. M. (1998). The effect of particle form on sieve analysis: a test by image analysis. *Engineering Geology, 50*(1-2), 111-124.

Foerster, S. F., Louge, M. Y., Chang, H., & Allia, K. (1994). Measurements of the collision properties of small spheres. *Physics of Fluids, 6*(3), 1108-1115.

Fukunishi, A., & Mori, Y. (2006). Adhesion force between particles and substrate in a humid atmosphere studied by atomic force microscopy. *Advanced Powder Technology, 17*(5), 567-580.

Gakis, G., Vergnes, H., Scheid, E., Vahlas, C., Caussat, B., & Boudouvis, A. G. (2018). Computational fluid dynamics simulation of the ALD of alumina from TMA and H2O in a commercial reactor. *Chemical Engineering Research and Design, 132*, 795-811.

Gallas, J. A., Herrmann, H. J., Pöschel, T., & Sokołowski, S. (1996). Molecular dynamics simulation of size segregation in three dimensions. *Journal of Statistical Physics, 82*(1), 443-450.

Galvin, J. E., & Benyahia, S. (2014). The effect of cohesive forces on the fluidization of aeratable powders. *AIChE journal, 60*(2), 473-484.

Ganapathy, S., & Parameswaran, M. (1987). Effect of material loading on the starting and transition over resonance of a vibratory conveyor. *Mechanism and Machine Theory, 22*(2), 169-176.

Gao, X., Yu, J., Lu, L., Li, C., & Rogers, W. A. (2021). Development and validation of SuperDEM-CFD coupled model for simulating non-spherical particles hydrodynamics in fluidized beds. *Chemical Engineering Journal, 420*, 127654.

Garg, R., Galvin, J., Li, T., & Pannala, S. (2012). Open-source MFIX-DEM software for gas–solids flows: Part I—Verification studies. *Powder technology, 220*, 122-137.

Ge, W., Chang, Q., Li, C., & Wang, J. (2019). Multiscale structures in particle–fluid systems: Characterization, modeling, and simulation. *Chemical Engineering Science, 198*, 198-223.

Geldart, D. (1973). Types of gas fluidization. *Powder technology, 7*(5), 285-292.

George, S., Ott, A., & Klaus, J. (1996). Surface chemistry for atomic layer growth. *The Journal of Physical Chemistry, 100*(31), 13121-13131.

George, S. M. (2010). Atomic layer deposition: an overview. *Chemical reviews, 110*(1), 111-131.

Gidaspow, D. (1986). Hydrodynamics of fiuidizatlon and heat transfer: Supercomputer modeling.

Gordon, R. G., Hausmann, D., Kim, E., & Shepard, J. (2003). A kinetic model for step coverage by atomic layer deposition in narrow holes or trenches. *Chemical Vapor Deposition, 9*(2), 73-78.

Goulas, A., & Van Ommen, J. R. (2013). Atomic layer deposition of platinum clusters on titania nanoparticles at atmospheric pressure. *Journal of Materials Chemistry A, 1*(15), 4647-4650.

Granneman, E., Fischer, P., Pierreux, D., Terhorst, H., & Zagwijn, P. (2007). Batch ALD: Characteristics, comparison with single wafer ALD, and examples. *Surface and Coatings Technology, 201*(22-23), 8899-8907.

Grillo, F., Kreutzer, M. T., & van Ommen, J. R. (2015). Modeling the precursor utilization in atomic layer deposition on nanostructured materials in fluidized bed reactors. *Chemical Engineering Journal, 268*, 384-398.

Grochowski, R., Walzel, P., Rouijaa, M., Kruelle, C. A., & Rehberg, I. (2004). Reversing granular flow on a vibratory conveyor. *Applied physics letters, 84*(6), 1019-1021.

Groner, M., Fabreguette, F., Elam, J., & George, S. (2004). Low-temperature Al2O3 atomic layer deposition. *Chemistry of materials, 16*(4), 639-645.

Gu, Y., Ozel, A., Kolehmainen, J., & Sundaresan, S. (2019). Computationally generated constitutive models for particle phase rheology in gas-fluidized suspensions. *Journal of Fluid Mechanics, 860*, 318-349.

Gu, Y., Ozel, A., & Sundaresan, S. (2016). A modified cohesion model for CFD–DEM simulations of fluidization. *Powder technology, 296*, 17-28.

Guerra-Nuñez, C., Döbeli, M., Michler, J., & Utke, I. (2017). Reaction and growth mechanisms in Al2O3 deposited via atomic layer deposition: elucidating the hydrogen source. *Chemistry of materials, 29*(20), 8690-8703.

Guo, Q., & Boyce, C. M. (2022). Structured bubbling in layered gas-fluidized beds subject to vibration: A CFD-DEM study. *AIChE journal*, e17709.

Guo, Q., Zhang, Y., Vazquez, C., Xi, K., & Boyce, C. M. (2022). Multi-Fluid Model Simulations of Gravitational Instabilities in Fluidized Binary Granular Materials. *AIChE journal*, e17714.

Hagemeier, T., Börner, M., Bück, A., & Tsotsas, E. (2015). A comparative study on optical techniques for the estimation of granular flow velocities. *Chemical Engineering Science, 131*, 63-75.

Hakim, L. F., George, S. M., & Weimer, A. W. (2005). Conformal nanocoating of zirconia nanoparticles by atomic layer deposition in a fluidized bed reactor. *Nanotechnology, 16*(7), S375.

Hakim, L. F., Portman, J. L., Casper, M. D., & Weimer, A. W. (2005). Aggregation behavior of nanoparticles in fluidized beds. *Powder technology, 160*(3), 149-160.

Halford, W., Lawler, C., Grima, A. P., & Arnold, P. C. (2013). Some influences on wall friction measurements-a preliminary investigation.

Halidan, M., Chandratilleke, G. R., Dong, K., & Yu, A. (2016). The effect of interparticle cohesion on powder mixing in a ribbon mixer. *AIChE journal, 62*(4), 1023-1037.

Hancock, B. C. (2019). The wall friction properties of pharmaceutical powders, blends, and granulations. *Journal of pharmaceutical sciences, 108*(1), 457-463.

Harsha, A., Limaye, P., Tyagi, R., & Gupta, A. (2016). Effect of Temperature on Galling Behavior of SS 316, 316 L and 416 Under Self-Mated Condition. *Journal of Materials Engineering and Performance, 25*(11), 4980-4987.

Hartig, J., Howard, H. C., Stelmach, T. J., & Weimer, A. W. (2021). DEM modeling of fine powder convection in a continuous vibrating bed reactor. *Powder technology*.

Hartig, J., Shetty, A., Conklin, D. R., & Weimer, A. W. (2022). Aeration and cohesive effects on flowability in a vibrating powder conveyor. *Powder technology, 408*, 117724. doi:https://doi.org/10.1016/j.powtec.2022.117724

Hashemisohi, A., Wang, L., & Shahbazi, A. (2019). Dense discrete phase model coupled with kinetic theory of granular flow to improve predictions of bubbling fluidized bed hydrodynamics. *KONA Powder and Particle Journal, 36*, 215-223.

Hashemnia, K., & Pourandi, S. (2018). Study the effect of vibration frequency and amplitude on the quality of fluidization of a vibrated granular flow using discrete element method. *Powder technology, 327*, 335-345.

Hastie, D. B., & Halford, W. G. (2016). Preliminary observations of the effect of plate roughness and particle size on the determination of wall friction.

Heijs, A. W., & Lowe, C. P. (1995). Numerical evaluation of the permeability and the Kozeny constant for two types of porous media. *Physical Review E, 51*(5), 4346.

Hirschberg, C., Jensen, N. S., Boetker, J., Madsen, A. Ø., Kääriäinen, T. O., Kääriäinen, M.-L., . . . Sun, C. C. (2019). Improving Powder Characteristics by Surface Modification Using Atomic Layer Deposition. *Organic Process Research & Development, 23*(11), 2362-2368.

Hogue, C., & Newland, D. (1994). Efficient computer simulation of moving granular particles. *Powder technology, 78*(1), 51-66.

Hoskins, A. L., McNeary, W. W., Millican, S. L., Gossett, T. A., Lai, A., Gao, Y., . . . Weimer, A. W. (2019). Nonuniform growth of sub-2 nanometer atomic layer deposited alumina films on lithium nickel manganese cobalt oxide cathode battery materials. *ACS Applied Nano Materials, 2*(11), 6989-6997.

Iams, A., Gao, M., Shetty, A., & Palmer, T. (2022). Influence of particle size on powder rheology and effects on mass flow during directed energy deposition additive manufacturing. *Powder technology, 396*, 316-326.

Inoue, G., Yokoyama, K., Ooyama, J., Terao, T., Tokunaga, T., Kubo, N., & Kawase, M. (2016). Theoretical examination of effective oxygen diffusion coefficient and electrical conductivity of polymer electrolyte fuel cell porous components. *Journal of Power Sources, 327*, 610-621.

Israelachvili, J. N. (2011). *Intermolecular and surface forces*: Academic press.

Jahani, M., Farzanegan, A., & Noaparast, M. (2015). Investigation of screening performance of banana screens using LIGGGHTS DEM solver. *Powder technology, 283*, 32-47.

Jänchen, J., Herzog, T. H., Gleichmann, K., Unger, B., Brandt, A., Fischer, G., & Richter, H. (2015). Performance of an open thermal adsorption storage system with Linde type A zeolites: Beads versus honeycombs. *Microporous and Mesoporous Materials, 207*, 179-184.

Jange, C. G., Taku, P., Peng, S., Dixon, M. P., Shetty, A., & Ambrose, R. K. (2020). Cohesivity assessment of semi-crystalline and crystalline powders using a Warren Springs cohesion tester. *Powder technology, 371*, 96-105.

Jerri, A. J. (2013). *The Gibbs phenomenon in Fourier analysis, splines and wavelet approximations* (Vol. 446): Springer Science & Business Media.

Jiang, M., Zhao, Y., Liu, G., & Zheng, J. (2011). Enhancing mixing of particles by baffles in a rotating drum mixer. *Particuology, 9*(3), 270-278.

Jillavenkatesa, A., Dapkunas, S. J., & Lum, L.-S. H. (2001). *Particle size characterization* (Vol. 960): National Institute of Standards and Technology.

Johnson, G., Rajagopal, K. R., & Massoudi, M. (1990). A review of interaction mechanisms in fluid-solid flows.

Jones, R., Pollock, H., Geldart, D., & Verlinden, A. (2003). Inter-particle forces in cohesive powders studied by AFM: effects of relative humidity, particle size and wall adhesion. *Powder technology, 132*(2-3), 196-210.

Jung, Y. S., Cavanagh, A. S., Dillon, A. C., Groner, M. D., George, S. M., & Lee, S.-H. (2009). Enhanced stability of LiCoO2 cathodes in lithium-ion batteries using surface modification by atomic layer deposition. *Journal of the Electrochemical Society, 157*(1), A75.

Jur, J. S., & Parsons, G. N. (2011). Atomic layer deposition of Al2O3 and ZnO at atmospheric pressure in a flow tube reactor. *ACS applied materials & interfaces, 3*(2), 299-308.

Kammer, D. C., & Tinker, M. L. (2004). Optimal placement of triaxial accelerometers for modal vibration tests. *Mechanical systems and signal processing, 18*(1), 29-41.

Katainen, J., Paajanen, M., Ahtola, E., Pore, V., & Lahtinen, J. (2006). Adhesion as an interplay between particle size and surface roughness. *Journal of colloid and interface science, 304*(2), 524-529.

Kaviany, M. (2012). *Principles of heat transfer in porous media*: Springer Science & Business Media.

Kawashima, K., Ito, T., & Nagata, Y. (2010). Detection and imaging of nonmetallic inclusions in continuously cast steel plates by higher harmonics. *Japanese Journal of Applied Physics, 49*(7S), 07HC11.

Kellogg, K. M., Liu, P., LaMarche, C. Q., & Hrenya, C. M. (2017). Continuum theory for rapid cohesive-particle flows: general balance equations and discrete-element-method-based closure of cohesion-specific quantities. *Journal of Fluid Mechanics, 832*, 345-382.

Kennard, E. H. (1938). *Kinetic theory of gases* (Vol. 483): McGraw-hill New York.

Kessels, W. E., & Putkonen, M. (2011). Advanced process technologies: Plasma, direct-write, atmospheric pressure, and roll-to-roll ALD. *Mrs Bulletin, 36*(11), 907-913.

Kim, H. (2011). Characteristics and applications of plasma enhanced-atomic layer deposition. *Thin Solid Films, 519*(20), 6639-6644.

Kim, J., Cote, L. J., Kim, F., & Huang, J. (2010). Visualizing graphene based sheets by fluorescence quenching microscopy. *Journal of the American Chemical Society, 132*(1), 260-267.

Kim, J., & Kim, T. W. (2009). Initial surface reactions of atomic layer deposition. *Jom, 61*(6), 17-22.

King, D. M., Spencer II, J. A., Liang, X., Hakim, L. F., & Weimer, A. W. (2007). Atomic layer deposition on particles using a fluidized bed reactor with in situ mass spectrometry. *Surface and Coatings Technology, 201*(22-23), 9163-9171.

Kobayashi, T., Tanaka, T., Shimada, N., & Kawaguchi, T. (2013). DEM–CFD analysis of fluidization behavior of Geldart Group A particles using a dynamic adhesion force model. *Powder technology, 248*, 143-152.

Kodam, M., Bharadwaj, R., Curtis, J., Hancock, B., & Wassgren, C. (2009). Force model considerations for glued-sphere discrete element method simulations. *Chemical Engineering Science, 64*(15), 3466-3475.

Koponen, A., Kataja, M., & Timonen, J. (1997). Permeability and effective porosity of porous media. *Physical Review E, 56*(3), 3319.

Kováčik, J. (1999). Correlation between Young's modulus and porosity in porous materials. *Journal of materials science letters, 18*(13), 1007-1010.

Kováčik, J. (2001). Correlation between shear modulus and porosity in porous materials. *Journal of materials science letters, 20*(21), 1953-1955.

Kroll, W. (1954). Über das Verhalten von Schüttgut in lotrechi schwingenden Gefäßen. *Forschung auf dem Gebiet des Ingenieurwesens A, 20*(1), 2-15.

Kruggel-Emden, H., Simsek, E., Wirtz, S., & Scherer, V. (2007). A comparative numerical study of particle mixing on different grate designs through the discrete element method. *Journal of Pressure Vessel Technology, 129*(4), 593-600.

Krynock, R. A. (1993). Vibratory blender/conveyor: Google Patents.

Kunii, D., & Levenspiel, O. (1991). *Fluidization engineering*: Butterworth-Heinemann.

Kuo, H. P., Knight, P. C., Parker, D. J., Tsuji, Y., Adams, M. J., & Seville, J. P. K. (2002). The influence of DEM simulation parameters on the particle behaviour in a V-mixer. *Chemical Engineering Science, 57*(17), 3621-3638. doi:https://doi.org/10.1016/S0009-2509(02)00086-6

Lacey, P. M. C. (1954). Developments in the theory of particle mixing. *Journal of applied chemistry, 4*(5), 257-268.

Lakomaa, E.-L. (1994). Atomic layer epitaxy (ALE) on porous substrates. *Applied surface science, 75*(1-4), 185-196.

Lakomaa, E.-L., Haukka, S., & Suntola, T. (1992). Atomic layer growth of TiO2 on silica. *Applied surface science, 60*, 742-748.

LaMarche, C., Liu, P., Kellogg, K., & Hrenya, C. (2017). Fluidized-bed measurements of carefully-characterized, mildly-cohesive (Group A) particles. *Chemical Engineering Journal, 310*, 259-271.

LaMarche, C. Q., Leadley, S., Liu, P., Kellogg, K. M., & Hrenya, C. M. (2017). Method of quantifying surface roughness for accurate adhesive force predictions. *Chemical Engineering Science, 158*, 140-153.

LaMarche, C. Q., Liu, P., Kellogg, K. M., Weimer, A. W., & Hrenya, C. M. (2015). A system-size independent validation of CFD-DEM for noncohesive particles. *AIChE journal, 61*(12), 4051-4058.

LaMarche, C. Q., Miller, A. W., Liu, P., & Hrenya, C. M. (2016). Linking micro-scale predictions of capillary forces to macro-scale fluidization experiments in humid environments. *AIChE journal, 62*(10), 3585-3597.

Lankhorst, A., Paarhuis, B., Terhorst, H., Simons, P., & Kleijn, C. (2007). Transient ALD simulations for a multi-wafer reactor with trenched wafers. *Surface and Coatings Technology, 201*(22-23), 8842-8848.

Li, J., Webb, C., Pandiella, S. S., & Campbell, G. M. (2003). Discrete particle motion on sieves—a numerical study using the DEM simulation. *Powder technology, 133*(1-3), 190-202.

Li, Z., Li, J., Liu, X., & Chen, R. (2021). Progress in enhanced fluidization process for particle coating via atomic layer deposition. *Chemical Engineering and Processing-Process Intensification, 159*, 108234.

Liang, X., Lynn, A. D., King, D. M., Bryant, S. J., & Weimer, A. W. (2009). Biocompatible interface films deposited within porous polymers by atomic layer deposition (ALD). *ACS applied materials & interfaces, 1*(9), 1988-1995.

Lim, G. (1997). On the conveying velocity of a vibratory feeder. *Computers & structures, 62*(1), 197-203.

Limtrakul, S., Rotjanavijit, W., & Vatanatham, T. (2007). Lagrangian modeling and simulation of effect of vibration on cohesive particle movement in a fluidized bed. *Chemical Engineering Science, 62*(1-2), 232-245.

Liu, D., van Wachem, B. G., Mudde, R. F., Chen, X., & van Ommen, J. R. (2016a). An adhesive CFD-DEM model for simulating nanoparticle agglomerate fluidization. *AIChE journal, 62*(7), 2259-2270.

Liu, D., van Wachem, B. G., Mudde, R. F., Chen, X., & van Ommen, J. R. (2016b). Characterization of fluidized nanoparticle agglomerates by using adhesive CFD-DEM simulation. *Powder technology, 304*, 198-207.

Liu, P., Brown, T., Fullmer, W. D., Hauser, T., Hrenya, C., Grout, R., & Sitaraman, H. (2016). *Comprehensive Benchmark Suite for Simulation of Particle Laden Flows Using the Discrete Element Method with Performance Profiles from the Multiphase Flow with Interface eXchanges (MFiX) Code*. Retrieved from

Liu, P., & Hrenya, C. M. (2014). Challenges of DEM: I. Competing bottlenecks in parallelization of gas–solid flows. *Powder technology, 264*, 620-626.

Llop, M. F., Madrid, F., Arnaldos, J., & Casal, J. (1996). Fluidization at vacuum conditions. A generalized equation for the prediction of minimum fluidization velocity. *Chemical Engineering Science, 51*(23), 5149-5157. doi:https://doi.org/10.1016/S0009-2509(96)00351-X

Longrie, D., Deduytsche, D., & Detavernier, C. (2014). Reactor concepts for atomic layer deposition on agitated particles: A review. *Journal of Vacuum Science & Technology A: Vacuum, Surfaces, and Films, 32*(1), 010802.

Longrie, D., Deduytsche, D., Haemers, J., Driesen, K., & Detavernier, C. (2012). A rotary reactor for thermal and plasma-enhanced atomic layer deposition on powders and small objects. *Surface and Coatings Technology, 213*, 183-191.

Lonie, K. (1983). A practical model for sub-resonant vibratory feeders. *Bulk Solids Handling, 3*(4), 741-746.

Loth, E. (2008). Compressibility and rarefaction effects on drag of a spherical particle. *AIAA journal, 46*(9), 2219-2228.

Lu, B., & Torquato, S. (1992). Lineal-path function for random heterogeneous materials. *Physical Review A, 45*(2), 922.

Lu, L., Gao, X., Dietiker, J.-F., Shahnam, M., & Rogers, W. A. (2022). MFiX based multi-scale CFD simulations of biomass fast pyrolysis: A review. *Chemical Engineering Science, 248*, 117131.

Lun, C., & Savage, S. (1987). A simple kinetic theory for granular flow of rough, inelastic, spherical particles.

Ma, J., van Ommen, J. R., Liu, D., Mudde, R. F., Chen, X., Pan, S., & Liang, C. (2019). Fluidization dynamics of cohesive Geldart B particles. Part II: Pressure fluctuation analysis. *Chemical Engineering Journal, 368*, 627-638.

Macdonald, I., El-Sayed, M., Mow, K., & Dullien, F. (1979). Flow through porous media-the Ergun equation revisited. *Industrial & Engineering Chemistry Fundamentals, 18*(3), 199-208.

MacDonald, S., & Stone, B. (1989). *An investigation of vibratory feeders.* Paper presented at the Proceedings of international conference of noise and vibration.

Mansour, W., Massoud, M., Morcos, W., & Lauzier, C. (1975). The mechanism of conveyance with bristled tracks.

Marring, E., Hoffmann, A., & Janssen, L. (1994). The effect of vibration on the fluidization behaviour of some cohesive powders. *Powder technology, 79*(1), 1-10.

Matte, H. R., Subrahmanyam, K., Rao, K. V., George, S. J., & Rao, C. (2011). Quenching of fluorescence of aromatic molecules by graphene due to electron transfer. *Chemical Physics Letters, 506*(4-6), 260-264.

Mawatari, Y., Tsunekawa, M., Tatemoto, Y., & Noda, K. (2005). Favorable vibrated fluidization conditions for cohesive fine particles. *Powder technology, 154*(1), 54-60.

Maydannik, P., Kääriäinen, T., & Cameron, D. (2011). An atomic layer deposition process for moving flexible substrates. *Chemical Engineering Journal, 171*(1), 345-349.

Maydannik, P. S., Kaariainen, T. O., & Cameron, D. C. (2012). Continuous atomic layer deposition: Explanation for anomalous growth rate effects. *Journal of Vacuum Science & Technology A: Vacuum, Surfaces, and Films, 30*(1), 01A122.

Maydannik, P. S., Kääriäinen, T. O., Lahtinen, K., Cameron, D. C., Söderlund, M., Soininen, P., . . . Zeng, X. (2014). Roll-to-roll atomic layer deposition process for flexible electronics encapsulation applications. *Journal of Vacuum Science & Technology A: Vacuum, Surfaces, and Films, 32*(5), 051603.

McCormick, J., Cloutier, B., Weimer, A., & George, S. (2007). Rotary reactor for atomic layer deposition on large quantities of nanoparticles. *Journal of Vacuum Science & Technology A: Vacuum, Surfaces, and Films, 25*(1), 67-74.

Mészáros, I. (2006). Magnetic characterisation of duplex stainless steel. *Physica B: Condensed Matter, 372*(1-2), 181-184.

Metcalf, T. H., Knight, J. B., & Jaeger, H. M. (1997). Standing wave patterns in shallow beds of vibrated granular material. *Physica A: Statistical Mechanics and its Applications, 236*(3-4), 202-210.

Meyer, B. A., & Smith, D. W. (1985). Flow through porous media: comparison of consolidated and unconsolidated materials. *Industrial & Engineering Chemistry Fundamentals, 24*(3), 360-368.

Millán, J. M. V. (2012). *Fluidization of fine powders: cohesive versus dynamical aggregation* (Vol. 18): Springer Science & Business Media.

Mishra, I., Liu, P., Shetty, A., & Hrenya, C. M. (2020). On the use of a powder rheometer to probe defluidization of cohesive particles. *Chemical Engineering Science, 214*, 115422.

Mishra, I., Molnar, M. J., Hwang, M. Y., Shetty, A., & Hrenya, C. M. (2022). Experimental validation of the extraction of a particle-particle cohesion model (square-force) from simple bulk measurements (defluidization in a rheometer). *Chemical Engineering Science*, 117782.

Molerus, O. (1982). Interpretation of Geldart's type A, B, C and D powders by taking into account interparticle cohesion forces. *Powder technology, 33*(1), 81-87.

Mollon, G., & Zhao, J. (2014). 3D generation of realistic granular samples based on random fields theory and Fourier shape descriptors. *Computer Methods in Applied Mechanics and Engineering, 279*, 46-65.

Mori, D., & Ishigami, G. (2015). Excavation model of soil sampling device based on particle image velocimetry. *Journal of Terramechanics, 62*, 19-29. doi:https://doi.org/10.1016/j.jterra.2015.02.001

Moskowitz, L. (1959). Vibratory feeding and conveying. *Automation, 6*, 78-82.

Mousa, M. B. M., Ovental, J. S., Brozena, A. H., Oldham, C. J., & Parsons, G. N. (2018). Modeling and experimental demonstration of high-throughput flow-through spatial atomic layer deposition of Al2O3 coatings on textiles at atmospheric pressure. *Journal of Vacuum Science & Technology A: Vacuum, Surfaces, and Films, 36*(3), 031517.

Munjiza, A., & Cleary, P. W. (2009). Industrial particle flow modelling using discrete element method. *Engineering Computations*.

Nadler, S., Bonnefoy, O., Chaix, J.-M., Thomas, G., & Gelet, J.-L. (2011). Parametric study of horizontally vibrated grain packings. *The European Physical Journal E, 34*(7), 1-10.

Nam, C. H., Pfeffer, R., Dave, R. N., & Sundaresan, S. (2004). Aerated vibrofluidization of silica nanoparticles. *AIChE journal, 50*(8), 1776-1785.

Navarro, H. A., & de Souza Braun, M. P. (2013). Determination of the normal spring stiffness coefficient in the linear spring–dashpot contact model of discrete element method. *Powder technology, 246*, 707-722.

Okabe, S., Kamiya, Y., Tsujikado, K., & Yokoyama, Y. (1985). Vibratory feeding by nonsinusoidal vibration—optimum wave form.

Okabe, S., Yokoyama, Y., & Boothroyd, G. (1988). Analysis of vibratory feeding where the track has directional friction characteristics. *The International Journal of Advanced Manufacturing Technology, 3*(4), 73-85.

Opila, R. L., & Oleson, A. P. (1963). Method for modifying a carbohydrate material: Google Patents.

Ottino, J., & Khakhar, D. (2000). Mixing and segregation of granular materials. *Annual review of fluid mechanics, 32*(1), 55-91.

Oviroh, P. O., Akbarzadeh, R., Pan, D., Coetzee, R. A. M., & Jen, T.-C. (2019). New development of atomic layer deposition: processes, methods and applications. *Science and technology of advanced materials, 20*(1), 465-496.

Pak, H., & Behringer, R. (1993). Surface waves in vertically vibrated granular materials. *Physical review letters, 71*(12), 1832.

Pan, D. (2019). Numerical study on the effectiveness of precursor isolation using N2 as gas barrier in spatial atomic layer deposition. *International Journal of Heat and Mass Transfer, 144*, 118642.

Pan, D., Jen, T.-C., & Yuan, C. (2016). Effects of gap size, temperature and pumping pressure on the fluid dynamics and chemical kinetics of in-line spatial atomic layer deposition of Al2O3. *International Journal of Heat and Mass Transfer, 96*, 189-198.

Papadikis, K., Bridgwater, A., & Gu, S. (2008). CFD modelling of the fast pyrolysis of biomass in fluidised bed reactors, Part A: Eulerian computation of momentum transport in bubbling fluidised beds. *Chemical Engineering Science, 63*(16), 4218-4227.

Parameswaran, M., & Ganapathy, S. (1979). Vibratory conveying—Analysis and design: A review. *Mechanism and Machine Theory, 14*(2), 89-97.

Paranjpe, A., Gopinath, S., Omstead, T., & Bubber, R. (2001). Atomic layer deposition of AlO x for thin film head gap applications. *Journal of the Electrochemical Society, 148*(9), G465.

Parker, J. M. (2016). *A Baseline Drag Force Correlation for CFD Simulations of Gas-Solid Systems.* Paper presented at the 2016 NETL Workshop on Multiphase Flow ScienceMorgantown, WV.

Parsons, G. N., Elam, J. W., George, S. M., Haukka, S., Jeon, H., Kessels, W., . . . Rossnagel, S. M. (2013). History of atomic layer deposition and its relationship with the American Vacuum Society. *Journal of Vacuum Science & Technology A: Vacuum, Surfaces, and Films, 31*(5), 050818.

Patankar, S. V. (2018). *Numerical heat transfer and fluid flow*: CRC press.

Philippsen, C. G., Vilela, A. C. F., & Dalla Zen, L. (2015). Fluidized bed modeling applied to the analysis of processes: review and state of the art. *Journal of Materials Research and Technology, 4*(2), 208-216.

Pinon, A., Wierez-Kien, M., Craciun, A., Beyer, N., Gallani, J., & Rastei, M. (2016). Thermal effects on van der Waals adhesive forces. *Physical Review B, 93*(3), 035424.

Podczeck, F., & Mia, Y. (1996). The influence of particle size and shape on the angle of internal friction and the flow factor of unlubricated and lubricated powders. *International Journal of Pharmaceutics, 144*(2), 187-194.

Poodt, P., Cameron, D. C., Dickey, E., George, S. M., Kuznetsov, V., Parsons, G. N., . . . Vermeer, A. (2012). Spatial atomic layer deposition: A route towards further industrialization of atomic layer deposition. *Journal of Vacuum Science & Technology A: Vacuum, Surfaces, and Films, 30*(1), 010802.

Poodt, P., Lankhorst, A., Roozeboom, F., Spee, K., Maas, D., & Vermeer, A. (2010). High-speed spatial atomic-layer deposition of aluminum oxide layers for solar cell passivation. *Advanced materials, 22*(32), 3564-3567.

Portillo, P. M., Ierapetritou, M. G., & Muzzio, F. J. (2008). Characterization of continuous convective powder mixing processes. *Powder technology, 182*(3), 368-378.

Poux, M., Fayolle, P., Bertrand, J., Bridoux, D., & Bousquet, J. (1991). Powder mixing: some practical rules applied to agitated systems. *Powder technology, 68*(3), 213-234.

Puurunen, R. L. (2004). Random deposition as a growth mode in atomic layer deposition. *Chemical Vapor Deposition, 10*(3), 159-170.

Puurunen, R. L. (2005). Surface chemistry of atomic layer deposition: A case study for the trimethylaluminum/water process. *Journal of applied physics, 97*(12), 9.

Rabinovich, Y. I., Adler, J. J., Ata, A., Singh, R. K., & Moudgil, B. M. (2000). Adhesion between nanoscale rough surfaces: I. Role of asperity geometry. *Journal of colloid and interface science, 232*(1), 10-16.

Raganati, F., Chirone, R., & Ammendola, P. (2018). Gas–solid fluidization of cohesive powders. *Chemical Engineering Research and Design, 133*, 347-387.

Redford, A., & Boothroyd, G. (1967). Vibratory feeding. *Proceedings of the Institution of Mechanical Engineers, 182*(1), 135-152.

Reid, R. C., Prausnitz, J. M., & Poling, B. E. (1987). The properties of gases and liquids.

Remy, B., Glasser, B. J., & Khinast, J. G. (2010). The effect of mixer properties and fill level on granular flow in a bladed mixer. *AIChE journal, 56*(2), 336-353.

Ritala, M., & Leskelä, M. (2002). Atomic layer deposition *Handbook of Thin Films* (pp. 103-159): Elsevier.

Rogers, S. R., Bowden, D., Unnikrishnan, R., Scenini, F., Preuss, M., Stewart, D., . . . Dye, D. (2020). The interaction of galling and oxidation in 316L stainless steel. *Wear, 450*, 203234.

Sandlin, M. J. (2017). *Experimental verification of numerical models of granular flow through wire mesh screens.* Georgia Institute of Technology.

Sarno, L., Carravetta, A., Tai, Y. C., Martino, R., Papa, M. N., & Kuo, C. Y. (2018). Measuring the velocity fields of granular flows – Employment of a multi-pass two-dimensional particle image velocimetry (2D-PIV) approach. *Advanced Powder Technology, 29*(12), 3107-3123. doi:https://doi.org/10.1016/j.apt.2018.08.014

Schertz, C. E. (1962). *Motion of granular material on an oscillating conveyor*: Iowa State University.

Schofield, R., & Yousuf, M. (1973). The design of a linear "out of phase" vibratory conveyor.

Schulze, D. (2003). Time-and Velocity-Dependent Properties of Powders Effecting Slip-Stick Oscillations. *Chemical Engineering & Technology: Industrial Chemistry-Plant Equipment-Process Engineering-Biotechnology, 26*(10), 1047-1051.

Schulze, D. (2008). Powders and bulk solids. *Behaviour, characterization, storage and flow. Springer, 22*.

Seville, J. P. K., Willett, C. D., & Knight, P. C. (2000). Interparticle forces in fluidisation: a review. *Powder technology, 113*(3), 261-268. doi:https://doi.org/10.1016/S0032-5910(00)00309-0

Sgriccia, M. T. (1953). Feeder bowl: Google Patents.

Shaeri, M. R., Jen, T.-C., & Yuan, C. Y. (2015). Reactor scale simulation of an atomic layer deposition process. *Chemical Engineering Research and Design, 94*, 584-593.

Shahmohammadi, M., Mukherjee, R., Sukotjo, C., Diwekar, U. M., & Takoudis, C. G. (2022). Recent Advances in Theoretical Development of Thermal Atomic Layer Deposition: A Review. *Nanomaterials, 12*(5), 831.

Sharma, K., Hall, R. A., & George, S. M. (2015). Spatial atomic layer deposition on flexible substrates using a modular rotating cylinder reactor. *Journal of Vacuum Science & Technology A: Vacuum, Surfaces, and Films, 33*(1), 01A132.

Shen, L., & Chen, Z. (2007). Critical review of the impact of tortuosity on diffusion. *Chemical Engineering Science, 62*(14), 3748-3755.

Silbert, L. E., Ertaş, D., Grest, G. S., Halsey, T. C., Levine, D., & Plimpton, S. J. (2001). Granular flow down an inclined plane: Bagnold scaling and rheology. *Physical Review E, 64*(5), 051302.

Simsek, E., Wirtz, S., Scherer, V., Kruggel-Emden, H., Grochowski, R., & Walzel, P. (2008). An experimental and numerical study of transversal dispersion of granular material on a vibrating conveyor. *Particulate Science and Technology, 26*(2), 177-196.

Sloot, E., & Kruyt, N. P. (1996). Theoretical and experimental study of the transport of granular materials by inclined vibratory conveyors. *Powder technology, 87*(3), 203-210.

Smith, K., Butterbaugh, J., & Beaudoin, S. (2013). Effects of Coating Thickness on Particle Adhesion in Microelectronics-Based Systems. *ECS Journal of Solid State Science and Technology, 2*(11), P488.

Snyder, M. Q., Trebukhova, S. A., Ravdel, B., Wheeler, M. C., DiCarlo, J., Tripp, C. P., & DeSisto, W. J. (2007). Synthesis and characterization of atomic layer deposited titanium nitride thin films on lithium titanate spinel powder as a lithium-ion battery anode. *Journal of Power Sources, 165*(1), 379-385.

Sønsteby, H. H., Yanguas-Gil, A., & Elam, J. W. (2020). Consistency and reproducibility in atomic layer deposition. *Journal of Vacuum Science & Technology A: Vacuum, Surfaces, and Films, 38*(2), 020804.

Spencer, I. J. A., & Hall, R. A. (2018). Continuous spatial atomic layer deposition process and apparatus for applying films on particles: Google Patents.

Srinath, K., & Karmakar, R. (1988). Vibratory conveying by non-sinusoidal excitation. *Proceedings of the Institution of Mechanical Engineers, Part C: Journal of Mechanical Engineering Science, 202*(6), 405-408.

Standards, N. I. o., & Technology. (2022). NIST Chemistry WebBook, SRD 69.

Staniforth, J. N. (1982). Determination and handling of total mixes in pharmaceutical systems. *Powder technology, 33*(2), 147-159.

Stelzer, E. H. (2002). Beyond the diffraction limit? *Nature, 417*(6891), 806-807.

Straßburger, G., & Rehberg, I. (2000). Crystallization in a horizontally vibrated monolayer of spheres. *Physical Review E, 62*(2), 2517.

Strempel, V. E., Naumann d'Alnoncourt, R., Drieß, M., & Rosowski, F. (2017). Atomic layer deposition on porous powders with in situ gravimetric monitoring in a modular fixed bed reactor setup. *Review of Scientific Instruments, 88*(7), 074102.

Sullivan, J. F., & White, J. D. (1988). Apparatus and method for conveying material: Google Patents.

Sundaresan, S. (2000). Modeling the hydrodynamics of multiphase flow reactors: current status and challenges. *AIChE journal, 46*(6), 1102-1105.

Syamlal, M., Rogers, W., & OBrien, T. J. (1993). *MFIX documentation theory guide*. Retrieved from

Tahmasebpoor, M., de Martín, L., Talebi, M., Mostoufi, N., & van Ommen, J. R. (2013). The role of the hydrogen bond in dense nanoparticle–gas suspensions. *Physical Chemistry Chemical Physics, 15*(16), 5788-5793.

Tan, S., & Newton, J. (1990). Powder flowability as an indication of capsule filling performance. *International Journal of Pharmaceutics, 61*(1-2), 145-155.

Terao, H., & Sunakawa, H. (1984). Effects of oxygen and water vapour introduction during MOCVD growth of GaAlAs. *Journal of Crystal Growth, 68*(1), 157-162.

Thielicke, W. (2014). The flapping flight of birds. *Diss. University of Groningen*.

Thielicke, W., & Stamhuis, E. (2014). PIVlab–towards user-friendly, affordable and accurate digital particle image velocimetry in MATLAB. *Journal of Open Research Software, 2*(1).

Tjaden, B., Cooper, S. J., Brett, D. J., Kramer, D., & Shearing, P. R. (2016). On the origin and application of the Bruggeman correlation for analysing transport phenomena in electrochemical systems. *Current opinion in chemical engineering, 12*, 44-51.

Tomadakis, M. M., & Robertson, T. J. (2005). Viscous permeability of random fiber structures: comparison of electrical and diffusional estimates with experimental and analytical results. *Journal of Composite Materials, 39*(2), 163-188.

Tsuji, Y., Kawaguchi, T., & Tanaka, T. (1993). Discrete particle simulation of two-dimensional fluidized bed. *Powder technology, 77*(1), 79-87.

Tsuji, Y., Tanaka, T., & Ishida, T. (1992). Lagrangian numerical simulation of plug flow of cohesionless particles in a horizontal pipe. *Powder technology, 71*(3), 239-250.

Tupolskikh, T., Gucheva, N., & Kirishiev, O. (2018). *Simulation of the process of movement of bulk material in a vibrating conveyor-mixer.* Paper presented at the MATEC Web of Conferences.

Tyagi, P., Goulet, T., Riso, C., & Garcia-Moreno, F. (2019). Reducing surface roughness by chemical polishing of additively manufactured 3D printed 316 stainless steel components. *The International Journal of Advanced Manufacturing Technology, 100*(9), 2895-2900.

Umbanhowar, P. B., Lueptow, R. M., & Ottino, J. M. (2019). Modeling segregation in granular flows. *Annual Review of Chemical and Biomolecular Engineering, 10*, 129-153.

Uryadov, G., Katterfeld, A., & Krause, F. (2008). DEM Simulation of the Bulk Solid Reaction on Vibratory Conveyors. *Bulk Europe*.

Vakis, A., Yastrebov, V., Scheibert, J., Nicola, L., Dini, D., Minfray, C., . . . Limbert, G. (2018). Modeling and simulation in tribology across scales: An overview. *Tribology International, 125*, 169-199.

Valdesueiro, D., Hettinga, H., Drijfhout, J. P., Lips, P., Meesters, G. M., Kreutzer, M. T., & Van Ommen, J. R. (2017). Tuning roughness and gloss of powder coating paint by encapsulating the coating particles with thin Al2O3 films. *Powder technology, 318*, 401-410.

Valverde, J. M., & Castellanos, A. (2006). Effect of vibration on agglomerate particulate fluidization. *AIChE journal, 52*(5), 1705-1714.

van der Hoef, M. A., van Sint Annaland, M., Deen, N., & Kuipers, J. (2008). Numerical simulation of dense gas-solid fluidized beds: a multiscale modeling strategy. *Annu. Rev. Fluid Mech., 40*, 47-70.

Van Ommen, J., & Goulas, A. (2019). Atomic layer deposition on particulate materials. *Materials Today Chemistry, 14*, 100183.

van Ommen, J. R., Kooijman, D., Niet, M. d., Talebi, M., & Goulas, A. (2015). Continuous production of nanostructured particles using spatial atomic layer deposition. *Journal of Vacuum Science & Technology A: Vacuum, Surfaces, and Films, 33*(2), 021513.

van Ommen, J. R., Valverde, J. M., & Pfeffer, R. (2012). Fluidization of nanopowders: a review. *Journal of nanoparticle research, 14*(3), 1-29.

Visser, J. (1972). On Hamaker constants: A comparison between Hamaker constants and Lifshitz-van der Waals constants. *Advances in colloid and interface science, 3*(4), 331-363.

Voigt, P., Haimi, E., Lahtinen, J., Cheah, Y. W., Mäkelä, E., Viinikainen, T., & Puurunen, R. L. (2019). Nickel supported on mesoporous zirconium oxide by atomic layer deposition: initial fixed-bed reactor study. *Topics in Catalysis, 62*(7), 611-620.

Wahl, E. A. (1967). Vibratory conveyor-mixer apparatus: Google Patents.

Wang, H., Zhou, T., Yang, J. S., Wang, J. J., Kage, H., & Mawatari, Y. (2010). Model for Calculation of Agglomerate Sizes of Nanoparticles in a Vibro-fluidized Bed. *Chemical Engineering & Technology: Industrial Chemistry-Plant Equipment-Process Engineering-Biotechnology, 33*(3), 388-394.

Wang, J. (2020). Continuum theory for dense gas-solid flow: A state-of-the-art review. *Chemical Engineering Science, 215*, 115428.

Wang, J., van der Hoef, M. A., & Kuipers, J. (2010). CFD study of the minimum bubbling velocity of Geldart A particles in gas-fluidized beds. *Chemical Engineering Science, 65*(12), 3772-3785.

Wang, X., Nie, Z., Gong, J., & Liang, Z. (2021). Random generation of convex aggregates for DEM study of particle shape effect. *Construction and Building Materials, 268*, 121468.

Wang, Y., Li, Z., Wang, J., Li, J., & Lin, Y. (2011). Graphene and graphene oxide: biofunctionalization and applications in biotechnology. *Trends in biotechnology, 29*(5), 205-212.

Wank, J. R., George, S. M., & Weimer, A. W. (2001). Vibro-fluidization of fine boron nitride powder at low pressure. *Powder technology, 121*(2-3), 195-204.

Wank, J. R., George, S. M., & Weimer, A. W. (2004). Nanocoating individual cohesive boron nitride particles in a fluidized bed by ALD. *Powder technology, 142*(1), 59-69.

Weidenbaum, S. S. (1958). Mixing of solids *Advances in Chemical Engineering* (Vol. 2, pp. 209-324): Elsevier.

Weimer, A. W. (2019). Particle atomic layer deposition. *Journal of nanoparticle research, 21*(1), 9.

Wes, G., Stemerding, S., & van Zuilichem, D. (1990). Control of flow of cohesive powders by means of simultaneous aeration, and vibration. *Powder technology, 61*(1), 39-49.

West, B., O'Connor, D., Parno, M., Krackow, M., & Polashenski, C. (2021). Bonded discrete element simulations of sea ice with non-local failure: Applications to Nares Strait. *Journal of Advances in Modeling Earth Systems*, e2021MS002614.

Wilson, C., McCormick, J., Cavanagh, A., Goldstein, D., Weimer, A., & George, S. (2008). Tungsten atomic layer deposition on polymers. *Thin Solid Films, 516*(18), 6175-6185.

Winkler, G. (1978). Analysing the vibrating conveyor. *International Journal of Mechanical Sciences, 20*(9), 561-570. doi:https://doi.org/10.1016/0020-7403(78)90014-0

Winkler, G. (1979). Analysing the hopping conveyor. *International Journal of Mechanical Sciences, 21*(11), 651-658.

Woodcock, C., & Mason, J. (2012). *Bulk solids handling: an introduction to the practice and technology*: Springer Science & Business Media.

Xu, P., & Yu, B. (2008). Developing a new form of permeability and Kozeny–Carman constant for homogeneous porous media by means of fractal geometry. *Advances in water resources, 31*(1), 74-81.

Xu, Y., Musser, J., Li, T., Padding, J. T., & Rogers, W. A. (2017). Particles climbing along a vertically vibrating tube: numerical simulation using the Discrete Element Method (DEM). *Powder technology, 320*, 304-312.

Yang, R., Zou, R., Yu, A., & Choi, S. (2008). Characterization of interparticle forces in the packing of cohesive fine particles. *Physical Review E, 78*(3), 031302.

Yanguas-Gil, A., & Elam, J. W. (2011). Diffusion-Reaction Model of ALD in Nanostructured Substrates: Analytic Approximations to Dose Times as a Function of the Surface Reaction Probability. *ECS Transactions, 41*(2), 169.

Yanguas-Gil, A., & Elam, J. W. (2014a). Analytic expressions for atomic layer deposition: Coverage, throughput, and materials utilization in cross-flow, particle coating, and spatial atomic layer deposition. *Journal of Vacuum Science & Technology A: Vacuum, Surfaces, and Films, 32*(3), 031504.

Yanguas-Gil, A., & Elam, J. W. (2014b). A Markov chain approach to simulate atomic layer deposition chemistry and transport inside nanostructured substrates. *Theoretical Chemistry Accounts, 133*(4), 1-13.

Yanguas-Gil, A., Libera, J. A., & Elam, J. W. (2021). Reactor scale simulations of ALD and ALE: Ideal and non-ideal self-limited processes in a cylindrical and a 300 mm wafer cross-flow reactor. *Journal of Vacuum Science & Technology A: Vacuum, Surfaces, and Films, 39*(6), 062404.

Yanguas-Gil, A., & Elam, J. W. (2012). Self-Limited Reaction-Diffusion in Nanostructured Substrates: Surface Coverage Dynamics and Analytic Approximations to ALD Saturation Times. *Chemical Vapor Deposition, 18*(1-3), 46-52.

Yao, W., Guangsheng, G., Fei, W., & Jun, W. (2002). Fluidization and agglomerate structure of SiO2 nanoparticles. *Powder technology, 124*(1), 152-159. doi:https://doi.org/10.1016/S0032-5910(01)00491-0

Yaraghi, A., Ebrahimi, M., Ein-Mozaffari, F., & Lohi, A. (2018). Mixing assessment of non-cohesive particles in a paddle mixer through experiments and discrete element method (DEM). *Advanced Powder Technology, 29*(11), 2693-2706.

Ylilammi, M., Ylivaara, O. M., & Puurunen, R. L. (2018). Modeling growth kinetics of thin films made by atomic layer deposition in lateral high-aspect-ratio structures. *Journal of applied physics, 123*(20), 205301.

Zaera, F. (2012). The surface chemistry of atomic layer depositions of solid thin films. *The journal of physical chemistry letters, 3*(10), 1301-1309.

Zhang, Y., Ding, Y., & Christofides, P. D. (2019). Multiscale computational fluid dynamics modeling of thermal atomic layer deposition with application to chamber design. *Chemical Engineering Research and Design, 147*, 529-544.

Zhang, Y., Ding, Y., & Christofides, P. D. (2020). Multiscale computational fluid dynamics modeling and reactor design of plasma-enhanced atomic layer deposition. *Computers & Chemical Engineering, 142*, 107066.

Zhang, Y., Lim, E. W. C., & Wang, C.-H. (2007). Pneumatic transport of granular materials in an inclined conveying pipe: Comparison of computational fluid dynamics− discrete element method (CFD−DEM), electrical capacitance tomography (ECT), and particle image Velocimetry (PIV) results. *Industrial & Engineering Chemistry Research, 46*(19), 6066-6083.

Zhao, Y., Phalswal, P., Shetty, A., & RP, K. A. (2021). Effects of Powder Vibration and Time Consolidation on Soft and Hard Wheat Flour Properties. *KONA Powder and Particle Journal*, 2021007.

Zhao, Z., Liu, D., Ma, J., & Chen, X. (2020). Fluidization of nanoparticle agglomerates assisted by combining vibration and stirring methods. *Chemical Engineering Journal, 388*, 124213.

Zhong, R., Xu, M., Netto, R. V., & Wille, K. (2016). Influence of pore tortuosity on hydraulic conductivity of pervious concrete: Characterization and modeling. *Construction and Building Materials, 125*, 1158-1168.

Zhu, C., Yu, Q., Dave, R. N., & Pfeffer, R. (2005). Gas fluidization characteristics of nanoparticle agglomerates. *AIChE journal, 51*(2), 426-439.